Ph. D Thesis

Processing and characterization of novel biodegradable and bioresorbable PLA/Mg composites for osteosynthesis

Author: Sandra Carolina Cifuentes

SUPERVISORS

José Luis González Carrasco (CENIM-CSIC)
Mª del Rosario Benavente Castro (ICTP-CSIC)

SUPERVISOR AT UC3M

Elena Gordo

Centro Nacional de Investigaciones Metalúrgicas (CENIM-CSIC)

Instituto de Ciencia y Tecnología de Polímeros (ICTP-CSIC)

Leganés, Madrid, a ____ de _____ de 2015

CSIC
CONSEJO SUPERIOR DE INVESTIGACIONES CIENTÍFICAS

Universidad Carlos III de Madrid
www.uc3m.es

Ph D Thesis

Processing and characterization of novel biodegradable and bioresorbable PLA/Mg composites for medical applications

Author: Sandra Carolina Cifuentes Cuéllar

Supervisors: José Luis González Carrasco

Mª Rosario Benavente Castro

Firma del Tribunal Calificador:

Firma

Presidente:

Vocal:

Secretario:

Calificación:

Leganés, Madrid, a ____ de _____ de 2015

Acknowledgements / Agradecimientos

Este es el fin de una etapa llena de aprendizajes y de buenas anécdotas. Alcanzar esta meta no hubiera sido posible sin el apoyo de muchas personas que me han obsequiado herramientas para sortear los obstáculos que he encontrado en el camino y que han estado a mi lado para celebrar los éxitos y para aprender de los fracasos. Sólo quiero darles las gracias de corazón a todos aquellos que han sido parte de este asombroso viaje y que han sido testigos y partícipes de mi evolución como persona y como científica.

A mis directores de tesis, José Luis y Charo por haber confiado en mí, por sus enseñanzas para la vida, por ser humanos, por formarme como científica, por transmitirme su conocimiento con cariño, motivación e ilusión. Especialmente a Charo, gracias por habernos abierto desinteresadamente las puertas del ICTP, esta tesis no habría sido lo mismo sin la valiosa colaboración con ustedes.

A mis suegros, Loli y Eduardo porque sin su ayuda, apoyo y cariño no lo habría logrado. Porque su influencia en mí me hace cada vez mejor persona, porque aprendo cada vez más de ustedes, porque su familia es mi modelo, porque adoro lo feliz que hacen a Sofia, porque simplemente los admiro y quiero mucho.

A mi familia, papi, mami, Andre, abuelita, tita Nelly porque sus abrazos se sienten desde lolejos, porque me han dado las alas para poder volar, porque me han enseñado la virtud del esfuerzo y me han inculcado valores que me han llevado a ser quien soy hoy.

A Sandra Cabeza, por su amistad, por su cariño, comprensión, apoyo. Por ser la mejor ami ga en mis momentos más difícles, por su empatía, por los cafés y los helados.

A Amalia, por ser mi mano derecha, por su apoyo incondicional , por su lealtad, motivación y empuje.

A Judit por su amistad, su compañía, por su confianza, su canto, por su alegría.

A Sandra Barriuso, por su amistad, por la complicidad, la comprensión, por la tortilla de patatas y el gazpacho.

A Eimear, por su gran filosofía de vida, por su hermosa energía, por su apoyo, ánimo, consejos, por su amistad que no conoce fronteras.

A Marcela Lieblich por sus consejos, por la música, el arte, por la cultura, por los libros, por Roma

A Vicente Lorenzo, por su motivación, por transmitir su pasión por enseñar, por emocionarse con las matemáticas, por abrirme las puertas de su laboratorio, por las dudas resueltas y las huellas impresas.

A Raquel Gavilán, por haberme hecho recordar la motivación, ilusión y amor por la ciencia, por su enorme talento fotográfico, por el arte, por su optimismo.

A Javier Hidalgo por su amabilidad, por enseñarme y ayudarme con el equipo y los ensayos de reología y por su gran ejemplo.

A Emilio Frutos, por enseñarme a usar el indentador, por su tiempo, por su motivación, por sus ideas.

A Elena Gordo por su guía, total apoyo y dísposición de colaboracíón y por el ánimo.

A Alberto, Esther, Kesman, Edurne, Elvira, Marcos, Floppy porque he aprendido de cada uno de ustedes, porque hemos recorrido juntos este camino, porque hemos compartido sueños, frustraciones, alegrías y tristezas.

A Tim Osswald, por haberme abierto las puertas de su centro, por su apoyo, por creer en mí, por las carreras hasta Picnic Point.

A Nora Catalina y Valerie Abreu por haber sido mi apoyo durante mi estancia en Madison, por las barbacoas, por Monona Terrace, por contagiarme su espíritu soñador y echado pa´lante.

A Elizabeth Rangel y Vanessa Avenza, por la inmensa suerte de haberlas conocido en el máster del ICTP, por su apoyo incondicional, por su optimismo. Por ayudarme a relativizar las cosas, por ser una gran influencia en mi vida.

A los excelentes profesionales que componen los servicios generales (Esperanza Benito), taller de mantenimiento (Alberto) y laboratorio de caracterización (Justyna) del ICTP, muchas gracias por su excelente trabajo, puntualidad y buena disposición. A mis compañeros del departamento de Química y Física de polímeros, especialmente a Antonio por su ayuda conlas medidas de viscosidad, Kike y Tomás por su ayuda con los DSC´s y por compartir las hermosas experiencias de la paternidad, Ernesto Pérez por resolver mis dudas con los Rayos cX, infinitas gracias.

A mis compañeros del CENIM, los de Metalurgia física: Jesús Chao por su guía, orientación y enseñanzas con los ensayos de propiedades mecánicas, a Gerardo y Ricardo, por sus consejos sobre las etapas de la vida y al laboratorio de microscopía, Paloma y Alfonso por su servicio. Los de reciclado de materiales: Félix, por su guía y orientación inicial sobre temas de degradación térmica. Los de corrosión: Alejandro Samaniego por su ayuda con la puesta en marcha del laboratorio de liberación de hidrógeno. A los del taller y especialmente a Paco, por la fabricación de los moldes y la resolución de los problemas técnicos de los equipos.

Al gran equipo de BIOMAGCOM, Laura Saldaña, Beatriz Olalde, Garbiñe Atorrasagasti, Nerea Argarate, Ciro Pérez, Maria Coronada Fernández, Maria Luisa González, Amparo Gallardo, Miguel Angel Pacha, porque trabajar con ustedes ha sido toda una fortuna, gracias por haberme dado la oportunidad de aprender de ustedes.

Al CELERA Talent Team y especialmente a Oihana y Luna, porque conocerlos precisamente en la última etapa de mi tesis, fue el empujón que necesitaba para fortalecerme, recuperar energías y seguir adelante con optimismo y alegría.

Por último quisiera dedicar muy especialmente esta tesis a las personas más importantes para mí, los dos amores de mi vida, Rubén y Sofía, mi razón de ser y mi alegría. Porque su luz ilumina mi mundo, porque vivo por su sonrisa, porque hacen que cada día me sienta muy afortunada. Ustedes dos son el regalo más bonito que me ha dado la vida. LOS AMO.

Dedicated to the loves of my life

Rubén & Sofía

Your smile lights up my world

ABSTRACT

This doctoral thesis deals with the development of radically new composites for biodegradable and biocompatible implants of interest in bone repair, overcoming the disadvantages implicit in the use of permanent implants. The material consists of a polymeric matrix (Poly-L-lactic acid, Poly-L,D-lactic acid) reinforced with Mg or Mg5Zn particles, profiting advantages of both materials. The research of the feasibility of processing these composites by processes used in industry, and their suitability in osteosynthesis applications is the focus of this thesis. The project addresses the optimization of manufacturing techniques, design of PLA/Mg composites and their assessment for medical applications by means of physico-chemical, mechanical characterization and *in vitro* degradation tests.

Processability has been demonstrated by high temperature processing techniques such as extrusion/compression and injection moulding. Thermal stability characterization has demonstrated that Mg decreases the thermal degradation of the composite, being the effect more detrimental when increasing the volume fraction of Mg. In all cases, however, the upper limit of the processing window is well above 200 ºC, which enables the use of industrial processes for manufacturing PLA/Mg composites. The scaling up of the extrusion process using a mid-size extruder enabled the reduction of the thermal degradation of the material and allowed the incorporation of Mg particles up to a 15 wt.% within both polymeric matrices.

Mechanical characterization has been performed through compression/tensile tests and micro-indentation instrumented experiments, obtaining information on Young`s modulus and hardness over a wide range of strain rates. Mg particles have an effect during the elastic and post yield regimes but do not affect the yield point, as they increase the compressive Young´s modulus and the compressive strength at plateau of polymers but do not increase the compressive strength at yield. Instrumented indentation results show that addition of Mg particles increases the resistance of the polymer to plastic flow and hardness.

The *in vitro* studies demonstrate that the degradation rate of these materials depend in great extent on crystalline degree, Mg content and Mg particle shape. All the composites release hydrogen at rates that could be tolerated by human body and, when immersed in PBS, they did not surpass the buffer capacity of the solution. *In vitro* studies performed on composites with 10 wt.% of particles, show that the material composed by an amorphous PLDA matrix reinforced with spherical particles of Mg exhibits the best degradation behaviour. PLDA10Mg-SPH underwent a loss of compressive resistance of 4% after 7 days, and 40% after 28 days.

Novel PLA/Mg composites have a great potential as resorbable and biocompatible materials for osteosynthesis, due to their controllable degradation rate and adequate mechanical properties.

Abbreviations and symbols Aa - Ec	
A	Arrhenius pre-exponential constant
A	Projected contact area (indentation tests)
Al	Aluminium
Ag	Silver
ATR	Attenuated Total Reflectance
AZ31	Mg alloy containing Al 3% and Zn 1%
AZ91	Mg alloy containing Al 9% and Zn ~1%
c	Concentration (g/dl)
Ce	Cerium
CENIM	National Centre for Metallurgical Research
CLSM	Confocal Laser Scanning Microscopy
C_p	Specific heat capacity
CR	Cooling Rate
CR10	Cooling at a rate of 10 ºC/min
CR10F10	Heating at 10ºC/min after cooling at 10ºC/min
CSIC	Spanish National Research Council
Cu	Copper
Dry(t)	Sample weight after drying
DSC	Differential Scanning Calorimetry
DSI	Depth Sensing Indentation
E	Young´s modulus
E^*	Elastic modulus at plane strain conditions
E_a	Activation energy
E_c	Compressive Young´s Modulus (Compression tests)
E_c	Corrected Young´s Modulus (Indentation tests)
ECAP	Equal Channel Angular Pressing
E_c^{lower}	Composite elastic modulus predicted by a series (Reuss) arrangement
E_c^{upper}	Composite elastic modulus predicted by a parallel (Voigt) arrangement

Abbreviations and symbols Ef - Hc	
E_f	Elastic modulus of the particulate filler
E_i	Diamond indenter Young´s modulus
E_m	Elastic modulus of the matrix
E_r	Reduced elastic modulus (indentation tests)
E_{rc}	Corrected reduced Young´s modulus (indentation tests)
ETSII	Escuela Técnica Superior de Ingenieros Industriales - UPM
ε	Strain
$\dot{\varepsilon}$	Strain rate
η	Apparent viscosity of the melt
η_0	Zero viscosity
η_1, τ_2	Viscosity and retardation time (time dependent properties)
η*	Complex viscosity
[η]	Intrinsic viscosity
η_{inh}	Inherent viscosity
η_{red}	Reduced viscosity
f	Corrective factor in Hoffman Lauritzen equation
F10	First heating at 10ºC /min
f_c	Crystallinity degree
Fe	Iron
FTIR	Fourier Transform Infrared Spectroscopy
G	Radial growth of the spherulite
G_0	Pre-exponential factor in Hoffmann Lauritzen equation
$\dot{\gamma}$	Shear rate
h	Depth (indentation tests)
H	Berkovich Hardness
$\dot{h}$	Displacement rate (indentation tests)
HA	Hydroxyapatite
h_c	Contact depth (indentation tests)

Abbreviations and symbols Hcc - Nd	
ΔH_{cc}	Enthalpy of cold crystallization
$\dot{h}_{ih}$	Indenter displacement rate recorded at the end of the load hold (indentation tests)
ΔH_m	Enthalpy of melting
ΔH_m^0	Enthalpy of 100% crystalline PLLA
HPT	High Pressure Torsion
h_{red}	Normalized depth with respect to the initial depth (indentation tests)
ICTP	Institute of Polymer Science and Technology
IR	Infrared
IRR	Irregular shape particles
k	Thermal degradation rate constant (Chapter 4)
K_g	Nucleation constant related to the energy needed to form nuclei of critical size (Chapter 3)
LAE442	Mg alloy containing Li, Al and Rare earths
L/D	Length/Diameter ratio
Li	Lithium
LSHR	Large Strain Hot Rolling
Lu	Lutetium
m, k	Modified Cross mathematical model constants (Chapter 5)
m, K(T)	Ozawa kinetic parameters (Chapter 3)
Mass(0)	Initial weight of the sample
MFI	Melt Flow Index
Mg	Magnesium
Mn	Manganese
MSCs	Mesenchymal stem cells
M_v	Viscosity average molecular weight
n	Order of thermal degradation reaction (Chapter 4)
nCATS	National Centre for Advanced Tribology - Southampton
n, k	Avrami contants (Chapter 3)
Nd	Neodymium

Abbreviations and symbols Ni - Sc	
Ni	Nickel
ν	Poisson´s ratio (Chapter 6)
ν_i	Diamond indenter Poisson´s ratio
P	Load (indentation tests)
$\dot{P}$	Loading rate (indentation tests)
PBS	Phosphate Buffered Saline
PCL	Polycaprolactone
PDLA	Poly-D-lactic acid
PDLLA	Racemic poly-D,L-lactic acid
PEC	Polymer Engineering Center
PGA	Polyglycolic acid
PIM	Powder Injection Moulding
PLA	Polylactic acid
PLDA	Polylactic acid provided by Natureworks PLA 2002D
PLDLA	Poly-L,D-lactic acid
PLDLLA	Poly-L-lactide-co-D,L-lactide
PLGA	Poly lactic-co-glycolic acid
PLLA	Poly-L-lactic acid
Pr	Praseodymium
PSD	Position Sensitive Device
Q	Quenching thermal treatment
R	Gas constant (8.3143 kJ/mol)
RE	Rare Elements
ROP	Ring Opening Polymerization
S	Thermal treatment consisting on slow cooling from the melt at 3 ºC/min
S	Stiffness (indentation tests)
SBF	Simulated Body Fluid
S_c	Corrected contact stiffness (indentation tests)

Abbreviations and symbols Se - To	
Se	Selenium
SEM	Scanning Electrom Microscopy
Si	Silicon
SPD	Severe Plastic Deformation
SPH	Spherical particles
SSA	Strain softening amplitude
σ	Stress
σ_c	Compressive strength at Yield
$t_{1/2}$	Half crystallization time
T_{50}	Temperature of 50% weight loss in thermal degradation
T_c	Crystallization temperature
T_{cc}	Cold crystallization temperature
TCP	Tricalcium Phosphates
T_e	Final thermal degradation temperature
T_g	Glass transition temperature
TGA	Thermogravimetric analysis
Ti	Titanium
T_{inf}	Temperature where the mobility of the viscous flow stop
T_m	Melting temperature
T_m^0	The equilibrium melting temperature
TMP	Thermomechanical processes
T_o	Onset temperature of thermal degradation

Abbreviations and symbols Tp - Zr	
T_p	Temperature of greatest rate of change on the weight loss curve in thermal degradation
t_{red}	Normalized time with respect to the total hold time (indentation tests)
TT	Thermal treatment at 125 ºC during one hour
τ_y	Threshold shear stress
U	The energy required for the transport of macromolecules in the melt (Chapter 3)
U-Wisc	University of Wisconsin – Madison
v	Cooling rate
V_f	Particle volume fraction
W_0	Initial weight of sample during TGA experiments
WAXD	Wide-angle X-ray diffraction
WE43	Mg alloy containing Y and RE
WE54	Mg alloy containing Y and RE
Wet(t)	Sample weight after immersion time t
W_t	Weight of the sample at any time during the thermal degradation process
wt.%	Weight fraction
$X_c(t)$	Relative crystallinity
X_f	Filler strengthening factor
Y	Yttrium
ZEK100	Mg alloy containing Zn, RE and Zr
ZM21	Mg alloy containing Zn and Mn
Zn	Zinc
Zr	Zirconium

Table of contents

CHAPTER 1
INTRODUCTION

"Here and elsewhere we shall not obtain the best insight into things until we actually see them growing from the beginning"

Aristotle

Table of contents

1. INTRODUCTION

Society is facing great challenges in medicine due to the increasing world population and the inherent desire of mankind to maximize life expectancy. The demand for orthopaedic implants is closely linked to an aging population and also related to the increasing number of bone fractures that result from sports injuries and accidents. According to data from the Orthopaedic Industry (Report 2009 – 2010), more than 50 million fractures occur worldwide every year, and more than 8 million fracture repair procedures were performed globally in 2009 [1]. Based on population demographics, statistics show that in the next decade the incidence of fractures will likely not slow. More than seven thousand millions inhabitants of the world will continue to be active and grow old.

The overall concern for healthcare spending makes hospitals adopt some strategies to decrease costs, but without neglecting their active involvement in improving the quality of life of patients. This situation makes palpable the need of gathering efforts to provide patients with osteosynthesis implants that satisfy their requirements and simultaneously reduce costs of medical devices, surgical procedures and recovery treatments to a minimum.

1.1 Osteosynthesis implants

The objective of an osteosynthesis implant is the anatomical repair together with the functional restoration. This means that plates and screws that are used for bone fixation have to support and join the bone fragments and with this induce the healing of the tissue. To accomplish their function, the implants have to combine excellent biocompatibility with long-term biomechanical behaviour. They have to be strong but flexible in order to resist pressurized load and also deformation [2, 3].

Titanium alloys (Ti-6Al-4V among others) have been since the 1980's the key materials for this application, due to their chemical passivity, excellent biocompatibility and because they have a good long-term biomechanical performance [2]. However, permanent implants present some disadvantages, which represent serious nuisances for the patients. After the tissue has sufficiently healed a second surgical procedure is often required to remove the implant to avoid detrimental side effects associated with the ion release or inhomogeneous stress transfer (stress shielding) due to the higher Young´s modulus of Ti in comparison with cortical bone. These effects can reduce the stimulation of new bone growth and remodeling [4]. Complications related to thermal conductivity, metal hypersensitivity, chemical carcinogenesis, and/or infection can also occur and make it necessary to remove the implant [5]. The procedure of removing the implant may be challenging and lead to complications, such as neurovascular injury, refracture,

or recurrence of deformity [6] (Figure 1.1). Moreover, the use of permanent implants is restricted for young patients, because they would inhibit the bone growth [7, 8].

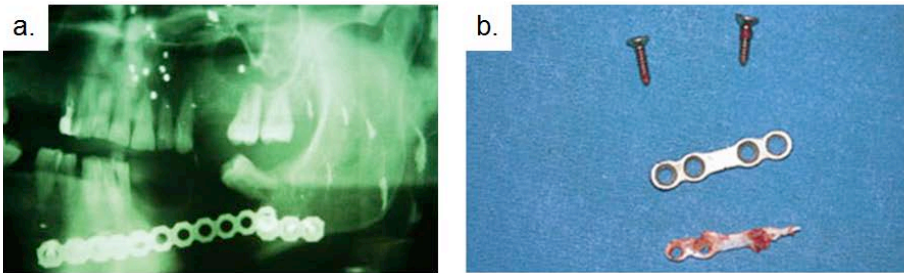

Figure 1.1. Titanium plate fracture (a) and removal of a miniplate with bone neoformation over it (b) (Figures modified from Acero *et al.* [2])

The development of biodegradable and bioresorbable materials seeks to overcome the disadvantages implicit in the use of permanent implants. New materials for osteosynthesis must fulfill an additional requirement: to be metabolized by the human body without leaving trace, and gradually lose their mechanical strength while the bone tissue is regenerated. In that way, the system bone + implant can maintain its mechanical strength (Figure 1.2). To accomplish this, there are three challenges to be addressed: good mechanical properties, control of degradation times and the biocompatibility of degradation products [9].

In this regard many materials have appeared as potential candidates for the development of bioresorbable implants. Within the polymers, the poly (α-hydroxy acids) are the most studied and the ones that are currently used for surgical implants [10, 11] . Among the metals, magnesium (Mg) and its alloys have emerged as a possible solution [12]. On the side of the ceramic materials, studies emphasize on calcium phosphates, hydroxyapatite and bioglasses, but have mainly been used as bone graft substitutes rather than bone fixation implants [13].

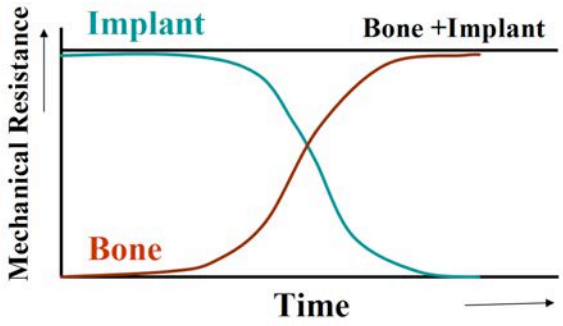

Figure 1.2 Ideal behaviour of the system bone + implant

1.1.1 Poly (α-hydroxyacids) as biodegradable materials for osteosynthesis implants

The preferred materials for biodegradable implants come from the poly (α-hydroxy acids) family. These materials are polyesters with aliphatic ester linkages in their backbone that are susceptible to hydrolysis. The most commonly used in surgical applications are polyglycolic acid (PGA) and polylactic acid (PLA) (Figure 1.3).

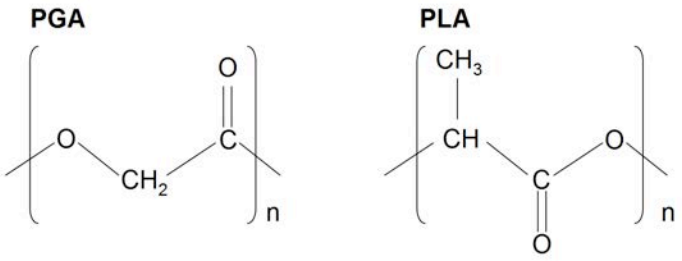

Figure 1.3 Structural formulas of polyglycolic acid (PGA) and polylactic acid (PLA)

PGA presents excellent mechanical properties, being stiffer than PLA. Its Young's modulus can reach values of approximately 7 GPa. Therefore, the first generation of biodegradable implants was made out of PGA [14]. However, it degrades rapidly forming glycolic acid and releasing debris out from the implant causing inflammation from a foreign body reaction to the surrounding tissue [15, 16]. Pure PGA is no longer considered to be suitable for orthopaedic implants, but it is used for surgical sutures. PLA degrades at a much slower rate, and has become the next widely utilized material for osteosynthesis. Copolymers combining PLA with PGA, poly lactic-co-glycolic acid (PLGA), are being developed to overcome the drawbacks of PGA in bone fixation [17].

The idea of using PLA for orthopaedic implants was proposed by Kulkarni et al. in 1966, almost 50 years ago [18] and significance advances have been made since then. In the 1970's, Cutright et al. performed the first experimental study that used polylactic acid for osteosynthesis [19]. During the 1980's, the suitability of PLA plates and screws was tested in animals with promising results that led to various clinical trials [20-23]. Osteosynthesis implants made of polylactic acid have gained US Food and Drug Administration (FDA) approval for clinical use [24], and they are currently commercially available. They have demonstrated to be biocompatible and to degrade into non-toxic components with controllable rates. In paediatric cranio-maxillofacial surgery, biodegradable polymers have totally replaced titanium alloys [25].

Unlike PGA, PLA is constituted by chiral molecules that exist in two optically active forms: L- and D-. PLA can be produced by condensation polymerization from the basic building block

lactic acid or via ring-opening polymerization (ROP) that converts lactide – the cyclic dimer of lactic acid (Figure 1.4) – to PLA. ROP has been the preferred route to produce PLA for biomedical applications [26]. Polymerization of L-lactide produces poly-L-lactic acid, also named poly-L-lactide (PLLA). Copolymerization of mixtures of L-lactide with D-lactide in equal proportions leads to the synthesis of the racemic polylactide (PDLLA). Copolymerization of L-lactide and D,L-lactide in different proportions produce non-racemic copolymers poly(L-lactide-co-D,L-lactide) (PLDLLA). The ratio of L- to the D-isomer influences the ultimate properties of the material. The ability to control the stereochemical architecture allows control over the degree of crystallinity, mechanical properties, degradation rate, and the processing temperatures of the material. Therefore a great variety of products are offered that are specifically tailored to each processing and application. The most common L-lactide : D-lactide mixtures in the orthopaedic literature are 70:30, 80:20, 85:15 and 96:4 [27].

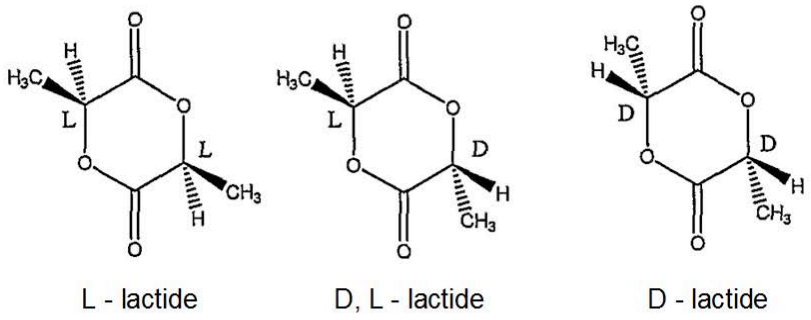

Figure 1.4 Cyclic dimmers of lactic acid: L-lactide, D-lactide and D,L-lactide

1.1.1.1 Processing of polylactic acid

PLA can be processed similar to any engineering thermoplastic. The material can be melted to form fibers, rods or moulded parts. PLA can be extruded, injection moulded, compression moulded, or solvent spun or cast. Processed material can also be machined into final parts [28].

Special care should be taken due to the sensitivity of polymer bonds to hydrolysis and to depolymerization induced by temperature [26]. To avoid hydrolytic degradation during melt processing, the contact of the polymer with moisture should be prevented and/or the polymer should be dried before thermally processing. Processing temperature, shear rate, residence time, and their interactions have a strong effect on PLA degradation. The main consequence of thermal degradation and degradation by hydrolysis is the loss of molecular weight that implies a reduction on the mechanical properties of the material. The effect of several processing parameters on polymer´s degradation during processing has been reported by Oepen & Michaeli [29, 30].

Oepen & Michaeli concluded that among the parameters that influence the molecular weight reduction during the process, temperature is the one that shows the greatest effect. Thermally initiated chemical degradation can occur at temperatures above 180 ºC. In extrusion the process temperature must be greater than the melting temperature T_m to form a homogeneous melt, but it must be also low enough to minimize the reduction of molecular weight. As processing temperature increases, molecular reduction grows increasingly sensitive to longer residence times [30].

Therefore, during melt processing, polylactic acid can suffer changes on its chain structure either by thermal degradation or by hydrolysis. PLA undergoes thermal degradation at temperatures above 200 ºC [31]. It proceeds initially by hydrolysis (Figure 1.5) and it is followed by oxidative main-chain scission and inter or intramolecular transesterification reaction [32-34]. Intermolecular transesterification reactions lead to the formation of monomers and oligomeric esters (Figure 1.6), intramolecular transesterification produces monomers and oligomeric lactides of low molecular weight [35-37].

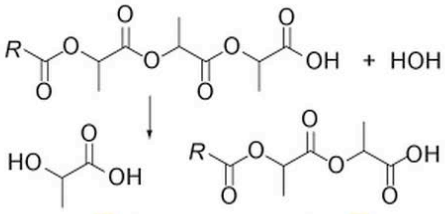

Figure 1.5 Hydrolysis of PLA [38, 39]

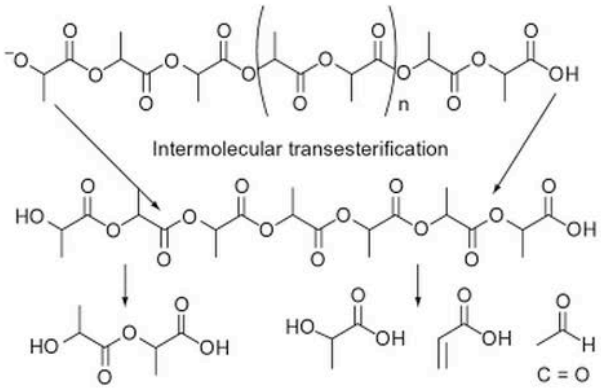

Figure 1.6 Intermolecular transesterification of PLA [26, 39]

Zipper-like depolimerization can also occur at temperatures above 200 ºC (Figure 1.7); this reaction is catalyzed by residual metals from polymerization catalysts (Figure 1.8). Common polymerization catalysts are Sn, Zn or Al compounds. The only catalyst approved by the FDA is

the Sn 2-ethylhexanoate ($Sn(Oct)_2$) [26]. The residual catalysts effect on thermal degradation of PLA has been reported to exhibit the following order: Al > Zn > Sn [40].

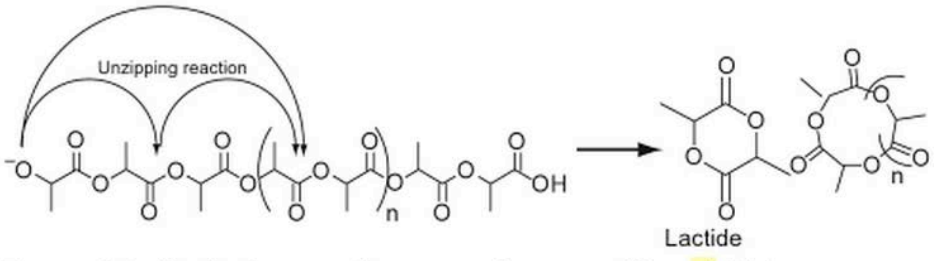

Figure 1.7 Unzipping depolymerization of PLA [39]

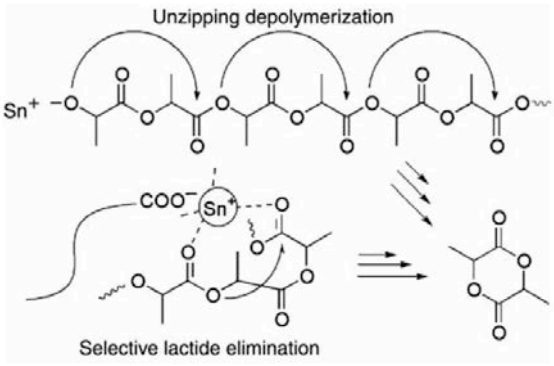

Figure 1.8 Unzipping depolimerization of PLA catalyzed by residual Sn catalyst [26]

1.1.1.2 Mechanical properties of polylactic acid

Mechanical properties of polylactic acid depend on the molecular weight, distribution of the stereoisomers L- and D-, and crystallinity degree. The later depends on thermal history. PLLA is a semi-crystalline polymer that can acquire high crystallinity degrees ranging from 45% to 75% after annealing treatments [41]. The initial crystallinity of PLLA can be minimized by the manufacturing process by subjecting the material to fast cooling after moulding or by incorporating D-isomer units in the chain. PLA's with D-isomer content greater than ~8 - 15 % (depending on the molecular weight) are amorphous [42-44]. Processing conditions can be adjusted to obtain a desired crystallinity degree. This allows tailoring of mechanical properties as they depend on the crystalline fraction (Figure 1.9) [45].

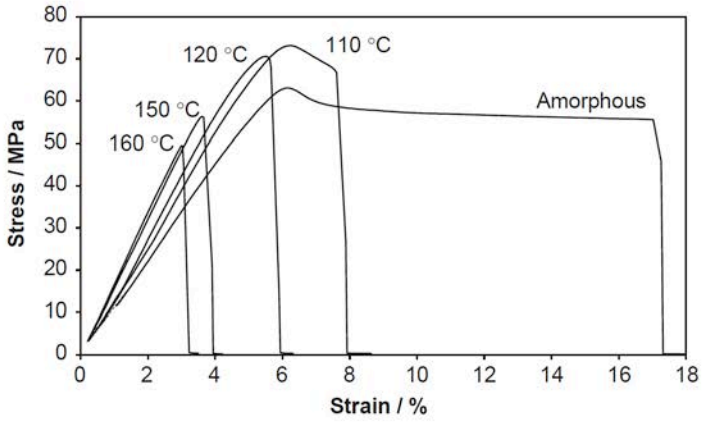

Figure 1.9 Tensile test stress *vs* strain curves of amorphous PLLA and PLLA crystallized under isothermal treatments [45]

Given its stereoregularity PLLA exhibits better mechanical properties than PLDLLA, it has higher elastic modulus, tensile and flexural strength (Table 1.1). PLLA and the copolymers having a high composition ratio of L-lactide have found applications in orthopaedic surgery, drug control / release devices, materials for suture and surgical meshes [46].

In Table 1.1 it is observed that the mechanical strength of polymers is significantly smaller than that of Ti. This implies that polymeric implants need to be designed thicker and wider than the corresponding metallic implant to provide sufficient fixation stability. Moreover they are not suitable for high-load bearing applications and are preferred for the treatment of fractures of small bones [47, 48]. The bulkiness of the implants results in an uncomfortable state for the patient who complains regarding the postoperative palpability of the device [49-52]. Additionally, implants of large volume are associated with higher risk of postoperative tissue reactions [53].

Table 1.1 Mechanical properties of some materials used for osteosynthesis implants in comparison with cortical bone [54, 55]

Material	Modulus (GPa)	Tensile Strength (MPa)	Elongation (%)
PLLA	2.7 – 5.1	40 - 140	5 - 10
PLDLLA	1.0 – 2.7	42 – 51	3 - 10
Ti	110 - 117	620	18
Cortical bone	3.3 – 20.0	50 - 190	1

Another drawback of polymeric implants in comparison with metallic ones is that, while metals can endure any static load below the yield strength up to relative high temperatures (half the

melting temperature), polymers are prone to creep under relative low stresses at ambient temperature. Creep is the principal cause of loosening of biodegradable polymeric fixations [56]. Loosening and failure of an implant is attributed to the molecular mobility that leads to plastic flow due to an external stress [27].

Table 1.2 Mechanical properties of PLA/ceramic composites under compression (Comp), bending (Bend) or tensile (Tens) tests.

Ref.	Material	Filler content (wt.%)	Young's Modulus (GPa)	Strength (MPa)
[62]	PLLA	0	4.8 (Comp)	123 (Comp)
	PLLA/HA	20 – 50	5.3 – 6.5 (Comp)	107 – 115 (Comp)
[64]	PLLA	0	2.5 (Bend)	35 (Bend)
	PLLA / Calcium Carbonates	10 – 70	2.5 – 6 (Bend)	20 – 50 (Bend)
[65]	PLDLLA	0	3.7	73 (Tens)
	PLDLLA/α-TCP	25	4.6 – 4.9	52 – 54 (Tens)
[66]	PLLA/HA	50 – 85	3 – 10 (Bend)	60 – 125 (Bend)
[67]	PLLA/HA	-	4 – 10 (Comp)	100 – 140 (Comp)
[68]	PLLA	0	3.1 (Bend)	131 (Bend)
	PLLA/HA	10 – 30	3.2 – 4.5(Bend)	91 – 123 (Bend))
	PLLA/β-TCP	20	3.6 (Bend)	123 (Bend)

HA: Hydroxyapatite TCP: Tricalcium phosphates

In order to overcome these weaknesses, strategies to improve mechanical performance have gained interest. Törmälä *et al.* [57-59] have enhanced the mechanical properties of PLLA by a self-reinforcing strategy of the polymer matrix with oriented fibers or fibrils of the same material. These materials present bending modulus that range from 3 to 10 GPa and have been clinically used since 1984 [60].

Another approach to strengthen polymer materials is the reinforcement of polymer matrix with bone-analogue inorganic phases (bioglasses, hydroxiapatite) [61-69]. Table 1.2 shows some

mechanical properties of PLA reinforced with ceramics. It is observed that initial mechanical stiffness (modulus) is always improved with high reinforcement contents. However, despite the initial higher stiffness, it has been found that compression and tensile strength decrease with the addition of ceramic particles [62, 65, 67] and bending strength is improved only in some cases [64].

1.1.1.3 Degradation of polylactic acid

The ester groups of PLA can be hydrolytically degraded in the presence of water. Degradation proceeds by the diffusion of water within the bulk which causes hydrolysis of polymer chains. Hydrolytic scission leads to the decrease of molecular weight, loss of strength and subsequently loss of implant mass and diffusion of by-products into the surroundings [10, 26, 60]. The main product of PLA degradation is lactic acid which is metabolized by the human body through the citric acid cycle and converted to carbon dioxide and water [60].

Osteosynthesis devices based on PLA should have an appropriate hydrolytic degradation rate in accordance with the healing rate of the bone. The hydrolytic degradation rate of poly lactic acid depends on material factors such as the molecular weight, crystallinity, or L-D- ratio, and medium factors such as temperature, pH or the presence of enzymes [10, 26].

Degradation of implants in the human body occurs at 37 ºC and neutral pH (7.4). *In vitro* studies of PLA for biomedical applications are performed trying to replicate these conditions [70-75]. Immersion media are buffer solutions that keep pH within the physiological range and simulate the ions concentration of body fluids. Although degradation rate of a material implanted in the body usually is lower than that obtained under in vitro conditions [76], *in vivo* degradation behaviour can be predicted by means of *in vitro* studies to some extent [77].

Degradation behaviour of PLA can be controlled by the manipulation of material parameters. Molecular weight is a crucial factor. High molecular weight polymers have slow degradation rates. The longer the polymer chain the more hydrolytic chain scissions are necessary to produce erosion and mass loss in the implant [78]. The addition of D-units in PLA increases the rate of degradation. While complete degradation of a PLLA implant can take as long as ten years [79, 80], racemic PDLLA degrades over in only 60 days [11]. The incorporation of D-lactyl units within L-configured lactyl units reduces the chain regularity and causes disordered chain packing that leads to a higher supply rate of water through the matrix which increases the hydrolytic degradation rate of the polymer [78].

The crystallinity degree is another important factor to take into account when talking about PLA hydrolytic degradation. It is unclear the effect of PLA crystalline fraction on its degradation rate. While some studies indicate that hydrolytic degradation rate decreases with increasing crystalline fraction [75, 81-83], others have demonstrated the opposite [71, 72, 74]. The first

behaviour is attributed to the higher stability of crystals in comparison with amorphous domains. Water diffuses easier in amorphous polymers than in semi-crystalline polymers. Crystalline regions in semi-crystalline polymers are more resistant to hydrolysis than amorphous and therefore amorphous polymers degrade faster than semi-crystalline [81, 82]. However, the opposite behavior, the enhanced hydrolysis with the increasing crystallinity degree, is explained by the higher density of terminal groups in the amorphous domains of the semi-crystalline polymer. Hydrophilic terminal groups increase the diffusion of water within the matrix which accelerates hydrolysis and causes a faster hydrolytic degradation in a semi-crystalline polymer [26, 71, 74].

The addition of fillers has a dramatic effect on the degradation kinetics of PLA. Hydrolytic degradation of PLA is enhanced by the presence of ceramic reinforcements. Mechanical performance of samples deteriorates quickly with immersion in simulated body fluids solutions and specimens loss nearly the 80% of the strength in only 20 days [66]. An additional complication regarding in vitro degradation of polymer/ceramic composites is that HA and calcium phosphates hardly dissolve under physiological conditions [84, 85]. Approaches with soluble calcium phosphates have appeared [86, 87] but due to the fast loss of strength, this type of composites is preferred for non-load bearing applications like bone grafts substitutes rather than for bone fixation.

1.1.1.4 Biocompatibility of polylactic acid

Bioresorbable devices based on PLA have demonstrated to be suitable for the treatment of bone fractures and have gained an excellent patients' and surgeons' acceptance [88-90]. However, some long-term studies regarding PLLA implants report the appearance of mild foreign body reactions in animals [91] and severe foreign body reactions in the treatment of fractures in humans [92]. The response is attributed to stable PLLA particles that are still detected at the implantation site after almost complete reabsorption of the implant. The particles remain in the tissue for long periods accompanied with inflammatory cells and encapsulated in a fibrous tissue [60]. Although foreign body reactions are more severe with bulky or large volume implants, it seems that all biodegradable implants induce foreign body reactions. They also appear at the time of implant's terminal degradation [60, 92, 93]. Nevertheless, this is not considered a problem as long as it does not cause any clinical symptoms and do not influence the functional result of the treatment [93].

The ideal behaviour of a biodegradable osteosynthesis device implies that the implant completely disappears being replaced by bone. There are studies that confirm this behaviour [80, 94-96] but, unfortunately, there are several others that have concluded that the polymer is not replaced by bone [80, 96-99]. This situation leads to seek solutions that could improve the biocompatibility of biodegradable polymers. The incorporation of bioactive ceramic substances (HA, TCP) within the polymeric matrix is an approach that enhances the osseointegration [86,

96, 100] but, as explained in the previous section of this chapter, the polymer/ceramic approach is preferred for non-load bearing applications due to the fast lost of mechanical performance.

1.1.2 Magnesium as a biodegradable material for osteosynthesis implants

Magnesium (Mg) is an exceptional lightweight alkaline metal which finds extensive applications in the automotive industry [101]. In the human body, Mg is naturally found in bone tissue and is a key mineral for bone health. It is essential for many biochemical reactions and plays an important role in the absorption and metabolism of calcium [102, 103]. For this reason, Mg is a material with great potential to be used for bone repair.

Mg and its alloys are presented as an interesting alternative option to develop biodegradable osteosynthesis materials for load bearing applications due to their appropriate mechanical properties and physiological features. From the perspective of mechanical features this metal has good compatibility with human bone since Mg density of 1.74 g/cm3, Young´s modulus of 41 – 45 GPa and compressive yield strength between 65 – 100 MPa are close to those of natural bone (1.8 – 2.1 g/cm^3, 3 – 20 GPa and 130 – 180 MPa) [104].

The first surgical attempt at using Mg to fix a fracture was performed in the year 1907 by Lambotte [104]. The result was disappointing as pure Mg implant corroded too rapidly *in vivo*, releasing a high amount of hydrogen gas that compromised the mechanical stability of the implant. Even today, more than a century after that, the fast degradation rate in physiological environment and the evolution of hydrogen hinders Mg successful application for bone repair.

During the last decade, the scientific community has gathered many efforts on the improvement of Mg corrosion resistance. This intensive research has led in 2013 to the first results of a controlled clinical pilot study with a Mg-based alloy [105]. Currently, the company Syntellix offer biodegradable Mg screws which are used in foot surgery. This implant has a licensing for medical use in Europe.

1.1.2.1 Processing of Mg and its alloys

Primary fabrication processes for Mg and Mg alloys include casting process and powder metallurgy. Ingots can be converted into products of different shape by thermo-mechanical processes (TMP) that also improve the mechanical properties of the initial material by grain refinement and the production of a more uniform microstructure. The quality of the part can be improved by severe plastic deformation processes like ECAP (Equal Channel Angular Pressing) or HPT (High Pressure Torsion) [106, 107].

Magnesium Powder Injection Moulding (PIM) is a technique that offers the opportunity for manufacturing parts that are complex in shape. This process enables the economic fabrication of parts in an industrial scale and with high automation level. Given the importance and

versatility of this technique, breakthrough research is focused on the improvement of the process chain of Mg powder injection moulding for manufacturing biodegradable Mg and Mg alloys implants [108, 109].

1.1.2.2 Mechanical properties of Mg and its alloys

The limitations of Mg mechanical performance reside basically on its poor cold-forming properties. There are mainly two approaches that seek the improvement of the mechanical properties (1) alloying and (2) plastic deformation. Both focus on the grain refinement as a strategy to enhance Mg ductility at room temperature and improve its formability.

Mg-based alloys which impart a fine grain structure, enhanced mechanical properties and ease the manufacturing process can be enclosed in two groups. Those that contain 2 – 10% Al with trace additions of Zn and Mn and those that contain rare earth elements in combination with Zn, Y or Ag and a small amount of Zr [110]. Examples of Mg-Al-Zn alloys are AZ31 and AZ91. Incorporation of Al not only improves mechanical properties but also the corrosion resistance. Incorporation of Mn increases the yield strength slightly and enhances ductility. Rare earth elements improve the creep resistance of Mg alloys at high temperature and can strengthen the material by solid solution [12, 111]. These Mg-based alloys have been originally designed as solutions that solve the requirements of the automobile industry. Due to their commercial availability, they have been useful starting points for the research of suitable Mg alloys for biomedical applications. Therefore, during the last decade their biological behaviour has been investigated *in vitro* and *in vivo* [112-115]. The best results have been obtained with Mg–Al and Mg–RE alloy systems, however, some concern exists since once degraded the implant these elements might challenge the biocompatibility [116-118]. Moreover, RE elements are considered “critical raw materials” and, therefore, their replacement is strongly suggested by the newest European regulations [119].

The specific design of alloys intended to repair bone fractures includes the incorporation of biologically important elements like Ca and Zn. Calcium is a refining agent and contributes to grain boundary and precipitate strengthening. Zn improves the strength of Mg by solid solution strengthening [12]. Fully crystalline or amorphous (i.e. metallic glasses) compositions of binary alloys Mg-Ca, Mg-Zn and ternary alloys Mg-Zn-Ca, have been thoroughly studied and show also improvements on mechanical strength [120-125]. Due to the lack of dislocations of metallic glasses they exhibit better mechanical strength and modulus than those of their crystalline counterparts, whereas they present lower ductility and hence limited forming ability [126]. Various mechanical properties of Mg alloys are listed in Table 1.3 and compared with those of pure Mg and cortical bone.

Severe plastic deformation techniques (SPD) like equal channel angular pressing (ECAP), large-strain hot rolling (LSHR) or high pressure torsion (HPT) have proven to be effective for

achieving grain refinement down to the sub-micrometer range. The grain refinement leads to enhanced hardness and superplastic elongations that allow processing of commercial magnesium alloys at low temperatures [127-129].

Table 1.3 Mechanical properties of Mg alloys compared with those of pure Mg and cortical bone
Ref: [120, 130-132]

Material	Density	Compressive Strength (MPa)	Tensile Strength (MPa)	E (GPa)	Elongation %
Cortical bone	1.8 – 2.1	90 - 120	35 - 283	3 - 23	1 – 2.1
Pure Mg (cast)	1.74	20 - 115	90 - 190	45	9
AZ31 (Extruded)	1.78	83 - 97	241 - 260	45	7
AZ91 (Die cast)	1.81	160	230	45	3
WE43	1.84		280	44	10
LAE442			247		18
MgZnMn			280		22
Mg1Ca		273	233 - 257		11
MgZn		434	280	42	18 - 20
MgZnCa (glass)		716 - 854	675 - 894	48	<2

E: Young´s modulus WE43: Mg alloy with Y, Nd and Zr LAE442: Mg alloy with Li, Al, Se and Mn

1.1.2.3 Degradation of Mg and its alloys

With the contact of water, Mg forms hydroxides and release hydrogen according to the following equation 1.1.

$$Mg + 2H_2O \rightarrow Mg^{2+} + 2(OH)^- + H_2 \qquad \text{Equation 1.1}$$

Mg exhibits a rapid initial corrosion rate until a protective layer of hydroxide is formed at high pH (>11.5) on Mg surface and diminishes the corrosion kinetics. Unfortunately, in the presence of solutions that contain chloride such the human physiological environment, Mg corrosion behaviour is even worse. Chlorine ions present in human body fluids transform $Mg(OH)_2$ into

soluble $MgCl_2$ (Equation 1.2) decreasing the protected area and enhancing the dissolution of the metal [111].

$$Mg(OH)_{2(solid)} + 2Cl^- \rightarrow MgCl_{2(soluble)} + 2(OH)^- \quad \text{Equation 1.2}$$

The main concerns regarding the applicability of Mg biodegradable implants rely on the hydrogen release and the alkalization of the surface. One single gram of Mg produces 1 L of H_2. The danger of hydrogen generation depends on the rate of its production and the capacity of the human body to metabolize the gas in the implantation site. If large volumes of hydrogen are evolved from the implant at a rate difficult to deal with by the body, the gas can be accumulated in bubbles at implant surroundings compromising its stability, or leading to necrosis of tissues. Much more worrying is the possibility that bubbles can reach the blood circulatory system causing an embolism that eventually could lead to the patient death [133]. Due to the important risk that H_2 evolution implies in biomedical applications, it is determinant the measurement of Mg corrosion kinetics through hydrogen collection experiments, in order to assess the applicability of a Mg-based material as a biodegradable implant [134].

Studies of Mg corrosion behaviour have demonstrated the capacity of this metal to increase pH of neutral buffered solutions – phosphate buffered saline (PBS), Hank solution, simulated body fluid (SBF) or cell culture medium - over 10 in less than 24 hours [134, 135]. This behaviour implies that a corroding Mg-based implant can exceed the buffer capacity of the physiological environment leading to local alkalization. As several physiological reactions are pH dependent, the local alkalization increases the risk of an alkaline poisoning effect if the *in vivo* pH exceeds 7.8. [133].

The scientific community has gathered efforts to slow down Mg corrosion in order to reach slower H_2 evolution and OH- ions generation rates suitable for the human body to deal with. There are mainly three strategies to achieve this objective: (1) tailoring the composition, (2) tailoring the microstructure, (3) surface treatments and coatings.

In pure Mg the presence of impurity elements such as Fe, Ni or Cu plays a detrimental role on its corrosion behaviour. Guangling Song [133] has demonstrated that purification of Mg can be employed to remarkably improve Mg corrosion resistance, as high purity Mg (HP-Mg) evolves only 0.008 ml/cm^2/day in comparison with 26 ml/cm^2/day that commercial purity Mg (CP-Mg) releases. Alloying is another approach used to control Mg corrosion rate. It is important to take into account that none of the alloying elements improve the corrosion behaviour of HP-Mg [12, 133]. However, given the poorer mechanical properties of HP-Mg in comparison with CP-Mg, there is a need to find strategies that slow down Mg corrosion rate maintaining or improving the mechanical performance.

Most alloying elements are less damaging than the impurity elements and can improve CP-Mg corrosion behaviour without the detriment of the mechanical properties. Corrosion resistant alloys designed for the needs in transportation industry, have been screened for their suitability as temporary biomaterials. Al containing alloys – AZ31 and AZ91 – are the most studied [115, 136-138]). Also commercial alloys with rare elements (WE43, WE54, ZM21, ZEK100, LAE442) were found to retard the biodegradation process [113, 115, 137, 139-141] . Nevertheless, *in vivo* studies have demonstrated that the hydrogen evolution of these alloys is still too rapid as gas pockets were generated around the implants [115] and the mechanical strength was lost at early stages of implantation [131].

Lower hydrogen evolution rates have been reached by alloying Mg with Zn and Ca. Investigations with binary alloys, have demonstrated that Mg-Ca [142-144] and Mg-Zn [120, 123, 145] can gradually degrade maintaining a good mechanical performance and releasing lower volumes of H_2 than Mg. Ternary Mg-Ca-Zn [121, 122, 124, 125], Mg-Zn-Y [146] or Mg-Mn-Zn [147, 148] alloys have also been proposed as candidates for biodegradable implants due to their controllable degradation rates.

Further improvements on Mg corrosion resistance can be obtained by controlling the microstructure of the alloy either by grain refinement or amorphization. In a fine microstructure the grain boundaries can act as corrosion barriers that lead to enhance the corrosion resistance. Severe plastic deformation processes like ECAP have been used to obtain fine grain alloys that exhibit improved corrosion behaviour [149-152]. It has been found that amorphous single-phase structures have significantly improved corrosion characteristics than crystalline alloys [153]. This idea motivates research focused on obtaining glassy Mg alloys “without clinically observable hydrogen evolution” [121, 122, 125, 132].

Amorphous alloys have made great progress in the development of Mg-based osteosynthesis implants, however, an initially low degradation rate has not been reached yet and local alkalization is still occurring. It is desirable to avoid high pH during the firsts degradation stages in order to prevent further deterioration of the adjacent tissue and ensure proper tissue healing and growth [154]. The way to mitigate degradation in the initial stage is by surface treatments or coatings. Different coating processes are reviewed in the literature [155], but among these processes, polymeric coatings showed a higher improvement in the initial corrosion protection and a better initial cytocompatibility [112].

Polymeric coatings on Mg-based alloys are made of biodegradable polymers like PLLA [156-161], PLGA [154, 162, 163] or polycaprolactone (PCL) [156, 159, 161, 162, 164-166]. They retard the initial degradation rate of Mg alloys controlling the local alkalization due to OH- ions liberation and delaying H_2 release. Corrosion behaviour can be tailored by the physical

properties of the coating. It has been found that the polymer molecular weight [159], the film porosity [164], thickness [154, 159, 165], and adhesion strength [158, 159] influence the degradation kinetics of the bulk. However, concerns appear as polymer coatings can accelerate Mg corrosion in a long term. Coating offers only a temporary protection. The film degrades at some point exposing fresh reactive Mg surface that starts to corrode. Degradable polymers degrade acidic and Mg corrodes faster in acids. Moreover, as polymer degrades, Mg reactive area increases enhancing bulk corrosion rate. Polymer coated-Mg could achieve a faster degradation rate than the bare alloy [154, 167] (Figure 1.10).

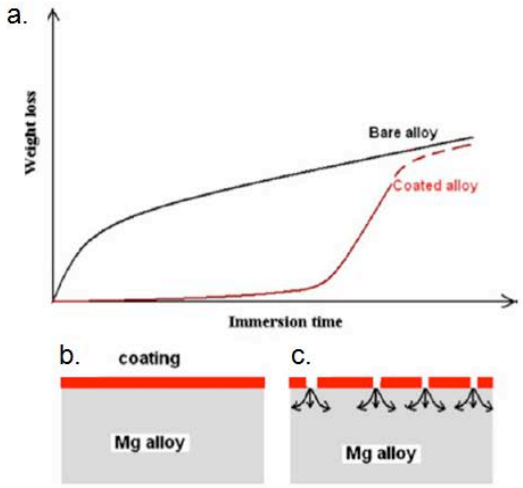

Figure 1.10 Degradation model for polymer coated Mg according to Li et al [154]

1.1.2.4 Biocompatibility of Mg and its alloys

Physiologically, Mg is an essential mineral for bone formation and plays an important role in the regulation of calcium homeostasis (regulation of the concentration of calcium ions in the extracellular fluid) inducing the mineralization process of bone tissue [168]. Its beneficial role enhancing the osteoblastic response and reducing bacterial adhesion has been also pointed out [169, 170]. Although the biocompatibility of most of the Mg-alloys under study have been demonstrated by new bone formation and the enhancement of the mineralized bone area in comparison with degradable polymers [115, 171], the suitability of Mg alloys containing Al and REs for biomedical applications opens a debate due to the potential toxicity of these elements.

Al is known to have adverse neurotoxic effects, it is linked to dementia and Alzheimers disease [116, 172, 173]. Some rare earth elements (Pr, Ce, Y and Lu) have been found to be toxic for humans [117]. Moreover, some of the alloys containing REs have shown pathological effects on the host tissue [113]. The concern around Al and REs long term physiological effect have lead to study the impact of RE on different cells. These studies performed by Feyerabend *et al.* [174]

have determined acceptable RE amounts on alloy compositions that may not compromise the biocompatibility of Mg-based biodegradable implants. Consequently, under certain levels, REs elements could be suitable for biomedical Mg materials.

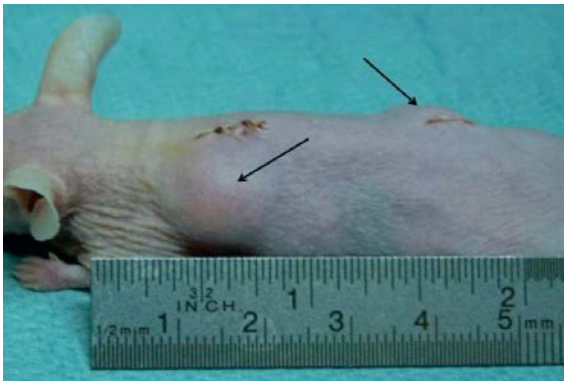

Figure 1.11 A mouse is shown after one day implantation of RE containing Mg alloy disks. Arrows indicate the development of clinically visible subcutaneous gas cavities around the implants [175]

Despite the intensive research focused towards improvement of Mg corrosion resistance, hydrogen evolution and subcutaneous gas bubbles formation keeps being an unresolved problem inherent to Mg-based alloys (Figure 1.11). Animal studies in rabbits and dogs have determined that large-volume Mg implants present incomplete resorption accompanied with gas formation [114]. Witte *et al.* [115] have studied the in vivo corrosion of alloys containing Al and REs and have found that all of the Mg alloys implanted exhibited clinically and radiographically visible subcutaneous gas bubbles. Although glassy alloys have overcome to some extent the problem of large volume hydrogen release, the main drawback of this approach is the early loss of the implant mechanical strength and the limited formability. Additionally, *in vivo* studies have demonstrated that bulk metallic glasses induce a pH value increase that lead to bone damage and osteolysis [122].

1.2 Motivation

Eliminating the need for permanent implants removal is the driving force that motivates the research on the development of materials suitable for biodegradable implants. The second surgery intended to remove Ti or stainless steel implants, not only is not exempt of risks and complications for the patient, but also has important economic implications, including the costs of the intervention by itself and the productive time that patients lose during their postoperative recovery. If patients are provided with resorbable implants that can be metabolized by the human body once the bone tissue has healed, their well-being together with the saving on expenses for the healthcare system would be incremented.

The most common resorbable implants that are commercially available are based on biodegradable polymers. Their main *in vivo* complications are associated with foreign body reactions, osteolysis and weaker mechanical properties in comparison with permanent metallic devices. These limitations hinder their commercialization for the treatment of long-bone fractures. However, they have found a niche in low-load bearing applications such as ankle, knee and hand surgery, or cranio-maxillofacial surgery [28]. Bioretec, Inion Oy, DePuy Synthes (Johnson & Johnson), Zimmer are some of the most important global manufacturers of implants that are committed to the growth of bioresorbable orthopaedic fixation market. Research & Development in this field seeks to expand its range of applications, improve patient outcome and user friendliness, and offer the patient and the surgeon, more comfort and confidence.

Biodegradable implants industry is conservative regarding the acceptance of new materials or new designs. Although in the last decade research on Mg as a biomaterial for orthopaedic applications has increased exponentially, there is currently only one company in Europe that manufactures resorbable implants based on Mg alloys. This company, Syntellix, offers a compression screw made out of an Al-free Mg alloy that contains rare elements. The application is focused only on the treatment of hallux valgus [105]. Syntellix opens an alternative path in the development of bone fixation implants as it proposes the replacement of resorbable polymers by Mg-based alloys. In order to expand the application of these promising materials in the biodegradable device arena, the main problem to be solved is their high corrosion rate.

The solution of the main drawbacks of biodegradable polymers and Mg is the objective that has motivated scientists of AVANZA group at CENIM-CSIC to develop a new material that could simultaneously address the lack of bioactivity and low mechanical properties of polymers and the high degradation rate of Mg and its alloys. The pioneer proposal consists in the incorporation of Mg particles within a matrix based on a biodegradable polymer that is currently used for osteosynthesis applications.

The polymeric matrix could benefit from Mg particles as they could provide mechanical reinforcement and enhance bioactivity reducing polymer osteolytic and foreign body reactions. The Mg in turn would benefit from the polymeric matrix as it would control the corrosion rate, by reducing the alkalinization of the surface and hydrogen release. A synergistic effect would occur in which the disadvantages of one material would be mitigated by the advantages of the other.

These ideas have boosted the birth of patents that focus on the development of a new generation of polymer/Mg composite materials with enhanced mechanical properties, better biocompatibility and adjustable degradation rate. The first patent that provided a proof of concept was the Spanish patent WO 2011/161292A1 presented by González-Carrasco *et al.* [176]. The invention provides a composite based on a PLLA matrix reinforced with Mg micro-particles meant for osteosynthesis and tissue engineering. The Chinese patent, CN102764454A, proposes a composite based on a poly(lactic-co-glycolic acid) (PLGA) matrix reinforced with wires of a Mg alloy that contains Al, Zn and Mn for bone tissue repair scaffolds and fracture fixing [177]. The US patent WO 2010/101901A2 proposes self-buffering medical implants that include a bioerodible polymer and a bioerodible metal mainly for applications in stents, scaffolds and orthopaedic implants [178].

The first paper regarding novel PLLA/Mg composites for orthopaedic applications was published by CENIM-CSIC researchers in 2012 [179]. Specimens of PLLA loaded with 30 wt. % of Mg particles were fabricated by solvent casting and further compression moulding. Reinforcement with Mg particles demonstrated to improve PLLA compressive mechanical properties (Figure 1.6). Other studies regarding PLLA/Mg composites have been performed by researchers from the Institute of Metal Research of the Chinese Academy of Science [180]. They have incorporated 3 – 7 wt. % of Mg and Mg fluoride particles within a PLLA matrix. Although these composites showed lower mechanical properties than the neat PLLA, they exhibited better cytocompatibility. Polymer/Mg composites appear, therefore, as materials with great potential for use in biodegradable implants.

Patents and scientific articles consider the use of organic solvents for the production of the composites. There are some concerns regarding the toxicity of residual solvents, especially when chlorinated solvents (chloroform, dichloromethane) are used in the manufacturing process of implants. Remnants of organic solvents can compromise the biocompatibility of implants and can cause adverse outcomes as they decrease the activity of proteins [181-184]. Therefore, the need of manufacturing these novel Polymer/Mg materials by solvent-free processes appears in order to encourage and foster their successful development for biomedical applications.

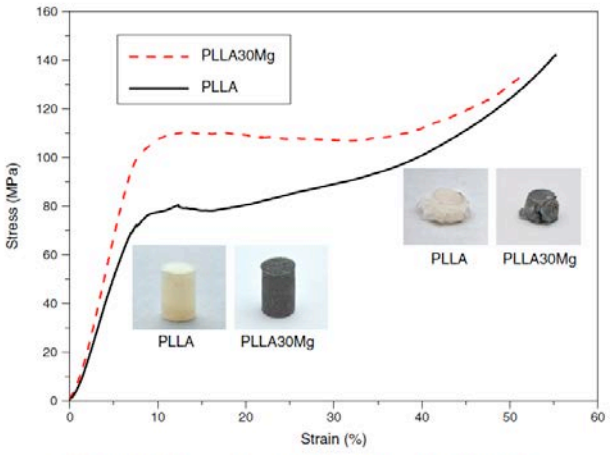

Figure 1.6 Compression stress *vs* strain for PLLA and PLLA reinforced with 30 wt. % Mg particles (S.C. Cifuentes *et al.* [179])

1.3 Objectives

The main objective of this thesis is to design and develop novel biodegradable and bioresorbable biomaterials for osteosynthesis devices, eliminating the need of a second surgery, which will yield a cost-effective approach even when the initial cost of the resorbable implant could be higher than the permanent one. The material should have a controllable degradation rate and adequate mechanical properties. It must also be biocompatible.

Specific objectives:

- ✓ Design of novel polylactic acid/Mg composites: a proof of concept
- ✓ Study the feasibility of processing by means of solvent-free common processes used in industry, such as extrusion/compression and injection moulding
- ✓ Assessment of the material processability by means of physico-chemical characterization and thermal degradation
- ✓ Optimisation and scaling up of the manufacturing process
- ✓ Study of crystallization kinetics of polymeric matrices to select optimal thermal treatments to tailor the crystallinity degree of composites.
- ✓ Study of the influence of Mg particles content, polymer matrix nature and crystallinity degree on mechanical properties of the composite.
- ✓ Study of the relevance of material parameters (polymer nature and crystallinity, Mg particle content, shape and composition) on the *in vitro* degradation behaviour of composites.

1.4 Thesis Overview

The memory of this thesis is presented as detailed below. Chapters are organized to facilitate reading and to track easily the information in each chapter.

Chapter 2 explains the materials and methods used to fulfil the objectives of this thesis.

Given that PLA crystalline degree plays an important role tailoring mechanical performance and degradation rate, **Chapter 3** consists on the study of the effect of processing and thermal history on PLA crystallization kinetics. Optimal thermal treatments to tailor the crystallinity degree of PLA are obtained.

The study of the suitability of processing PLA/Mg composites by extrusion is addressed in **Chapter 4**. The effects of Mg particle content on the polymer thermal stability and melting behaviour, as well as the effect on the mechanical properties are thoroughly analysed.

In **Chapter 5** the processability of PLA/Mg composites by injection moulding is studied. This chapter gathers the results from a research project carried out at the Polymer Engineering Center in the University of Wisconsin Madison in United States. It shows the effect of Mg particles on rheological properties and mechanical performance of PLA.

Chapter 6 is dedicated to the scale-up and optimization of the manufacturing process of PLA/Mg composites by extrusion/compression. The sensitivity of mechanical properties to strain rate together with the influence of magnesium content on the material response are thoroughly analysed by means of compression and instrumented indentation tests.

The *in vitro* degradation behaviour of injection moulded composites manufactured in Chapter 5 is elucidated in **Chapter 7**. The effect on degradation kinetics of crystalline degree and Mg content of composites is studied. The biocompatibility of the materials is assessed using human messenchymal stem cells.

Chapter 8 is focused on the relevance of polymeric matrix properties – nature and crystallinity - and Mg particles composition and shape, on the control of the degradation rate of novel PLA/Mg composites. Materials studied in this chapter have been fabricated using the scaled-up manufacturing process explained in Chapter 6.

Chapter 9 gathers the main conclusions of this doctoral thesis.

1.5 References

[1] Wright S. Global Orthopaedic Markets - Bridging the Divide. Great Britain1999.

[2] Acero J, Calderon J, Salmeron J, Verdaguer J, Concejo C, Somacarrera M. The behaviour of titanium as a biomaterial: microscopy study of plates and surrounding tissues in facial osteosynthesis. Journal of Cranio-Maxillofacial Surgery 1999;27:117-23.

[3] Mantripragada VP, Lecka-Czernik B, Ebraheim NA, Jayasuriya AC. An overview of recent advances in designing orthopedic and craniofacial implants. Journal of Biomedical Materials Research Part A 2013;101:3349-64.

[4] Nagels J, Stokdijk M, Rozing PM. Stress shielding and bone resorption in shoulder arthroplasty. Journal of Shoulder and Elbow Surgery 2003;12:35-9.

[5] Matthew IR, Frame JW. Policy of consultant oral and maxillofacial surgeons towards removal of miniplate components after jaw fracture fixation: pilot study. British Journal of Oral and Maxillofacial Surgery 1999;37:110-2.

[6] Busam ML, Esther RJ, Obremskey WT. Hardware removal: indications and expectations. Journal of the American Academy of Orthopaedic Surgeons 2006;14:113-20.

[7] Wong L, Dufresne C, Richtsmeier J, Manson P. The effect of rigid fixation on growth of the neurocranium. Plastic and Reconstructive Surgery 1991;88:395 - 403.

[8] Yu J, Bartlett S, Goldberg D, Gannon F, Hunter J, Habecker P, et al. An experimental study of the effects of craniofacial growth on the long-term positional stability of microfixation. Journal of Craniofacial Surgery 1996;7:64 - 8.

[9] Törmälä P, Pohjonen T, Rokkanen P. Bioabsorbable polymers: materials technology and surgical applications. Proceedings of the Institution of Mechanical Engineers, Part H 1998;212:101-11.

[10] Eglin D, Alini M. Degradable polymeric materials for osteosynthesis: tutorial. European Cells & Materials 2008;16:80-91.

[11] Maurus PB, Kaeding CC. Bioabsorbable implant material review. Operative Techniques in Sports Medicine 2004;12:158-60.

[12] Witte F, Hort N, Vogt C, Cohen S, Kainer KU, Willumeit R, et al. Degradable biomaterials based on magnesium corrosion. Current Opinion in Solid State and Materials Science 2008;12:63-72.

[13] Cao W, Hench LL. Bioactive materials. Ceramics International 1996;22:493-507.

[14] Rokkanen P, Vainionpää S, Törmälä P, Kilpikari J, Böstman O, Vihtonen K, et al. Biodegradable implants in fracture fixation: early results of treatment of fractures of the ankle. The Lancet 1985;325:1422-4.

[15] Weiler A, Helling H-J, Kirch U, Zirbes TK, Rehm KE. Foreign-body reaction and the course of osteolysis after polyglycolide implants for fracture fixation: Experimental study in sheep. The Journal of Bone & Joint Surgery (Br) 1996;78-B:369-76.

[16] Böstman OM, Pihlajamäki HK. Adverse tissue reactions to bioabsorbable fixation devices. Clinical Orthopaedics and Related Research 2000;371:216-27.

[17] Nair LS, Laurencin CT. Biodegradable polymers as biomaterials. Progress in Polymer Science 2007;32:762-98.
[18] Kulkarni R, Pani K, Neuman C, F L. Polylactic acid for surgical implants. Archives of Surgery 1966;93:839-43.
[19] Cutright DE, Hunsuck EE, Beasley JD. Fracture reduction using a biodegradable material, polylactic acid. Journal of Oral Surgery 1971;29:393-7.
[20] Gerlach KL, J E. In vivo evaluation of 8 different polymers for use as osteosythesis material in maxillofacial surgery. In: Pizzoferrato A, Marchetti PG, Ravagliori A, Lee ACJ, editors. Biomaterials and Clinical Applications. Amsterdam: Elsevier Science Publisher 1987. p. 439 - 45.
[21] Gerlach KL, Krause HR, Eitenmüller J. Use of absorbable osteosynthesis material for mandibular fracture treatment of dogs. In: Pizzoferrato A, Marchetti PG, Ravagliori A, Lee ACJ, editors. Biomaterials and Clinical Applications. Amsterdam: Elsevier Science Publisher; 1987. p. 459-64.
[22] Bos RRM. Ph D Thesis: Poly-L-lactide osteosynthesis. Development of bioresorbable bone plates and screws. The Netherlands: University of Groningen; 1989.
[23] Suuronen R, Laine P, Pohjonen T, Lindqvist C. Sagittal ramus osteotomies fixed with biodegradable screws: A preliminary report. Journal of Oral and Maxillofacial Surgery 1994;52:715-20.
[24] Tan L, Yu X, Wan P, Yang K. Biodegradable Materials for Bone Repairs: A Review. Journal of Materials Science & Technology 2013;29:503-13.
[25] Cembranos JLL-C. Osteosíntesis maxilofacial con materiales reabsorbibles. Controversias en Cirugía Oral y Maxilofacial: Parte II. Revista Española de Cirugía Oral y maxilofacial 2004;26:369-83.
[26] Auras R, Lim LT, Selke SEM, Tsuji H. Poly-lactic acid. Synthesis, Structures, Properties, and Applications: John Wiley & Sons, Inc. New Jersey; 2010.
[27] Smit TH, Engels TAP, Söntjens SHM, Govaert LE. Time-dependent failure in load-bearing polymers: a potential hazard in structural applications of polylactides. Journal of Materials Science: Materials in Medicine 2010;21:871-8.
[28] Middleton JC, Tipton AJ. Synthetic biodegradable polymers as orthopedic devices. Biomaterials 2000;21:2335-46.
[29] von Oepen R, Michaeli W. Injection moulding of biodegradable implants. Clinical Materials 1992;10:21-8.
[30] Michaeli W, Oepen VR. Processing of Degradable Polymers. Annual Technical Conference - ANTEC. New Orleans1993. p. 796-804.
[31] Södergård A, Näsman JH. Stabilization of poly(l-lactide) in the melt. Polymer Degradation and Stability 1994;46:25-30.
[32] Fan Y, Nishida H, Shirai Y, Tokiwa Y, Endo T. Thermal degradation behaviour of poly(lactic acid) stereocomplex. Polymer Degradation and Stability 2004;86:197-208.

[33] Witzke DR. Introduction to Properties, Engineering, and Prospects of Polylactide Polymers: Michigan State University. Department of Chemical Engineering; 1997.
[34] Hyon SH, Jamshidi K, Ikada Y. Effects of residual monomer on the degradation of DL-lactide polymer. Polymer International 1998;46:196-202.
[35] Wachsen O, Platkowski K, Reichert KH. Thermal degradation of poly-l-lactide—studies on kinetics, modelling and melt stabilisation. Polymer Degradation and Stability 1997;57:87-94.
[36] Kopinke FD, Remmler M, Mackenzie K, Möder M, Wachsen O. Thermal decomposition of biodegradable polyesters—II. Poly(lactic acid). Polymer Degradation and Stability 1996;53:329-42.
[37] Carrasco F, Pagès P, Gámez-Pérez J, Santana OO, Maspoch ML. Processing of poly(lactic acid): Characterization of chemical structure, thermal stability and mechanical properties. Polymer Degradation and Stability 2010;95:116-25.
[38] Al-Itry R, Lamnawar K, Maazouz A. Improvement of thermal stability, rheological and mechanical properties of PLA, PBAT and their blends by reactive extrusion with functionalized epoxy. Polymer Degradation and Stability 2012;97:1898-914.
[39] Sin LT, Rahmat AR, Rahman WA. Polylactic acid: PLA Biopolymer Technology and Applications. Oxford: Elsevier; 2012.
[40] Cam D, Marucci M. Influence of residual monomers and metals on poly (l-lactide) thermal stability. Polymer 1997;38:1879-84.
[41] Södergård A, Stolt M. Properties of lactic acid based polymers and their correlation with composition. Progress in Polymer Science 2002;27:1123-63.
[42] Ghosh S, Viana JC, Reis RL, Mano JF. Effect of processing conditions on morphology and mechanical properties of injection-molded poly(l-lactic acid). Polymer Engineering & Science 2007;47:1141-7.
[43] Pyda M, Bopp RC, Wunderlich B. Heat capacity of poly(lactic acid). The Journal of Chemical Thermodynamics 2004;36:731-42.
[44] Kolstad JJ. Crystallization kinetics of poly(L-lactide-co-meso-lactide). Journal of Applied Polymer Science 1996;62:1079-91.
[45] Renouf-Glauser AC, Rose J, Farrar DF, Cameron RE. The effect of crystallinity on the deformation mechanism and bulk mechanical properties of PLLA. Biomaterials 2005;26:5771-82.
[46] Chu C-C. Biodegradable polymeric materials an updated overview. In: Bronzino JD, editor. The Biomedical Engineering Handbook: Boca Raton: CRC Press LLC; 2003. p. 95 - 115.
[47] Ahl T, Dalén N, Lundberg A, Wykman A. Biodegradable fixation of ankle fractures. A roentgen stereophotogrammetric study of 32 cases. Acta Orthopaedica Scandinavica 1994;65:166-70.
[48] Bucholz RW, Henry S, Henley MB. Fixation with bioabsorbable screws for the treatment of fractures of the ankle. Journal of Bone and Joint Surgery American volume 1994;76:319-24.
[49] Bell RB, Kindsfater CS. The Use of Biodegradable Plates and Screws to Stabilize Facial Fractures. Journal of Oral and Maxillofacial Surgery 2006;64:31-9.

[50] Cheung LK, Yip IHS, Chow RLK. Stability and morbidity of Le Fort I osteotomy with bioresorbable fixation: a randomized controlled trial. International Journal of Oral and Maxillofacial Surgery 2008;37:232-41.
[51] Imola MJ, Hamlar DD, Shao W, Chowdhury K, Tatum S. Resorbable plate fixation in pediatric craniofacial surgery: long-term outcome. Archives of Facial Plastic Surgery 2001;3:79-90.
[52] Kim YK, Kim SG. Treatment of mandible fractures using bioabsorbable plates. Plastic and Reconstructive Surgery 2002;110:25-31.
[53] Eitenmüller J, David A, Pommer A, Muhr G. Surgical treatment of ankle joint fractures with biodegradable screws and plates of poly-l-lactide. Chirurg 1996;67:413-8.
[54] Gogolewski S. Bioresorbable polymers in trauma and bone surgery. Injury 2000;31, Supplement 4:D28-D32.
[55] Huiskes R, Mow VC. Biomechanics of bone. In: Mow VC, Huiskes R, editors. Basic orthopaedic biomechanics and mechanobiology. Philadelphia: Lippincott Williams & Wilkins; 2005.
[56] Claes LE. Mechanical characterization of biodegradable implants. Clinical Materials 1992;10:41-6.
[57] Törmälä P, Pohjonen T. Ultrahigh-strength selfreinforced polylactide composites and their surgical applications. Macromolecular Symposia 1997;123:123-31.
[58] Tunc DC. Body-absorbable osteosynthesis devices. Clinical Materials 1991;8:119-23.
[59] Mano JF, Sousa RA, Boesel LF, Neves NM, Reis RL. Bioinert, biodegradable and injectable polymeric matrix composites for hard tissue replacement: state of the art and recent developments. Composites Science and Technology 2004;64:789-817.
[60] Peltoniemi H, Ashammakhi N, Kontio R, Waris T, Salo A, Lindqvist C, et al. The use of bioabsorbable osteofixation devices in craniomaxillofacial surgery. Oral Surgery, Oral Medicine, Oral Pathology, Oral Radiology, and Endodontology 2002;94:5-14.
[61] Huan Zhou JGL, Sarit B. Bhaduri. Fabrication aspects of PLA-CaP/PLGA-CaP composites for orthopedic applications: A review. Acta Biomaterialia 2012;8:1999-2016.
[62] Shikinami Y, Okuno M. Bioresorbable devices made of forged composites of hydroxyapatite (HA) particles and poly-L-lactide (PLLA): Part I. Basic characteristics. Biomaterials 1999;20:859-77.
[63] Shikinami Y, Okuno M. Bioresorbable devices made of forged composites of hydroxyapatite (HA) particles and poly l-lactide (PLLA). Part II: practical properties of miniscrews and miniplates. Biomaterials 2001;22:3197-211.
[64] Kasuga T, Maeda H, Kato K, Nogami M, Hata K-i, Ueda M. Preparation of poly(lactic acid) composites containing calcium carbonate (vaterite). Biomaterials 2003;24:3247-53.
[65] Kunze C, Freier T, Helwig E, Sandner B, Reif D, Wutzler A, et al. Surface modification of tricalcium phosphate for improvement of the interfacial compatibility with biodegradable polymers. Biomaterials 2003;24:967-74.

[66] Russias J, Saiz E, Nalla RK, Gryn K, Ritchie RO, Tomsia AP. Fabrication and mechanical properties of PLA/HA composites: A study of in vitro degradation. Materials Science and Engineering C 2006;26:1289 - 95.

[67] Ignjatovic N, Uskokovic D. Synthesis and application of hydroxyapatite/polylactide composite biomaterial. Applied Surface Science 2004;238:314-9.

[68] Damadzadeh B, Jabari H, Skrifvars M, Airola K, Moritz N, Vallittu P. Effect of ceramic filler content on the mechanical and thermal behaviour of poly-L-lactic acid and poly-L-lactic-co-glycolic acid composites for medical applications. Journal of Materials Science: Materials in Medicine 2010;21:2523-31.

[69] Stefan L, Valentine R, Tobias JB, Marc S, Claudio D, Peter N, et al. Improved degradation and bioactivity of amorphous aerosol derived tricalcium phosphate nanoparticles in poly(lactide-co-glycolide). Nanotechnology 2006;17:2054.

[70] Tsuji H. In vitro hydrolysis of blends from enantiomeric poly(lactide)s. Part 4: well-homo-crystallized blend and nonblended films. Biomaterials 2003;24:537-47.

[71] Tsuji H, Del Carpio CA. In Vitro Hydrolysis of Blends from Enantiomeric Poly(lactide)s. 3. Homocrystallized and Amorphous Blend Films. Biomacromolecules 2002;4:7-11.

[72] Tsuji H, Ikada Y. Properties and morphology of poly(l-lactide) 4. Effects of structural parameters on long-term hydrolysis of poly(l-lactide) in phosphate-buffered solution. Polymer Degradation and Stability 2000;67:179-89.

[73] Tsuji H, Ikarashi K. In Vitro Hydrolysis of Poly(l-lactide) Crystalline Residues as Extended-Chain Crystallites:#II. Effects of Hydrolysis Temperature. Biomacromolecules 2004;5:1021-8.

[74] Tsuji H, Mizuno A, Ikada Y. Properties and morphology of poly(L-lactide). III. Effects of initial crystallinity on long-term in vitro hydrolysis of high molecular weight poly(L-lactide) film in phosphate-buffered solution. Journal of Applied Polymer Science 2000;77:1452-64.

[75] Tsuji H, Tezuka Y, Yamada K. Alkaline and enzymatic degradation of L-lactide copolymers. II. Crystallized films of poly(L-lactide-co-D-lactide) and poly(L-lactide) with similar crystallinities. Journal of Polymer Science Part B: Polymer Physics 2005;43:1064-75.

[76] Henn GG, Birkinshaw C, Buggy M, Jones E. A Comparison of In-Vitro and In-Vivo Degradation of Poly(D,L-lactide) Bio-Absorbable Intra-Medullary Plugs. Macromolecular Bioscience 2001;1:219-22.

[77] Tsuji H. Polylactides. In: Doi Y, Steinbüchel A, editors. Biopolymers Weinheim, Germany: Wiley-VCH; 2002. p. 129-77.

[78] Saha SK, Tsuji H. Effects of molecular weight and small amounts of d-lactide units on hydrolytic degradation of poly(l-lactic acid)s. Polymer Degradation and Stability 2006;91:1665-73.

[79] Andriano KP, Pohjonen T, Törmälä P. Processing and characterization of absorbable polylactide polymers for use in surgical implants. Journal of Applied Biomaterials 1994;5:133-40.

[80] Barber FA, Dockery WD. Long-Term Absorption of Poly-L-Lactic Acid Interference Screws. Arthroscopy: The Journal of Arthroscopic & Related Surgery 2006;22:820-6.

[81] Cam D, Hyon S-h, Ikada Y. Degradation of high molecular weight poly(l-lactide) in alkaline medium. Biomaterials 1995;16:833-43.
[82] Tsuji H, Ikada Y. Properties and morphology of poly(L-lactide). II. Hydrolysis in alkaline solution. Journal of Polymer Science Part A: Polymer Chemistry 1998;36:59-66.
[83] Tsuji H, Miyauchi S. Poly(l-lactide): 7. Enzymatic hydrolysis of free and restricted amorphous regions in poly(l-lactide) films with different crystallinities and a fixed crystalline thickness. Polymer 2001;42:4463-7.
[84] Klein CPAT, Driessen AA, Degroot K, Vandenhooff A. Biodegradation behavior of various calcium phosphate materials in bone tissue. Journal of Biomedical Materials Research 1983;17:769 - 84.
[85] Denissen HW, Degroot K, Makkes PC, Vandenhooff A, Klopper PJ. Tissue-response to dense apatite implants in rats. Journal of Biomedical Materials Research 1980;14:713-21.
[86] Navarro M, Ginebra MP, Planell JA, Barrias CC, Barbosa MA. In vitro degradation behavior of a novel bioresorbable composite material based on PLA and a soluble CaP glass. Acta Biomaterialia 2005;1:411-9.
[87] Navarro M, Michiardi A, Castaño O, Planell JA. Biomaterials in orthopaedics. Journal of the Royal Society Interface 2008;5:1137-58.
[88] Laine P, Kontio R, Lindqvist C, Suuronen R. Are there any complications with bioabsorbable fixation devices? A 10 year review in orthognathic surgery. International Journal of Oral and Maxillofacial Surgery 2004;33:240-4.
[89] Lajtai G, Humer K, Aitzetmüller G, Unger F, Noszian I, Orthner E. Serial Magnetic Resonance Imaging Evaluation of a Bioabsorbable Interference Screw and the Adjacent Bone. Arthroscopy: The Journal of Arthroscopic & Related Surgery 1999;15:481-8.
[90] Ignatius AA, Claes LE. In vitro biocompatibility of bioresorbable polymers: poly(L, DL-lactide) and poly(L-lactide-co-glycolide). Biomaterials 1996;17:831-9.
[91] Suuronen R, Pohjonen T, Hietanen J, Lindqvist C. A 5 year in vitro and in vivo study of the biodegradation of polylactide plates. Journal of Oral and Maxillofacial Surgery 1998;56:604-14.
[92] Bergsma JE, de Bruijn WC, Rozema FR, Bos RRM, Boering G. Late degradation tissue response to poly(l-lactide) bone plates and screws. Biomaterials 1995;16:25-31.
[93] Rokkanen PU, Böstman O, Hirvensalo E, Mäkelä EA, Partio EK, Pätiälä H, et al. Bioabsorbable fixation in orthopaedic surgery and traumatology. Biomaterials 2000;21:2607-13.
[94] Lajtai G, Schmiedhuber G, Unger F, Aitzetmüller G, Klein M, Noszian I, et al. Bone tunnel remodeling at the site of biodegradable interference screws used for anterior cruciate ligament reconstruction: 5-year follow-up. Arthroscopy: The Journal of Arthroscopic & Related Surgery 2001;17:597-602.
[95] Morgan CD, Gehrmann RM, Jayo MJ, Johnson CS. Histologic findings with a bioabsorbable anterior cruciate ligament interference screw explant after 2.5 years in vivo. Arthroscopy: The Journal of Arthroscopic & Related Surgery 2002;18:1-6.

[96] Prokop A, Höfl A, Hellmich M, Jubel A, Andermahr J, Emil Rehm K, et al. Degradation of poly-L/DL-lactide versus TCP composite pins: A three-year animal study. Journal of Biomedical Materials Research Part B: Applied Biomaterials 2005;75B:304-10.

[97] Järvelä T, Nurmi JT, Paakkala A, Moisala AS, Kaikkonen A, Järvinen M. Improving biodegradable interference screw properties by combining polymers. In: Prodromos C, Brown C, Fu FH, Georgoulis AD, Gobbi A, Howell SM, et al., editors. The anterior cruciate ligament: reconstruction and basic science. Philadelphia: Elsevier; 2008. p. 386-91.

[98] Marumo K, Sato Y, Suzuki H, Kurosaka D. MRI study of bioabsorbable poly-l-lactic acid devices used for fixation of fracture and osteotomies. Journal of Orthopaedic Science 2006;11:154-8.

[99] Weiler A, Hoffmann RFG, Bail HJ, Rehm O, Südkamp NP. Tendon healing in a bone tunnel. Part II: Histologic analysis after biodegradable interference fit fixation in a model of anterior cruciate ligament reconstruction in sheep. Arthroscopy: The Journal of Arthroscopic & Related Surgery 2002;18:124-35.

[100] Ignatius A, Augat P, Claes L. Degradation behavior of composite pins made of tricalcium phosphate and poly(L,DL-lactide). Journal of biomaterials science Polymer edition 2001;12:185-94.

[101] Easton M, Beer A, Barnett M, Davies C, Dunlop G, Durandet Y, et al. Magnesium Alloy Applications in Automotive Structures. The Journal of The Minerals, Metals & Materials Society 2008;60:57-62.

[102] Saris N-EL, Mervaala E, Karppanen H, Khawaja JA, Lewenstam A. Magnesium: An update on physiological, clinical and analytical aspects. Clinica Chimica Acta 2000;294:1-26.

[103] Okuma T. Magnesium and bone strength. Nutrition 2001;17:679-80.

[104] Staiger MP, Pietak AM, Huadmai J, Dias G. Magnesium and its alloys as orthopedic biomaterials: A review. Biomaterials 2006;27:1728-34.

[105] Windhagen H, Radtke K, Weizbauer A, Diekmann J, Noll Y, Kreimeyer U, *et al.* Biodegradable magnesium-based screw clinically equivalent to titanium screw in hallux valgus surgery: short term results of the first prospective, randomized, controlled clinical pilot study. BioMedical Engineering OnLine 2013;12:62-.

[106] Dewidar M, Yoon H-C, Lim J. Mechanical properties of metals for biomedical applications using powder metallurgy process: A review. Metals and Materials International 2006;12:193-206.

[107] Sanjari M, Kabir ASH, Farzadfar A, Utsunomiya H, Petrov R, Kestens L, et al. Promotion of texture weakening in magnesium by alloying and thermomechanical processing. II: rolling speed. Journal of Materials Science 2014;49:1426-36.

[108] Wolff M, Schaper JG, Dahms M, Ebel T, Kainer KU, Klassen T. Magnesium powder injection moulding for biomedical application. Powder Metallurgy 2014;57:331-40.

[109] Wolff M. Looking to the future: Magnesium powder injection moulding. PIM International 2008;2:63-5.

[110] Shaw BA. Corrosion resistance of magnesium alloys. In: Stephen D, editor. ASM handbook volume 13a: corrosion: fundamentals, testing and protection. UK: ASM International; 2003.
[111] Xin Y, Hu T, Chu PK. In vitro studies of biomedical magnesium alloys in a simulated physiological environment: A review. Acta Biomaterialia 2011;7:1452-9.
[112] Wu G, Ibrahim JM, Chu PK. Surface design of biodegradable magnesium alloys — A review. Surface and Coatings Technology 2013;233:2-12.
[113] Dziuba D, Meyer-Lindenberg A, Seitz JM, Waizy H, Angrisani N, Reifenrath J. Long-term in vivo degradation behaviour and biocompatibility of the magnesium alloy ZEK100 for use as a biodegradable bone implant. Acta Biomaterialia 2013;9:8548-60.
[114] Witte F. The history of biodegradable magnesium implants: A review. Acta Biomaterialia 2010;6:1680-92.
[115] Witte F, Kaese V, Haferkamp H, Switzer E, Meyer-Lindenberg A, Wirth CJ, et al. In vivo corrosion of four magnesium alloys and the associated bone response. Biomaterials 2005;26:3557-63.
[116] El-Rahman SSA. Neuropathology of aluminum toxicity in rats (glutamate and GABA impairment). Pharmacological Research 2003;47:189-94.
[117] Nakamura Y, Tsumura Y, Tonogai Y, Shibata T, Ito Y. Differences in Behavior among the Chlorides of Seven Rare Earth Elements Administered Intravenously to Rats. Fundamental and Applied Toxicology 1997;37:106-16.
[118] Yang W, Zhang P, Liu J, Xue Y. Effect of Long-Term Intake of Y3+ in Drinking Water on Gene Expression in Brains of Rats. Journal of Rare Earths 2006;24:369-73.
[119] Commission E. Report on Critical Raw Materials for the EU Report of the Ad hoc Working Group on defining critical raw materials. 2014.
[120] Zhang S, Zhang X, Zhao C, Li J, Song Y, Xie C, et al. Research on an Mg–Zn alloy as a degradable biomaterial. Acta Biomaterialia 2010;6:626-40.
[121] González S, Pellicer E, Fornell J, Blanquer A, Barrios L, Ibáñez E, et al. Improved mechanical performance and delayed corrosion phenomena in biodegradable Mg–Zn–Ca alloys through Pd-alloying. Journal of the Mechanical Behavior of Biomedical Materials 2012;6:53-62.
[122] Wang YB, Xie XH, Li HF, Wang XL, Zhao MZ, Zhang EW, et al. Biodegradable CaMgZn bulk metallic glass for potential skeletal application. Acta Biomaterialia 2011;7:3196-208.
[123] Zhang S, Li J, Song Y, Zhao C, Zhang X, Xie C, et al. In vitro degradation, hemolysis and MC3T3-E1 cell adhesion of biodegradable Mg–Zn alloy. Materials Science and Engineering: C 2009;29:1907-12.
[124] Wang HX, Guan SK, Wang X, Ren CX, Wang LG. In vitro degradation and mechanical integrity of Mg–Zn–Ca alloy coated with Ca-deficient hydroxyapatite by the pulse electrodeposition process. Acta Biomaterialia 2010;6:1743-8.
[125] Gu X, Zheng Y, Zhong S, Xi T, Wang J, Wang W. Corrosion of, and cellular responses to Mg–Zn–Ca bulk metallic glasses. Biomaterials 2010;31:1093-103.

[126] Pellicer E, González S, Blanquer A, Suriñach S, Baró MD, Barrios L, et al. On the biodegradability, mechanical behavior, and cytocompatibility of amorphous Mg72Zn23Ca5 and crystalline Mg70Zn23Ca5Pd2 alloys as temporary implant materials. Journal of Biomedical Materials Research Part A 2013;101A:502-17.
[127] del Valle JA, Carreño F, Ruano OA. Influence of texture and grain size on work hardening and ductility in magnesium-based alloys processed by ECAP and rolling. Acta Materialia 2006;54:4247-59.
[128] Figueiredo RB, Aguilar MTP, Cetlin PR, Langdon TG. Processing magnesium alloys by severe plastic deformation. Materials Science and Engineering 2014;63:1-9.
[129] Chen Y-j, Wang Q-d, Lin J-b, Liu M-p, Hjelen J, Roven HJ. Grain refinement of magnesium alloys processed by severe plastic deformation. Transactions of Nonferrous Metals Society of China 2014;24:3747-54.
[130] Poinern GEJ, Brundavanam S, Fawcett D. Biomedical Magnesium Alloys: A Review of Material Properties, Surface Modifications and Potential as a Biodegradable Orthopaedic Implant. American Journal of Biomedical Engineering 2012;2:218-40.
[131] Gu X-N, Zheng Y-F. A review on magnesium alloys as biodegradable materials. Frontiers of Materials Science in China 2010;4:111-5.
[132] Zberg B, Uggowitzer PJ, Löffler JF. MgZnCa glasses without clinically observable hydrogen evolution for biodegradable implants. Nature Materials 2009;8:887-91.
[133] Song G. Control of biodegradation of biocompatible magnesium alloys. Corrosion Science 2007;49:1696-701.
[134] Virtanen S. Biodegradable Mg and Mg alloys: Corrosion and biocompatibility. Materials Science and Engineering: B 2011;176:1600-8.
[135] Lorenz C, Brunner JG, Kollmannsberger P, Jaafar L, Fabry B, Virtanen S. Effect of surface pre-treatments on biocompatibility of magnesium. Acta Biomaterialia 2009;5:2783-9.
[136] Montoya R, Iglesias C, Escudero ML, García-Alonso MC. Modeling in vivo corrosion of AZ31 as temporary biodegradable implants. Experimental validation in rats. Materials Science and Engineering: C 2014;41:127-33.
[137] Witte F, Fischer J, Nellesen J, Crostack H-A, Kaese V, Pisch A, et al. In vitro and in vivo corrosion measurements of magnesium alloys. Biomaterials 2006;27:1013-8.
[138] Zhu Y, Wu G, Zhang Y-H, Zhao Q. Growth and characterization of Mg(OH)2 film on magnesium alloy AZ31. Applied Surface Science 2011;257:6129-37.
[139] Hort N, Huang Y, Fechner D, Störmer M, Blawert C, Witte F, et al. Magnesium alloys as implant materials – Principles of property design for Mg–RE alloys. Acta Biomaterialia 2010;6:1714-25.
[140] Huehnerschulte TA, Angrisani N, Rittershaus D, Bormann D, Windhagen H, Meyer-Lindenberg A. In Vivo Corrosion of Two Novel Magnesium Alloys ZEK100 and AX30 and Their Mechanical Suitability as Biodegradable Implants. Materials 2011;4:1144-67.

[141] Krause A, von der Höh N, Bormann D, Krause C, Bach F-W, Windhagen H, et al. Degradation behaviour and mechanical properties of magnesium implants in rabbit tibiae. Journal of Materials Science 2010;45:624-32.

[142] Li Z, Gu X, Lou S, Zheng Y. The development of binary Mg–Ca alloys for use as biodegradable materials within bone. Biomaterials 2008;29:1329-44.

[143] Kim W-C, Kim J-G, Lee J-Y, Seok H-K. Influence of Ca on the corrosion properties of magnesium for biomaterials. Materials Letters 2008;62:4146-8.

[144] Wan Y, Xiong G, Luo H, He F, Huang Y, Zhou X. Preparation and characterization of a new biomedical magnesium–calcium alloy. Materials & Design 2008;29:2034-7.

[145] Zhang X. In vivo biodegradable binary Mg–Zn alloy. Chinese Patent no. ZL 200510111795.4 2005.

[146] Zhang E, He W, Du H, Yang K. Microstructure, mechanical properties and corrosion properties of Mg–Zn–Y alloys with low Zn content. Materials Science and Engineering: A 2008;488:102-11.

[147] Zhang E, Xu L, Yu G, Pan F, Yang K. In vivo evaluation of biodegradable magnesium alloy bone implant in the first 6 months implantation. Journal of Biomedical Materials Research Part A 2009;90A:882-93.

[148] Xu L, Yu G, Zhang E, Pan F, Yang K. In vivo corrosion behavior of Mg-Mn-Zn alloy for bone implant application. Journal of Biomedical Materials Research Part A 2007;83A:703-11.

[149] Alvarez-Lopez M, Pereda MD, del Valle JA, Fernandez-Lorenzo M, Garcia-Alonso MC, Ruano OA, et al. Corrosion behaviour of AZ31 magnesium alloy with different grain sizes in simulated biological fluids. Acta Biomaterialia 2010;6:1763-71.

[150] Aung NN, Zhou W. Effect of grain size and twins on corrosion behaviour of AZ31B magnesium alloy. Corrosion Science 2010;52:589-94.

[151] Hamu GB, Eliezer D, Wagner L. The relation between severe plastic deformation microstructure and corrosion behavior of AZ31 magnesium alloy. Journal of Alloys and Compounds 2009;468:222-9.

[152] op't Hoog C, Birbilis N, Estrin Y. Corrosion of Pure Mg as a Function of Grain Size and Processing Route. Advanced Engineering Materials 2008;10:579-82.

[153] Song G, Atrens A. Understanding Magnesium Corrosion—A Framework for Improved Alloy Performance. Advanced Engineering Materials 2003;5:837-58.

[154] Li J, Cao P, Zhang X, Zhang S, He Y. In vitro degradation and cell attachment of a PLGA coated biodegradable Mg6Zn based alloy. Journal of Materials Science 2010;45:6038-45.

[155] Hornberger H, Virtanen S, Boccaccini AR. Biomedical coatings on magnesium alloys – A review. Acta Biomaterialia 2012;8:2442-55.

[156] Ying C, Yang S, Shaoxiang Z, Jianan L, Changli Z, Xiaonong Z. Interaction between a high purity magnesium surface and PCL and PLA coatings during dynamic degradation. Biomedical Materials 2011;6:025005.

[157] Guo M, Cao L, Lu P, Liu Y, Xu X. Anticorrosion and cytocompatibility behavior of MAO/PLLA modified magnesium alloy WE42. Journal of Materials Science: Materials in Medicine 2011;22:1735-40.

[158] Lu P, Cao L, Liu Y, Xu X, Wu X. Evaluation of magnesium ions release, biocorrosion, and hemocompatibility of MAO/PLLA-modified magnesium alloy WE42. Journal of Biomedical Materials Research Part B: Applied Biomaterials 2011;96B:101-9.

[159] Xu L, Yamamoto A. Characteristics and cytocompatibility of biodegradable polymer film on magnesium by spin coating. Colloids and Surfaces B: Biointerfaces 2012;93:67-74.

[160] Gao JH, Shi XY, Yang B, Hou SS, Meng EC, Guan FX, et al. Fabrication and characterization of bioactive composite coatings on Mg–Zn–Ca alloy by MAO/sol–gel. Journal of Materials Science: Materials in Medicine 2011;22:1681-7.

[161] Xu L, Yamamoto A. In vitro degradation of biodegradable polymer-coated magnesium under cell culture condition. Applied Surface Science 2012;258:6353-8.

[162] Ostrowski N, Lee B, Enick N, Carlson B, Kunjukunju S, Roy A, et al. Corrosion protection and improved cytocompatibility of biodegradable polymeric layer-by-layer coatings on AZ31 magnesium alloys. Acta Biomaterialia 2013;9:8704-13.

[163] Xu X, Lu P, Guo M, Fang M. Cross-linked gelatin/nanoparticles composite coating on micro-arc oxidation film for corrosion and drug release. Applied Surface Science 2010;256:2367-71.

[164] Wong HM, Yeung KWK, Lam KO, Tam V, Chu PK, Luk KDK, et al. A biodegradable polymer-based coating to control the performance of magnesium alloy orthopaedic implants. Biomaterials 2010;31:2084-96.

[165] Degner J, Singer F, Cordero L, Boccaccini AR, Virtanen S. Electrochemical investigations of magnesium in DMEM with biodegradable polycaprolactone coating as corrosion barrier. Applied Surface Science 2013;282:264-70.

[166] Wang H, Zhao C, Chen Y, Li J, Zhang X. Electrochemical property and in vitro degradation of DCPD–PCL composite coating on the biodegradable Mg–Zn alloy. Materials Letters 2012;68:435-8.

[167] Seitz J-M, Eifler R, Vaughan M, Seal C, Hyland M, Maier HJ. Coating Systems for Biodegradable Magnesium Applications. Magnesium Technology 2014: John Wiley & Sons, Inc. Published Online; 2014. p. 371-4.

[168] Revell P, Damien E, Zhang X, Evans P, Howlett C. The effect of magnesium ions on bone bonding to hydroxyapatite coating on titanium alloy implants. Key Enginnering Materials 2004;254-256.

[169] Janning C, Willbold E, Vogt C, Nellesen J, Meyer-Lindenberg A, Windhagen H, et al. Magnesium hydroxide temporarily enhancing osteoblast activity and decreasing the osteoclast number in peri-implant bone remodelling. Acta Biomaterialia 2010;6:1861-8.

[170] Robinson DA, Griffith RW, Shechtman D, Evans RB, Conzemius MG. In vitro antibacterial properties of magnesium metal against Escherichia coli, Pseudomonas aeruginosa and Staphylococcus aureus. Acta Biomaterialia 2010;6:1869-77.

[171] Kraus T, Fischerauer SF, Hänzi AC, Uggowitzer PJ, Löffler JF, Weinberg AM. Magnesium alloys for temporary implants in osteosynthesis: In vivo studies of their degradation and interaction with bone. Acta Biomaterialia 2012;8:1230-8.
[172] Luckey TD, Venugopal B. Metal Toxicity in mammals. New York: Plenum Press; 1977.
[173] Ku C-H, Pioletti DP, Browne M, Gregson PJ. Effect of different Ti–6Al–4V surface treatments on osteoblasts behaviour. Biomaterials 2002;23:1447-54.
[174] Feyerabend F, Fischer J, Holtz J, Witte F, Willumeit R, Drücker H, et al. Evaluation of short-term effects of rare earth and other elements used in magnesium alloys on primary cells and cell lines. Acta Biomaterialia 2010;6:1834-42.
[175] Kuhlmann J, Bartsch I, Willbold E, Schuchardt S, Holz O, Hort N, et al. Fast escape of hydrogen from gas cavities around corroding magnesium implants. Acta Biomaterialia 2013;9:8714-21.
[176] González-Carrasco JL, Multigner M, Lieblich M, Muñoz M, Frutos E, Saldaña L, et al. Polymer and magnesium particle material for biomedical applications WO 2011/161292 A1. In: internacional O, editor.2011.
[177] Degradable absorptive poly lactic-co-glycolic acid (PLGA)-Mg series composite medical implant and preparation method thereof CN 102764454 A. China2012.
[178] Atanasoska L, Shippy JL, Holman T, Arney MS, Schoen-Le V, Genovese F, *et al.* Self-buffering medical implants WO 2010/101901A2. In: Bureau I, editor. US2010.
[179] Cifuentes SC, Frutos E, González-Carrasco JL, Muñoz M, Multigner M, Chao J, *et al.* Novel PLLA/magnesium composite for orthopedic applications: A proof of concept. Materials Letters 2012;74:239-42.
[180] Wan P, Yuan C, Tan L, Li Q, Yang K. Fabrication and evaluation of bioresorbable PLLA/magnesium and PLLA/magnesium fluoride hybrid composites for orthopedic implants. Composites Science and Technology 2014;98:36-43.
[181] Silver FH, Christiansen DL. Pathobiology and Response to Tissue Injury. Biomaterials Science and Biocompatibility. New York: Springer Science & Business media; 1999.
[182] Korpela M, Tähti H. Effects of industrial organic solvents on human erythrocyte membrane adenosine triphosphatase activities in vitro. Scandinavian Journal of Work, Environment & Health 1987;13:513-7.
[183] Forman S, Kás J, Fini F, Steinberg M, Ruml T. The effect of different solvents on the ATP/ADP content and growth properties of HeLa cells. Journal of Biochemical and Molecular Toxicology 1999;13:11-5.
[184] Chen Q-Z, Bretcanu O, Boccaccini AR. Inorganic and Composite Bioactive Scaffolds for Bone Tissue Engineering. In: Chu PK, Liu X, editors. Biomaterials Fabrication and Processing Handbook. United States of America: CRC Press Taylor & Francis Group; 2008.

CHAPTER 2

MATERIALS AND METHODS

"To accomplish great things, we must not only act, but also dream; not only plan, but also believe"

Anatole France

Table of contents

2. MATERIALS AND METHODS

The materials and methods used to fulfill the objectives of this doctoral thesis are overviewed and gathered in this chapter. Nonetheless, more detailed information regarding the materials fabricated and characterization techniques is given in each specific chapter. Figure 2.1 shows the methodology followed, indicating the three main stages in which this thesis consist of: raw materials characterization, design and processing of composites and *in vitro* characterization of composites.

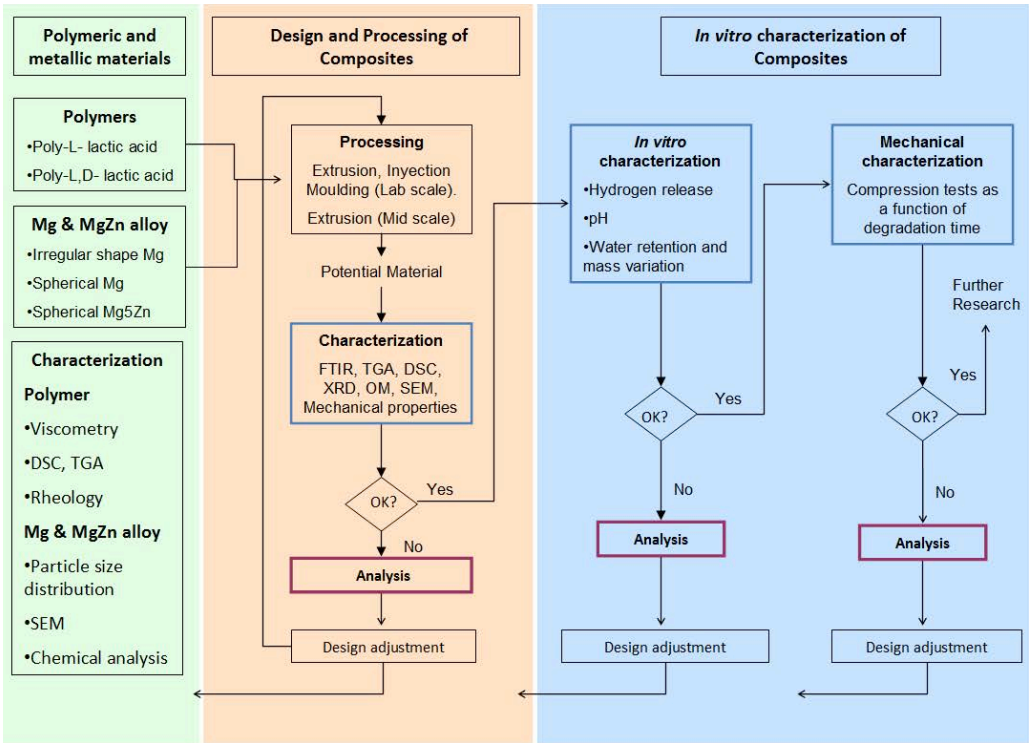

Figure 2.1 Scheme of the methodology followed during this doctoral thesis

Raw materials characterization is essential for a correct composite design and the adequate determination of processing parameters. During design and processing stage, the assessment of the processability of PLA/Mg composites is performed by means of their physico-chemical characterization, thermal stability and mechanical properties evaluation. Once composites with adequate mechanical properties are achieved, the *in vitro* characterization is performed by means of immersion tests were the hydrogen release, pH, water retention and mass variation of composites are studied. Composites that exhibit good *in vitro* performance are studied further to evaluate their mechanical behaviour as a function of degradation time.

2.1. Materials

Polymer/Mg composites were fabricated using for the matrix two types of commercial polylactic acids: poly-L-lactic acid (PLLA) and poly-L,D-lactic acid (PLDLA). For simplicity and to facilitate writing, the PLDLA will be named hereafter as PLDA.

PLLA was provided by Goodfellow as pellets of 5 mm of nominal size. PLDA was provided by Natureworks® as PLA polymer 2002D in pellet form and has a D-isomer content of 4.25%. Both polymers are specifically designed for conventional thermoplastic processes. Table 2.1 summarises some of their most relevant properties for melt processing.

Table 2.1 Properties of polylactic acid matrices

Material	D-isomer content (%)	Density (g/cm^3)	Melt Flow Index* (210 ºC/2.16Kg)	T_g (ºC)	T_m (ºC)
PLLA	0	1.25	35.8 g/ 10 min	61 ºC	170 ºC
PLDA	4.25	1.24	35.4 g/ 10 min	58ºC	160 ºC

* Measured at ICTP in a Gottfert MP-E rheometer

Three different types of Mg particles of less than 50 μm were used as reinforcement: Irregular flake-like Mg particles, spherical Mg and spherical Mg5Zn particles.

The irregular Mg particles were provided by Goodfellow, with a purity of 99.9% and a length to width ratio of 1.6:1. The binary alloy Mg5Zn was prepared at CENIM by die casting of pure Mg (99.9% Mg; 0.05% Cu, Fe, Si and Al; 0.001% Ni) and electrolytic zinc with a purity of 99.995%. Mg and Mg5Zn spherical particles were obtained by centrifugal atomization (TLS Technik, Germany) of cast ingots. The atomized powder was sieved to retain particles of less than 50 μm.

Figure 2.2 presents images of the three powders and their particle size distribution. The particle size distribution was measured by a Malvern 2000 laser-scattering particle size analyser. Irregular flake Mg particles had a median particle size of 24.6 μm, spherical Mg showed a particle diameter of 31.4 μm and spherical Mg5Zn a median particle diameter of 32.5 μm.

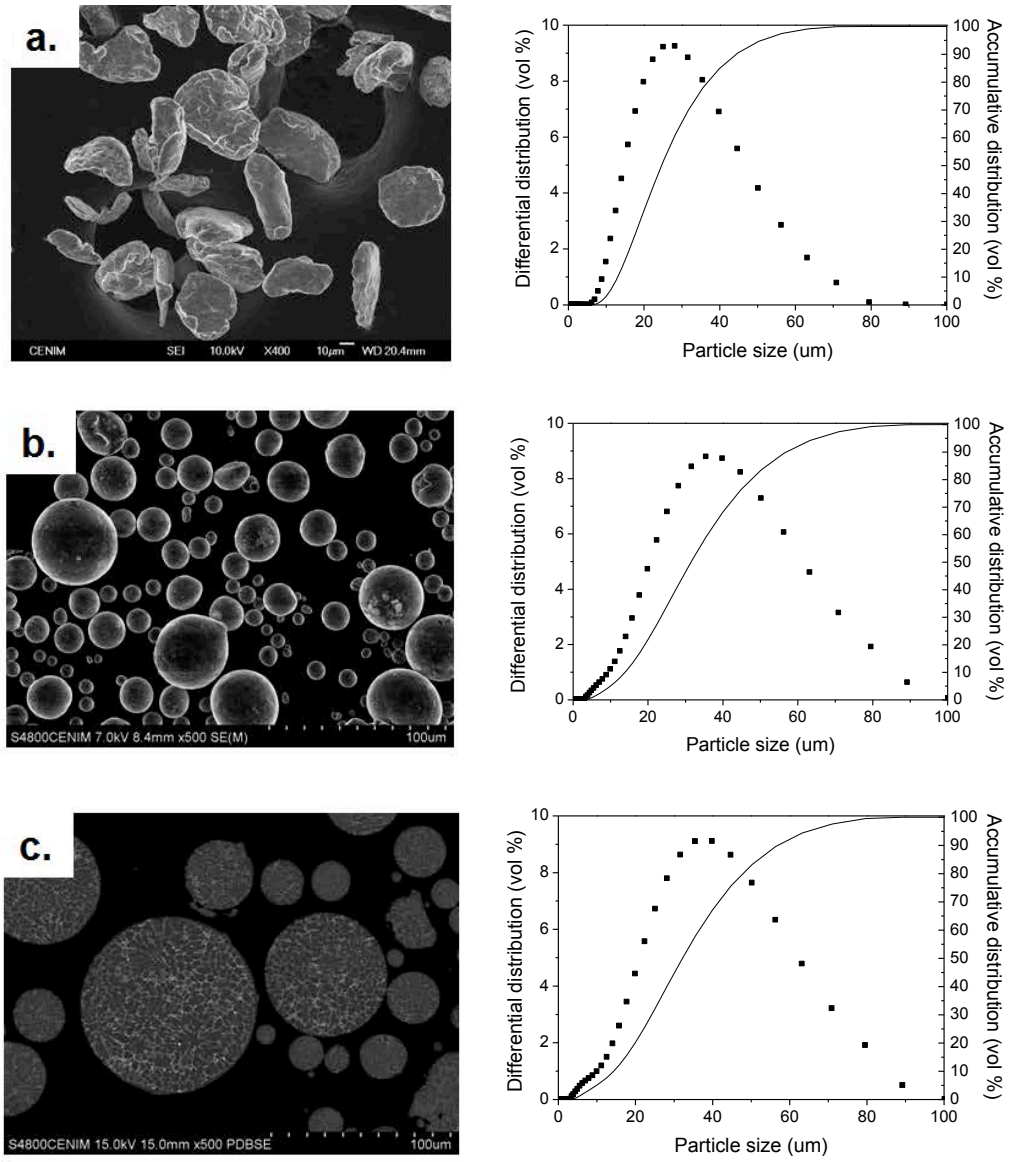

Figure 2.2 SEM images (left) and particle size distribution (right) of irregular flake like Mg particles (a), spherical Mg particles (b) and spherical Mg5Zn particles (c)

2.2. Processes

2.2.1. Lab scale extrusion/compression

A Haake Minilab extruder (Figure 2.3) with two conical co-rotating screws of small capacity (max. 7 cm^3) was used to fabricate PLLA/Mg composites with Mg contents of 0.5, 1, 3, 5 and 7 wt.% (Chapter 4). Temperature was set at 180 ºC, screw rotation speed at 80 rpm and residence time at 10 minutes.

With the extruded material, in a Collin P200P press films or discs of 12 mm diameter and 4 mm height were moulded. The material was first melted at 180ºC and then cooled under a specific thermal treatment.

Figure 2.3 Haake minilab extruder from ThermoScientific at the Institute of Polymer Science and Technology (ICTP-CSIC, Madrid)

2.2.2. Injection moulding

A BOY XS Injection Moulding machine was used to fabricate PLDA/Mg composites with Mg contents of 0.2, 0.5 and 1 wt.% (Chapter 5). Injection moulding parameters as melt processing temperature, mould temperature, holding pressure, back pressure, screw speed and cooling time were optimized to eliminate shrinkage, jetting, flash or incomplete injected parts. Table 2.2 shows the selected injection moulding parameters.

Dumbbell shaped specimens for tensile tests (Gage length: 14 mm, width and thickness: 3.2 mm) and cylinders for compression tests with a length/diameter ratio of 1.5 were fabricated by injection moulding. Cylinders were cut from the runners of injection moulded dumbbell samples.

Table 2.2 Injection Moulding parameters

Filling phase	
Pressure	250 bar
Screw speed	5% (start) – 25% (end)
Injection time	2 s
Holding Pressure phase	
Pressure	250 bar
Time	6 s
Plasticizing phase	
Back pressure	5 bar
Time	99 s
Screw speed	25%
Heating zones	
T1 Barrel transition zone	190 ºC
T2 Barrel metering zone	200ºC
T3 Nozzle	200ºC
Mould temperature	25ºC
Cooling time	45 s

Figure 2.4 Boy XS injection moulding machine at the Polymer Engineering Center, University of Wisconsin – Madison

2.2.3. Scale Up

A Rondol co-rotating twin-screw continuous extruder (Figure 2.5), with a screw diameter 10 mm and L/D= 20, was used to fabricate PLLA/Mg and PLDA/Mg composites with 1, 5, 10 and 15 wt.% of irregular shape Mg particles (Chapter 6) as well as composites with 10 wt.% of spherical Mg and Mg5Zn (Chapter 8). Temperatures of the barrel from the nozzle to the feed zone were: 180 ºC / 180 ºC / 160 ºC / 118 ºC. Screw speed was set at 40 rpm. The estimated residence time was 3 minutes.

Figure 2.5 Rondol twin-screw extruder at Escuela Técnica Superior de Ingenieros Industriales (ETSII), Universidad Politécnica de Madrid

Extruded filaments were grinded into small pellets in a grinder machine at room temperature. The material was then moulded into cylinders for mechanical tests (6 mm diameter and 9 mm height) or discs for cell culture tests (12 mm diameter and 2 mm height) using an OPAL 460 automatic hot mounting press. The mould was placed into the press, filled with the pellets, and then the material was heated at 190 ºC during 20 minutes to ensure temperature homogenization. The material is pressed at 130 bars and fast cooled afterwards. To manufacture crystalline samples, after the fast cooling, a thermal treatment program is set, and the sample is treated at 125 ºC during 30 minutes. Moulded samples are taken out from the mould using a special tool designed specifically for that task.

Figure 2.6 Opal 460 Hot mounting press at National Centre for Metallurgical Research (CENIM-CSIC)

2.3. Characterization

2.3.1. Viscometry

The average molecular weight of polymeric matrices was estimated by means of viscometry. Measurements were carried out by solving the samples in chloroform at 25ºC, using a Ubbelohde type or suspended level viscometer (Figure 2.7) according to ASTM D446 [1] the intrinsic viscosity of polymer is obtained.

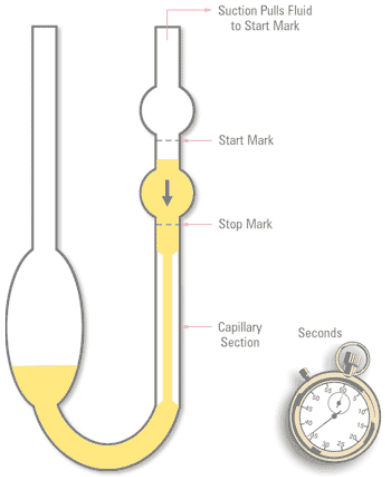

Figure 2.7 Ubbelohde viscometer

The viscometer consists of a reservoir, and a measuring bulb connected trough a capillary which is suspended above the reservoir. The polymer solution with a concentration of 1 g/dl is introduced into the reservoir and then sucked through the capillary and transported to the measuring bulb. The liquid travels back through the measuring bulb. The viscosity value is

provided by measuring the time of flow of the solution through two reference points in the bulb. A pressure-equalization tube extending from the end of the capillary and open to the atmosphere ensures that the pressure difference only depends on the hydrostatic pressure and no longer on the total volume of liquid.

The time it takes the polymer solution to flow from the start mark to the stop mark is compared to the time for the solvent flow. The flow time for either is proportional to the viscosity, and inversely proportional to the density, according to equations 2.1 and 2.2:

$$t_{solvent} = \frac{\eta_{solvent}}{\rho_{solvent}}$$ Equation 2.1

$$t_{solution} = \frac{\eta_{solution}}{\rho_{solution}}$$ Equation 2.2

The reduced viscosity is defined, therefore, as:

$$\eta_{red} = \frac{\eta_{solution}}{\eta_{solvent}}$$ Equation 2.3

Considering that the ratio $\rho_{solution}/\ \rho_{solvent} \approx 1$, the relative viscosity turns out to be a simple time ratio:

$$\eta_{rel} = \frac{t_{solution}}{t_{solvent}}$$ Equation 2.4

The increment in the solution viscosity with respect to that of the pure solvent is defined as the specific viscosity:

$$\eta_{sp} = \frac{\eta_{solution} - \eta_{solvent}}{\eta_{solvent}} = \eta_{rel} - 1$$ Equation 2.5

Both, the specific viscosity and the relative viscosity depend on the polymer concentration “c”. The intrinsic viscosity is defined as:

$$[\eta] = \lim_{c \to 0} \frac{\eta_{sp}}{c} = \lim_{c \to 0} \frac{\eta_r - 1}{c}$$ Equation 2.6

To determine the intrinsic viscosity it is necessary to measure the viscosities of solutions of various concentrations and extrapolate η_{sp}/c to zero concentration. According to Huggins [2] equation the dependence of the reduced viscosity, η_{red}, with c is linear and can be written as:

$$\eta_{red} = \frac{\eta_{sp}}{c} = [\eta] + k_H [\eta]^2 c \qquad \text{Equation 2.7}$$

where k_H is the dimensionless Huggins constant and the intrinsic viscosity, [η], is the intercept in a linear least-squares fit. Alternatively, the intrinsic viscosity can be obtained by linear extrapolation of the inherent viscosity which is defined as follows according to the Kraemer equation [3]:

$$\eta_{inh} = \frac{(\ln \eta_{rel})}{c} = [\eta] - k_K [\eta]^2 c \qquad \text{Equation 2.8}$$

where k_k is the Kraemer constant. In a linear extrapolation of a plot of η_{inh} *vs* c, the intercept is the inherent viscosity. The inherent viscosity is then determined in a dual Huggins-Kraemer plot where both plots, η_{red} *vs* c and η_{inh} *vs* c have the same intercept (Figure 2.8).

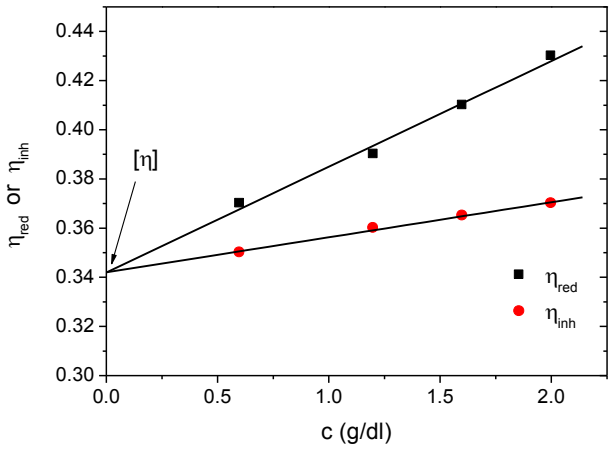

Figure 2.8 Calculation of the inherent viscosity by using the Huggins (η_{red} *vs* c) and the Kraemer (η_{inh} *vs* c) plots

The viscosity average molecular weight of the polymer can be determined from the intrinsic viscosity using the Mark-Houwink equation, which gives the relationship between intrinsic viscosity and molecular weight.

$$[\eta] = K\overline{M}_v^{\alpha} \qquad \text{Equation 2.9}$$

Table 2.3 summarises the Mark-Houwink constants for polylactic acid at the experimental conditions.

Table 2.3 Mark-Houwink constants for polylactic acid in chloroform at 25 ºC [4]

Material	Mark-Houwink equation	References
PLLA	$[\eta] = 4.41 \times 10^{-4} M_v^{0.72}$	[5] [6]
PLDA	$[\eta] = 2.21 \times 10^{-4} M_v^{0.77}$	[5] [6]

2.3.2. Microscopy

A NIKON SMZ 1500 stereoscopic microscope was used to take macroscopic images to study the morphology of the samples. Microstructure was studied by optical microscopy and scanning electron microscopy. Optical microscopy was performed using either an Olympus microscope (CENIM) or an optical polarising Carl Zeiss Amplival microscope (ICTP). Scanning electron microscopy was carried out in a cold-FEG Hitachi S4800 (CENIM).

Preparation of samples for microscopy consisted on cold mounting samples in epoxy resin, followed by grinding with abrasive papers (320 → 1200) and final polishing with diamond particles 9 μm in diameter. For scanning electron microscopy, samples were made electrically conductive by coating with a thin layer of carbon (for analysis) or gold-palladium alloy (for imaging).

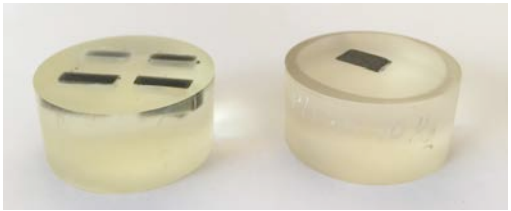

Figure 2.9 Prepared samples for microscopy

2.3.3. Fourier Transform Infrared Spectroscopy (FTIR)

The chemical functional groups of polylactic acids and their changes during processing were identified by Fourier Transform Infrared Spectroscopy. A Perkin Elmer FTIR spectrometer (ICTP) equipped with an Attenuated Total Reflectance (ATR) device was used to obtain the IR spectra of samples scanning in the 4000 to 650 cm^{-1} region.

Functional groups are identified through the vibrations generated within bonds in the material. Energy is absorbed differently depending on the vibrational transitions with different energy within bonds. Peaks in the infrared spectra represent different absorptions of chemical bonds. Some examples of molecular vibrations are shown in Figure 2.10.

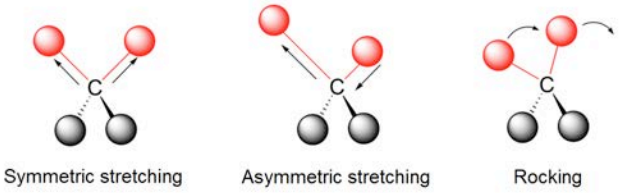

Figure 2.10 Some molecular vibrational modes

Table 2.4 Polylactic acid IR bands (Adapted from [7])

Region	Group or bond	Symbol
3600 – 3200 cm^{-1}	-OH stretching vibration (carboxyl acids and alcohols)	v
2995 cm^{-1}	Stretching asymmetric vibration of CH from CH_3	v_{as}
2944 cm^{-1}	Stretching symmetric vibration of CH from CH_3	v_s
2922 cm^{-1}	Stretching asymmetric vibration of CH_2	v_{as}
2879 cm^{-1}	Weak CH stretching vibration	v
2850 cm^{-1}	Stretching symmetric vibration of CH_2	v_s
1754 cm^{-1}	Stretching vibration of the carbonyl group C=O	v
1453 cm^{-1}	Asymmetric bending of the CH_3	δ_{as}
1382 cm^{-1}	Symmetric bending of the CH_3	δ
1360 cm^{-1}	CH bending (wagging)	δ
1266 cm^{-1}	Symmetric stretching vibration of the C-CO-O and stretching of CH	v_s
1208 cm^{-1}	Asymmetric stretching vibration of the C-CO-O	v_{as}
1182 cm^{-1}	Asymmetric rocking of CH_3	r_{as}
1130 cm^{-1}	Symmetric rocking of CH_3	r_s
1087 cm^{-1}	Asymmetric stretching vibration of O-C-CO	v_{as}
1045 cm^{-1}	Stretching of C-CH_3	v
956 cm^{-1}	C-C backbone stretching of C-CO-O and the CH_3 rocking	v, r
868 cm^{-1}	O-C-C in phase stretch	v

The most characteristic IR bands of polylactic acid are summarised in Table 2.4 and shown in Figure 2.11. The FTIR study is focused on the evolution of selected IR bands (carbonyl and esters groups) related to some representative groups (CH bending) to monitor the changes that PLA undergoes during processing [7].

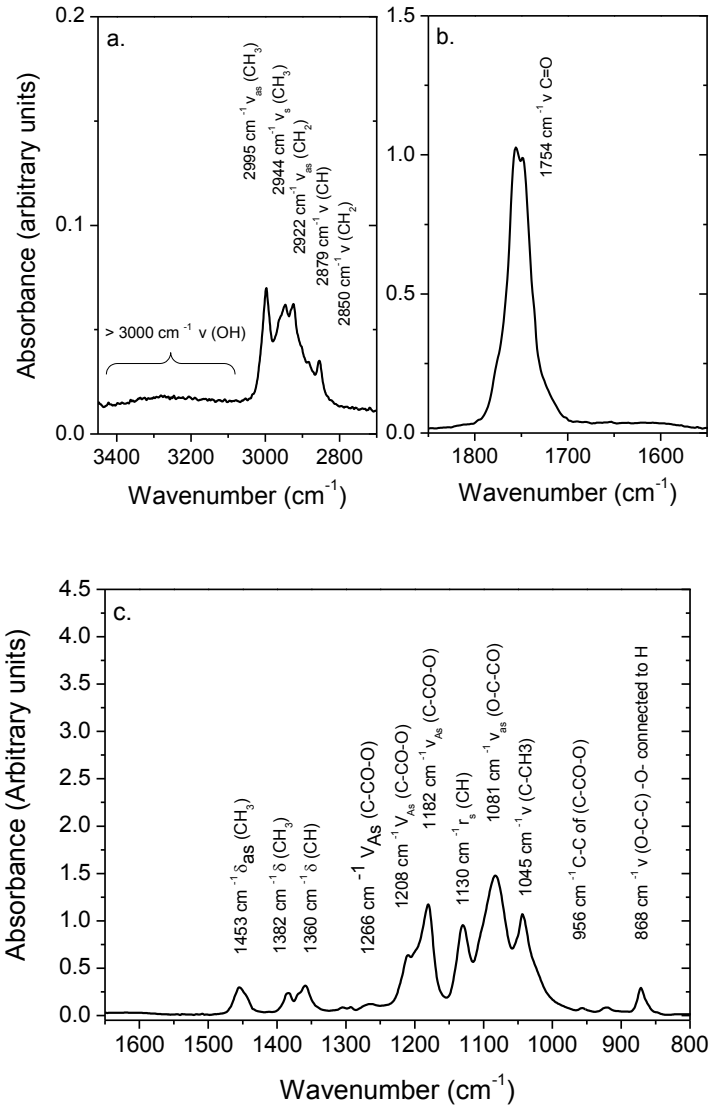

Figure 2.11 Polylactic acid IR spectra: OH and C-H region (a), carbonyl peak (b) and 1650 – 800 cm^{-1} region (c). [7]

2.3.4. X-Ray Diffraction

A Bruker D8 Advance diffractometer provided with a Goebel mirror and a PSD Vantec detector was used to probe the crystal structure of polymers and composites. The spectra was recorded in an angular range of 5º < 2θ < 40º at room temperature by CuKα radiation.

X-ray diffraction is a valuable technique for structural characterization of semicrystalline polymers such as polylactic acid, since it is able to distinguish between ordered and disordered states. Directions of the diffracted X-rays are related to the shape and dimensions of the unit cell of the crystal lattice and the intensity of the diffraction signals depends on the arrangement of atoms in the unit cell. In amorphous zones, dispersion takes place in all directions, yielding a constructive interference that leads to a very diffuse peak identified as “amorphous halo” (Figure 2.12 a).

Under normal conditions (melt, cold crystallization, thermal treatments), polylactic acid crystallizes in the α-form. The α-form is characterized by two antiparallel chains in a left handed 10_3 helix conformation packed in an orthorhombic (or pseudo-orthorhombic) unit cell. Packing of helices is nearly hexagonal [8]. The α-form has a limiting disordered modification, defined as the α´-form. The crystal structure of PLA has been widely investigated by XRD [8]. WAXD patterns of crystallized PLLA are shown in Figure 2.12 b. PLLA main diffractions are (110)/(200), (203) and (015) which occur at 16.3 º, 18.6 º and 22.3 º respectively [9-12]. The more orderly α form show new diffractions at 20.7 º, 22.9 º, 24.0 º and 25 º. The crystallinity degree of samples can be obtained by subtracting the amorphous halo, by comparison to the diffraction pattern obtained from a quenched sample.

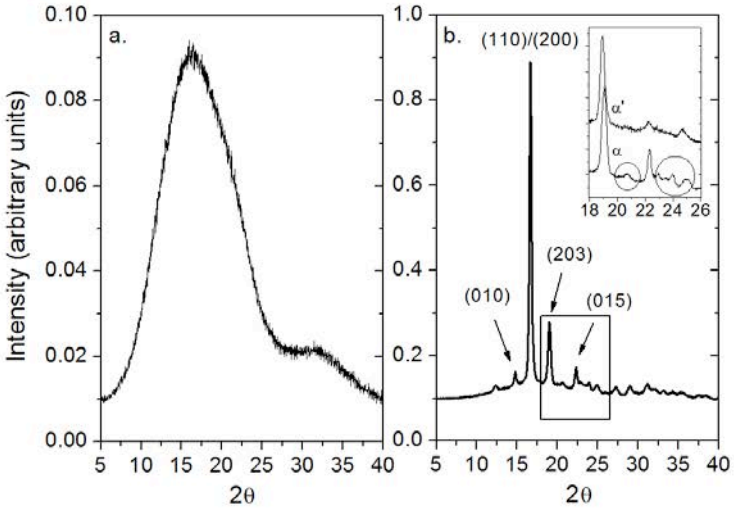

Figure 2.12 WAXD patterns of amorphous PLLA (a) and crystalline PLLA (b)

Figure 2.13 shows the X-ray diffractogram of Mg. Identification of principal diffractions was carried out following the patterns of the Joint Committee of Powder Diffraction Standards. The three strongest Mg reflections that correspond to the (100), (002) and (101) planes appear within 32º and 37º. This fact implies that these Mg peaks will be present in WAXD patterns of PLA/Mg composites, which are recorded in an angular range of 5º < 2θ < 40º. Mg content in PLA/Mg composites can be, therefore, correlated with the area under the strongest Mg reflection in the WAXD pattern of the composite.

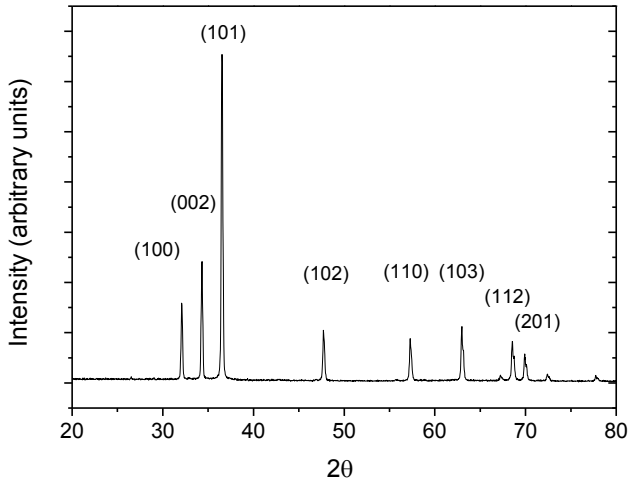

Figure 2.13 X-ray diffractogram of Mg powder

2.3.5. Differential Scanning Calorimetry (DSC)

A TA Q100 DSC was used to study the thermal behaviour of polymers and composites and to measure their crystalline fraction. Samples of 8 ± 0.5 mg were placed in aluminium pans. Experiments were performed under nitrogen atmosphere. Temperature and heat flow calibrations were carried out with indium and zinc standards.

A differential calorimetric scan displays the heat flow as a function of temperature or time and allows the observation of different thermal transitions. Figure 2.14 shows the glass transition, aging, cold crystallization, melting and their corresponding temperatures for PLLA and PLDA during heating at 10 ºC/min. Glass transition temperature was determined as the midpoint of the transformation (1/2 ΔC_p) neglecting the aging peak. Crystallization and melting temperatures were determined at the minimum or maximum point of the transformation peak [13].

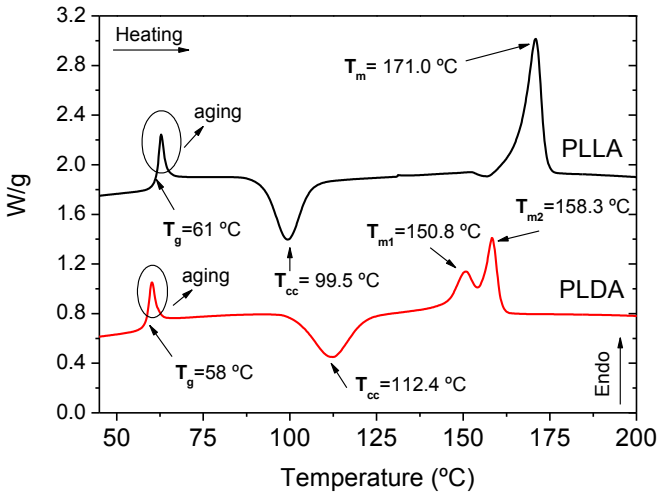

Figure 2.14 DSC scans at 10 ºC/min for extruded PLLA and PLDA

In Chapter 3, DSC was used to study the kinetic crystallization behavior of polymeric matrices by isothermal (hot and cold crystallization) and dynamic crystallization from the melt [14, 15]. A new sample was used for each measurement to avoid degradation during thermal analysis.

For isothermal methods, each sample was melted at 220 ºC for 2 min, in order to erase its thermal history. Then, for hot-crystallization, the sample was cooled from the melt to the chosen crystallization temperature, T_c, at a fast rate (50 ºC/min) to avoid any nucleation of crystals during cooling. For cold-crystallization, the sample was cooled to 25 ºC at 50 ºC/min and then heated at the same rate to the desired crystallization temperature, T_c. In both cases, the sample is kept at T_c until complete crystallization is reached and evidenced by the completion of the exotherm in the thermogram when no noticeable change in the heat flow is detected. After the isothermal step, the sample was heated to 220 ºC at 10 ºC/min.

Dynamic crystallization experiments were performed at various cooling rates (CR): 1, 3, 5, 10, 20, 30 and 40 ºC/min. Before the crystallization protocol, the samples were melted at 220 ºC during 2 minutes to ensure complete melting and erase all the previous thermal history. Once the sample was cooled down at determined CR, the sample was melted at a rate of 10 ºC/min.

Thermal behaviour and crystalline degree of PLA/Mg composites were studied by means of DSC. The experimental design was based on a first heating (F10) from 25 ºC to 220 ºC, followed by a cooling (CR10) to 25 ºC and a second heating to 220 ºC (CR10F10). All the steps were carried out at 10 ºC/min.

The crystalline fraction was calculated by measuring the enthalpy of melting ΔH_m and cold crystallization ΔH_{cc} from the heating curves using Equation 2.10, where ΔH_m^0 is the enthalpy of 100% crystalline PLLA (93.1 J/g) [16].

$$f_c = \frac{(\Delta H_m - \Delta H_{cc})}{\Delta H_m^0} \qquad \text{Equation 2.10}$$

2.3.6. Thermogravimetric analysis (TGA)

A thermogravimetric analyser, TGA model TAQ500 was used to study the thermal stability and the Mg content of PLA/Mg composites. Thermogravimetric analysis monitors the change in mass of a sample, as it is heated, as a function of temperature or time. Two types of experiments were carried out: Isothermal experiments at 180 ºC during 16 hours, and dynamic measurements at 10 ºC/min from 30 ºC to 650 ºC. The experiments were carried out under nitrogen atmosphere (90 ml /min). Three independent experiments were performed for each material using 10 ± 0.5 mg for each sample. Isothermal experiments allow the determination of the kinetic parameters for thermal decomposition of PLLA as a function of Mg content (Chapter 4).

For dynamic conditions and for each material, the onset temperature (T_o), the temperature of greatest rate of change on the weight loss curve (T_p), the temperature of 50% weight loss (T_{50}) and the final temperature (T_e) were determined. T_o and T_e were calculated by finding the intersection of the baseline and the extrapolated tangent at the inflection point of the weight loss curve (Figure 2.15). T_p, also known as the inflection point, was calculated from the first derivative of the weight loss curve (Figure 2.16) [17].

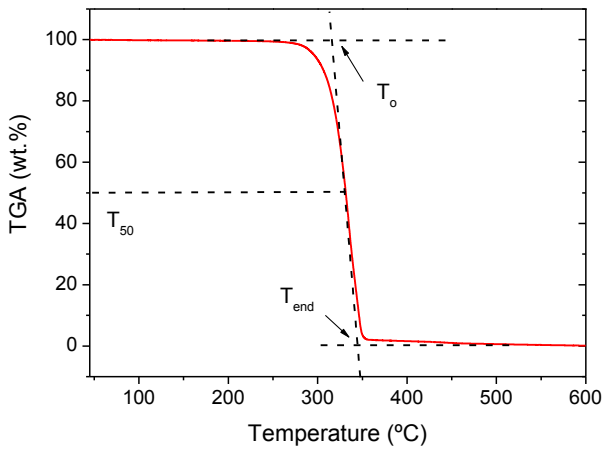

Figure 2.15 Determination of thermogravimetric parameters of PLA from TGA curve

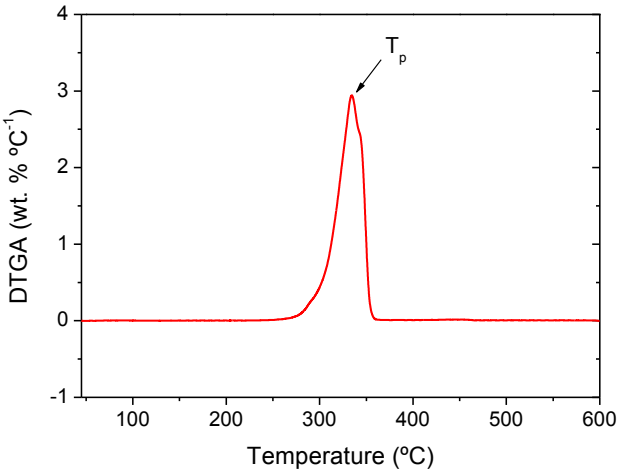

Figure 2.16 Determination of T_p from the first derivative of TGA curve

2.3.7. Rheology

Parallel plate rheometer

A strain controlled ARES rheometer (TA Instruments) (PEC-U Wisc), equipped with a 25 mm parallel plate flow geometry, was used to study the rheological behaviour of polymeric matrices (PLLA and PLDA) and their viscosity temperature dependence. The polymer melt is sheared between two parallel surfaces and the viscosity is determined by measuring the resistance to the rotational force.

Figure 2.17 Scheme of a parallel plate rheometer

The linear viscoelastic behaviour of polymer melts was determined by a strain sweep test at 0.1 Hz of frequency. The viscoelastic behaviour was further characterized by a frequency sweep test at 10 % strain over a frequency range from 0.1 to 70 Hz (from high to low frequency) at 180 ºC, 190 ºC, 200 ºC and 210 ºC. The data is represented in a plot of complex viscosity (η*) *vs* frequency.

The dependence of viscosity of polymer melts on temperature can be expressed in the Arrhenius form,

$$\eta^* = A\exp\left(\frac{E_a}{RT}\right) \qquad \text{Equation 2.11}$$

$$\ln(\eta^*) = \ln(A) + \frac{E_a}{RT} \qquad \text{Equation 2.12}$$

where η* is the complex viscosity, R is the gas constant, A is a constant and Ea is the flow activation energy. The activation energy results from the slope of the plot ln(η) *vs* 1/RT, and indicates the viscosity dependence on the temperature [18].

Capillary rheometer

A HAAKE Rheoflixer high-pressure capillary rheometer (UC3M) was used to study the rheological behaviour of polymer and composite melts. The rheometer is equipped with a capillary die of 1 mm diameter and 30 mm in length. The pressure drop at the capillary entrance was acquired by a transducer pressure sensor with maximum pressure of 1400 bar. The relationships between the apparent viscosity and the shear rate, in a range from 10 to 10^4 s^{-1} at 170, 180 and 190 ºC, were obtained.

In capillary rheometry the material melt is extruded through a die at a controlled piston speed while pressure is recorded. The conditions that polymers experience during injection moulding are reproduced. The piston speed can be converted into a value for the shear rate, and the pressure into a value for the shear stress.

The behaviour of the material is described by a modified Cross mathematical model (Equation 2.13).

$$\eta = \frac{\tau_y}{\dot{\gamma}} + \frac{\eta_0}{1 + \left(k\dot{\gamma}\right)^m} \qquad \text{Equation 2.13}$$

The model describes the apparent viscosity of the melt (η) as a function of the shear rate ($\dot{\gamma}$). It supposes the occurrence of a threshold shear stress (τ_y) and a zero viscosity (η_0) considered as the viscosity during the Newtonian plateau at low shear rates. Constants m and k are parameters related to the shift in the melt flow from Newtonian to pseudoplastic behaviour [18, 19].

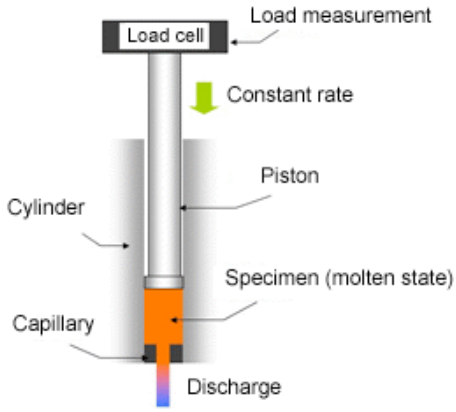

Figure 2.18 Scheme of a capillary rheometer

2.4. Mechanical characterization

2.4.1. Stress *vs* strain curves

Stress *vs* strain (σ *vs* ε) curves are obtained from tensile or compression tests where a specimen is deformed under a constant strain rate, and the stress necessary to deform the material is recorded. The evaluation of the mechanical behaviour of a sample provides fundamental material property data that is critical for component design and for the assessment of its performance in a given application.

For tensile tests an Instron 5969 testing machine was used according to ASTM D638M Standard Test Method for Tensile Properties of Plastic. For each condition, five dumbbell-shaped specimens (gage length: 14 mm, width and thickness: 3.2 mm) were tested at a strain rate of 10^{-3} s^{-1} and ambient conditions (Chapter 5).

The compressive mechanical behaviour was studied in a universal machine EM2/100/FR-10kN Micro Tests at ambient conditions, using a strain rate of 10^{-3} s^{-1}. In Chapter 6 three different strain rates were used: $0.5x10^{-3}$ s^{-1}, $5x10^{-3}$ s^{-1} and $50x10^{-3}$ s^{-1} to study the viscoelastic behaviour

of PLLA/Mg and PLDA/Mg composites. Five cylinders with L/D = 1.5 were tested for each material.

From the stress-strain curves the Young´s modulus, the yield strength and the strength at the strain-softening plateau were obtained (Figure 2.19) [20].

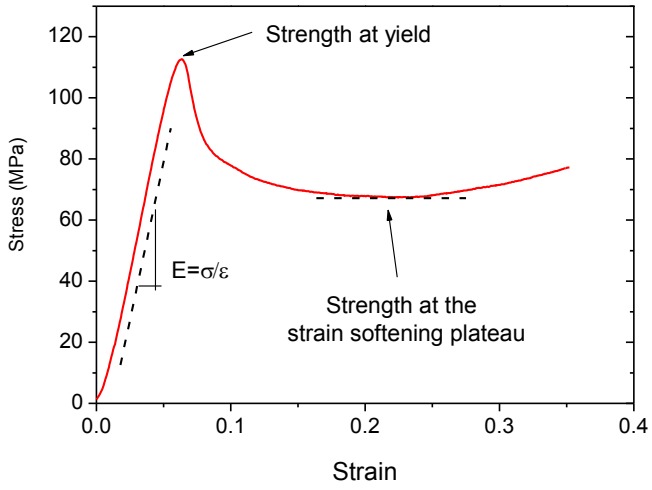

Figure 2.19 Typical stress-strain curve and the determination of mechanical properties

2.4.2. Micro-indentation tests

Micro-indentation measurements were performed using a NanoTest Advantage from Micromaterials at Southampton University in the National Center for Advanced Tribology (nCATS). The elastic modulus and hardness of PLLA/Mg and PLDA/Mg composites with 1, 5, 10 and 15 wt.% of Mg content were determined at different strain rates (Chapter 6). Micro-indentations were performed with a Berkovich (three-sided pyramidal) diamond indenter, using a load of 2000 mN for three different loading-unloading rates (25, 50, 200, 400 and 800 mN/s). A maximum hold time of 15 s was applied. In all cases at least 12 indentations have been performed on different regions of the polymer surface.

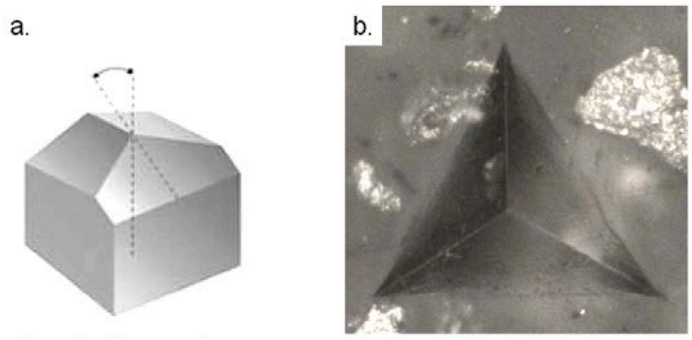

Figure 2.20 Berkovich indenter (a) and residual indentation print on a PLA/Mg composite (b)

Mechanical parameters are calculated from the projected contact area of the indentation print (Figure 2.20). This area is determined from the load *vs* depth (P *vs* h) indentation curve and from the geometry of the indenter. Figure 2.21 shows a typical indentation curve and the most important parameters used to determine the contact area. The zone enclosed by the circle corresponds to the dwell period during the hold at peak load. The measurement of depth as a function of time (relaxation) during the "hold at peak period" allows the measurement of creep response in visco-elastic materials. In Figure 2.16, h_{red} and t_{red} are the normalized parameters with respect to the initial depth, h_0, and the total hold time, t_T. The values of the creep curve result from the ratio of $\Delta h/h_0$ and t/t_T.

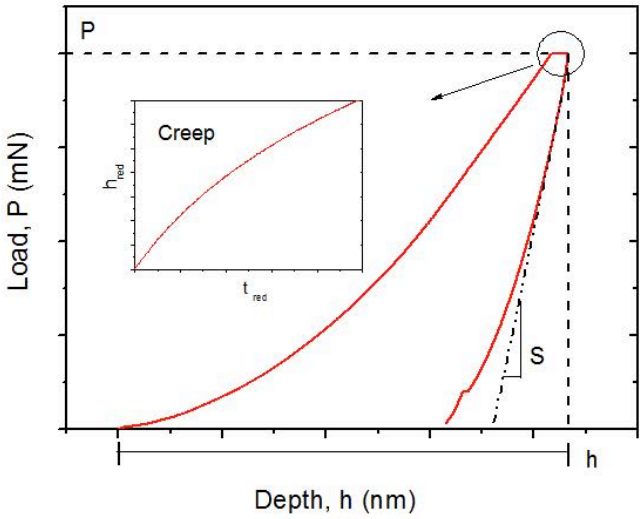

Figure 2.21 Load *vs* depth curve of an micro-indentation instrumented test

Oliver and Pharr [21] found a relationship between the load, P, and the contact depth, h, through the stiffness, S, that allows the determination of the Young´s modulus and hardness of materials by indentation techniques. In viscoelastic materials the stiffness must be corrected due to the creep effects during unloading [22]. Calculation of mechanical parameters and creep studies are explained with further detail in Chapter 6.

2.5. In vitro biodegradation tests

2.5.1 Hydrogen release

Hydrogen collector set up consisted of an inverted funnel and a burette placed directly above the sample (Figure 2.22 a). Samples were immersed in phosphate buffered saline (PBS) in a beaker placed in a thermostatic bath at a constant temperature of 37 ± 1 ºC (Figure 2.22 c). The burette (10 ml) was filled with PBS and hydrogen release was measured by the displacement of PBS level in the burette as H_2 gas evolves (Figure 2.22 b).

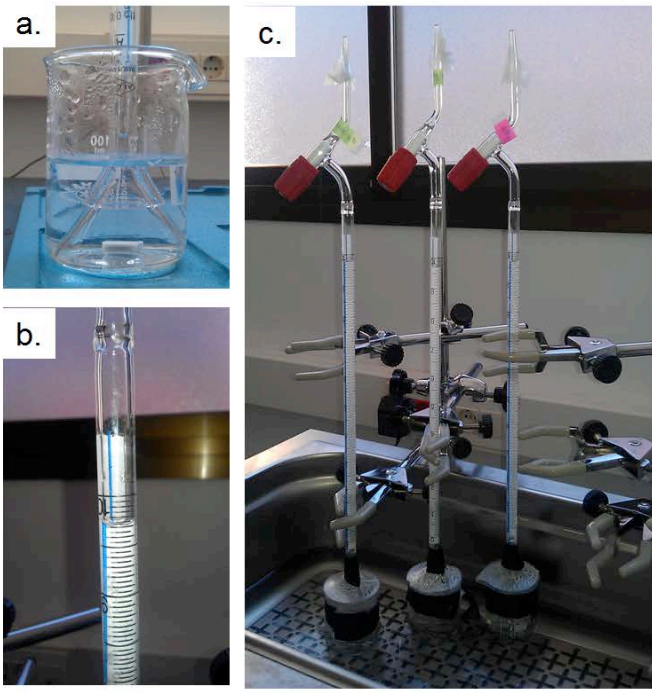

Figure 2.22 Experimental set up for hydrogen release measurements

The ratio of the volume of dissolution media (ml) to the sample surface area (cm^2) was 20:1. The results correspond to average values of three specimens. The media was fully renovated every seven days. For injection moulded materials (Chapter 7), samples with a rectangular

prism shape (length: 9.7 ± 0.2 mm, width: 3.3 ± 0.1 mm, height: 8.8 ± 0.5 mm) were used and hydrogen evolution was measured twice a day during 21 days. For materials fabricated by the scale up process (Chapter 8), cylindrical shape specimens (height: 9 mm, diameter: 6 mm) were used and experiments were performed during 7 days and during 28 days.

2.5.2 pH

For the study of pH evolution, specimens were individually introduced into a test tube containing the media in a ratio of volume of media (ml) to specimen surface (cm^2) of 20:1, and then closed to avoid evaporation. Experiments were performed in parallel in a buffered media (PBS) and in distilled water, to study the nature of degradation products by measuring pH changes also in a non buffered media. The media were fully renovated every seven days. Experiments were run at a constant temperature of 37 ± 1 ºC, by introducing the test tubes in a thermostatic bath. The results correspond to average values of three specimens. pH was recorded with a Lazar equipment. The electrode was calibrated every day with standard solutions. Measurements were done after each hour for the first 10 h and then once a day until completion of the experiment. For injection moulded materials (Chapter 7), samples with a cylindrical shape (height: 7.3 ± 0.3 mm, diameter: 4.7 ± 0.1 mm) were used and measurements were performed once a day during 21 days. For materials fabricated by the scale up process (Chapter 8), cylindrical shape specimens (height: 9 mm, diameter: 6 mm) were used and two set of experiments were performed: one lasting 7 days and a second during 28 days.

2.5.3 Water retention and mass variation

The weight of the samples was measured before beginning the experiments and after 7 and 28 days in PBS. Wet samples, Wet (t), were weighted immediately after removing from the solution and drying their surface with a paper towel; dry samples, Dry (t), were measured after keeping them for 8 h under vacuum and 2 weeks in a desiccator. A precision balance was employed to weight all samples within an error of 0.00005 g (0.05mg).

Water accumulation was calculated from the wet mass, Wet (t), and the dried mass, Dry (t), as follows [23]:

$$\text{Water uptake} = \frac{\text{Wet(t)} - \text{Dry(t)}}{\text{Dry(t)}} * 100\% \qquad \text{Equation 2.14}$$

Mass variation was calculated from the dried sample, Dry(t), compared with its initial mass, Mass(0), as follows:

$$\text{Mass variation} = \frac{\text{Dry(t)} - \text{Mass(0)}}{\text{Mass(0)}} * 100\% \qquad \text{Equation 2.15}$$

2.6. References

[1] ASTM. D446-12 Standard Specifications and Operating Instructions for Glass Capillary Kinematic Viscometers. West Conshohocken, PA: ASTM International; 2012.

[2] Huggins ML. Theory of Solutions of High Polymers1. Journal of the American Chemical Society 1942;64:1712-9.

[3] Kraemer EO. Molecular weights of celluloses and cellulose derivatives. Industrial & Engineering Chemistry 1938;30:1200-3.

[4] Garlotta D. A Literature Review of Poly(Lactic acid). Journal of Polymers and the Environment 2001;9:63-84.

[5] Tsuji H, Ikada Y. Blends of isotactic and atactic poly(lactide)s: 2. Molecular-weight effects of atactic component on crystallization and morphology of equimolar blends from the melt. Polymer 1996;37:595-602.

[6] Perego G, Cella GD, Bastioli C. Effect of molecular weight and crystallinity on poly(lactic acid) mechanical properties. Journal of Applied Polymer Science 1996;59:37-43.

[7] Santonja L. Ph D Thesis: Contribution to the study of thermal, biological and photo degradation of polylactide. Valencia, Spain: Universitat Politècnica de València; 2012.

[8] Pan P, Inoue Y. Polymorphism and isomorphism in biodegradable polyesters. Progress in Polymer Science 2009;34:605-40.

[9] Pan P, Zhu B, Kai W, Dong T, Inoue Y. Effect of crystallization temperature on crystal modifications and crystallization kinetics of poly(L-lactide). Journal of Applied Polymer Science 2008;107:54-62.

[10] Kawai T, Rahman N, Matsuba G, Nishida K, Kanaya T, Nakano M, et al. Crystallization and Melting Behavior of Poly (L-lactic Acid). Macromolecules 2007;40:9463-9.

[11] Zhang J, Tashiro K, Tsuji H, Domb AJ. Disorder-to-Order Phase Transition and Multiple Melting Behavior of Poly(L-lactide) Investigated by Simultaneous Measurements of WAXD and DSC. Macromolecules 2008;41:1352-7.

[12] Yasuniwa M, Sakamo K, Ono Y, Kawahara W. Melting behavior of poly(L-lactic acid): X-ray and DSC analyses of the melting process. Polymer 2008;49:1943-51.

[13] Mandelkern L. Crystallization of polymers New York: McGraw Hill; 1964.

[14] Ozawa T. Kinetics of non-isothermal crystallization. Polymer 1971;12:150-8.

[15] Avrami M. Kinetics of Phase Change I General Theory. The Journal of Chemical Physics 1939;7:1103

[16] Lim LT, Auras R, Rubino M. Processing technologies for poly(lactic acid). Progress in Polymer Science 2008;33:820-52.

[17] Krevelen DWV. Properties of Polymers. Their correlation with chemical structure; Their numerical estimation and prediction from additive group contributions. New York: Elsevier; 1990.

[18] Malkin AY, Isayev AI. Rheology Concepts, Methods and Applications. Toronto: ChemTec Publishing; 2012.
[19] Cross MM. Rheology of non-Newtonian fluids: A new flow equation for pseudoplastic systems. Journal of Colloid Science 1965;20:417-37.
[20] Ward IM, Sweeney J. Mechanical Properties of Solids Polymers. New Delhi: Ed. John Wiley and Sons; 2013.
[21] Oliver WC, Pharr GM. An improved technique for determining hardness and elastic modulus using load and displacement sensing indentation experiments. Journal of Materials Research 1992;7:1564-83.
[22] Feng G, Ngan A. Effects of creep and thermal drift on modulus measurement using depth sensing indentation Journal of Materials Research 2002;17:660-8.
[23] Lehtonen TJ, Tuominen JU, Hiekkanen E. Resorbable composites with bioresorbable glass fibers for load-bearing applications. In vitro degradation and degradation mechanism. Acta Biomaterialia 2013;9:4868-77.

CRYSTALLIZATION KINETICS OF POLYMERIC MATRICES

CHAPTER 3

"Thoughts crystallize into habit and habit solidifies into circumstances"

Bryan Adams

Table of contents

3. CRYSTALLIZATION KINETICS OF POLYMERIC MATRICES

3.1 Introduction

Poly-L-lactic acid, and poly-L,D-lactic acid are semi-crystalline polymers; this implies that their mechanical properties as well as their biodegradation rate are determined by the details of their crystalline-amorphous structure, which strongly depends on the crystallization conditions. Relevant for orthopaedic applications is that partially crystalline morphologies are appropriate to systems requiring higher mechanical properties and slower biodegradation rates. Amorphous materials are suited for drug delivery systems where a faster biodegradation is required [1]. The crystalline fraction of these polymers can be tailored either by annealing treatments (isothermal crystallization from the glassy state), dynamic crystallization or isothermal crystallization from the melt.

PLLA and PLDA present polymorphism. According to the processing conditions they can develop α, β and γ crystal morphologies [2]. The form α grows during the cold crystallization, crystallization from the melt or in solution [3]. The form β grows under simultaneous stretching and rapid crystallization of the material [4] and γ is obtained by crystallization from hexamethylbenzene [5]. The form α has a modification, the α', which occurs at low temperatures during cold crystallization or crystallization from the melt [6, 7].

Some semi-crystalline polymers exhibit thermograms with multiple melting peaks whose magnitude and temperatures depend on the crystallization conditions. This phenomenon can be attributed to various causes such as polymorphisms, differences in crystal size and size distribution or the existence of melting and re-crystallization processes [7-9].

The development of a specific crystal morphology, which influences the final properties of the material, is determined by the control of the temperature during the thermal treatment at the final stage of the process. The study of the crystallization kinetics is therefore of great importance in polymer processing.

Crystallization kinetic studies can be performed either from the melt or from the solid state and can be done isothermally (with a constant temperature of crystallization, T_c) or non-isothermally (with a constant heating rate or cooling rate). The treatment of experimental data in each of these cases is different.

Two main processes take place during crystallization of polymers: nucleation and crystal growth. Nucleation is the initial process where a new ordered phase is formed within an amorphous matrix and crystal growth occurs at the expense of the other phase. The crystal structures are formed during nucleation and are responsible for the final properties of the material [10]. It is necessary to understand the processes of nucleation and growth to control

the size of the crystal structures. These processes are highly influenced by the structural characteristics of the polymer such as chemical structure, molecular weight and by the crystallization conditions. The crystallization conditions have a very significant effect on the mechanism involved and on the kinetics of the process.

It is known that poly-lactides have a low crystallization rate, and many efforts have been spent in order to enhance PLA´s crystallization rate with nucleating agents [11]. However, the effect of processing on crystallization kinetics is almost always ignored even when the polylactic acid is extremely sensitive to processing conditions. The reduction of PLA molecular weight takes place due to the thermo-mechanical history that the polymer undergoes during processing and can affect the crystallization kinetics [12].

This chapter addresses the effect of processing and the effect of crystallization conditions on PLA crystallization kinetics. For the study of the processing effect, isothermal crystallization experiments are performed on virgin and processed PLLA and PLDA. For the study of the crystallization conditions effect, isothermal experiments are carried out following two protocols: cooling the samples from the melt ("hot-crystallization") and heating the samples from the solid ("cold-crystallization"). Analysis of crystallization mechanism is performed by Avrami's theory. The melting behaviour after isothermal crystallization is analysed by DSC heating scans and the crystal morphology assessed by X-ray diffraction. Non-isothermal studies regarding the effect of different cooling rates on the crystallization behaviour of processed PLLA and PLDA are also addressed in this chapter. Dynamic crystallization kinetics is analysed by Ozawa's method.

The objective of this chapter is to understand the effect of different thermal treatments on crystallization kinetics and crystal morphology of polymeric matrices in order to choose the adequate processing conditions to tailor the final properties of the polymer by controlling the crystalline degree and/or the crystal morphology of the polymeric matrices.

3.2 Materials and methods

3.2.1 Materials

The materials used in this study were: commercial grade poly-L-lactic acid PLLA provided by Goodfellow, and commercial grade PLDA produced by Natureworks (trade name PLA2002D) with D content 4.25%. Studies were performed with virgin and processed materials.

Virgin materials: Pellets of PLLA and PLDA were pressed in a Collin P200P press at 190ºC and 30 bars (1 min) and then cooled under pressure between plates refrigerated with cold water to form films.

Processed materials: PLLA was extruded in a Haake Minilab extruder with two conical co-rotating screws of small capacity (max. 7 cm^3). Temperature was set at 180 ºC, screw rotation speed at 80 rpm and residence time at 10 minutes. Extruded PLLA is named hereafter "PLLA ext". PLDA was processed by injection moulding in a BOY XS micro injection moulding machine. The temperature at the metering zone and nozzle was 200 ºC and the mould temperature 25 ºC. The holding pressure was 250 bar, the plasticizing time was 99 s, injection time 2 s and holding pressure phase lasted 6 s. Injection moulded PLDA is named hereafter "PLDA IM".

A sample of 8 ± 2 mg was used for each material, each condition and each temperature studied to avoid degradation during thermal analysis. Crystallization behaviour was studied by DSC using a TA Instruments, Q100 connected to a cooling system and calibrated with different standards. Tests were performed in an inert atmosphere of nitrogen at a flow rate of 50 ml/min.

3.2.2 Isothermal crystallization theory

Kinetic behaviour analysis was performed by isothermal methods for two different crystallization conditions: crystallization from the melt ("hot-crystallization") and crystallization from the glassy state ("cold-crystallization").

Each sample was melted at 220 ºC for 2 min, in order to erase its thermal history. Then, for hot-crystallization, the sample was cooled from the melt to the chosen crystallization temperature, T_c, at a fast rate (50 ºC/min) to avoid any nucleation of crystals during cooling. For cold-crystallization, the sample was cooled to 25 ºC at 50 ºC/min and then heated at the same rate to the desired crystallization temperature, T_c. In both cases, the sample is kept at T_c until complete crystallization is reached and evidenced by the completion of the exotherm in the thermogram when no noticeable change in the heat flow is detected. After the isothermal step, the sample was heated to 220 ºC at 10 ºC/min.

X-ray scattering was used to probe the crystal structure of some thermal treatments. Samples were analyzed using a Bruker D8 Advance diffractometer provided with a Goebel mirror and a PSD Vantec detector by CuKα radiation. The spectra was recorded in an angular range of 5º < 2θ < 40º at room temperature.

Under isothermal conditions, the evolution of crystallinity of a sample over time to a given condition can be determined from experimental calorimetric results (equation 3.1). The advance of crystallinity is represented by X_c (t). The total crystallinity achieved under certain conditions corresponds to the value X_c (t) = 1 and is proportional to the energy involved in the process, that is, the integral of the crystallization peak $\Delta H(\infty)$.

The crystallinity evolved for a time t corresponds to the partial integral of the peak at that particular time ΔH(t). Thus, the evolution of the crystallization process can be assessed from calorimetric techniques by measuring the heat flow dH/dt of a sample. The relative crystallinity was determined from the integration of the crystallization peaks according to equation 3.1:

$$X_c(t) = \frac{\int_0^t (dH/dt)dt}{\int_0^\infty (dH/dt)dt} = \frac{\Delta H(t)}{\Delta H(\infty)} \qquad \text{Equation 3.1}$$

The crystallization rate can also be determined by monitoring the development of crystallinity. The overall crystallization rate is determined directly from the necessary time to reach the 50% of crystalline transformation, i.e. the half crystallization time, $t_{1/2}$. The crystallization rate is therefore related to the reciprocal of the half crystallization time ($1000/t_{1/2}$).

The influence that crystallization temperature exerts on crystallization rate is very important. In the case of crystallization from the melt the speed of the process depends on the difference between the melting temperature and the crystallization temperature ($T_m - T_c$). At elevated temperatures near the melting point, i.e. at low under-cooling, the crystallization rate is very slow. In the case of crystallization from the solid state, the process depends on the difference between crystallization temperature and glass transition temperature ($T_c - T_g$), so that high crystallization temperatures lead to high crystallization rates.

With the increment of the driven force of hot-crystallization (T_m - T_c) and cold-crystallization ($T_c - T_g$), crystallization rate reaches a maximum. From that point on, the crystallization rate decreases. The relationship between the crystallization rate with T_c responds to a Gaussian bell curve. Crystallization rate is slower in the temperature ranges close to the melting point and the glass transition. The existence of a maximum in the crystallization rate is inherent to a process controlled by an initial nucleation stage and the subsequent growth process.

3.2.2.1 Isothermal kinetic analysis by Avrami theory

The theory of Avrami [13] explains the type of nucleation and describes the relationship between the unconverted crystalline fraction, ($1-X_c$), with time according to equation 3.2.

$$1 - X_c = e^{-kt^n} \qquad \text{Equation 3.2}$$

The constant k is related with the crystallization rate and n is related to the type of nucleation together with the geometry of the crystal growth. These values are specific for every polymer. Avrami constants k and n are calculated by plotting $\ln(-\ln(1-X_c))$ vs $\ln(t)$. The slope corresponds to the Avrami exponent n, and the intercept to the constant ln k, as explained in equation 3.3.

$$\ln\left[-\ln\left(1-X_c\right)\right]=n\cdot\ln\left(t\right)+\ln\left(k\right)$$ Equation 3.3

The Avrami exponent, n, depends on the mechanism of crystal nucleation and growth. If the nucleation is homogeneous, n can take values 2, 3 and 4 corresponding to mono-, bi- and three-dimensional growth respectively. If in-homogeneities are present in the system they can act as crystallization nuclei and the nucleation is then heterogeneous. In such a case, values of n can range between 1 -2, 2-3 and 3-4 for mono-, bi- and three-dimensional growth respectively.

3.2.2.2 Kinetic regimes and nucleation constants (Hoffman-Lauritzen)

The Hoffman-Lauritzen methodology was performed to determine the crystallization regimes during crystallization from the melt. The theory indicates that crystallization can take place under three different regimes which rely on the crystallization temperature.

Regime I: Takes place at high temperatures (small under-cooling). Nucleation evolves completely before the nucleation of the next layer appears. The lateral growth rate is much faster than nucleation rate. It is associated with axialites.

Regime II: Takes place at lower temperatures. Many nuclei are formed and extend slowly. The nucleation rate is faster than lateral growth rate, and multiple nucleations occur. It is associated with spherulites.

Regime III: Occurs at lower temperatures than regime II, the separation between the nuclei reaches its minimum value, producing a multiple nucleation on the same layer. It is associated with spherulites.

Hoffman-Lauritzen relates the radial growth rate of the spherulite, G, with the crystallization temperature T_c, according to equation 3.4 [14]:

$$G=G_0\exp\left[-\frac{U}{R\left(T_c-T_{\inf}\right)}\right]\times\exp\left[-\frac{K_g}{T_c\Delta Tf}\right]$$ (Equation 3.4)

$$T_{\inf}=T_g-30^{\circ}C$$ (Equation 3.5)

$$\Delta T=T_m^0-T_c$$ (Equation 3.6)

$$f=\frac{2T_c}{T_c+T_m^0}$$ (Equation 3.7)

Where G_0 is the pre-exponential factor which includes those factors independent of temperature, U represents the energy required for the transport of macromolecules in the melt, is equal to 1500 cal/mol and is related with the growth process; T_c is the crystallization temperature; T_{inf} is the temperature where the mobility of the viscous flow stop, and is defined in equation 3.5. The second exponential in the equation 3.4 accounts for the free energy contribution for the growth of a critical size nucleus, which is inversely proportional to the undercooling, ΔT, defined in equation 3.6; T_m^0 is the equilibrium melting temperature; f is a corrective factor defined in equation 3.7 and K_g is the nucleation constant related to the energy needed to form nuclei of critical size [15, 16].

The study can also be performed from Avrami analysis results, if it is considered that the kinetic constant, k, is proportional to the rate of radial growth of the spherulites, G. This approach is valid when the process takes place through heterogeneous nucleation. A variant of equation 3.4 can be applied and proceed analogously [14]:

$$k = k_0 \exp\left[-\frac{U}{R(T_c - T_{\inf})}\right] \times \exp\left[-\frac{K_g}{T_c \Delta T f}\right] \qquad \text{(Equation 3.8)}$$

3.2.2.3 Equilibrium melting temperature Tm^0

The equilibrium melting temperature is an important parameter involved in the kinetic analysis. It is defined as the melting temperature that a crystal with infinite size would have and it would also correspond with the crystallization temperature of such crystal.

The method developed to obtain T_m^0 relies on the fact that the thermodynamic equilibrium is reversible, therefore the reverse processes of crystallization and melting should take place at the equilibrium point where $T_m = T_c$ where T_c is the crystallization temperature and T_m the experimental melting temperature.

T_m^0 can be obtained by the Hoffman-Weeks [17] method. If polymer samples are crystallized at different crystallization temperatures, T_c, and the melting temperature T_m is determined for each sample, T_m^0 is obtained as the intersect between the plot of the experimental T_m values vs T_c with the identity function $T_m = T_c$.

3.2.3 Dynamic crystallization theory

In non-isothermal experiments the crystallinity degree is developed with the increment or decrement of temperature at a constant heating or cooling rate, respectively. The fact that the crystalline degree can be calculated as a function of time makes it possible to also apply the theory of Avrami in this type of experiments.

Dynamic crystallization experiments have been performed for extruded PLLA and injection moulded PLDA at various cooling rates (CR): 1, 3, 5, 10, 20, 30 and 40ºC/min. A new sample was used for each measurement to avoid degradation during thermal analysis. Before the crystallization protocol, the samples were melted at 220 ºC during 2 minutes to ensure complete melting and erase all the previous thermal history. Once the sample was cooled down at determined CR, the sample was melted at a rate of 10ºC/min.

3.2.3.1 Non-isothermal kinetic analysis by Ozawa

Based on the Avrami method, several theories have been suggested to understand the nucleation and growth during dynamic crystallization [18, 19]. Assuming that non-isothermal crystallization process may be composed of infinitesimally small isothermal crystallization steps, Ozawa extended the Avrami equation to the non-isothermal condition [18, 20], and obtained the following equation:

$$1 - X_c = \exp\left[\frac{-K(T)}{v^m}\right] \quad \text{(Equation 3.9)}$$

$$\ln\left[-\ln\left(1 - X_c\right)\right] = \ln K(T) + m * \ln\left[\frac{1}{v}\right] \quad \text{(Equation 3.10)}$$

Where X_c is the relative crystallinity at temperature T; m is Ozawa exponent, which is related to the nucleation and growth process; K is a cooling function related to the overall crystallization rate and indicates how fast crystallization occurs and v is the cooling rate.

Ozawa´s crystallization parameters can be obtained from the plot of ln(-ln(1-X_c)) *versus* ln(1/v). The kinetic parameters m and K(T) are determined from the slope and intercept, respectively.

3.2.3.2 Activation energy determined by Kissinger model

In order to calculate the activation energy of the amorphous to crystalline phase transformation during the dynamic process, the Kissinger model has been used [21]. This model considers the variation of the peak temperature of the crystallization exotherm (T_c) with the cooling rate. According to Kissinger´s model, the activation energy ΔEa of phase transformation can be determined using the following equation:

$$ln\left(\frac{v}{T_c^2}\right) = -\frac{\Delta Ea}{RT_c} + C \quad \text{(Equation 3.11)}$$

Where T_c is the crystallization peak temperature for a given cooling rate v; ΔEa is the activation energy and R is the gas constant, 8,3143 kJ/mol. From the slope of the plot of ln(v/T_c^2) vs 1000/T_c the activation energy ΔEa can be determined.

3.3 Results and discussion

3.3.1 Isothermal crystallization

3.3.1.1 Evolution of crystallization

The isothermal crystallization kinetics was studied in samples crystallized following two different protocols: cooling from the melt and heating from the glassy state. The range of temperature is selected depending on the nature of the samples. Figures 3.1 and 3.2 present the heat released as a function of time during isothermal hot-crystallization (a, c) and cold-crystallization (b, d) for virgin (a, b) and processed (c, d) PLLA and PLDA.

The fraction of converted material after a period of time t (X_c) was calculated by the ratio of heat evolved at time t and the total heat generated during the complete phase transformation according to equation 3.1. Figures 3.3 and 3.4 plot the unconverted relative crystalline fraction as a function of time ($1-X_c$ vs t).

The evolution of the unconverted crystalline fraction over time (Figures 3.3 and 3.4) follows a sigmoidal curve, which consists of three distinct areas. Initially there is an initiation time, where crystallization has not happened yet, and it is related to the difficulty of formation of stable nuclei. Then crystallization evolves rapidly, as an autocatalytic process, and finally a state of "pseudoequilibrium" is reached until 100% of the maximum crystallinity of each polymer is reached.

The half crystallization time is obtained from Figures 3.3 and 3.4 as the time where $1-X_c$ is equal to 0.5. The reciprocal of half crystallization time ($1000/t_{1/2}$) is represented in Figure 3.5 and 3.6 as a function of isothermal crystallization temperature, T_c, for the different samples.

Materials that have been processed (PLLA ext and PLDA IM) present a much faster crystallization rate than the virgin ones. This is evidenced in Figures 3.1 and 3.2 where processed materials exotherms (c, d) are shifted to lower times in respect to virgin materials exotherms (a, b). The same occurs in Figures 3.3 and 3.4 where processed materials integrals (c, d) are shifted to the left side of the picture to lower values for ln(t).

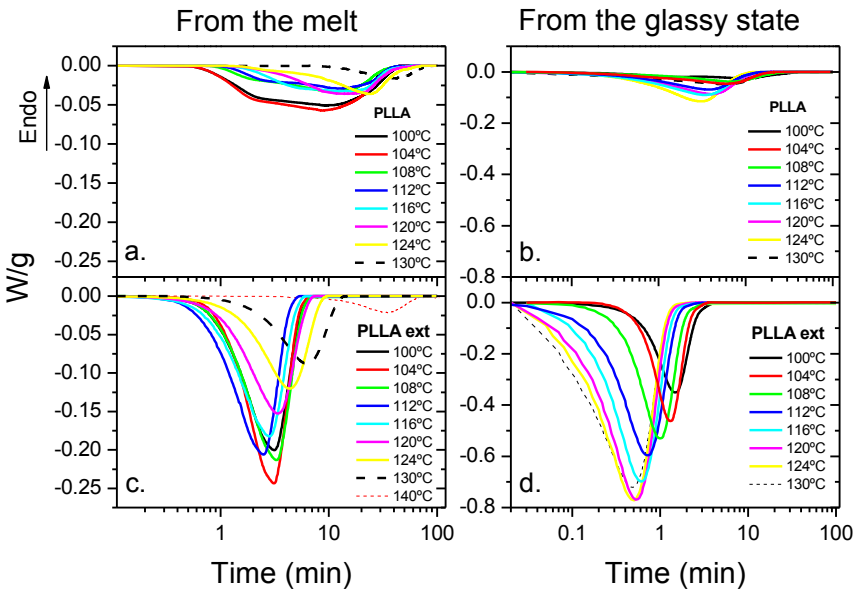

Figure 3.1 Crystallization exotherms of virgin PLLA (a, b) and extruded PLLA (c, d) isothermally crystallized from the melt (a, c) and from the glassy state (b, d) at the specified temperatures

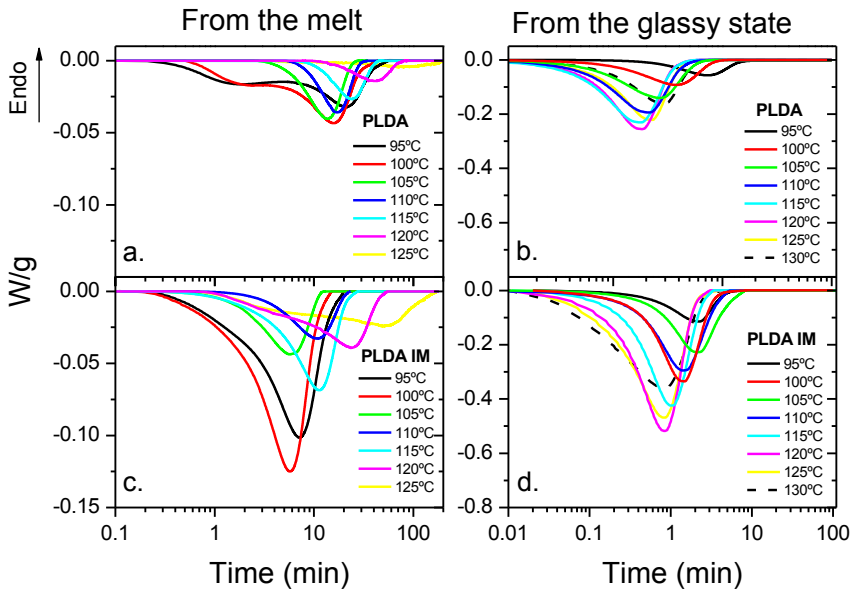

Figure 3.2 Crystallization exotherms of virgin PLDA (a, b) and PLDA processed by injection moulding (c, d) isothermally crystallized from the melt (a, c) and from the glassy state (b, d) at the specified temperatures

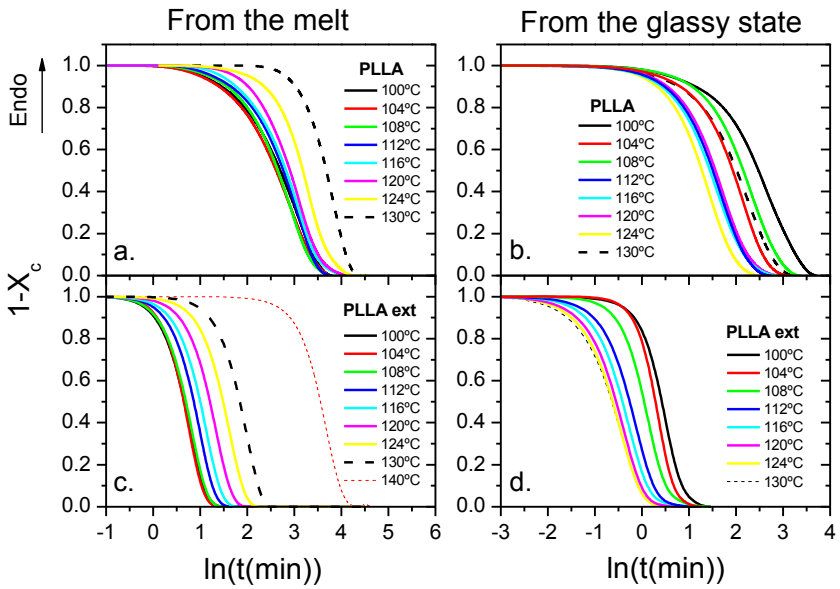

Figure 3.3 Unconverted relative crystalline fraction as a function of time for the isothermal crystallization from the melt (a, c) and from the glassy state (b, d) at the specified temperatures of virgin PLLA (a, b) and extruded PLLA (c, d)

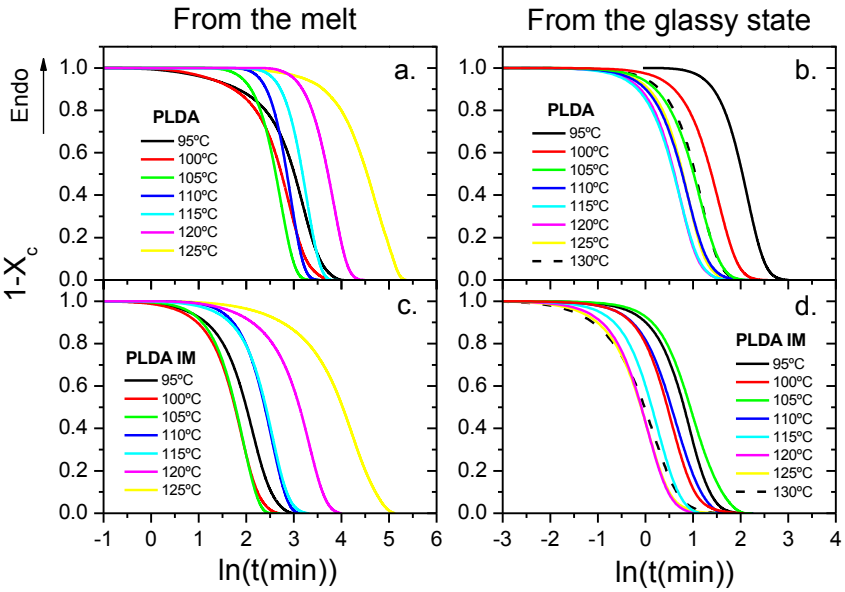

Figure 3.4 Unconverted relative crystalline fraction as a function of time for the isothermal crystallization from the melt (a, c) and from the glassy state (b, d) at the specified temperatures of virgin PLDA (a, b) and injection moulded PLDA (c, d)

In Figures 3.5 and 3.6 the points for the reciprocal half time of processed materials are always located above the values for virgin materials, which indicate that PLLA ext and PLDA IM have a higher crystallization rate than their virgin homologous. This result can be explained by the thermo-mechanical degradation that the materials underwent during processing. Probably the smaller chains resulted from the reduction of polymers molecular weight, can enhance a faster formation of stable nuclei.

The crystallization rate during crystallization from the glassy state (b) is much faster than the rate during crystallization from the melt (a) (Figures 3.5 and 3.6). The difference in between crystallization kinetics taking place at a given temperature during heating from the glass or cooling from the melt relies on the nucleation density [22, 23]. The behaviour can be explained in terms of formation of stable nuclei and the restrictions in the crystals surroundings. Taking into account the protocol of crystallization from the glassy state, crystal nuclei can be formed during the fast cooling from 220 ºC to 25 ºC and the fast heating from 25 ºC to T_c. Mobility of polymeric chains is higher at higher T_c and the polymer has more energy to organize its chains in a crystalline structure. Therefore crystallization from the glassy state is much faster than crystallization from the melt, given the easier formation of crystal nuclei.

When the sample is crystallized from the melt, crystallization takes longer induction times as the crystallization temperature approaches the melting temperature. The driven force in crystallization from the melt is the undercooling ($T_m - T_c$). Crystals nucleate easier at lower T_c. Whereas, the driven force during crystallization from the glassy state depends on the difference between T_c and T_g, which implies that higher T_c induces higher crystallization rates. As T_c approaches T_m the crystallization rate decreases and the common Gaussians behaviour that describes the relationship between the crystallization rate and T_c is observed. The maximum peak of crystallization rate is explained by the nucleation and transport factors that affect the kinetics.

According to Di Lorenzo studies on PLLA isothermal crystallization behaviour from the melt within 80 ºC and 150 ºC [15], the fastest crystallization rate occurs at 108 ºC. Iannace and Nicolais [16] observed a maximum in crystallization kinetics for PLLA around 105 ºC. In our study PLLA and extruded PLLA presented a maximum rate at 104 ºC (Figure 3.5 a). Pantani et al [23] found that virgin PLDA presents the fastest crystallization rate during isothermal crystallization from the melt at 115 ºC, and injected PLDA at 100 ºC. In our studies PLDA and PLDA IM evidence a maximum rate at 105 ºC (Figure 3.6 a). Small divergences between the results extracted from bibliography and ours can be explained in terms of the different molecular weight of the polymers, and the different thermal history.

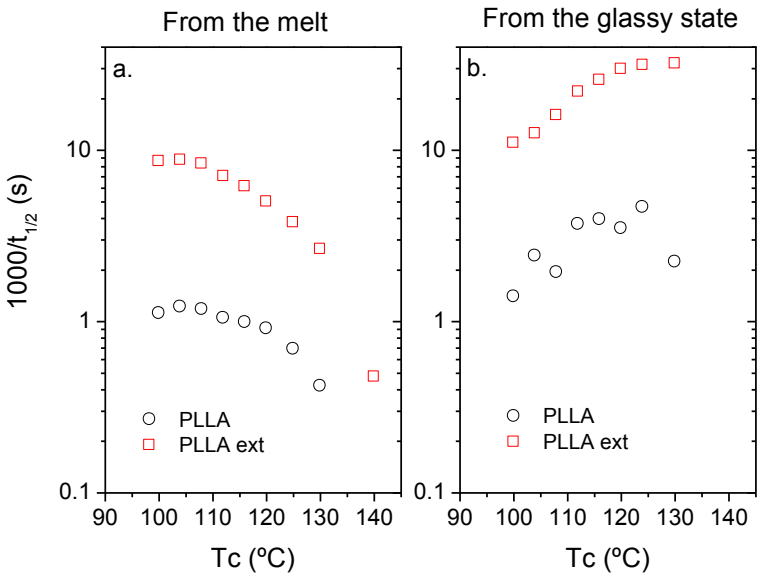

Figure 3.5 Reciprocal of half crystallization time as a function of temperature for the isothermal crystallization from the melt (a) and from the glassy state (b) of virgin PLLA and extruded PLLA

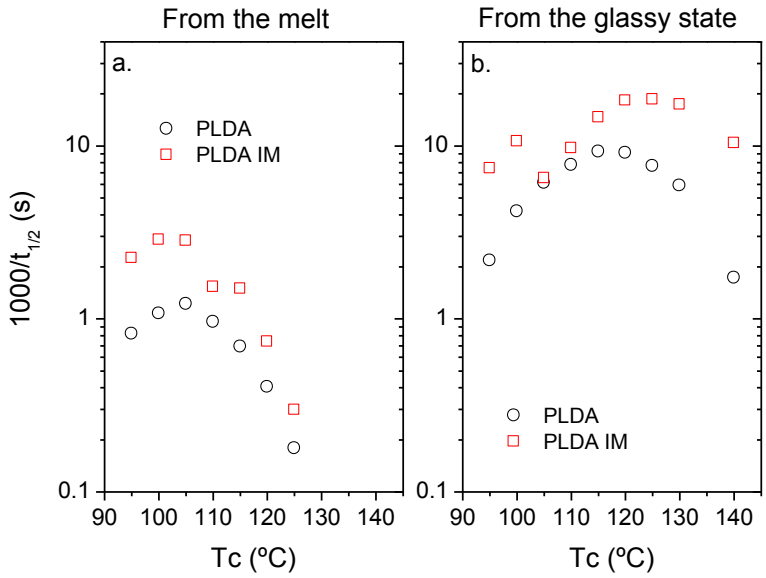

Figure 3.6 Reciprocal of half crystallization time as a function of temperature for the isothermal crystallization from the melt (a) and from the glassy state (b) of virgin PLDA and PLDA processed by injection moulding

The fastest crystallization rate during crystallization from the glassy state appears at 124 ºC for PLLA, 130 ºC for PLLA ext (Figure 3.5 b), 115 ºC for PLDA and 125 ºC for PLDA IM (Figure 3.6 b). The results for virgin PLDA are in agreement with the findings of De Santis *et al.* [22] and Pantani *et al*. [23] who also have found a maximum crystallization rate during isothermal crystallization from the glassy state at 115 ºC. A discontinuity is observed for PLDA IM within 95 ºC and 105 ºC (Figure 3.6 b). Discontinuities can be explained by changes in the crystallization mechanism or the formation of different crystal morphology, but also they can be due to the presence of heterogeneities. It is important to take into account that a new capsule was used for each experiment, and discontinuities can be explained also due to small variations in the samples.

3.3.1.2 Crystallization kinetics analysis (Avrami)

The analysis of isothermal crystallization kinetics was performed using the model described by Avrami in equation 3.2. Figures 3.7 and 3.8 plots the straight lines obtained by representing Avrami model according to equation 3.3. By plotting ln $(-\ln(1-X_c))$ vs ln (t) the Avrami constant k is obtained from the intercept ln k, and the constant n corresponds to the slope of the straight line.

Avrami constants values obtained at each crystallization temperature for each crystallization protocol are listed in Table 3.1 for PLLA and PLLA ext, and in Table 3.2 for PLDA and PLDA IM. The half time needed to achieve complete crystallization ($t_{1/2}$) is also listed in Tables 3.1 and 3.2.

Comparison between processed materials (c, d) and virgin materials (a, b) notes that, given the same temperature of crystallization, the rate constant k is larger (i.e. faster) and the half crystallization time is smaller for processed materials. The kinetic constant, k, of extruded PLLA crystallized from the melt (Table 3.1 c) is about one order of magnitude faster if compared to the virgin material (Table 3.1 a). At T_c = 130 ºC, extruded PLLA needs 6.3 minutes to achieve the 50% of complete crystallization with a k=3.07E-03 which is two orders of magnitude faster than k value for virgin PLLA. Values for extruded PLLA crystallized from the solid (Table 3.1 d) are one to two orders of magnitude faster than virgin PLLA k values (Table 3.1 b).

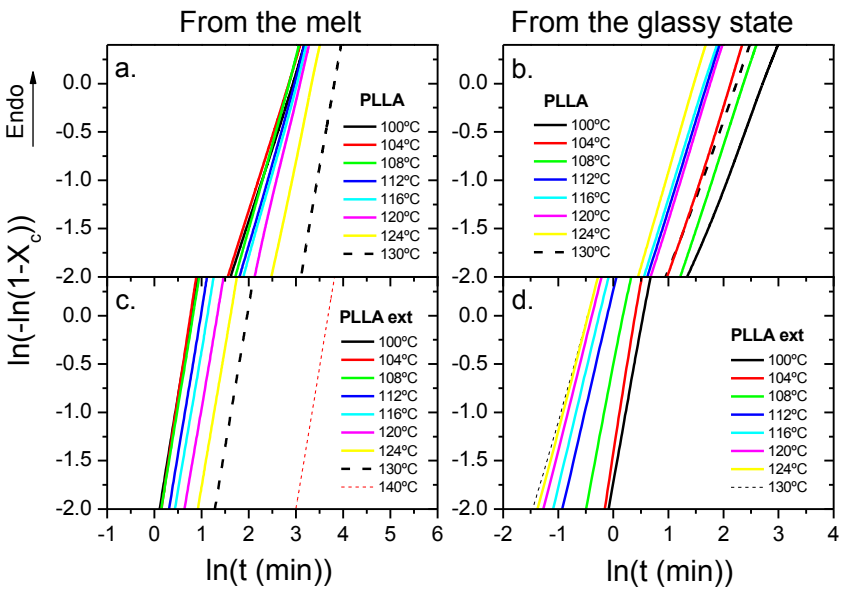

Figure 3.7 Avrami analysis of virgin PLLA (a, b) and extruded PLLA (c, d) isothermally crystallized from the melt (a, c) and from the glassy state (b, d) at the specified temperatures

Comparison between both crystallization protocols indicates that k constant is faster and $t_{1/2}$ is smaller for crystallization from the glassy state. At 130 ºC, the half crystallization time of extruded PLLA is only 0.5 minutes with a k=2.43 (Table 3.1 d), which is three orders of magnitude higher than the value obtained in the protocol from the melt (Table 3.1 c) . In the case of virgin PLLA, the kinetic constant, k, for the crystallization from the glassy state is one to three orders of magnitude faster than k for the protocol from the melt. Virgin PLLA needs 39.7 minutes to achieve the 50% of complete crystallization from the melt at 130 ºC (Table 3.1 a), but if the protocol is from the glassy state, it takes only 7.5 minutes with a k three orders of magnitude faster (Table 3.1 b).

During hot-crystallization, k values of injection moulded PLDA are one to three orders of magnitude faster than k values for virgin PLDA. PLDA IM needs approximately the half of the time that virgin PLDA takes to achieve the 50% of complete crystallization during crystallization from the melt at 120 ºC (Table 3.2 a, c). PLDA IM kinetic constant at that temperature (k=1.45E-03) is three orders of magnitude faster than virgin PLDA k value (Table 3.2).

Table 3.1 Avrami constants of virgin PLLA (a, b) and extruded PLLA (c, d) isothermally crystallized from the melt (a, c) and from the glassy state (b, d) at the specified temperatures

PLLA							
a. From the melt				b. From the glassy state			
T_c (ºC)	n	k (s^{-1})	$t_{1/2}$ (min)	T_c (ºC)	n	k (s^{-1})	$t_{1/2}$ (min)
130	2.8	2.08E-05	39.7	130	1.5	3.09E-02	7.5
125	2.3	4.31E-04	24.1	125	2.0	5.58E-02	3.6
120	2.1	1.73E-03	18.3	120	1.8	3.84E-02	4.8
116	2.3	5.42E-03	16.8	116	1.8	4.86E-02	4.2
112	2.1	6.40E-03	15.9	112	1.8	4.33E-02	4.5
108	2.3	6.83E-03	14.2	108	1.7	1.61E-02	8.6
104	2.4	1.24E-02	13.7	104	1.7	2.50E-02	6.9
100	2.3	1.22E-02	14.9	100	1.5	1.83E-02	11.9
PLLA ext							
c. From the melt				d. From the glassy state			
T_c (ºC)	n	k (s^{-1})	$t_{1/2}$ (min)	T_c (ºC)	n	k (s^{-1})	$t_{1/2}$ (min)
140	2.9	2.17E-05	35.0				
130	3.0	3.07E-03	6.3	130	2.0	2.43E+00	0.5
125	2.9	9.29E-03	4.4	125	2.2	2.66E+00	0.5
120	2.9	2.09E-02	3.3	120	2.3	2.38E+00	0.6
116	2.9	3.73E-02	2.7	116	2.4	1.87E+00	0.7
112	3.0	5.31E-02	2.4	112	2.5	1.32E+00	0.8
108	3.0	8.56E-02	2.0	108	3.0	6.07E-01	1.0
104	3.3	8.12E-02	1.9	104	3.2	2.42E-01	1.3
100	3.0	9.50E-02	1.9	100	2.8	1.78E-01	1.5

PLDA crystallization from the glassy state is one to five orders of magnitude faster than the crystallization from the melt. At 120 ºC for example, the value of k for virgin PLDA crystallized from the melt is 2.46E-06, and it takes 41.2 minutes for the material to achieve the half of complete crystallization. If the protocol from the solid is applied, k value increases five orders of

magnitude (k=1.39E-01), and PLDA needs only 1.8 minutes to achieve the 50% of complete crystallization. Kinetic constants of PLDA IM for the protocol from the glassy state are one to two orders of magnitude faster than the protocol from the melt. At 120 ºC, injected PLDA takes less than a minute to achieve the half of the complete crystallization, with a k which is two orders of magnitude faster than the k obtained when PLDA IM is crystallized from the melt (Table 3.2).

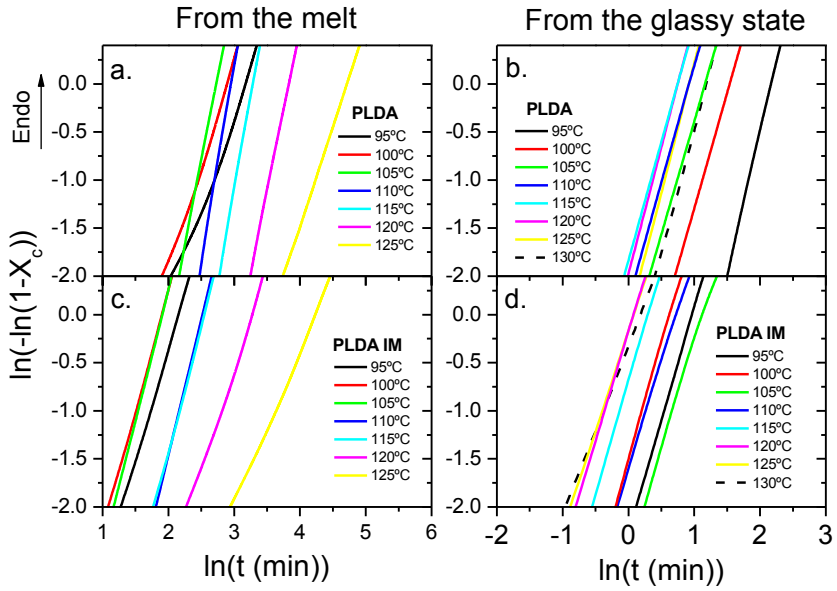

Figure 3.8 Avrami analysis of virgin PLDA (a, b) and PLDA processed by injection moulding (c, d) isothermally crystallized from the melt (a, c) and from the glassy state (b, d) at the specified temperatures

It can be concluded, that the fastest rates are obtained during crystallization from the glassy state with the processed materials. The optimal temperature for PLLA ext is T_c = 130 ºC and for PLDA IM is T_c = 125 ºC. The faster crystallization from the glassy state can be explained due to the easier thermal activation that induces a faster organization of polymer chains. Crystallization mechanisms are also different, during hot-crystallization nucleation dominates, however during cold-crystallization diffusion and kinetic factors related to molecular mobility dominate. The faster crystallization of processed materials was explained before and it was attributed to the smaller chains resulted from the molecular weight reduction induced by thermo-mechanical degradation that the materials underwent during processing.

During crystallization from the melt, virgin PLLA and extruded PLLA exhibit n values between the ranges 2.1 – 2.8 and 2.9 – 3.3 respectively. The Avrami exponent values indicate that PLLA

has a trend from two- to three dimensional crystal growth. Values of n found in this research are similar to Avrami exponents reported for neat PLLA by other authors. Zhou *et al.* [24] reported n values within 2.6 and 2.9 in the isothermal temperature range of 90 – 140 ºC; Tsuji *et al.* [25] found Avrami exponents ranging from 2.3 and 3.2 at T_c= 90 – 125 ºC; Kolstad [26] calculated n values from 2.5 to 3.3 at T_c= 90 – 130 ºC and Iannace and Nicolais [16] from 2.8 and 3.2 at T_c=90-130 ºC.

Table 3.2 Avrami constants of virgin PLDA and PLDA processed by injection moulding (IM) isothermally crystallized from the melt and from the glassy state at the specified temperatures

PLDA							
a. From the melt				b. From the glassy state			
T_c (ºC)	n	k (s^{-1})	$t_{1/2}$ (min)	T_c (ºC)	n	k (s^{-1})	$t_{1/2}$ (min)
				130	2.5	4.89E-02	2.8
125	2.1	5.27E-05	93.7	125	2.6	8.57E-02	2.2
120	3.4	2.46E-06	41.2	120	2.6	1.39E-01	1.8
115	3.9	2.61E-06	24.1	115	2.5	1.59E-01	1.8
110	4.2	4.62E-06	17.4	110	2.5	1.05E-01	2.2
105	3.5	6.68E-05	13.7	105	2.3	6.46E-02	2.7
100	2.0	2.43E-03	15.5	100	2.4	2.50E-02	4.0
95	1.9	2.53E-03	21.4	95	3.1	1.39E-03	7.7
PLDA IM							
c. From the melt				d. From the glassy state			
T_c (ºC)	n	k (s^{-1})	$t_{1/2}$ (min)	T_c (ºC)	n	k (s^{-1})	$t_{1/2}$ (min)
				130	1.7	7.11E-01	1.0
125	1.5	1.34E-03	56.0	125	2.1	8.32E-01	0.9
120	2.0	1.45E-03	22.6	120	2.3	8.41E-01	0.9
115	2.3	2.23E-03	11.2	115	2.4	5.07E-01	1.1
110	2.6	3.22E-03	7.6	110	2.3	2.01E-01	1.7
105	2.5	2.08E-03	10.3	105	2.4	7.73E-02	2.6
100	2.3	1.16E-02	5.8	100	2.5	2.22E-01	1.6
95	2.2	8.51E-03	7.4	95	2.3	1.03E-01	2.3

Virgin PLDA and injection moulded PLDA show n values between the ranges 1.9 – 4.2, and 1.5 – 2.7 when they are isothermally crystallized from the melt. These indicate a mixture of bi- and three-dimensional heterogeneous growth. These results are in agreement with Tsuji *et al.* [25] who found that Avrami exponent ranges between 2.04 and 4.66 for PLLA with different contents of poly-D-lactic acid (PDLA), which is an indication of three-dimensional growth of crystallites. However, our findings deviate from the Avrami index reported by Pantani *et al.* [23] who found a single value for PLDA and injected PLDA exponents at T_c = 90 – 130 ºC : n=2.8 for virgin PLDA and n=2.9 for injected PLDA. Nonetheless, Pantani *et al.* determined a similar conclusion, that PLDA n values confirm a spherical (three dimensional) growth of heterogeneously nucleated crystals.

The differences between calculated data and values reported in references can be attributed to divergences during the parameters used for Avrami fitting like the determination of the onset of crystallization or induction time, the range of relative degree of crystallinity, or the establishment of a base line [27].

During isothermal crystallization by heating from the solid state, n for virgin PLLA exhibits considerably lower values than those obtained with the “from the melt” protocol. Avrami index ranging from 1.5 and 2 suggests a heterogeneous bi-dimensional growth (Table 3.1 b). These lower values for n probably can be explained due to a large nucleation density, as the presence of heterogeneities, like stable nuclei, could interfere with the radial growth of the spherulites. On the contrary, Avrami index for PLLA during the protocol from the melt ranges from 2.1 to 2.8 indicating a mixture of bi- and three-dimensional heterogeneous growth. This type of growth and crystal geometry is also exhibited by PLLA ext, PLDA and PLDA IM.

3.3.1.3 Melting behaviour after isothermal crystallization

Figure 3.9 and 3.10 report the DSC heating scans after isothermal crystallization from the melt and from the glassy state for virgin and processed PLLA and PLDA respectively.

Melting curves for PLLA show two endothermic peaks at $T_c \leq 120$ ºC for both protocols and both materials (virgin and extruded) (Figure 3.9). No evident differences are noticed depending on the effect of processing or crystallization protocol, the melting behaviour is similar for all the conditions. On increasing T_c, the height of the lower temperature peak increases with respect to the higher temperature peak, and it is also shifted toward higher melting temperatures. For $T_c \geq 120$ ºC only one peak is detected, and a progressive shift of the melting temperature toward higher temperatures is noticed on increasing the crystallization temperature.

Melting curves for PLDA show a similar behaviour (Figure 3.10). At lower crystallization temperatures two peaks are detected, that progressively turn into one peak at certain critical T_c. That critical crystallization temperature seems to have a correlation with both the crystallization

protocol and the nature of the material. Virgin PLDA crystallized from the melt evidenced the lowest critical T_c at 115 ºC (Figure 3.10 a). Injected PLDA crystallized from the glassy state evidenced the highest critical T_c at 130 ºC (Figure 3.10 d).

The presence of two melting peaks can be attributed either to melt-recrystallization phenomenon or changes in crystal morphology. To analyze in detail this phenomenon, and understand what is occurring, X-ray scattering was used to probe the crystal structure of some thermal treatments at crystallization temperatures lower and higher than critical T_c.

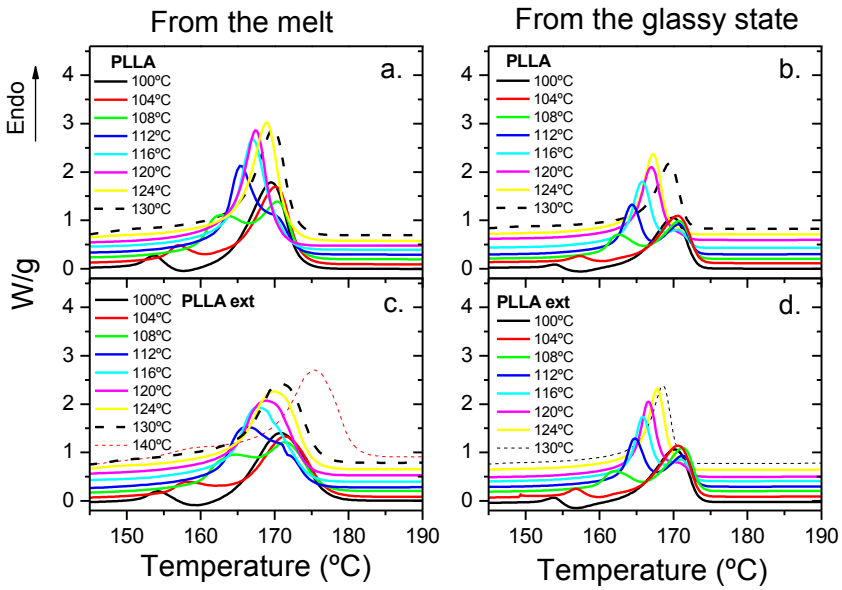

Figure 3.9 Subsequent melting endotherms of virgin PLLA (a, b) and extruded PLLA (c, d) after isothermal crystallization from the melt (a, c) and from the glassy state (b, d) at the specified temperatures

As commented in the introduction, PLLA and PLDA can crystallize into three forms (α, β and γ), generally referred to as polymorphism. The three structural modifications are characterized by different helix conformation and cell symmetries. The α' form is the most common crystalline form, it grows upon melt or cold crystallization. Its main diffractions are (110)/(200), (203) and (015) which occur at 16.3 º, 18.6 º and 22.3 º respectively [6, 9, 28, 29]. The α' form can evolve into a more orderly form which is called α. WAXD patterns of the α-form show new diffractions at 20.7 º, 22.9 º , 24.0 º and 25 º [2].

The materials subjected under X-ray studies were the processed polymers thermal treated under the protocol from the glassy state (annealed). PLLA ext crystal structure was studied at 100 ºC and 124 ºC and PLDA IM at 95 ºC, 115 ºC and 130 ºC.

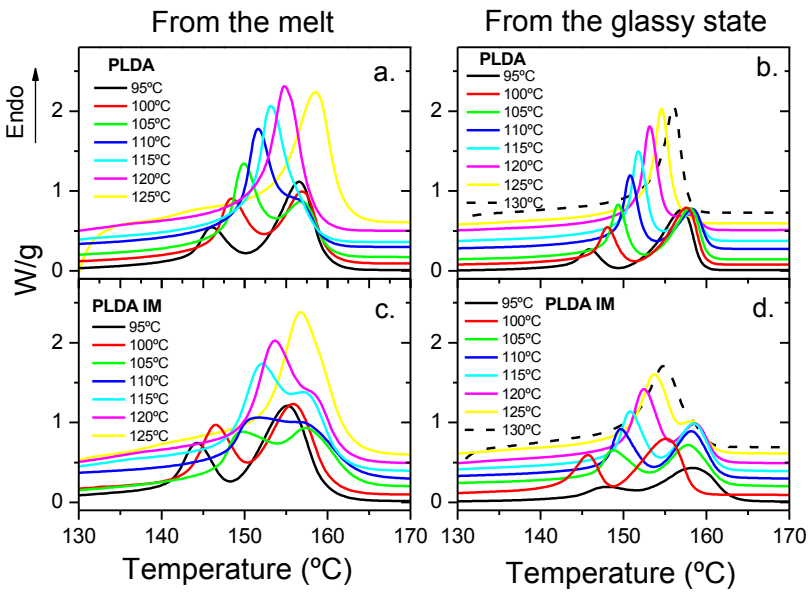

Figure 3.10 Subsequent melting endotherms of virgin PLDA (a, b) and PLDA processed by injection moulding (c, d) after isothermal crystallization from the melt (a, c) and from the glassy state (b, d) at the specified temperatures

Figure 3.11 shows WAXD patterns of PLLA ext crystallized from the glassy state at 100 ºC and 124 ºC. At 100 ºC the WAXD pattern shows the reflections reported for α'-form crystals [6, 9, 28, 29]. It is observed that at 124 ºC the two strong reflections, (110)/(200) and (203) planes, shift to higher 2θ than at 100 ºC. The diffraction at 22.3º gains intensity at high T_c. WAXD patterns at 124 ºC show the new diffractions that characterize the α-form [2]. The multiple melting behaviour of PLLA can be explained therefore by the recognition of the existence of these two different crystal forms. At T_c<124 ºC the disordered α'-form is produced, but at $T_c \geq$ 124 ºC the order α-form is predominantly developed.

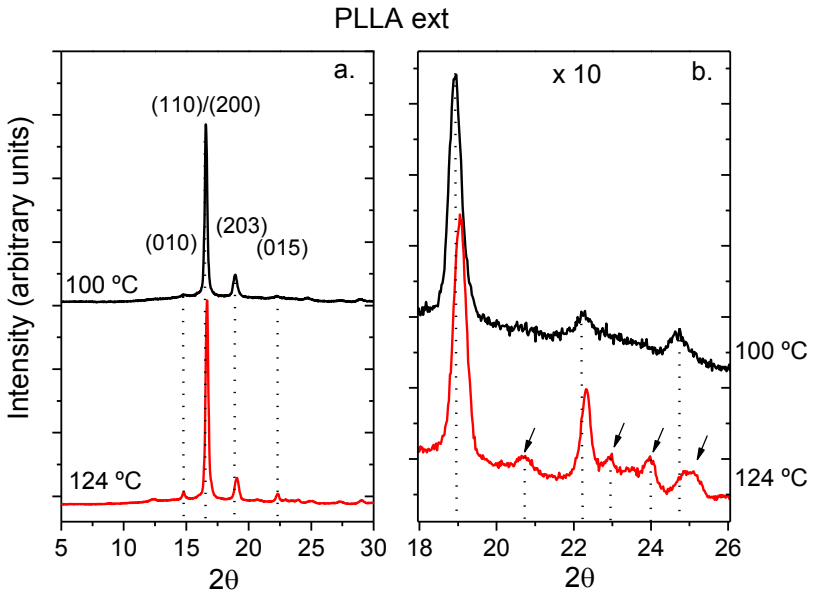

Figure 3.11 WAXD patterns of extruded PLLA isothermally crystallyzed from the glassy state at 100 ºC and 124 ºC

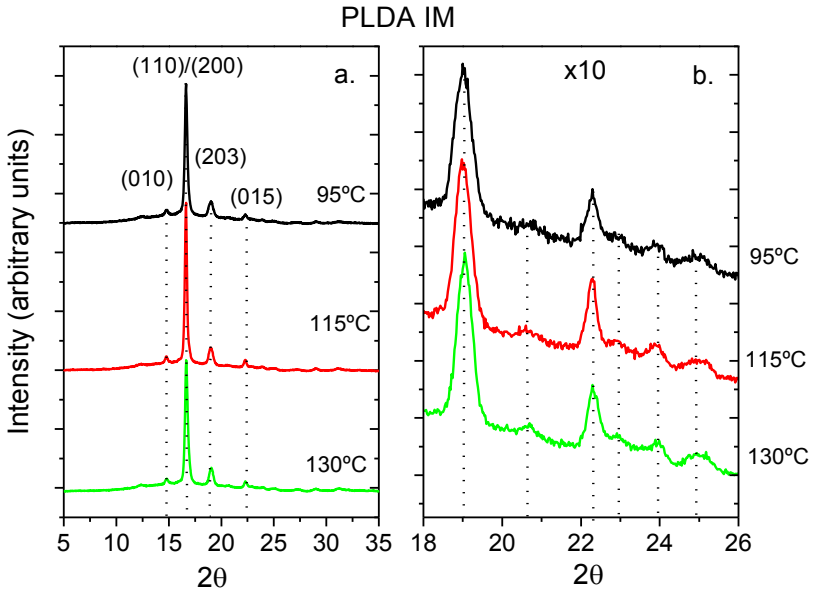

Figure 3.12 WAXD patterns of injected PLDA isothermally crystallyzed from the glassy state at 95, 115 and 130 ºC.

Figure 3.12 shows WAXD patterns of PLDA IM crystallized at 95 ºC, 115 ºC and 130 ºC. Diffractograms at all the three temperatures are very similar between them. There are no significant differences that could indicate the presence of a different crystal form. As T_c increases, the peaks intensity grows which means that the crystals formed gain more order. At all temperatures the reflections are characteristics of the α-form.

Figure 3.13 shows the WAXD patterns of extruded PLLA isothermally crystallized at 100 ºC recorded upon heating. During the heating process the major peak (110/200) at 16.3º and the peak (015) at 18.6º begin to appear at higher 2θ from 158 ºC. From that temperature on also the peak at 22º gains intensity and a new peak is visible at 23 º. The peak that appears at 24.4º at T<158ºC, appears at higher 2θ at T≥158 ºC. These results revealed that α'-form crystals generated by annealing PLLA at 100 ºC, transform into their α-counterparts upon heating above 158 ºC.

It has been revealed that at low T_c, the melting behavior of PLLA corresponds to a polymorphic phase transition, at intermediate T_c it is changed to the usual melt-recrystallization mechanism evidenced by two endothermic peaks [9] and at high T_c perfect α-form crystals are generated and they melt directly evidenced by a single melting peak [8] .

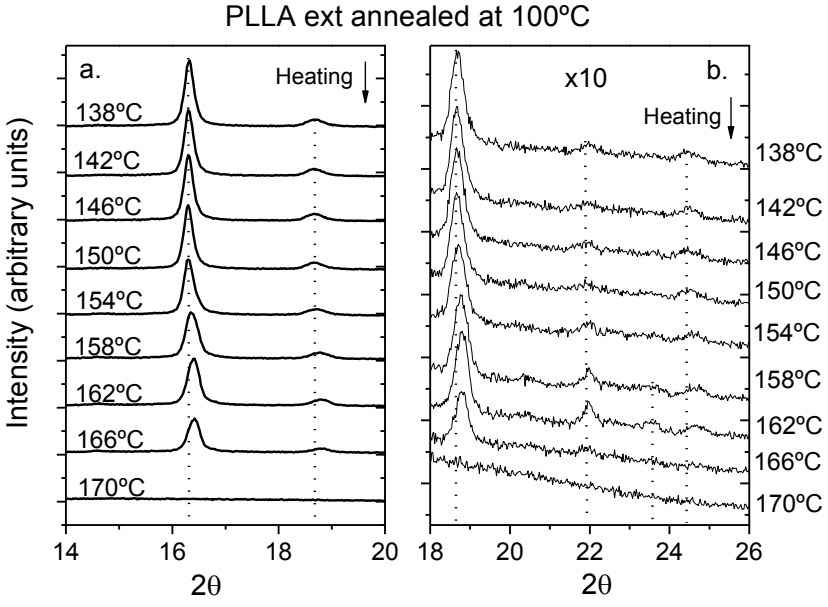

Figure 3.13 WAXD patterns of extruded PLLA annealed at 100 ºC recorded upon heating

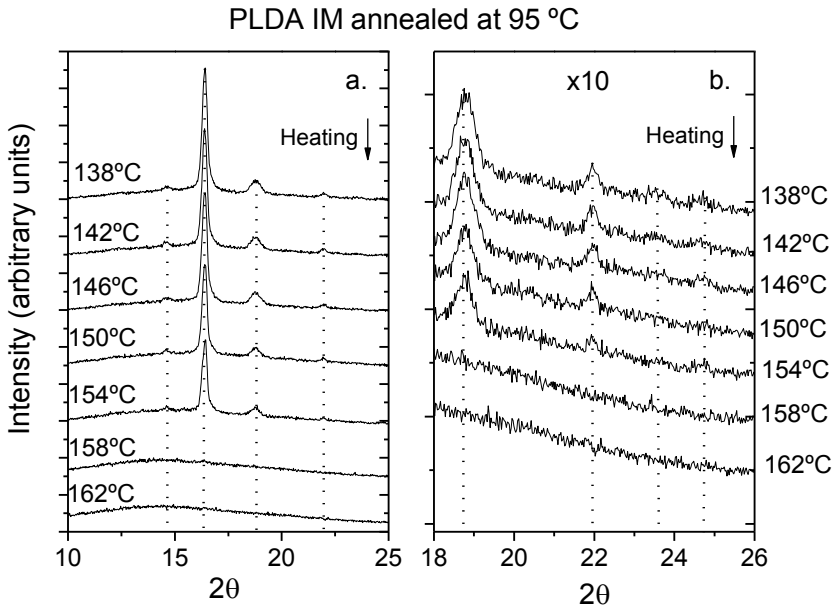

Figure 3.14 WAXD patterns of injected PLDA annealed at 95 ºC recorded upon heating

Figure 3.14 shows the WAXD patterns of injected PLDA annealed at 95ºC recorded upon heating. During heating smaller peaks at 18.7º, 21.9º, 23.5º and 24.7º lose intensity from 142 ºC. Intensity of the major peak at 16.4º begins to decrease from 150 ºC until it completely disappears at the melting temperature (158 ºC). This behavior evidences the melt-recrystallization phenomenon.

3.3.1.4 Enthalpy of melting

The total heat absorbed during melting ΔH_m is obtained from the integrals of the endotherms of Figures 3.9 and 3.10. Enthalpy of melting is reported as a function of the crystallization temperature in Figure 3.15 for virgin and processed PLLA crystallized from the melt (a) and from the glassy state (b). For all materials and conditions, the enthalpy of fusion shows and increasing trend with T_c. There is only an exception for crystallization from the glassy state at 130 ºC, where ΔH_m decreases in respect with the enthalpy at 122 ºC. At each T_c, the enthalpy of fusion is always larger when the annealing protocol is applied, for both, virgin and extruded PLLA. This occurs except for the case at 130 ºC, where the value of enthalpy of fusion is smaller than that obtained when the material is crystallized from the melt. Values for extruded PLLA ΔH_m are very similar or in some cases slightly higher than virgin PLLA. This suggests that extruded PLLA can acquire a higher degree of crystallinity and has more packaging ability than virgin PLLA, probably due to its shorter molecular weight.

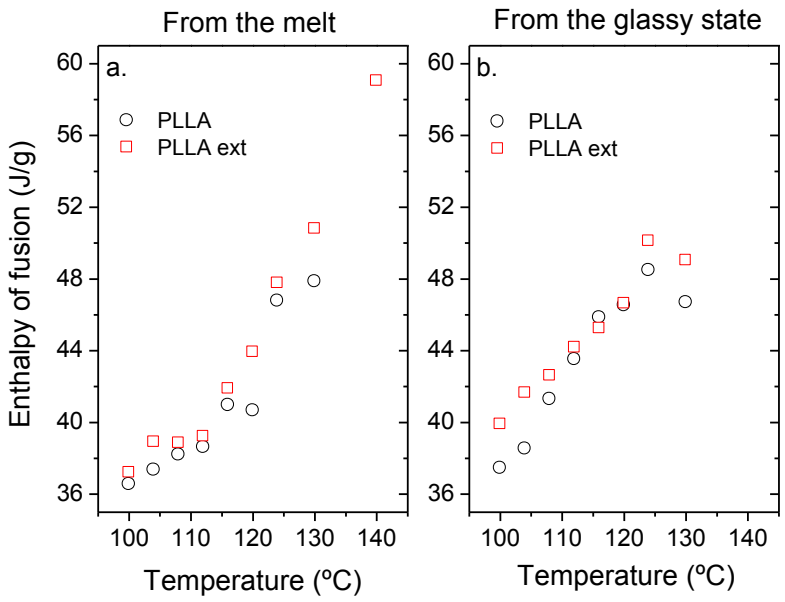

Figure 3.15 Enthalpy of melting as a function of crystallization temperature for virgin PLLA and extruded PLLA isothermally crystallized from the melt (a) and from the glassy state (b)

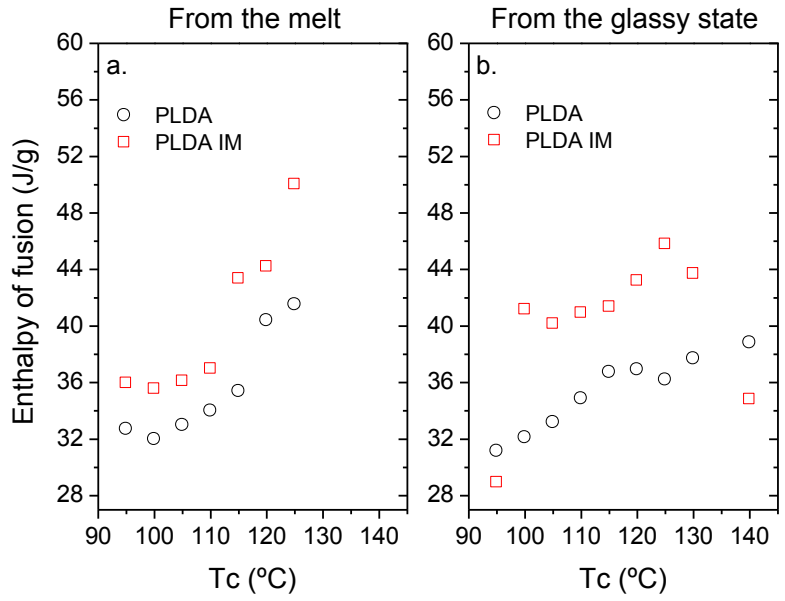

Figure 3.16 Enthalpy of melting as a function of crystallization temperature for virgin PLDA and PLDA processed by injection moulding isothermally crystallized from the melt (a) and from the glassy state (b)

Figure 3.16 plots the enthalpy of melting as a function of T_c for virgin PLDA and injected PLDA isothermally crystallized from the melt (a) and from the glassy state (b). PLDA and PLDA IM enthalpy of fusion increases with T_c when the protocol "from the melt" is applied. The same trend is observed in the case of virgin PLDA crystallized from the glassy state, but PLDA IM presents a different behaviour. Enthalpy of fusion of annealed PLDA IM starts increasing with T_c, it shows a maximum at 125 ºC and then starts decreasing with T_c. This behaviour is related with the shorter polymer chains of PLDA IM that can induce a larger density of stable nuclei at high crystallization temperature, which could impede the progress of the crystallization degree within that condition.

Enthalpy of fusion of PLDA IM is always higher than values of PLDA, for both protocols. The only exceptions occur for crystallization from the solid state at the highest and lowest temperatures. This evidences that the injected material can acquire a higher crystalline fraction than its virgin homologous, probably due to easier packaging ability given its shorter molecular weight. The exceptions can be explained in terms of mobility and formation of nuclei. At 95 ºC probably the mobility is not enough to allow an efficient crystal growth. At T_c>125 ºC probably a larger density of nuclei hinders the diffusion and the progress of the crystallization.

In the case of virgin PLDA, the heat absorbed during crystallization from the melt is similar to the heat absorbed during the protocol from the solid state. In the case of injected PLDA, the enthalpy of fusion during crystallization from the solid state is higher than the calculated during crystallization from the melt at T_c<125 ºC.

Findings obtained in this section of the chapter have a tremendous practical and industrial importance. It has been demonstrated that similar crystallinity degrees can be obtained with both protocols, therefore the decision of the suitable protocol to tailor the crystallinity of the material lies in its efficiency and kinetics. Taking into account that the protocol from the glassy state is one to two orders faster than the protocol from the melt, it seems that the most suitable processing step in order to effectively control the crystallinity degree of the material is crystallization from the solid state.

In injection moulding this means, for example, that the same crystallinity degree could be obtained either by keeping the sample inside the mould at 105 ºC during 20 minutes or by adopting a post-processing step by heating an amorphous injected sample in an oven at 105 ºC during 5 minutes (Table 3.2 c, d). The first option sounds unfeasible to be performed in an industry, whereas the second one evidently is more affordable.

3.3.1.5 Hoffman-Lauritzen analysis of spherulite growth rate

As already indicated, for the calculations of the nucleation constant K_g for a heterogeneous nucleation process the modified Hoffman-Lauritzen equation can be applied (Equation 3.8). The equilibrium melting temperature is an important parameter in this equation and was determined by the Hoffman-Weeks [17] linear extrapolation method (Figure 3.17 for virgin (a) and extruded PLLA (b) and Figure 3.18 for virgin (a) and injected (b) PLDA). From Figures 3.9 and 3.10 the melting temperature is determined at each T_c. The equilibrium melting temperature is obtained by the extrapolation of the experimental results to the identity function $T_m = T_c$ as shown in Figures 3.17 and 3.18.

Only data above 108 ºC was used in order to obtain a good linear regression evidenced by a correlation coefficient close to 1. The equilibrium melting temperature obtained for processed materials is very close to the values obtained for virgin materials. T_m^0 values calculated in this research are lower to those reported in references which are close to 207 ºC for PLLA [16, 30]. Divergences can be related to differences in molecular weight and also to the variation of equilibrium temperature with the range of temperatures selected for the extrapolation.

Values for Kg can be obtained from the slopes of the plot $\ln(k)+U/R(T_c-T_{inf})$ versus $1/T_c\Delta Tf$ (Figure 3.19). T_g = 60.8 ºC and T_g = 59.8 ºC were used for PLLA and PLDA respectively. Figure 3.19 shows the results of Hoffman Lauritzen treatment for virgin and processed PLLA and PLDA crystallized from the melt.

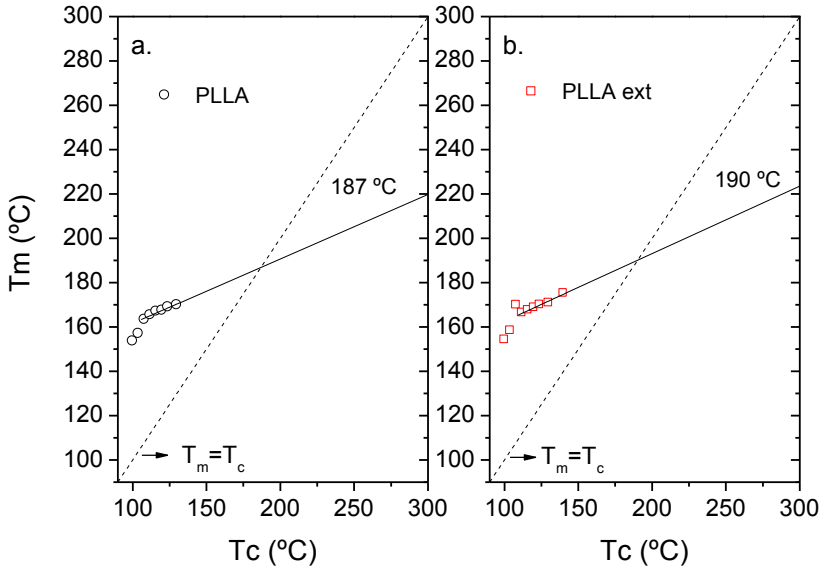

Figure 3.17 Determination of the equilibrium melting temperature T_m^o by Hoffman-Weeks linear extrapolation for virgin PLLA (a) and extruded PLLA (b) isothermally crystallized from the melt

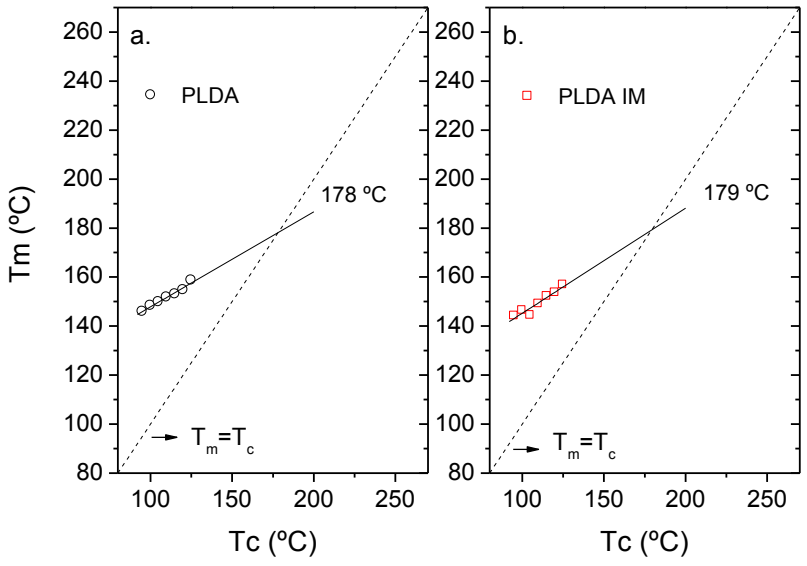

Figure 3.18 Determination of the equilibrium melting temperature T_m^o by Hoffman-Weeks linear extrapolation for virgin PLDA (a) and PLDA processed by injection moulding (b) isothermally crystallized from the melt

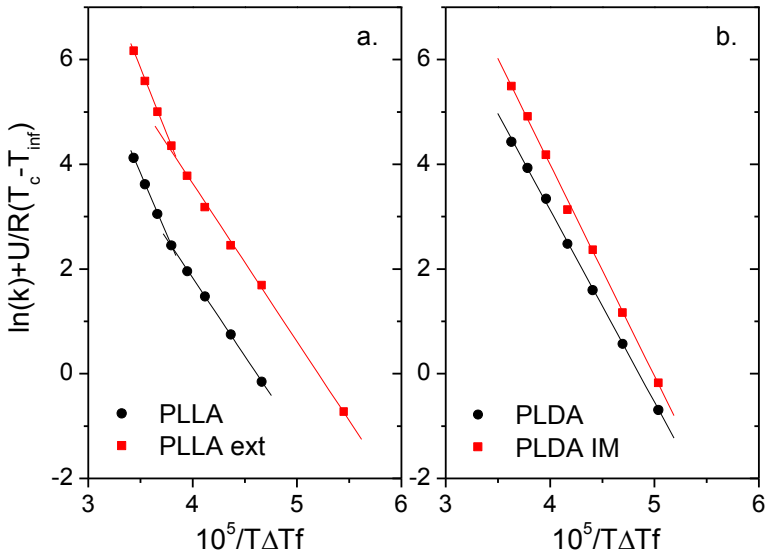

Figure 3.19 Hoffman-Lauritzen analysis of spherulite growth rate data of virgin and processed PLLA and PLDA

Two regions with different slopes are evidenced for PLLA and PLLA ext, indicating a change of regime around 112 ºC. For 112 ºC $\leq T_c \leq$ 130 ºC, Kg is equal to 4.65E5 K^2 for PLLA, and 5.00E5 K^2 for extruded PLLA (Table 3.3). For $T_c \leq$ 112 ºC, Kg acquires the value around 3.00E5 for both materials. Values for Kg are close to those obtained in literature [15, 16, 30]. The presence of two regions is considered as an indication of a transition from regime II to regime III [15, 16].

Hoffman Lauritzen analysis for PLDA and PLDA IM only shows one region with one slope. Kg=3.67E5 for PLDA and Kg=4.04E5 for PLDA IM. This indicates that PLDA does not undergo a regime transition.

Table 3.3 Hoffman Lauritzen Kg values obtained for virgin and processed PLLA and PLDA

	PLLA	PLLA ext		PLDA	PLDA IM
Kg II	2.99E+05	3.02E+05	**Kg**	3.67E+05	4.04E+05
Kg III	4.65E+05	5.00E+05			

3.3.2 Dynamic crystallization

Studies of dynamic crystallization are particularly interesting because they are close to the conditions of polymer processing on an industrial scale, where crystallization occurs under non-isothermal conditions. Dynamic hot-crystallization studies were performed on processed materials (PLLA ext and PLDA IM) at different cooling rates (CR): 1, 3, 5, 10, 20, 30 and 40ºC/min.

3.3.2.1 Crystallization dependence with the cooling rate (Ozawa analysis)

The non-isothermal crystallization curves for both materials are presented in Figure 3.20. It is observed that for PLLA ext is easier to form crystals under dynamic conditions from the melt than for PLDA IM. Extruded PLLA crystallizes at crystallization rates lower than 10 ºC/min and injected PLDA at CR lower than 5 ºC/min. PLLA ext exothermic peaks are more evident than PLDA IM peaks. A decrease in the crystallization temperature and a smaller exothermic trace is mainly observed with the increment of the cooling rate.

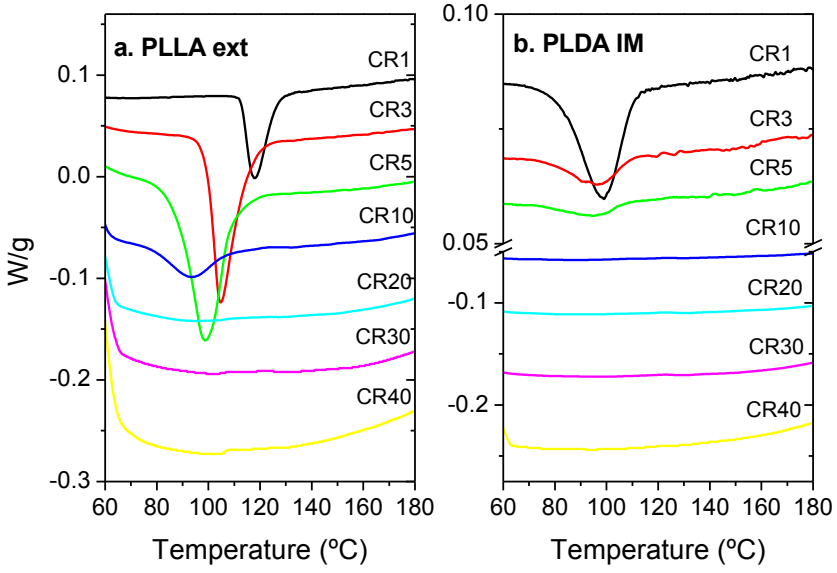

Figure 3.20 DSC thermograms of non-isothermal melt crystallization of extruded PLLA (a) and injection moulded PLDA (b)

This trend can be clearly observed in Figure 3.21, by plotting the temperature of crystallization versus the cooling rate. An exponential decay is reflected, more evident for PLLA ext than for PLDA IM which shows lower values for T_c. This behaviour is explained because the incorporation of D-lactyl units in PLDA chains affects markedly the crystallization ability [31]. The presence of D-lactyl units could introduce more disorder in the chain, thus producing a

higher crystalline imperfection, and with this decreasing the crystallization temperature values for PLDA.

The fraction of converted material after a period of time t (X_c) was calculated by the ratio of heat evolved at temperature T and the total heat generated during the complete phase transformation ($\Delta H(T) / \Delta H(\infty)$). Figure 3.22 plots the unconverted relative crystalline fraction as a function of temperature ($1-X_c$ vs T). The resulting curves have a sigmoidal shape, where the inflection point corresponds to the minimum of the exotherms shown in Figure 3.20.

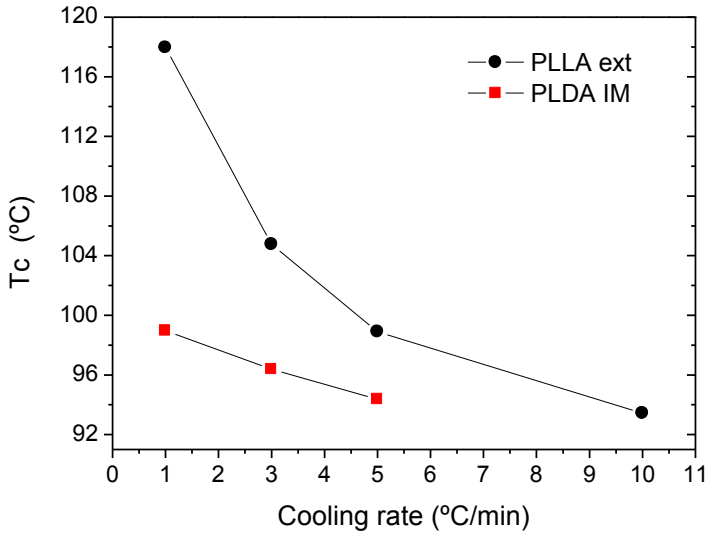

Figure 3.21 Crystallization temperature evolution with the cooling rate for extruded PLLA and injection moulded PLDA

Ozawa´s crystallization parameters can be obtained from the plot of $\ln(-\ln(1-X_c))$ versus $\ln(1/v)$ (Figure 3.23). The kinetic parameters m and K(T) are determined from the slope and intercept, respectively (Table 3.4). Points at the upper right correspond to the last stages of crystallization process; points at the lower left correspond to the beginning of the crystallization process. The lines appear to be almost parallel for PLDA IM up to 104 ºC, giving similar slopes or Ozawa exponent m between 0.2 and 0.4. At higher temperatures than 104 ºC Ozawa exponent increases and reaches the value 2.8 at 110 ºC. The similar behavior can indicate that the mechanism of nucleation and growth is not modified during the non-isothermal crystallization at temperatures lower than 104 ºC.

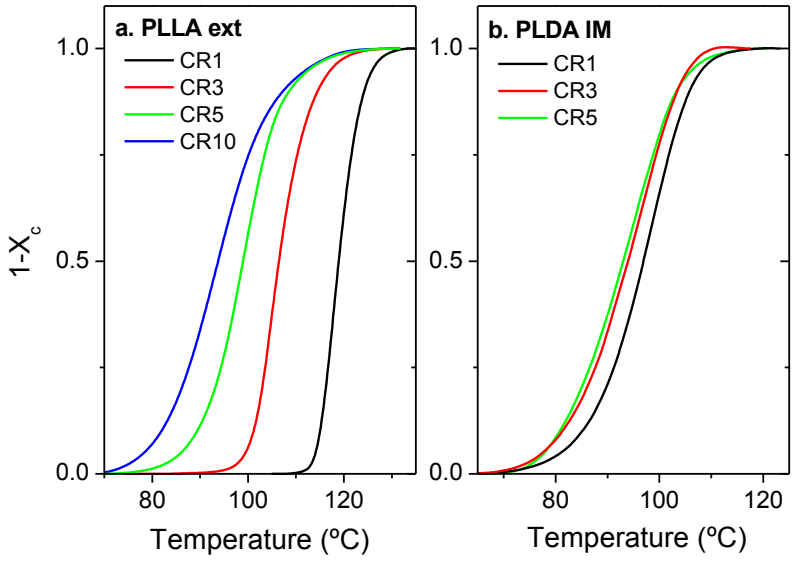

Figure 3.9 Variation of the relative degree of crystallinity as a function of temperature at indicated cooling rates during dynamic crystallization of extruded PLLA (a) and injection moulded PLDA (b)

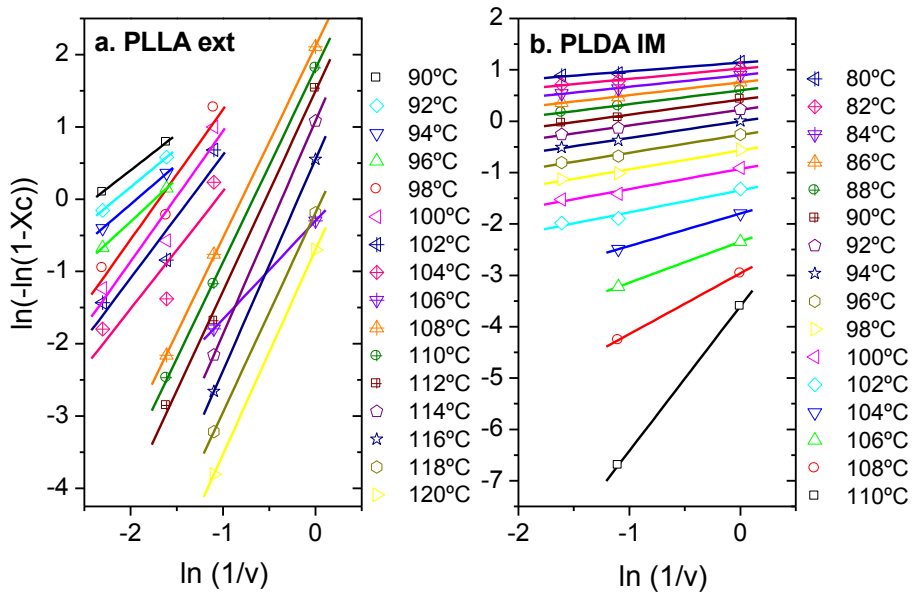

Figure 3.23 Ozawa plots of ln(-ln(1-Xc)) versus ln(1/v) for dynamic crystallization of extruded PLLA (a) and injection moulded PLDA (b)

In the case of PLLA ext a more irregular behavior is observed. Exponents, m, range from 1.0 to 2.9, indicating a continuous change in the mechanism of nucleation and growth. Ozawa exponent m increases with temperature. Other authors have found a unique value close to three for PLLA´s Ozawa exponent, which implies a three-dimensional spherical growth crystallization [31-34]. The different results obtained could be related with the different molecular weight of the PLLA studied. References used virgin PLLA and we are studying a processed PLLA, which has undergone a thermo-mechanical history. Crystallization kinetics are strongly dependent on the molecular weight of PLLA [8].

The cooling function K(T) determined for each temperature, shows a decrease with increasing temperature, as shown in Figure 3.24. This exponential dependence of the cooling constant K(T) has also been found for other polymers [35, 36]. It is of particular interest the behavior of extruded PLLA. Three different abrupt changes in lnK(T) behaviour clearly differentiate three stages with temperature: 90-96 ºC, 98-106 ºC and 108-120 ºC. These could be related with changes in polymer crystallization mechanisms, or changes in crystal morphologies. Abrupt changes in DSC thermograms during dynamic crystallization of PLLA have been reported in literature [15]. This anomalous result may be due to the implication of different crystalline morphologies occurring during the crystallization process, as seen in the subsequent melting behaviour for slow crystallization (Section 3.3.2.2).

In order to calculate the activation energy of the amorphous to crystalline phase transformation during the dynamic process, the Kissinger model has been used [21] and results are shown in Figure 3.25 for both materials. According to Figure 3.25, the activation energy for PLDA non-isothermal crystallization is 407 kJ/mol, 3.5 times larger than the activation energy for PLLA (116 kJ/mol). This indicates that the presence of D-lactyl units in PLDA increases the energy barrier for non-isothermal crystallization and causes the reduction of PLDA crystallization ability. However, other authors have found that the activation energy for PLLA and PLDA (2% D-lactyl units) have the same activation energy for dynamic crystallization [31]. It is possible that the effect of D-lactyl units becomes evident in crystallization kinetics at contents higher than 2%. The value for the activation energy is close to others reported in the literature [31, 37].

Table 3.4 Dynamic crystallization kinetic parameters based on Ozawa method for extruded PLLA and injection moulded PLDA

PLLA ext			PLDA IM		
T (ºC)	**ln k(T)**	**m**	**T (ºC)**	**ln k(T)**	**m**
90	2.39	1.0	80	1.14	0.2
92	2.29	1.1	82	1.02	0.2
94	2.13	1.1	84	0.89	0.2
96	2.06	1.2	86	0.76	0.2
98	3.04	1.8	88	0.60	0.3
100	2.74	1.8	90	0.42	0.3
102	2.32	1.7	92	0.22	0.3
104	1.73	1.6	94	0.00	0.3
106	-0.30	1.4	96	-0.27	0.3
108	2.12	2.6	98	-0.57	0.4
110	1.80	2.7	100	-0.93	0.4
112	1.49	2.8	102	-1.35	0.4
114	1.08	2.9	104	-1.80	0.6
116	0.55	2.9	106	-2.35	0.8
118	-0.19	2.8	108	-2.96	1.2
120	-0.70	2.8	110	-3.60	2.8

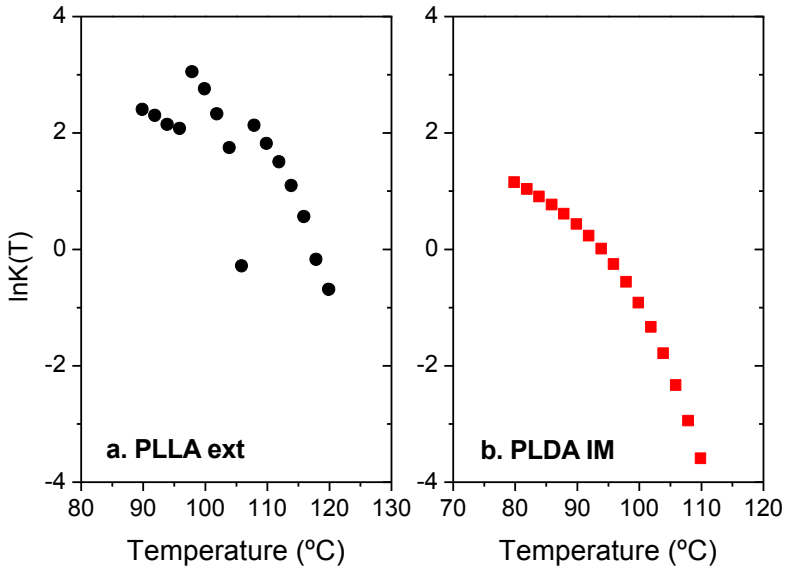

Figure 3.24 Behaviour of the function lnK(T) with temperature for extruded PLLA (a) and injected PLDA (b)

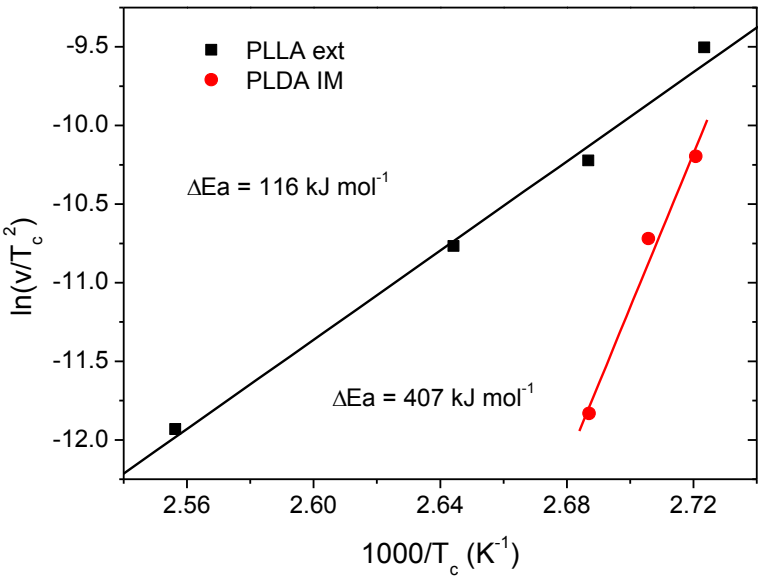

Figure 3.25 Kissinger plots for evaluating the activation energy for dynamic crystallization of extruded PLLA and injected PLDA

3.3.2.2 Melting behaviour after dynamic crystallization

The melting behaviour after the non-isothermal crystallization process at determined cooling rates for extruded PLLA and injected PLDA is presented in Figure 3.26.

At the fastest cooling rates (CR40, CR30 and CR20), extruded PLLA shows the typical thermogram for amorphous polymers, the glass transition temperature followed by a cold crystallization exotherm and a subsequent melting endotherm. At a cooling rate of 10 ºC/min (CR10) and 5 ºC/min (CR5) two cold crystallization processes appear. The first cold crystallization exotherm is followed by a little exotherm peak prior to the dominant melting peak. This peak corresponds to α´-form crystals transforming to their α-counterparts upon heating [2]. The first cold crystallization exotherm practically disappears at CR 5 indicating that an almost complete crystallization is achieved when cooling PLLA at 5 ºC/min.

The subsequent endotherm of the sample crystallized at CR10 presents a double melting peak which corresponds to melt-recrystallization mechanisms. At CR5 only one melting peak appears due to the fusion of α-form crystals. However, samples crystallized at CR3 do not present cold crystallization processes and during the melting endotherm a small shoulder is observed at low temperature close to 155 ºC. The shoulder could be ascribed to the transformation of the α´-form to α-form. At T > 155 ºC the endotherm shows two peaks, which correspond to melt-recrystallization phenomena [2, 9]. At CR1 a single melting peak is evidenced, indicating that perfect α-form crystals are generated and they melt directly without melt-recrystallization [8].

At cooling rates higher than 1 ºC/min, PLDA IM exhibits characteristic DSC curves of amorphous materials (Figure 3.26 b). The thermogram is composed by a cold crystallization exotherm followed by a multiple melting peak, which is indicative of melt-recrystallization behaviour. At CR1 PLDA IM crystallizes without achieving complete crystallization. This is evidenced by the small cold crystallization peak that appears during heating.

The difference between the total heat absorbed during melting ΔH_m and the total heat released during cold crystallization ΔH_{cf} is reported as the enthalpy of the material during the crystallization process. The enthalpy of processed PLLA and PLDA crystallized at different cooling rates as a function of the cooling rate is presented in Figure 3.27. It is observed that the enthalpy of melting increases with decreasing cooling rates.

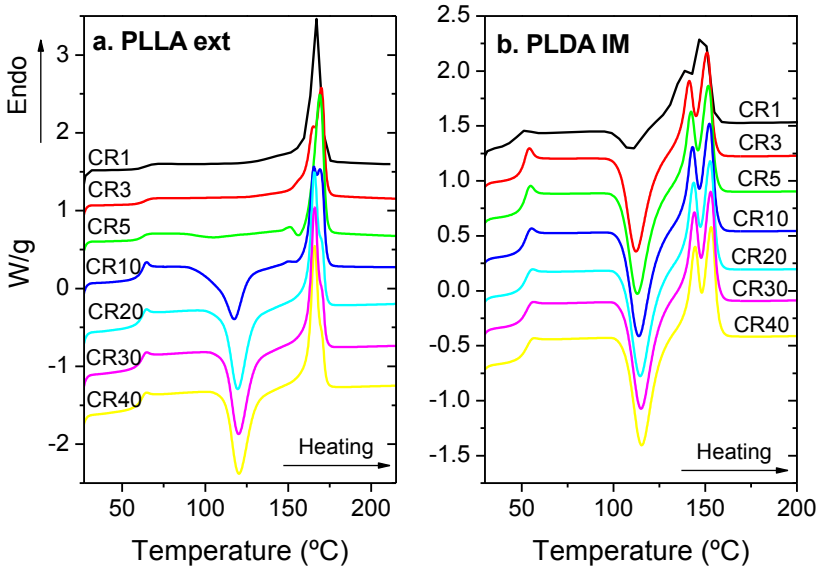

Figure 3.26 Subsequent melting endotherms of extruded PLLA (a) and PLDA processed by injection moulding (b) after dynamic crystallization at the specified cooling rates (CR)

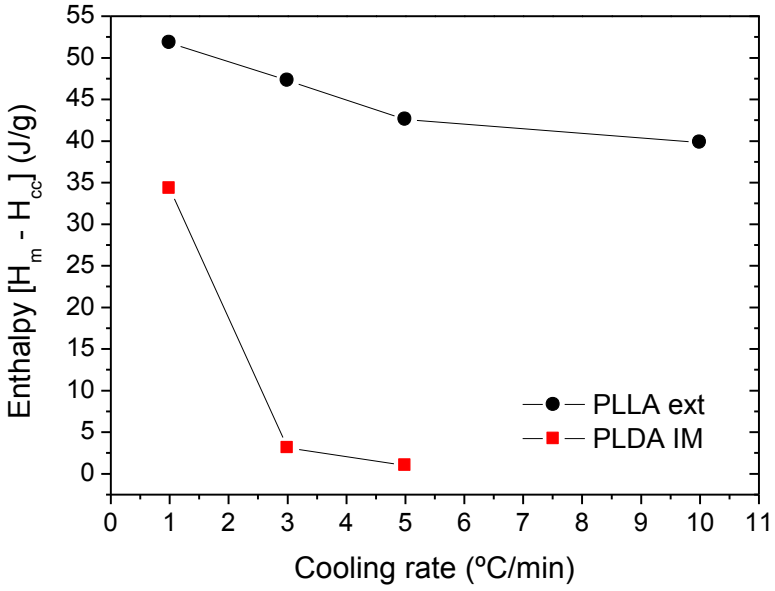

Figure 3.27 Enthalpy as a function of cooling rate for extruded PLLA and PLDA processed by injection moulding

PLLA ext shows higher enthalpy values than PLDA IM at all cooling rates. This result is in agreement with previous conclusions of this chapter that indicate the greater difficulty of PLDA IM in terms of its ability to form crystals. At CR3 and CR5, PLDA IM exhibits very low enthalpy values, which indicates that at this crystallization rates the material does not have enough time to acquire enough energy to effectively crystallize during cooling. At CR1 the enthalpy increases exponentially, and the material has enough time to acquire the enough energy to organize its chains. However, as seen in Figure 3.26, the material does not crystallize completely. PLLA ext crystallizes completely at CR < 5ºC/min and partially at CR10. Values of enthalpy grow moderately with the decrement of the cooling rate ranging from 40 J/g at CR10 to 52 J/g at CR1.

Comparing the enthalpy obtained during dynamic crystallization (Figure 3.27) with the enthalpy obtained during isothermal treatments (Figures 3.15 and 3.16) an analysis of the optimal process to tailor the material properties can be performed. For PLDA IM it is noted that isothermal treatments are more efficient developing crystalline domains than non-isothermal ones. For PLLA ext, although both treatments can tailor the crystallinity of the material and the maximum enthalpy achieved is similar in both cases (~ 52 J/g) isothermal treatments appear to be more efficient as well.

In the case of PLDA IM, for example, to develop a crystallinity fraction of 0.37 (correlated with an enthalpy of 34 J/g) with dynamic conditions it is necessary to cool the material from the melt at a very low rate of 1ºC/min. This process takes almost 200 minutes, if we are talking about cooling the polymer from 220 ºC to ambient temperature. On the contrary, during an isothermal process from the glassy state at 125 ºC (See Table 3.2 and Figure 3.18) only two minutes are needed to develop a higher crystallinity fraction (f_c=0.50, correlated with an enthalpy of 46 J/g).

In the case of crystallization under dynamic conditions of extruded PLLA, a crystalline fraction of 0.43 (correlated with an enthalpy of 40 J/g) can be obtained by cooling the material at 10 ºC/min. This process would take around 20 minutes, if the material is cooled from 220 ºC to ambient temperature. The same crystalline fraction can be evolved during an isothermal treatment at 100 ºC during 3 minutes (See Table 3.1 d and Figure 3.17 d).

3.4 Conclusions

The effect of processing on crystallization kinetics of PLLA and PLDA has been elucidated by the Avrami analysis of isothermal crystallization from the melt and from the glassy state. Processed materials have a higher crystallization rate than their virgin homologous. This is evidenced by a larger rate constant k and smaller half crystallization times. The thermo-mechanical degradation that the processed materials underwent during processing reduces their molecular weight and induces a faster crystallization.

The crystallization rate during crystallization from the glassy state is much faster than the rate during crystallization from the melt. This is due to the easier formation of stable nuclei during the crystallization from the solid.

Avrami constant n values show that PLLA and PLDA present a heterogeneous nucleation and bi-dimensional to three-dimensional spherulitic growth when they are crystallized from the solid state and from the melt.

When polymers are crystallized from the melt or from the glassy state they present a maximum crystallization rate at certain temperature, which is correlated with the temperature range where the lowest activation energy is reached.

The double melting behaviour of PLLA is explained at low crystallization temperatures by a polymorphic phase transition, at intermediate T_c corresponds to the usual melt-recrystallization mechanism, and at high T_c corresponds to the melting of perfect α-form crystals. The melting behavior of PLDA is explained by melt-recrystallization phenomenon.

For all materials and conditions the enthalpy of fusion shows an increasing trend with T_c. Similar crystallinity degrees can be obtained with both protocols (from the melt and from the glassy state), therefore the decision of the suitable protocol to tailor the crystallinity of the material lies in its efficiency and kinetics.

According to the Hoffman-Lauritzen analysis, during hot-crystallization PLLA presents a change of crystallization regime at 112 ºC, whereas PLDA does not undergo any regime transition.

Taking into account that the protocol from the glassy state is one to two orders faster than the protocol from the melt state, it seems that the most suitable processing step in order to effectively control the crystallinity degree of the material is crystallization from the solid state.

During dynamic crystallization it is evidenced that the incorporation of D-lactyl units in PLDA chains affects markedly its crystallization ability. PLDA needs to overcome a higher energy barrier than PLLA in order to crystallize under non –isothermal conditions.

The enthalpy of fusion decreases with cooling rates. Isothermal treatments are more efficient developing crystalline domains than non-isothermal ones.

3.5 References

[1] Gilding DK, Reed AM. Biodegradable polymers for use in surgery—polyglycolic/poly(actic acid) homo- and copolymers: 1. Polymer 1979;20:1459-64.

[2] Pan P, Inoue Y. Polymorphism and isomorphism in biodegradable polyesters. Progress in Polymer Science 2009;34:605-40.

[3] Alemán C, Lotz B, Puiggali J. Crystal Structure of the α-Form of Poly(l-lactide). Macromolecules 2001;34:4795-801.

[4] Puiggali J, Ikada Y, Tsuji H, Cartier L, Okihara T, Lotz B. The frustrated structure of poly(l-lactide). Polymer 2000;41:8921-30.

[5] Cartier L, Okihara T, Ikada Y, Tsuji H, Puiggali J, Lotz B. Epitaxial crystallization and crystalline polymorphism of polylactides. Polymer 2000;41:8909-19.

[6] Pan P, Zhu B, Kai W, Dong T, Inoue Y. Effect of crystallization temperature on crystal modifications and crystallization kinetics of poly(L-lactide). Journal of Applied Polymer Science 2008;107:54-62.

[7] Pan P, Zhu B, Kai W, Dong T, Inoue Y. Polymorphic Transition in Disordered Poly(l-lactide) Crystals Induced by Annealing at Elevated Temperatures. Macromolecules 2008;41:4296-304.

[8] Pan P, Kai W, Zhu B, Dong T, Inoue Y. Polymorphous Crystallization and Multiple Melting Behavior of Poly(l-lactide): Molecular Weight Dependence. Macromolecules 2007;40:6898-905.

[9] Yasuniwa M, Sakamo K, Ono Y, Kawahara W. Melting behavior of poly(L-lactic acid): X-ray and DSC analyses of the melting process. Polymer 2008;49:1943-51.

[10] Mandelkern L. Crystallization of polymers New York: McGraw Hill; 1964.

[11] Dobreva T, Benavente R, Pereña JM, Pérez E, Avella M, García M, et al. Effect of different thermal treatments on the mechanical performance of poly(L-lactic acid) based eco-composites. Journal of Applied Polymer Science 2010;116:1088-98.

[12] Wachsen O, Platkowski K, Reichert KH. Thermal degradation of poly-l-lactide—studies on kinetics, modelling and melt stabilisation. Polymer Degradation and Stability 1997;57:87-94.

[13] Avrami M. Kinetics of Phase Change. II Transformation - Time Relations for Random Distribution of Nuclei. The Journal of Chemical Physics 1940;8:212-24.

[14] Hoffman JD. Regime III crystallization in melt-crystallized polymers: The variable cluster model of chain folding. Polymer 1983;24:3-26.

[15] Di Lorenzo ML. Crystallization behavior of poly(l-lactic acid). European Polymer Journal 2005;41:569-75.

[16] Iannace S, Nicolais L. Isothermal crystallization and chain mobility of poly(L-lactide). Journal of Applied Polymer Science 1997;64:911-9.

[17] Hoffman J, Weeks J. Melting Process and the Equilibrium Melting Temperature of Polychlorotrifluoroethylene. Journal of Research of the National Bureau of Standards - A Physics and Chemistry 1961;66A:13-28.

[18] Ozawa T. Kinetics of non-isothermal crystallization. Polymer 1971;12:150-8.

[19] Harnisch K, Muschik H. Determination of the Avrami exponent of partially crystallized polymers by DSC- (DTA-) analyses. Colloid & Polymer Sci 1983;261:908-13.
[20] Ozawa T. Non-isothermal kinetics and generalized time. Thermochimica Acta 1986;100:109-18.
[21] Kissinger HE. Reaction Kinetics in Differential Thermal Analysis. Analytical Chemistry 1957;29:1702-6.
[22] De Santis F, Pantani R, Titomanlio G. Nucleation and crystallization kinetics of poly(lactic acid). Thermochimica Acta 2011;522:128-34.
[23] Pantani R, De Santis F, Sorrentino A, De Maio F, Titomanlio G. Crystallization kinetics of virgin and processed poly(lactic acid). Polymer Degradation and Stability 2010;95:1148-59.
[24] Zhou WY, Duan B, Wang M, Cheung WL. Isothermal and Non-isothermal Crystallization Kinetics of Poly(L-Lactide)/Carbonated Hydroxyapatite Nanocomposite Microspheres. In: Reddy B, editor. Advances in Diverse Industrial Applications of Nanocomposites2011.
[25] Tsuji H, Takai H, Saha SK. Isothermal and non-isothermal crystallization behavior of poly(l-lactic acid): Effects of stereocomplex as nucleating agent. Polymer 2006;47:3826-37.
[26] Kolstad JJ. Crystallization kinetics of poly(L-lactide-co-meso-lactide). Journal of Applied Polymer Science 1996;62:1079-91.
[27] Lorenzo AT, Arnal ML, Albuerne J, Müller AJ. DSC isothermal polymer crystallization kinetics measurements and the use of the Avrami equation to fit the data: Guidelines to avoid common problems. Polymer Testing 2007;26:222-31.
[28] Kawai T, Rahman N, Matsuba G, Nishida K, Kanaya T, Nakano M, et al. Crystallization and Melting Behavior of Poly (L-lactic Acid). Macromolecules 2007;40:9463-9.
[29] Zhang J, Tashiro K, Tsuji H, Domb AJ. Disorder-to-Order Phase Transition and Multiple Melting Behavior of Poly(L-lactide) Investigated by Simultaneous Measurements of WAXD and DSC. Macromolecules 2008;41:1352-7.
[30] Vasanthakumari R, Pennings AJ. Crystallization kinetics of poly(l-lactic acid). Polymer 1983;24:175-8.
[31] Liu Y, Wang L, He Y, Fan Z, Li S. Non-isothermal crystallization kinetics of poly(L-lactide). Polymer International 2010;59:1616-21.
[32] He Y, Fan Z, Wei J, Li S. Morphology and melt crystallization of poly(L-lactide) obtained by ring opening polymerization of L-lactide with zinc catalyst. Polymer Engineering & Science 2006;46:1583-9.
[33] He Y, Fan Z, Hu Y, Wu T, Wei J, Li S. DSC analysis of isothermal melt-crystallization, glass transition and melting behavior of poly(l-lactide) with different molecular weights. European Polymer Journal 2007;43:4431-9.
[34] He Y, Wu T, Wei J, Fan Z, Li S. Morphological investigation on melt crystallized polylactide homo- and stereocopolymers by enzymatic degradation with proteinase K. Journal of Polymer Science Part B: Polymer Physics 2008;46:959-70.
[35] Eder M, Wlochowicz A. Kinetics of non-isothermal crystallization of polyethylene and polypropylene. Polymer 1983;24:1593-5.

[36] López LC, Wilkes GL. Non-isothermal crystallization kinetics of poly(p-phenylene sulphide). Polymer 1989;30:882-7.

[37] Li M, Hu D, Wang Y, Shen C. Nonisothermal crystallization kinetics of poly(lactic acid) formulations comprising talc with poly(ethylene glycol). Polymer Engineering & Science 2010;50:2298-305.

PROCESSABILITY OF NOVEL PLLA/Mg COMPOSITES BY EXTRUSION

CHAPTER 4

"Science is the process that takes us from confusion to understanding in a manner that`s precise, predictive and reliable – a transformation, for those lucky enough to experience it, that is empowering and emotional"

Brian Greene

Table of contents

4. PROCESSABILITY OF NOVEL PLLA/Mg COMPOSITES BY EXTRUSION

4.1 Introduction

The novel bioresorbable PLLA/Mg composites are being investigated as a new strategy to modulate the degradation rate of Mg and simultaneously, improve the bioactivity and mechanical properties of PLLA. While it has been demonstrated that these composites can be fabricated by solvent casting techniques [1], it should be taken into consideration that remnants of chlorinated solvents (chloroform, dichloromethane) could compromise the bio-compatibility of implants [2-4]. With regards to their high temperature processability it has been demonstrated that although thermal decomposition of the polymer is accelerated by the presence of Mg particles, the processability of the composites is not compromised [5]. Success of the material for a specific application will obviously depend on the appropriate design of the composite and on the corresponding processing route. Nonetheless, manufacturing PLLA/Mg composites by melting processes raises new challenges for materials science and engineering.

In the field of bio-resorbable composites, extrusion has been employed as a method to prepare homogeneous blends of ceramic fillers (hydroxyapatite, bio-glasses, tricalcium phosphates) and polymeric matrices [6-8] giving them form of pins, screws or rods, or to fabricate medical polymer/ceramic masterbatchs [9-11]. Regarding the manufacturing of bioresorbable PLLA/Mg composites by extrusion, few or nothing has been reported.

The main complication of melt-extrusion is related to the tendency of PLLA to undergo thermal degradation during processing above 200 ºC [12-14]. The poor thermal stability of PLLA during high processing temperatures can lead to depolymerization and water traces can cause hydrolysis of PLLA ester linkages during high temperature processing. The net effect is a reduction of the molecular weight which affects final product properties, including physical and mechanical properties, biodegradation kinetics and biological response [15, 16].

An additional consideration is that thermal stability of PLLA can also be altered by the presence of metallic compounds. It has been demonstrated that residual metal catalysts (Sn, Fe, Zn, Al) reduce the thermal stability of PLLA [17, 18]. Some Mg and Ca compounds have been found to be effective catalysts that selectively depolymerise PLLA into L,L-lactide, and in fact they are used to control PLLA depolymerisation for feedstock recycling [17, 19-22]. Degradation mechanisms of PLLA-Ca, PLLA/CaO and PLLA/MgO are shown in Figure 4.19. The analysis of MgO, CaO and calcium salts induced effects on PLLA thermal degradation revealed that the selective depolymerization to L,L-lactide formation occurs at 250 – 320 ºC by unzipping

mechanisms. In a temperature range lower than 250 ºC, metal oxides cause racemization of lactide and the production of oligomers other than lactides [18, 23].

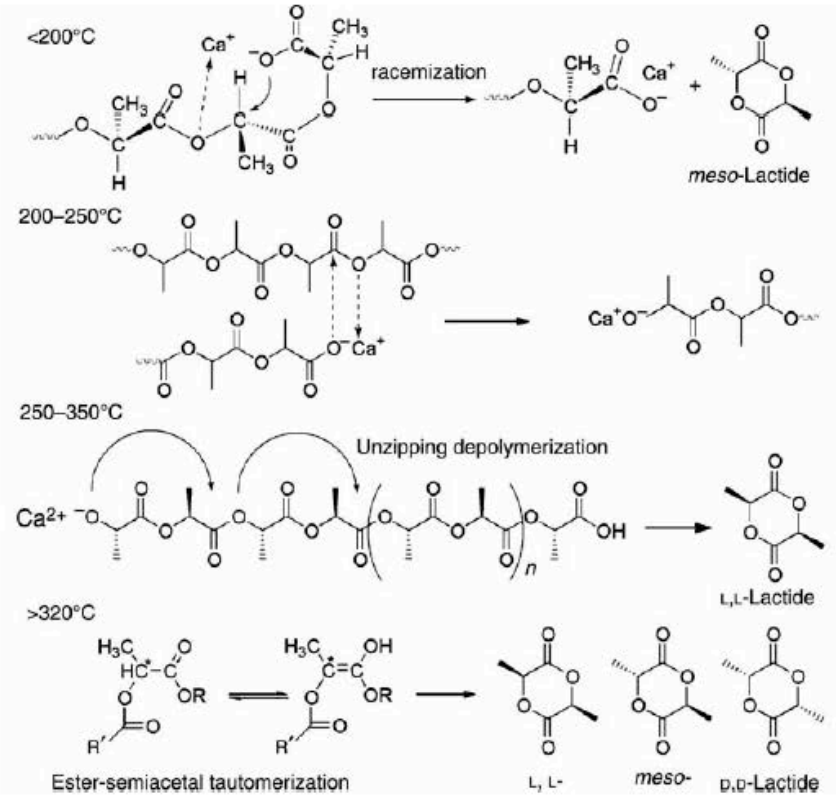

Figure 4.1 Degradation mechanisms of PLLA-Ca, PLLA/CaO and PLLA/MgO composites [23]

To the author knowledge there are not published reports regarding the thermal degradation mechanisms of PLLA reinforced with metallic Mg particles. Taking into account that chemical reactivity of pure Mg is much higher than MgO reactivity – Mg particles can spontaneously ignite and react violently with oxidising agents [5]-, adding magnesium particles into a PLLA matrix seems to impose additional challenges and serious technical limitations during melt processing.

In order to move forward PLLA/Mg composites development, this chapter addresses the study of the suitability of processing these novel materials by extrusion. Processability is assessed by means of the physico-chemical characterization and mechanical properties evaluation of extruded PLLA/Mg composites. The effects of Mg particles content on PLLA thermal stability and melting behaviour, as well as its effect on the mechanical properties are thoroughly analysed.

4.2 Materials and methods

4.2.1 Materials

A poly-L-lactic acid provided by Goodfellow was reinforced with irregular shape Mg particles of 50 μm. PLLA pellets were mixed with 0.5, 1, 3, 5 and 7 wt.% of Mg particles in the dry state prior to extrusion.

Materials were compounded in a Haake Minilab extruder with two conical co-rotating screws of small capacity (max. 7 cm^3). Temperature was set at 180 ºC, screw rotation speed at 80 rpm and residence time at 10 minutes. Extruded PLLA/Mg composites are named hereafter as PLLAXMg, where X refers to Mg content. Extruded materials were used for thermal stability measurements.

With the extruded composites, films of 0.5 mm thick were fabricated by compression moulding in a Collin P200P press. Samples were first melted at 180 ºC and then cooled under two different thermal treatments: quenched from the melt (Q), and slowly cooled from the melt at 3 ºC/min (S). These films were used for morphological and thermal characterization studies.

PLLAXMg discs of 12 mm diameter and 4 mm height were moulded by compression in a Collin P200P press under the quenching (Q) treatment. These samples were used for mechanical characterization by compression tests.

4.2.2 Physico-chemical characterization

4.2.2.1 Viscosity average molecular weight

The average molecular weight of PLLA virgin and processed PLLA was estimated by means of viscometry. Measurements were carried out by solving the samples in chloroform at 25 ºC, using a Ubbelohde type or suspended level viscometer. The intrinsic viscosity of PLLA and extruded PLLA was obtained according to ASTM D446 [24]. The value was used to determine the viscosity average molecular weight of both samples with the following Mark-Houwink equation [23, 25-28]:

$$[\eta] = 4.41 \times 10^{-4} M_v^{0.72} \qquad \text{Equation 4.1}$$

4.2.2.2 Thermal stability

Thermal stability was studied by thermogravimetry using a Mettler Toledo thermogravimetric analyser (TGA, model TAQ500). The experiments were carried out under nitrogen atmosphere (90 ml/min). Two temperature programs were run: one dynamic measurement from 30 ºC to 650 ºC at a heating rate of 10 ºC/min and another isothermal experiment at 180 ºC during 16 hours.

For dynamic conditions and for each material, the onset temperature (T_o), the temperature of greatest rate of change on the weight loss curve (T_p), the temperature of 50% weight loss (T_{50}) and the final temperature (T_e) were determined. T_o and T_e were calculated by finding the intersection of the baseline and the extrapolated tangent at the inflection point of the weight loss curve. T_p, also known as the inflection point, was calculated from the first derivative of the weight loss curve.

For isothermal conditions the extent of conversion was defined by:

$$\alpha = \frac{W_o - W_t}{W_0} \qquad \text{Equation 4.2}$$

where W_0 is the initial weight of sample and W_t is the weight at any time during the thermal degradation process. The kinetic equation for thermal decomposition of solid matter can be written as:

$$\frac{d\alpha}{dt} = k(1-\alpha)^n \qquad \text{Equation 4.3}$$

where k is the reaction rate constant that depends on temperature and n is the order of the reaction. Assuming a first-order reaction and integrating Equation 4.3, the following expression results to describe the thermal decomposition of the material:

$$\ln(1-\alpha) = -k * (t - t_0) \qquad \text{Equation 4.4}$$

where t_0 is the time at the start of the constant-temperature period. For the first order kinetics a plot of ln(1-α) versus t will yield a straight line, with a slope equal to –k.

4.2.2.3 Thermal behaviour

The crystallinity degree of the materials and its melting and crystallization behaviour were characterized by means of differential scanning calorimetry on a TA Q100 DSC under nitrogen atmosphere, using 8 ± 0.5 mg of each sample. The experimental design was based on a first heating (F10) from 25 ºC to 220 ºC, followed by a cooling (CR10) to 25 ºC and a second heating to 220 ºC (CR10F10). All the steps were carried out at 10 ºC/min.

The crystalline fraction was calculated by measuring the enthalpy of melting ΔH_m and cold crystallization ΔH_{cc} from the heating curves using Equation 4.5, where ΔH_m^0 is the enthalpy of 100% crystalline PLLA (93.1 J/g) [29].

$$f_c = \frac{(\Delta H_m - \Delta H_{cc})}{\Delta H_m^0}$$ Equation 4.5

4.2.2.4 Morphology and crystal structure

Morphology of the composites was studied by macrographs and the dispersion of Mg particles in the polymer matrix analyzed using an optical polarising microscope (Carl Zeiss Amplival microscope).

X-ray scattering was used to probe the crystal structure of each thermal treatment, Q and S. Samples were analyzed using a wide angle X-ray diffraction, WAXD, apparatus (Bruker D8 Advanced Diffractometer provided with a PSD Vantec detector) by CuK_α radiation. The spectra was recorded in an angular range of $5º < 2\theta < 40º$ at room temperature. The crystallinity degree of slow cooled samples is obtained by subtracting the amorphous halo, by comparison to the diffraction pattern obtained from the quenched samples.

4.2.2.5 ATR-FTIR

Fourier Transform Infrared Spectroscopy was applied to identify the chemical functional groups of PLLA and their changes during processing of compression tests discs. The FTIR spectra were obtained with a Perkin Elmer spectrometer in the 4000 to 650 cm^{-1} region, using an Attenuated Total Reflectance (ATR) modulus.

The most representative bands of PLLA and the region where they are found are listed in Table 4.1.

Table 4.1 FTIR spectra regions of PLLA groups and bonds

Region	Group or bond
3600 – 3200 cm^{-1}	-OH stretching vibration (carboxyl acids and alcohols)
3100 - 2800 cm^{-1}	Stretching vibrations of the C-H bonds of the polymeric chain
1754 cm^{-1}	Carbonyl group C=O
1460 - 1300 cm^{-1}	Vibration of the C-C bonds of the polymeric chain
1360 cm^{-1}	Related to the CH bending (wagging)
1300 – 800 cm^{-1}	Related to C-O vibrations appear overlapped with contributions from the C-H bonds.
1182 cm^{-1}	Asymmetric stretching vibration of the C-CO-O
1087 cm^{-1}	Related to the asymmetric stretching vibration of O-C-CO

The study has been focused on the evolution of selected IR bands (carbonyl and esters groups) related to some representative groups (CH bending) to monitor the changes that Mg particles induce to PLLA during processing.

4.2.3 Mechanical characterization

The compressive mechanical behaviour was studied in a universal machine EM2/100/FR-10kN Micro Tests at ambient conditions, using a strain rate of $5x10^{-4}$ s^{-1}. Five discs (12 mm diameter and 4 mm height) were tested for each material. From the stress-strain curves the yield strength and the Young´s modulus were obtained.

Experimental moduli were compared with theoretical moduli according to the Reuss and Voigt Models. Generally, the modulus of composites should be lower than an upper-bound and higher than a lower bound [30] . The upper bound of the elastic modulus of a particulate composite can be predicted by a parallel (Voigt) arrangement assuming iso-strain criteria [30-32] :

$$E_c^{upper} = E_f V_f + E_m(1-V_f) \qquad \text{Equation 4.6}$$

where E_c is the modulus of the composite, E_f the modulus of the particulate filler, E_m the modulus of the polymer matrix and V_f is the particle volume fraction. And the lower bound of the elastic modulus of the composite can be predicted by a series (Reuss) arrangement assuming iso-stress criteria [30-32] :

$$E_c^{lower} = \frac{E_f E_m}{E_f(1-V_f)+E_m V_f} \qquad \text{Equation 4.7}$$

An approximate method, the modified rule of mixtures, can be used for simplicity and without loss of accuracy, to predict the elastic modulus of particulate composites [32, 33]:

$$E_c = \chi_f E_f V_f + E_m(1-V_f) \qquad \text{Equation 4.8}$$

where $0 < X_f < 1$ is the filler strengthening factor. The elastic moduli predicted by Equation 4.8 fall between those predicted by the Reuss (Equation 4.7) and Voigt (Equation 4.6) models. The modified rule of mixtures equation was used to analyse Mg particles strengthening factor.

4.3 Results and discussion

4.3.1 Effect of processing and Mg particles on PLLA thermal stability

The effect of processing on PLLA thermal stability was assessed by comparing the molecular weight of virgin PLLA and processed PLLA. The molecular weight was measured by means of viscometry. Figure 4.2 compares the intrinsic viscosity of PLLA in pellet form to that obtained for extruded PLLA. In Figure 4.2 black squares correspond to the reduced viscosity or Huggins (η_{red} *vs* c) plot and red circles correspond to the inherent viscosity or Kraemer (η_{inh} *vs* c) plot. The

lines are the linear extrapolations of Huggins and Kraemer plots to find the inherent viscosity in the intercept, black lines are for PLLA pellet and red lines are for extruded PLLA. Table 4.2 shows the values of the viscosity average molecular weight estimated by the Mark-Houwink equation for PLLA using the values obtained from Figure 4.2 for intrinsic viscosity.

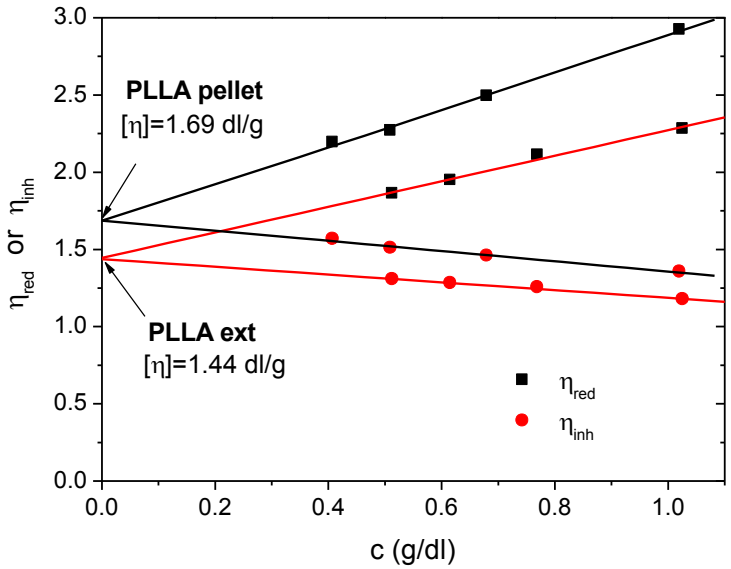

Figure 4.2 Huggins-Kraemer plot to determine the intrinsic viscosity of PLLA in pellet form and extruded PLLA

Table 4.2 Viscosity average molecular weight of PLLA in pellet form and extruded PLLA

PLLA pellet M_v	PLLA ext M_v	Reduction M_v
95 kDa	76 kDa	20 %

The comparison of the molecular weight of virgin and extruded polymer indicates that the solely processing of PLLA by extrusion causes a reduction of almost 20% in the viscosity average molecular weight, as shown in Table 4.2. This implies that the temperature and shear rate that the polymer underwent during extrusion are enough to conduce a significant thermo-mechanical degradation that shortens the molecular weight of PLLA.

Given that the contribution of shear stress on thermo-mechanical degradation can be enhanced by the presence of reinforcement particles during extrusion, the effect of Mg content on the thermal stability of PLLA was evaluated by thermogravimetric analysis. Dynamic studies were performed by heating the samples at 10 ºC/min to 650 ºC, isothermal studies were carried out at

180 ºC during 16 hours. Results from dynamic studies are illustrated in Figures 4.3 to 4.6. Isothermal thermogravimetric analysis results are shown in Figures 4.7 and 4.8.

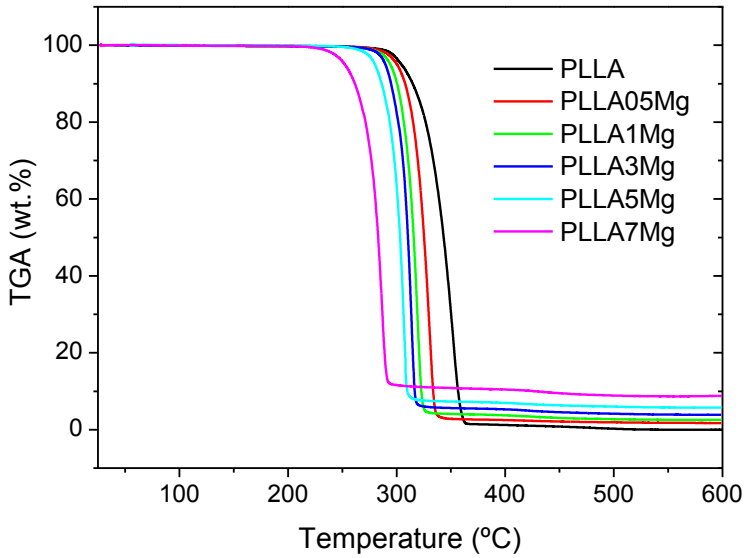

Figure 4.3 Thermal degradation of PLLAXMg composites under dynamic conditions X = 0, 0.5, 1, 3, 5 and 7 wt.% of Mg.

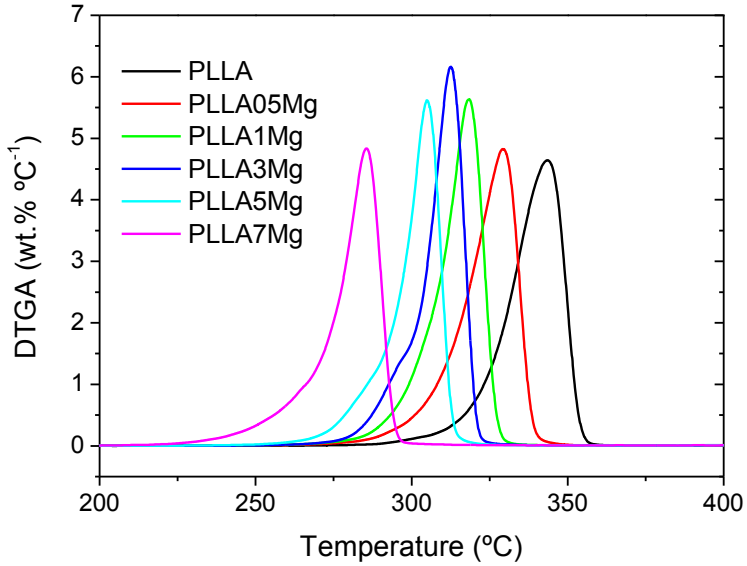

Figure 4.4 DTGA curves of PLLAXMg composites with X = 0, 0.5, 1, 3, 5 and 7 wt.% of Mg

Figure 4.3 shows the thermal-induced weight loss curves of PLLAXMg composites under dynamic heating conditions by TGA. Figure 4.4 shows the first-order derivative curves of thermograms with respect to temperature and each peak represents the inflection temperature of the TGA curve which corresponds to T_p. Figure 4.5 illustrates the relationship of the onset temperature of decomposition (T_o), the temperature of maximum weight loss rate (T_p), the temperature of 50% weight loss (T_{50}) and the temperature where decomposition ends (T_e) with Mg content of composites. The corresponding onset and endset temperatures of the degradation step were obtained by a tangential intercept method onto the TGA curve.

All samples undergo one simple thermal decomposition step (Figures 4.3 and 4.4). According to Figures 4.3 – 4.5, Mg particles act as depolymerisation catalysts as the parameters (T_0, T_p, T_{50}, T_e) are shifted downwards with increasing Mg content. However, it is observed that the onset degradation temperatures for PLLA and PLLAXMg composites are above the processing temperature. This implies that although Mg accelerates the thermal degradation of PLLA it does not compromise the temperature window required for commercial processing. The beginning of the temperature window is defined by the minimum temperature at which the material can be melted and moulded and the upper end is defined by the temperature at which the material begins to degrade (T_o). The processing window becomes narrower with the increment of Mg content (Figure 4.3). Nonetheless, it is not recommended to process PLLA at temperatures higher than 210ºC [29].

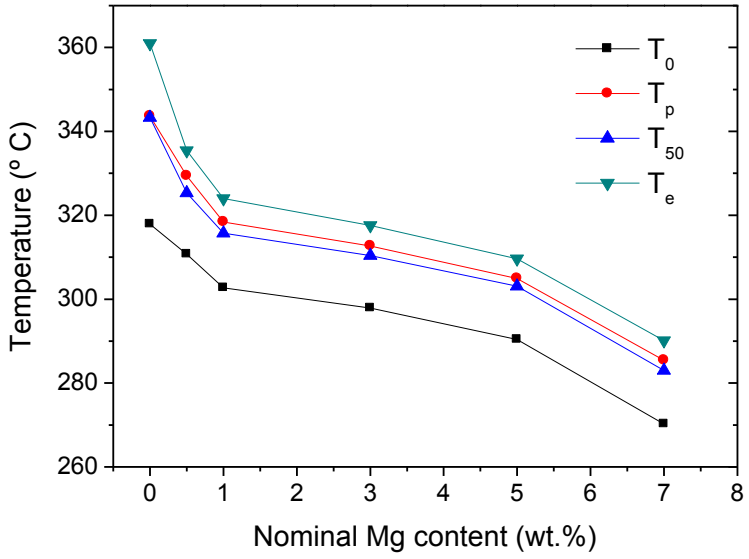

Figure 4.5 Thermal stability parameters of PLLAXMg composites as a function of Mg content with X = 0, 0.5, 1, 3, 5 and 7 wt. % of Mg

Figure 4.6 shows a comparison between the Mg content of composites obtained by TGA studies with the nominal Mg content. Measured filler content is very close to the theoretical concentration of Mg indicating that particles are homogeneously distributed within the polymeric matrix. A deviation is observed at 7 wt.% of nominal Mg content, probably due to the formation of agglomerates at that high particle content.

The isothermal weight loss of PLLAXMg composites compared with that of PLLA was investigated at 180 ºC. Figure 4.7 plots ln(1-α) against time, the slope of these curves gives the values for the degradation rate constant, k(T), and are shown as a function of Mg content in Figure 4.8. As exposed in Figure 4.7, under isothermal conditions, increasing Mg content decreases thermal degradation time to reach the same extent of conversion. The conversion of PLLA greatly depends on Mg content. Higher Mg content results in a higher degradation rate constant. In Figure 4.8, it can be seen that PLLA thermal degradation rate has an exponential growth as the Mg content increases.

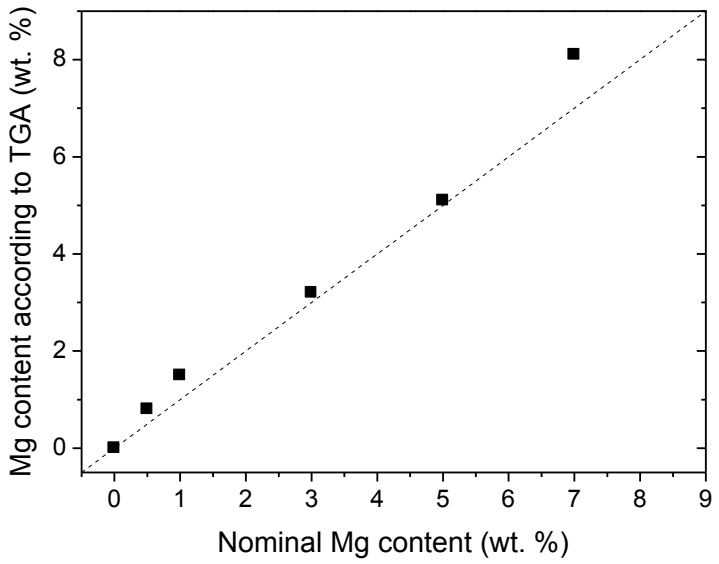

Figure 4.6 Mg content of PLLAXMg composites according to thermogravimetric analysis

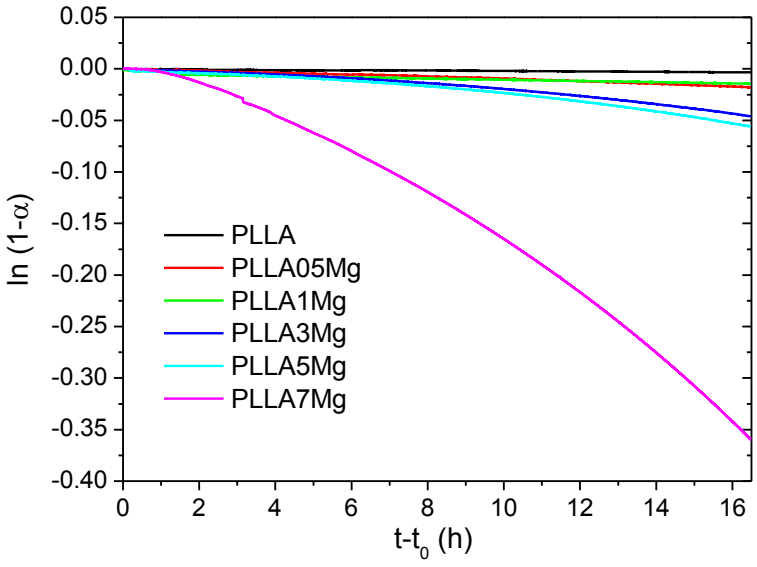

Figure 4.7 The curve of ln(1-α) *vs* time for PLLAXMg composites

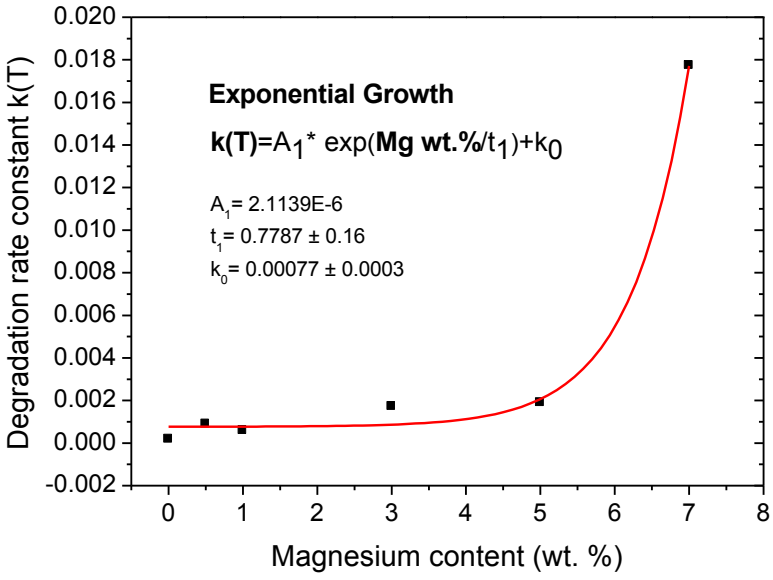

Figure 4.8 Degradation rate contant k(T) as a function of Mg content

4.3.2 Morphology of films

The aspect of the PLLAXMg composites films prepared with both thermal treatments, quenching (Q) and slow cooling from the melt (S), is shown in Figure 4.9 by macrographs. The distribution of the metallic particles among the polymeric matrix can be observed in Figure 4.10 by polarized optical microscopy.

Figure 4.9 shows that voids and agglomeration of Mg particles appear at a Mg content of 7 wt.% in films fabricated under a quenching treatment. Under the slow cooling treatment, voids and Mg particles agglomeration is more evident and appear at a lower Mg content (5 wt.%). Besides the poor dispersion of the Mg particles in the films with 7 wt.%, these films had a more fragile appearance and were more easily broken during handling.

Polarized optical micrographs of quenched films (Figure 4.10 a) show a homogeneous distribution of Mg particles within the PLLA matrix. Whereas slow cooled films (Figure 4.10 b) evidence a uniform distribution only at low Mg contents (0.5, 1, 3 wt.%). Agglomeration of Mg is evidenced at 5 wt.% and at 7wt.%. In Figure 4.10 b, polymer spherulites can be clearly seen within the voids formed in the material with 7 wt.% of Mg, this indicates that the voids are not empty spaces, but zones were the polymer is placed preferentially. During the slow cooling, the polymeric matrix has more time and energy to organize its chains; this implies that the Mg within the matrix can also organize and arrange its distribution. The result is the formation of perfect circular zones where polymer with low content of Mg is placed.

Morphology results indicate that the extrusion residence time is enough to obtain a homogeneous dispersion of fillers within the matrix. However, when the composite is compression moulded, special attention should be taken to avoid the agglomeration of particles and formation of voids, as far as for a residence time of 50 min during the “S” treatment only low Mg contents yielded homogeneous films.

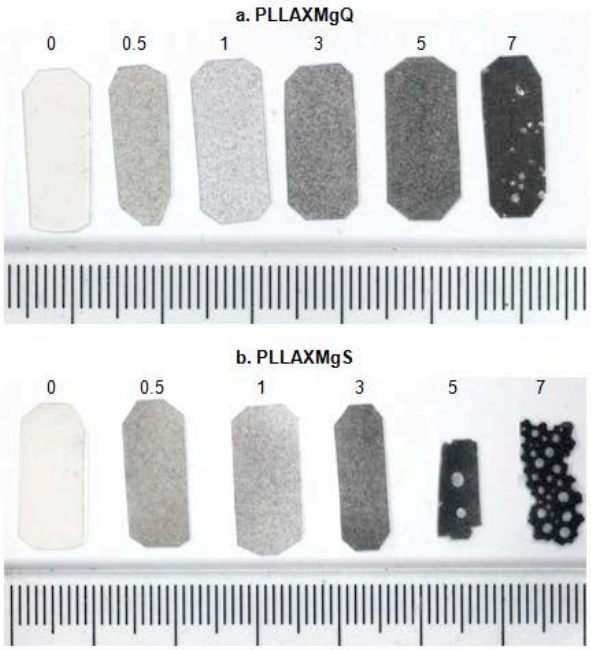

Figure 4.9 Macrographs of quenched (a) and slow cooled from the melt PLLAXMg films (X=0, 0.5, 1, 3, 5 and 7 wt.% of Mg content)

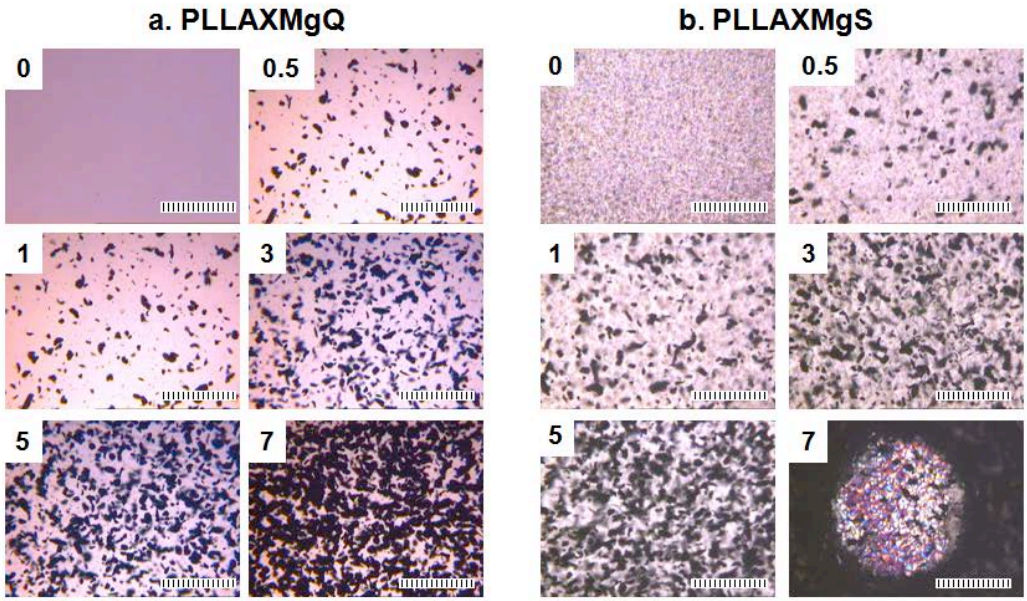

Figure 4.10 Distribution of Mg particles incorporated in a PLLA matrix observed by a polarized light microscope. Films of PLLAXMg quenched (a) and cooled at 3 ºC/min from the melt (b) with X=0, 0.5, 1, 3, 5 and 7 wt.% Mg. (Scale bar 500 μm)

4.3.3 Thermal behaviour

The effect of Mg on the melting behaviour of PLLA was analysed by DSC and representative results are shown in Figures 4.11 and 4.12. Figure 4.11 illustrates the first heating (F10) scans for quenched (a) and slow cooled from the melt (b) PLLAXMg composites. Thermal properties calculated from these curves are listed in Table 4.3 for quenched (Q) materials and in Table 4.4 for slow cooled from the melt (S) materials.

In Figure 4.11a, the first heating (F10) indicates that the quenched treatment produces totally amorphous materials. Mg particles do not induce any change on the glass transition temperature (T_g) of the polymer, however it induces changes on the cold crystallization temperature (T_{cc}) and on the melting peak. It seems that Mg particles act as nucleating agents and enhance PLLA crystallization ability under dynamic conditions. The shift to lower temperatures of T_{cc} for PLLAXMg composites in comparison with PLLA evidences the nucleating effect of Mg. The cold crystallization temperature decreased from 108.9 ºC for processed PLLA to 101.5 ºC for PLLA5Mg. However, the relationship between T_{cc} reduction and Mg content is not clear. The melting temperature shows a decrease of few Celsius degrees with the addition of Mg. Such behaviour confirms the nucleation effect of Mg and the formation of smaller crystals. PLLA and PLLAXMg composites show a multiple melting behaviour that consists on the appearance of an exothermic peak prior to the dominant melting peak. The exothermic peak could correspond to the transformation of α'-form crystals into their α-form counterparts [34] (Chapter 3).

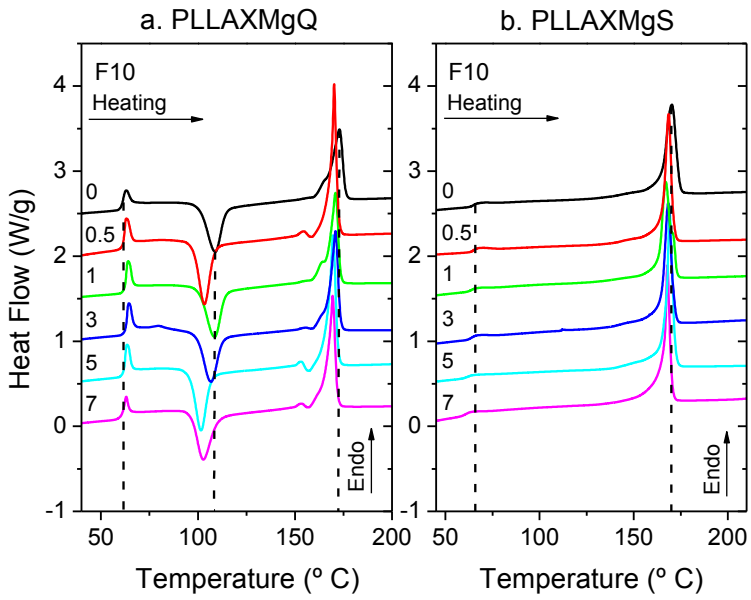

Figure 4.11 DSC of quenched (a) and slow cooled from the melt (b) PLLAXMg composites reinforced with X= 0, 0.5, 1, 3, 5 and 7 wt.% Mg

Table 4.3 Thermal properties of quenched PLLAXMg composites reinforced with 0.5, 1, 3, 5 and 7 wt.% of Mg particles.

PLLAXMgQ (F10)					
MATERIAL	**T_m (º C)**	**T_g (º C)**	**T_{cc} (º C)**	**ΔH (J/g)**	**f_c**
PLLAQ	173.0	60	108.9	3.7	0.04
PLLA05MgQ	170.2	61	103.2	1.0	0.01
PLLA1MgQ	170.9	62	108.6	2.2	0.02
PLLA3MgQ	170.9	62	106.6	0.8	0.01
PLLA5MgQ	169.5	61	101.5	0.6	0.01
PLLA7MgQ	169.4	60	102.8	2.4	0.03

Experimental errors: Tm and T_{cc} ± 0.5º C, T_g ± 2º C and f_c ± 0.04

Table 4.4 Thermal properties of slow cooled PLLAXMg composites reinforced with X= 0.5, 1, 3, 5 and 7 wt.% of Mg particles.

PLLAXMgS (F10)					
MATERIAL	**T_m (ºC)**	**T_g (ºC)**	**T_{cc} (ºC)**	**ΔH (J/g)**	**f_c**
PLLAS	170.3	64	-	49.3	0.53
PLLA05MgS	168.5	65	-	48.5	0.52
PLLA1MgS	167.1	63	-	51.6	0.55
PLLA3MgS	168.4	63	-	53.7	0.58
PLLA5MgS	169.0	61	-	63.2	0.68
PLLA7MgS	167.9	61	-	58.1	0.62

Experimental errors: Tm and T_{cc} ± 0.5º C, T_g ± 2º C and f_c ± 0.04

In Figure 4.11b, the first heating (F10) indicates that the "S" treatment produces semi-crystalline materials with a high average crystalline fraction between 0.52 and 0.68 (Table 4.4). A decrement in T_g is correlated with the increment in Mg content. Cold crystallization peak does not appear in the thermograms indicating that materials have achieved complete crystallization. The melting temperature shows a decrease of few Celsius degrees with the addition of Mg. Such behaviour confirms the formation of smaller crystals due to the presence of Mg particles. The appearance of a single melting peak could account for the directly melting of perfect α-form crystals generated during the "S" treatment [35].

The effect of Mg on the crystallization behaviour of PLLA under dynamic conditions is observed during the cooling scans at 10 ºC/min (CR10) (Fig 4.12 a). A very odd trend is evidenced. As with 0.5, 1 and 3 wt. % of Mg content the crystallization ability of PLLA is slightly enhanced, at 5 wt. % of Mg crystallization ability of PLLA increases significantly, as evidenced by a larger exotherm. However at 7 wt. % the crystallization ability of PLLA decreases. The polymer is expected to reduce its ability to crystallize under dynamic conditions from the melt with increasing Mg content due to the spatial interferences that Mg particles could signify. The abnormal behaviour of crystallization enhancement at 5 wt. % could be explained by terms of a reduction in the molecular weight during processing which facilitates the formation of crystals. Smaller polymer chains crystallize easier and faster. The cooling behaviour of PLLA7Mg could be justified by the apparent thermal degradation of the composite matrix and the high Mg content that interfere with the polymeric matrix crystallization.

From the second heating scans (CR10F10) (Figure 4.12 b) the crystalline degree achieved during cooling at 10 ºC/min was measured (Table 4.5). PLLAXMg composites with Mg content of 0.5, 1 and 3 wt.% are able to crystallize under dynamic conditions at 10 ºC/min reaching a crystalline fraction similar to that of PLLA. However, PLLA5Mg reaches a crystalline fraction close to 0.45. The improvement of crystal nucleation of PLLA5Mg composite could be explained in terms of the reduction of PLLA molecular weight. PLLA7Mg is not able to crystallise under dynamic conditions and its heating thermogram is typical for materials that have undergone thermal degradation.

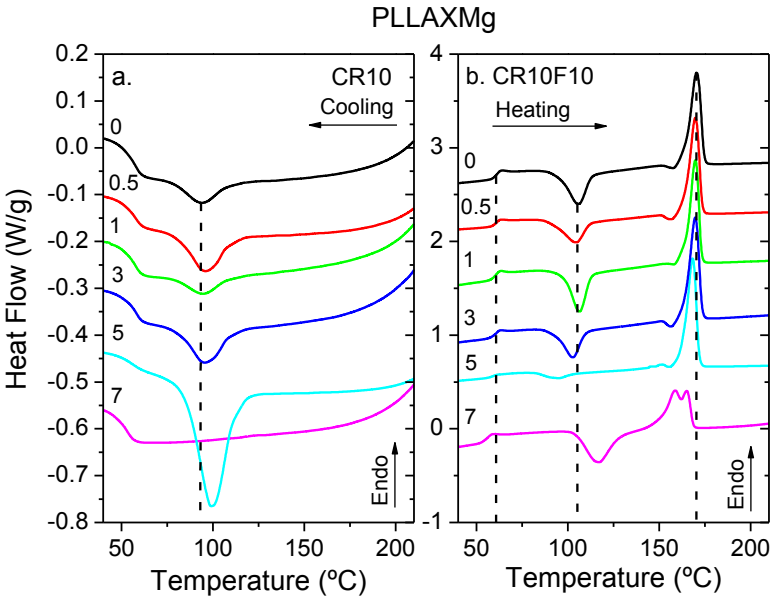

Figure 4.12 DSC scans of PLLAXMg composites reinforced with 0.5, 1, 3, 5 and 7 wt.% of Mg particles.

Table 4.5 Thermal properties of slow cooled PLLAXMg composites reinforced with X= 0.5, 1, 3, 5 and 7 wt.% of Mg particles.

CR10F10					
MATERIAL	**T_m (º C)**	**T_g (º C)**	**T_{cc} (º C)**	**ΔH (J/g)**	**f_c**
PLLA	170.4	60	106.1	8.0	0.08
PLLA05Mg	169.8	60	104.8	12.0	0.13
PLLA1Mg	169.7	60	106.4	8.3	0.09
PLLA3Mg	169.6	59	102.9	12.9	0.14
PLLA5Mg	168.3	59	94.9	41.5	0.45
PLLA7Mg	158.8	55	117.3	3.6	0.04

Experimental errors: Tm and T_{cc} ± 0.5 º C, T_g ± 2 º C and f_c ± 0.04.

4.3.4 X-Ray Diffraction

The WAXD patterns of PLLAXMg composites treated under both thermal treatments, Q and S, are shown in Figures 4.13 and 4.15 respectively. Figure 4.13 illustrates the typical diffractograms of amorphous materials, indicating that "Q" treatment was successful in producing totally amorphous samples. The three strong reflections at 32.2º, 34.4º and 36.6º, correspond to the (100), (002) and (101) Mg planes. The area under the (101) reflection can be correlated with Mg content of composites. Figure 4.14 shows that the Mg content measured by XRD approximates to the nominal values in all cases except for PLLA7Mg, where a big divergence between both values exists may be due to Mg particle agglomeration.

Figure 4.15 illustrates the WAXD pattern of PLLAXMg films crystallized by cooling under dynamic conditions from the melt. X-Ray Diffractograms of PLLA5MgS and PLLA7MgS films could not be obtained given the inhomogeneity of samples. The appearance of two diffractions around 24º instead of only one indicates that the perfect α-form is present in all materials and is formed under cooling at 3ºC/min. This result confirms that the single melting peak shown in previous DSC (F10) scans (Figure 4.11 b) accounts for the directly melting of perfect α-form crystals.

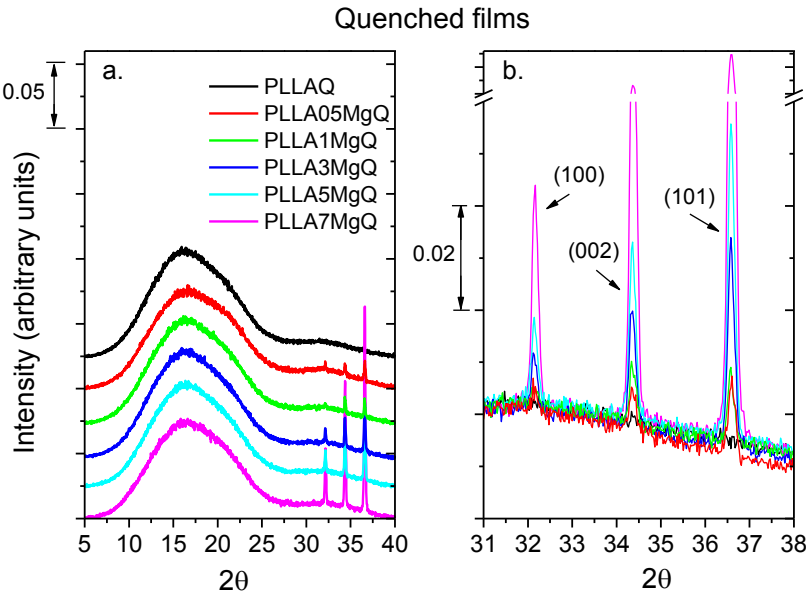

Figure 4.13 WAXD patterns of PLLAXMg films quenched from the melt (a) and a zoom of Mg strong reflections (b). X = 0, 0.5, 1, 3, 5 and 7 wt.% Mg

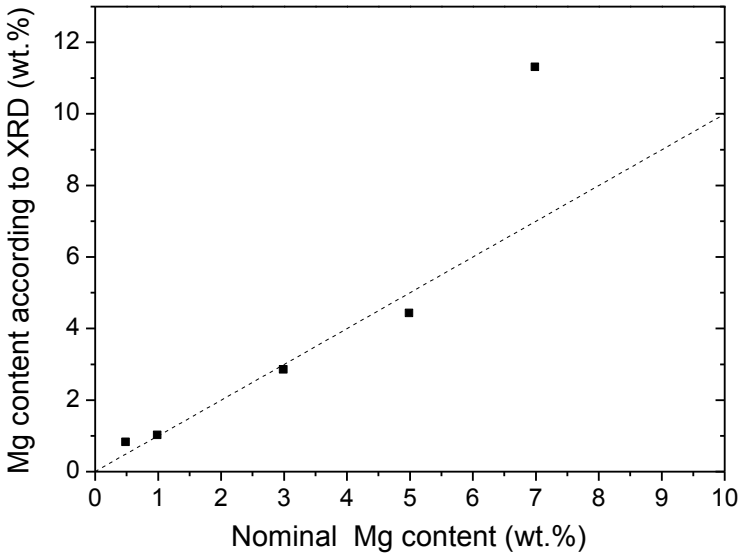

Figure 4.14 Mg content measured by XRD compared with nominal values

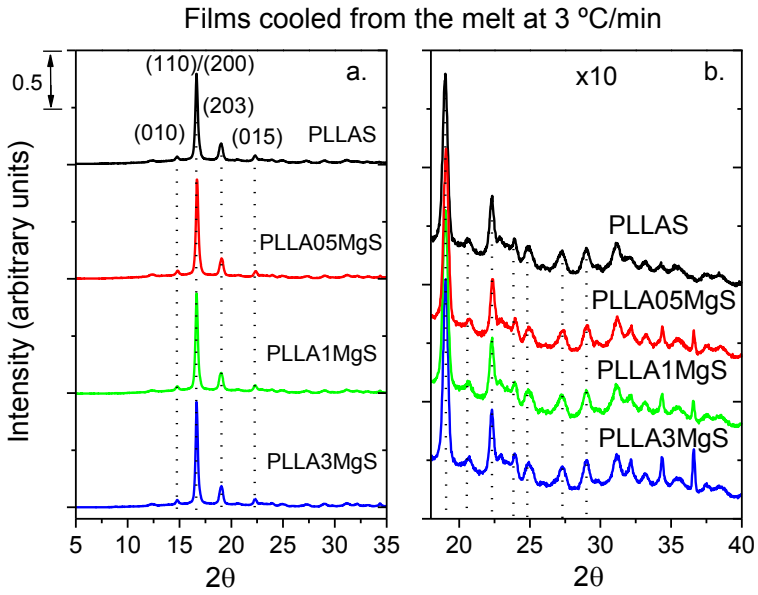

Figure 4.15 WAXD patterns of PLLA and PLLAXMg films slow cooled from the melt

Crystalline fraction obtained by DSC and X-Ray diffraction of composites cooled under "S" treatment is shown in Figure 4.16 for comparison of both characterization techniques. Both techniques, DSC and XRD lead to close crystallinity fraction values and show similar trends.

Crystallinity increases slightly with Mg content. The differences found between both methods are due to the different nature of the characterization techniques. By XRD some uncertainty is introduced as it is necessary to subtract the amorphous halo from the sample diffractogram. However, crystal content by DSC is calculated considering the value of enthalpy of fusion for 100% crystalline polylactic (93.1 J/g) used recurrently in the literature [29]. This value leads to lower crystalline fractions than that obtained by X-Ray.

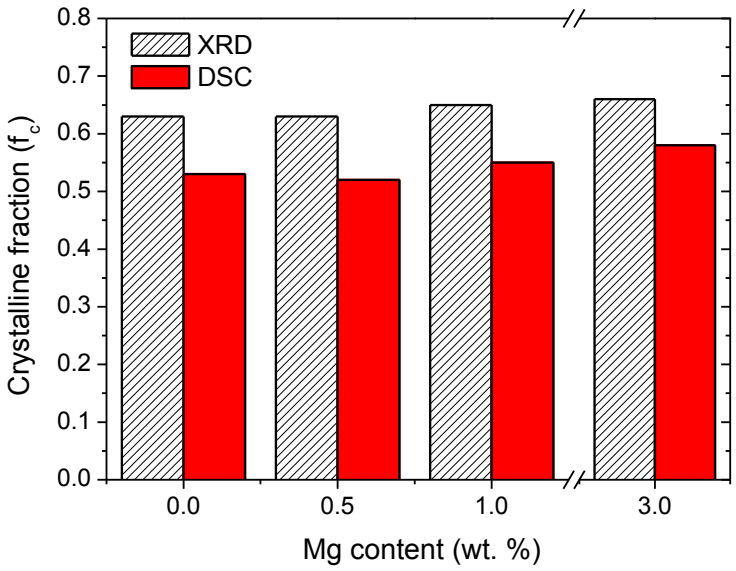

Figure 4.16 Crystalline fraction measured by DSC and X-ray diffraction for PLLAXMg composites with X=0, 0.5, 1 and 3 wt.% Mg content.

4.3.5 ATR-FTIR

The chemical structure changes of the polymeric matrix can be assessed by FTIR. In order to address and facilitate the analysis of Mg particles effect on PLLA molecular structure, it is supposed that the mechanisms implied in PLLA/Mg composites thermal degradation should be similar to those of PLLA/MgO compounds [20, 23]. In this sense, the cyclation of PLLA molecules and the formation of oligomers are expected.

Figure 4.20 shows the ATR-FTIR spectra of PLLAXMg composites with emphasis on the –OH and C-H region (a), carbonyl group region (b) and the 1700 – 800 cm^{-1} region (c). The study of the chemical changes that PLLA underwent has been performed by assessing the evolution of selected IR bands (-OH, carbonyl and esters groups) related to the CH bending.

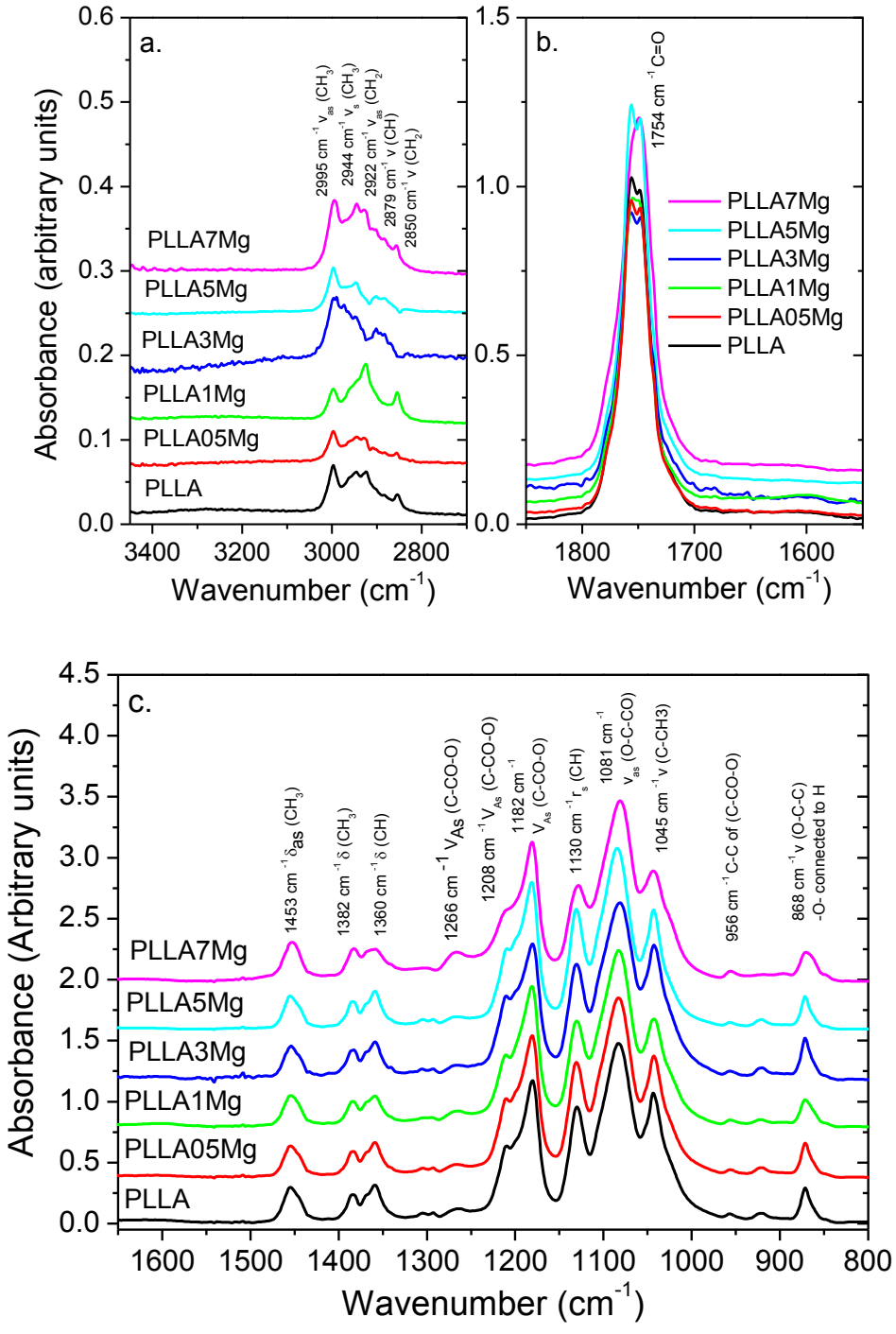

Figure 4.20 ATR-FTIR spectra of PLLAXMg composites with X= 0, 0.5, 1, 3, 5 and 7 wt.% of Mg

A decrease on the OH groups is expected as a consequence of PLLA molecules cyclation. However, these molecular changes cannot be seen in the infrared spectra of polylactic acid (Figure 4.20a) as the concentration of other groups (like carbonyl and esters) is higher than the –OH chain ends. No significant changes are evidenced within the area corresponded to OH characteristic band at wavenumbers larger than 3000 cm^{-1}.

Changes on the relative contribution of ester and carbonyl groups are expected due to hydrolysis and cyclation of PLLA. Shortening of polylactide molecules induces the formation of new carboxylic acid groups affecting the relative contributions of carbonyl (C=O 1754 cm^{-1}), carbon-carbonyl-oxygen linkage (C-CO-O 1182 cm^{-1}) and oxygen-carbon-carbonyl linkage (O-C-CO 1801 cm^{-1}) among other groups. Although ATR-FTIR spectra do not show remarkable changes of the absorbance intensity of these groups (Figure 4.20b, c), the evolution of the relative contribution of each peak as a function of Mg particle content was studied. The absorbance of the –CH bending at 1360 cm^{-1} was chosen as a reference given its invariance with PLLA degradation [36]

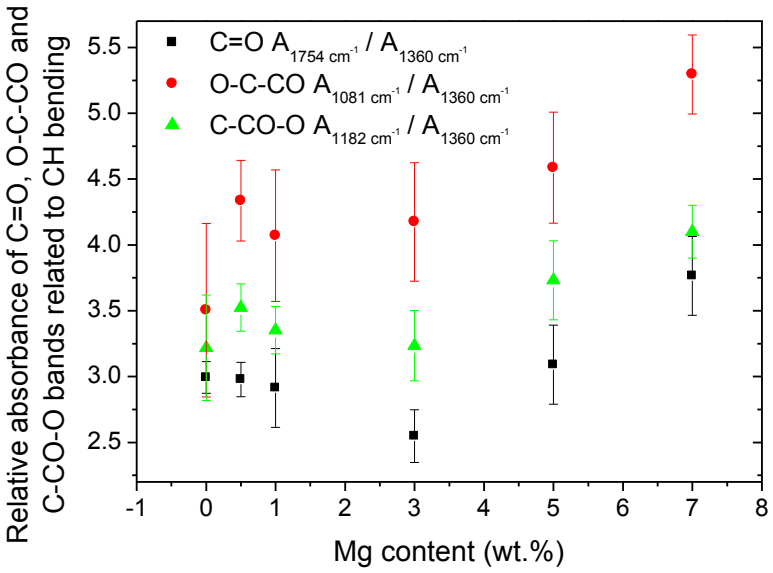

Figure 4.21 Relative absorbance of carbonyl and ester groups related to CH bending as a function of Mg content in PLLAXMg composites.

The dependence of carbonyl and ester relative contributions on Mg content is shown in Figure 4.21. No significant changes at contents lower than 3 wt.% are revealed. However, by increasing the amount of Mg, the relative contributions of the groups tend to increase in proportion to the Mg content. This evidences that Mg presence enhance the changes that PLLA chains can undergo during processing.

4.3.6 Mechanical properties as a function of Mg content

Addition of inorganic particles to a polymer matrix seeks the enhancement of the stiffness of the pure polymer matrix. If homogeneous filler dispersion is obtained, without polymer deterioration during blending, PLLA/Mg composites should possess improved mechanical properties compared to the neat PLLA prepared in the same condition for comparison.

Figure 4.22 shows the stress *vs* strain curves of the uniaxial compression tests performed to quenched PLLAXMg discs of 12 mm of diameter and 4 mm height. Curves are conveniently shifted in order to get more visual clarity. The deformation mechanism under compression is the same for all materials under study. Stress *vs* strain curves exhibit several characteristic stages of deformation. Initially the material shows a reversible (visco)-elastic deformation, where stress grows linearly proportional to strain and the elastic modulus is obtained. At a certain amount of stress, deformation becomes of an irreversible nature, which is recognisable by the yield point. After this point, a decrease in stress is observed, which is known as strain softening. With further deformation, an increase in stress is evidenced, which is referred to as strain hardening.

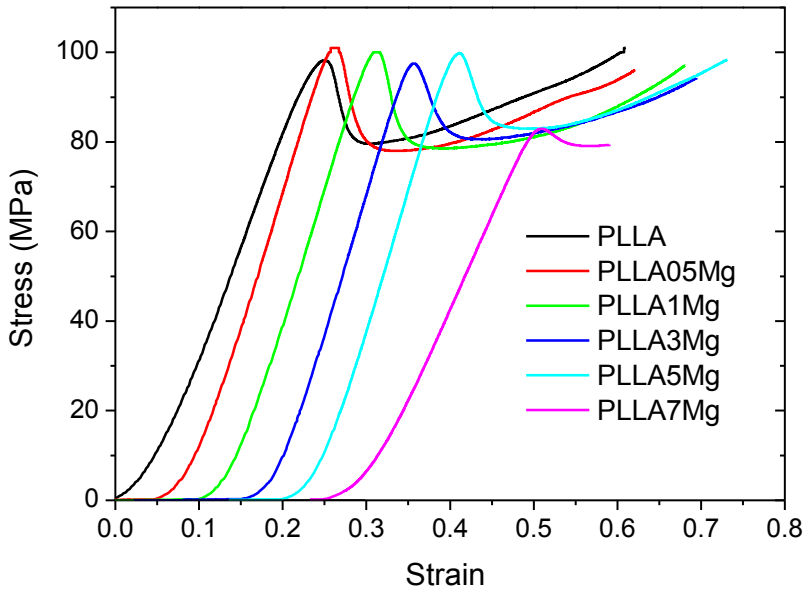

Figure 4.22 Compression stress *vs* strain curves for PLLAXMg composites with X= 0, 0.5, 1, 3, 5 and 7 wt.% of Mg (curves are shifted for visual clarity)

Results of Young´s modulus and compressive strength at yield as a function of Mg content are summarized in Figure 4.23. It is evidenced that Mg particles improve the mechanical properties of neat PLLA until 5 wt.% of Mg content. When the material has a 7 wt.% of Mg the mechanical compressive performance drops drastically.

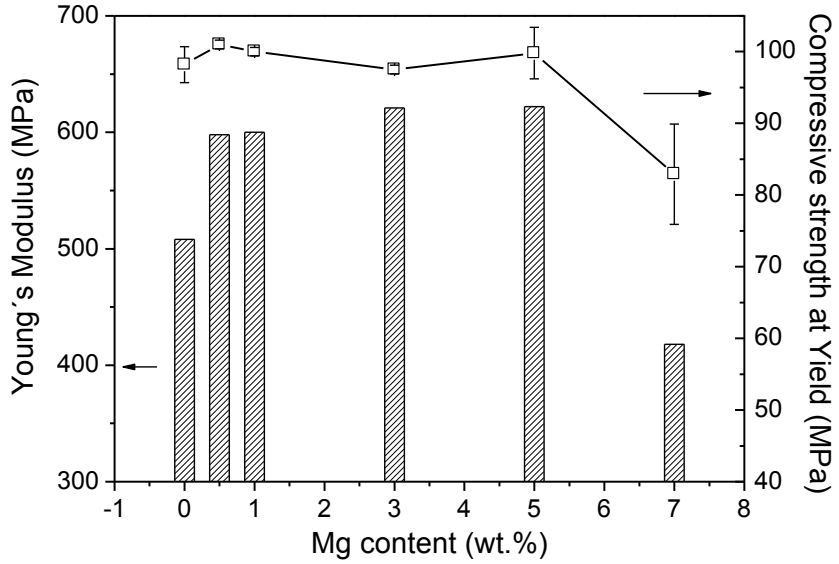

Figure 4.23 Mechanical properties of PLLAXMg composites as a function of Mg content

Experimental moduli were compared with theoretical moduli according to Reuss and Voigt Models. The corresponding modified rule of mixtures equation was also represented using different values for the filler strengthening factor (Figure 4.24). PLLAXMg composites moduli lie between the two Voigt-Reuss bounds, except for the material with 7 wt.% of Mg content that lies lower than the Reuss bound. According to the modified rule of mixtures, the particle strengthening factor was found to decrease with the increment of filler content. This dependence of X_f on Mg wt.% is shown in Figure 4.25 and exhibits an exponential decay.

The decrement on the filler strengthening factor could be related either with the Mg particles distribution within the matrix or with the thermal degradation effect of Mg particles on PLLA molecules.

Mg particles improve the mechanical properties of neat PLLA when the strengthening effect of fillers is greater than the thermal degradation effect, and when particles are not agglomerated, this occurs until 5 wt. % of Mg content. At 7 wt. %, Mg particles form aggregates and the effect of the filler on thermal degradation is greater than its reinforcement effect; the consequence is that mechanical properties drop drastically. These results imply that in the career to improve PLLA mechanical properties with Mg as a filler, there is a frontal competition between the reinforcement effect and the thermal degradation effect of Mg particles, which indicates the existence of a specific volume fraction of Mg for which the optimal mechanical properties are achieved.

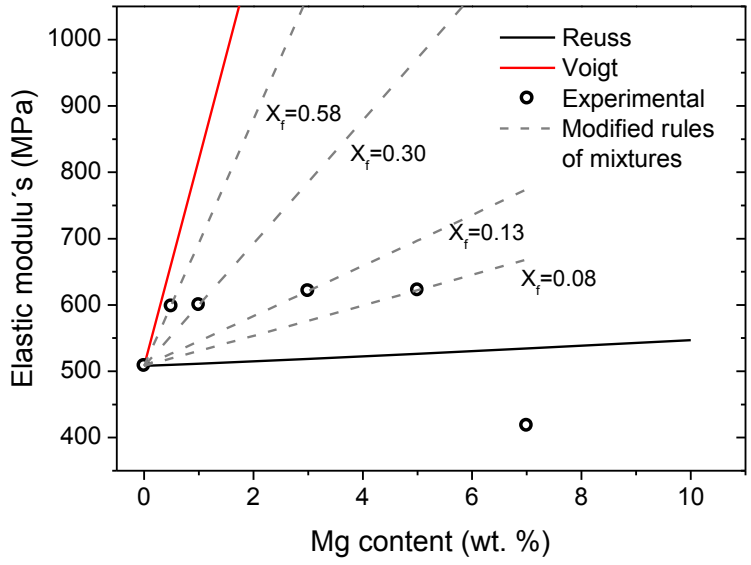

Figure 4.24 Comparison of experimental elastic modulus (points) of PLLAXMg composites with Reuss, Voigt and the modified rules of mixtures theoretical approaches (lines)

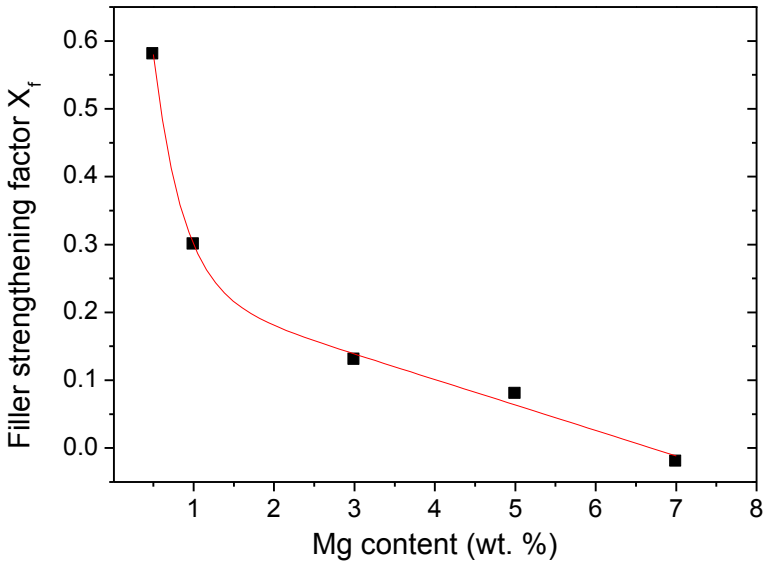

Figure 4.25 Filler strengthening factor as a function of Mg content

4.4 Conclusions

PLLA/Mg composites are suitable to be manufactured by extrusion and moulded by compression.

In order to improve mechanical properties of PLLA by reinforcing with Mg particles, two facts are important to take into account:

- ✓ Increasing Mg content within the polymeric matrix, increases PLLA thermal degradation rate.
- ✓ Mg particles strengthening factor decreases with the increment of Mg content.

Mg exerts two effects on PLLA mechanical properties; from one side there is a reinforcement positive effect that increases Young´s modulus with the increment of Mg content. On the other side there is a negative thermal degradation effect that reduces PLLA molecular weight and with this the mechanical properties. In order to obtain a total positive contribution of Mg particles improving the mechanical resistance of PLLA, a balance between both effects must be achieved.

In this sense, it is important to consider that there is a specific Mg content where the highest mechanical properties are achieved. For the experimental conditions used in this work, 5 wt.% of Mg resulted the optimal Mg content.

4.5 References

[1] Cifuentes SC, Frutos E, González-Carrasco JL, Muñoz M, Multigner M, Chao J, et al. Novel PLLA/magnesium composite for orthopedic applications: A proof of concept. Materials Letters 2012;74:239-42.

[2] Forman S, Kás J, Fini F, Steinberg M, Ruml T. The effect of different solvents on the ATP/ADP content and growth properties of HeLa cells. Journal of Biochemical and Molecular Toxicology 1999;13:11-5.

[3] Korpela M, Tähti H. Effects of industrial organic solvents on human erythrocyte membrane adenosine triphosphatase activities in vitro. Scandinavian Journal of Work, Environment & Health 1987;13:513-7.

[4] Silver FH, Christiansen DL. Pathobiology and Response to Tissue Injury. Biomaterials Science and Biocompatibility. New York: Springer Science & Business media; 1999.

[5] Cifuentes SC, Benavente R, González-Carrasco JL. Does magnesium compromise the high temperature processability of novel biodegradable and bioresorbables PLLA/Mg composites? Revista de Metalurgia 2014;50:1-11.

[6] L.M. Mathieu P-EB, J.-A.E. Manson. Processing of homogeneous ceramic/polymer blends for bioresorbable composites. Composites Science and Technology 2006;66:1606-14.

[7] Huan Zhou JGL, Sarit B. Bhaduri. Fabrication aspects of PLA-CaP/PLGA-CaP composites for orthopedic applications: A review. Acta Biomaterialia 2012;8:1999-2016.

[8] Wang M. Developing bioactive composite materials for tissue replacement. Biomaterials 2003;24:2133-51.

[9] C.G.Ambrose, Clanton TO. Bioabsorbable implants: review of clinical experience in orthopedic surgery. Annals of Biomedical Engineering 2004;32:171-7.

[10] Eglin D, Alini M. Degradable polymeric materials for osteosynthesis: tutorial. European Cells & Materials 2008;16:80-91.

[11] Middleton J, Tipton A. Synthetic biodegradable polymers as orthopaedic devices. Biomaterials 2000;21:2335-46.

[12] Gogolewski S, Jovanovic M, Perren SM, Dillon JG, Hughes MK. The effect of melt-processing on the degradation of selected polyhydroxyacids: polylactides, polyhydroxybutyrate, and polyhydroxybutyrate-co-valerates. Polymer Degradation and Stability 1993;40:313-22.

[13] Tsuji H, Fukui I. Enhanced thermal stability of poly(lactide)s in the melt by enantiomeric polymer blending. Polymer 2003;44:2891-6.

[14] Wang Y, Mano JF. Influence of melting conditions on the thermal behaviour of poly(l-lactic acid). European Polymer Journal 2005;41:2335-42.

[15] Ikarashi Y, Tsuchiya T, Nakamura A. Effect of heat treatment of poly(l-lactide) on the response of osteoblast-like MC3T3-E1 cells. Biomaterials 2000;21:1259-67.

[16] Ghosh S, Viana JC, Reis RL, Mano JF. Effect of processing conditions on morphology and mechanical properties of injection-molded poly(l-lactic acid). Polymer Engineering & Science 2007;47:1141-7.
[17] Cam D, Marucci M. Influence of residual monomers and metals on poly (l-lactide) thermal stability. Polymer 1997;38:1879-84.
[18] Fan Y, Nishida H, Shirai Y, Tokiwa Y, Endo T. Thermal degradation behaviour of poly(lactic acid) stereocomplex. Polymer Degradation and Stability 2004;86:197-208.
[19] Chiang M-F, Chu M-Z, Wu T-M. Effect of layered double hydroxides on the thermal degradation behavior of biodegradable poly(l-lactide) nanocomposites. Polymer Degradation and Stability 2011;96:60-6.
[20] Motoyama T, Tsukegi T, Shirai Y, Nishida H, Endo T. Effects of MgO catalyst on depolymerization of poly-l-lactic acid to l,l-lactide. Polymer Degradation and Stability 2007;92:1350-8.
[21] Fan Y, Nishida H, Hoshihara S, Shirai Y, Tokiwa Y, Endo T. Pyrolysis kinetics of poly(l-lactide) with carboxyl and calcium salt end structures. Polymer Degradation and Stability 2003;79:547-62.
[22] Fan Y, Nishida H, Shirai Y, Endo T. Racemization on thermal degradation of poly(l-lactide) with calcium salt end structure. Polymer Degradation and Stability 2003;80:503-11.
[23] Auras R, Lim LT, Selke SEM, Tsuji H. Poly-lactic acid. Synthesis, Structures, Properties, and Applications: John Wiley & Sons, INC.; 2010.
[24] ASTM. D446-12 Standard Specifications and Operating Instructions for Glass Capillary Kinematic Viscometers. West Conshohocken, PA: ASTM International; 2012.
[25] Spinu M, Jackson C, Keating M, Gardner K. Material design in poly(lactic acid) systems: block copolymers, star homo and copolymers, and stereocomplexes. . Journal of Macromolecular Science: Pure and Applied Chemistry 1996;A 33:1497-530.
[26] Tsuji H, Ikada Y. Blends of isotactic and atactic poly(lactide)s: 2. Molecular-weight effects of atactic component on crystallization and morphology of equimolar blends from the melt. Polymer 1996;37:595-602.
[27] Perego G, Cella GD, Bastioli C. Effect of molecular weight and crystallinity on poly(lactic acid) mechanical properties. Journal of Applied Polymer Science 1996;59:37-43.
[28] Garlotta D. A Literature Review of Poly(Lactic acid). Journal of Polymers and the Environment 2001;9:63-84.
[29] Lim LT, Auras R, Rubino M. Processing technologies for poly(lactic acid). Progress in Polymer Science 2008;33:820-52.
[30] Callister JW. Materials science and engineering: an introduction. New York: Wiley; 1999.
[31] Fu S-Y, Feng X-Q, Lauke B, Mai Y-W. Effects of particle size, particle/matrix interface adhesion and particle loading on mechanical properties of particulate–polymer composites. Composites Part B: Engineering 2008;39:933-61.
[32] Fu S-Y, Xu G, Mai Y-W. On the elastic modulus of hybrid particle/short-fiber/polymer composites. Composites Part B: Engineering 2002;33:291-9.

[33] Jayaraman K KM. Correction to the Fukuda-Kawata Young´s modulus theory and Fukuda-Chou strength theory for short fibre reinforced composite materials. Journal of Materials Science 1996;31:2059-64.

[34] Pan P, Inoue Y. Polymorphism and isomorphism in biodegradable polyesters. Progress in Polymer Science 2009;34:605-40.

[35] Pan P, Kai W, Zhu B, Dong T, Inoue Y. Polymorphous Crystallization and Multiple Melting Behavior of Poly(l-lactide):Molecular Weight Dependence. Macromolecules 2007;40:6898-905.

[36] Santonja L. Ph D Thesis: Contribution to the study of thermal, biological and photo degradation of polylactide. Valencia, Spain: Universitat Politècnica de València; 2012.

SUITABILITY OF NOVEL PLA/Mg COMPOSITES FOR INJECTION MOULDING

CHAPTER 5

"The only source of knowledge is experience"

Albert Einstein

Table of contents

5. SUITABILITY OF NOVEL POLYLACTIC ACID/Mg COMPOSITES FOR INJECTION MOULDING

5.1 Introduction

Medical devices industries prefer injection moulding rather than other moulding processes due to the significant cost savings and versatility. Most of the bioresorbable implants applied for bone fixation have complex 3D structures that need high precision manufacturing [1]. While it is true that complex 3D structures can be manufactured by 3D printing, research regarding production of implantable medical devices by this type of technology is currently under development [2] and, therefore, injection moulding is still the most widely method used for producing implantable devices. However, manufacturing implantable devices by injection moulding is a difficult task on its own that poses even more challenges when the components are based on bioresorbable polymers.

Biopolymer resins like polylactic acid require some care in moulding in order to not exceed their heat, shear and hydrolytic stability. During injection moulding the polymer underwent thermo-mechanical stresses that can induce its degradation. The material passes from a glassy state to a melt state by heating above the melting temperature, and then it is homogenized, plasticized and transported to a nozzle by means of a screw. At this stage, the polymer is injected into the cavity of a mould where it starts cooling down and return to a solid state before it is removed from the mould. Polylactic acid is tough to process because it has a small window between its melting point or processing temperature and the degradation temperature [3, 4]. Too much heat or too much exposure times can generate depolymerisation and result in monomer formation, which can change the mechanical properties and alter degradation kinetics of injected parts.

When manufacturing a bioresorbable device by injection moulding, it is necessary to pay extremely attention to melt temperature, and screw and injection speed, in order to ensure consistency and quality in the final part. Even if the temperature is carefully controlled, degradation can still occur due to the sensitivity of the polymer to residence time or shear rate [5].

Novel Polylactic acid / Mg composites seek to overcome the difficulties of currently available bioresorbable implants. Mg is an essential mineral for bone formation and also has antibacterial properties. Therefore, incorporation of Mg particles in a matrix of polylactic acid could give the polymer the ability to induce bone regeneration, have bactericidal properties and particles can also act as mechanical reinforcement.

The incorporation of Mg particles within the polymeric matrix, however, can also imply even more challenging difficulties for the injection moulding process. On the one hand, given the

severe particle matrix interactions, incorporation of particles in a polymeric matrix might induce significant changes in the rheological properties of the polymer [6]. On the other hand, the presence of metallic compounds can also alter the thermal stability of polylactic acid and induce cyclation of polymeric chains [4, 7].

Nowadays injection moulding is increasingly used within the medical device industry to produce bioresorbable implants. The implementation of a new material as polymer/Mg composites within the market, urges the reduction of investment risks in order to obtain important commercialization margins once the product is on the market. This could be achieved if the material is suitable to be manufactured by common processes available within implants industry.

This chapter studies the suitability of injection moulding of novel polylactic acid/Mg composites. The importance of this study relies in the need of bridging the gap between science and technology in order to attract the interest of bioresorbable implants industry and achieve their implication on the development of these novel materials.

The suitability of processing these novel composites by injection moulding is addressed by manufacturing the composites and assessing the quality of injected parts in terms of mechanical performance. Rheological properties, changes in polymer molecule and thermal properties are also characterized. This chapter gathers the preliminary results obtained at the Polymer Engineering Centre of the University of Wisconsin Madison in United States (PEC-U Wisc).

5.2 Materials and methods

5.2.1 Materials

Two polylactic acids were studied to test their suitability for injection moulding. Poly-L-lactic acid (PLLA) provided by Goodfellow and poly-L,D-lactic acid (PLDA) from Natureworks. Table 5.1 specifies their properties.

Table 5.1 Polylactic acid (PLA) properties

Material	D-isomer content (%)	Melt Flow Index (210 ºC/2.16Kg)	Tg (ºC)	Tm (ºC)
PLLA	0	35.8 g/ 10 min	60 ºC	170 ºC
PLDA	4.25	35.4 g/ 10 min	65 ºC	160 ºC

5.2.2 Processing

5.2.2.1 Injection moulding

PLA/Mg composites were manufactured in a BOY XS Injection Moulding machine. In order to eliminate the thermal degradation effects that could be introduced if an extrusion step is included prior injection moulding, the machine was fed with a dried mixture of polymer pellets and commercial purity Mg particles of about 50 μm. Mg particles have the property to stick over polymer pellets surface leading to homogeneous dried mixtures. The limit of Mg amount that can be fully stuck over the granules surface was found to be 1 wt.%. Therefore 0.2, 0.5 and 1 wt.% mass fractions were selected to manufacture the composites.

Dumbbell shaped specimens for tensile tests were fabricated (Figure 5.1). Cylinders of 4.7 ± 0.05 mm of diameter and 7.5 ± 0.3 mm height (L/D=1.5) were cut from the runners of injection moulded samples and used as specimens for compression tests (Figure 5.2).

Injection moulding parameters as melt processing temperature, mould temperature, holding pressure, back pressure, screw speed and cooling time were optimized to eliminate shrinkage, jetting, flash or incomplete injected parts. Table 5.2 shows the selected injection moulding parameters.

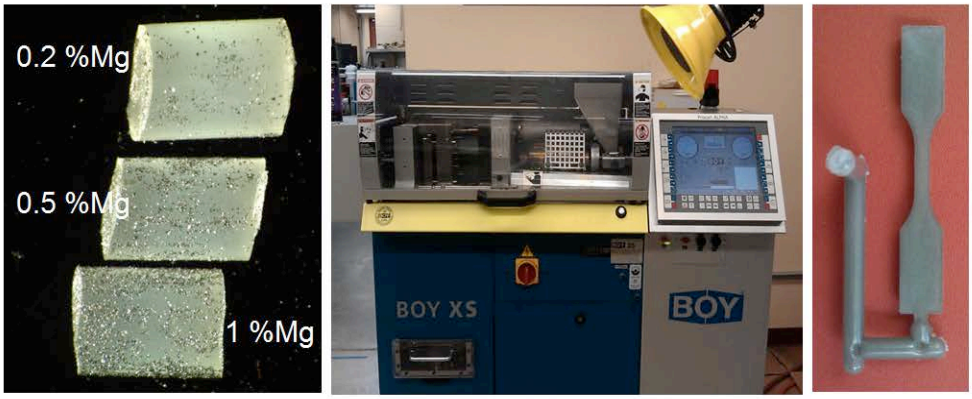

Figure 5.1 Fabrication of Polymer/Mg composites by injection moulding. Dumbbell-shaped test specimens (Gage length: 14 mm, Width and thickness: 3.2 mm)

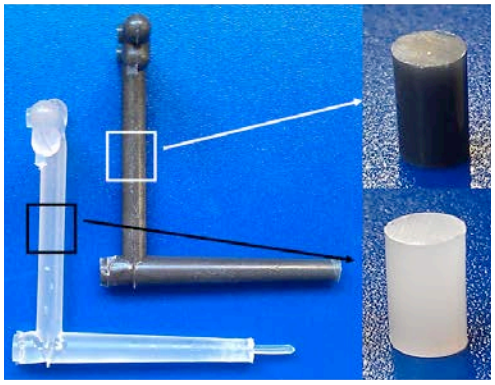

Figure 5.2 Compression tests specimens (diameter: 4.7 ± 0.05 mm, height: 7.5 ± 0.3 mm)

Table 5.2 Injection moulding parameters

Filling phase	
Pressure	250 bar
Screw speed	5% (start) – 25% (end)
Injection time	2 s
Holding pressure phase	
Pressure	250 bar
Time	6 s
Plasticizing phase	
Back pressure	5 bar
Time	99 s
Screw speed	25%
Heating zones	
T1 Barrel transition zone	190 ºC
T2 Barrel metering zone	200 ºC
T3 Nozzle	200 ºC
Mould temperature	25 ºC
Cooling time	45 s

5.2.2.2 Thermal treatment

With the aim of studying the effect of crystallinity degree on compressive mechanical properties of composites, crystalline samples were prepared by subjecting the runners of injection moulded parts under a thermal treatment at 125 ± 1 ºC during 1 hour in a Thermo Scientific Heraeus oven, then cylinders of 4.7 ± 0.05 mm of diameter and 7.5 ± 0.3 mm height (L/D=1.5) were cut from the runners and used for compression tests.

The thermal treatment was selected taking into account results from chapter 3. The largest enthalpy of melting achieved by PLDA IM during isothermal crystallization from the glassy state occurs at 125 ºC (Chapter 3 Figure 3.16b).

5.2.3 Rheological characterization

5.2.3.1 Parallel plate rheometer

A parallel plate rheometer is a rotational method that measures the viscoelastic behaviour of polymer melts by shearing the fluid between two surfaces. Viscosity is determined by measuring the resistance to the rotational force. Usually the rheological properties of a viscoelastic material are independent of strain up to a critical strain level. A strain sweep test establishes the extent of the material´s linearity. After the polymer melt´s linear viscoelastic region has been defined by a strain sweep, its viscoelastic behaviour can be further characterized using a frequency sweep at a strain below the critical strain. The temperature and strain are held constant in a frequency sweep and the viscoelastic properties are monitored as the frequency is varied.

Rheological behaviour of the polymeric matrices (PLLA and PLDA) and their temperature dependency was measured using a strain-controlled ARES rheometer (TA Instruments) equipped with a 25 mm parallel plate flow geometry. Frequency sweep tests were performed at 10% strain over a frequency range from 0.1 – 70 Hz (from high to low frequency) at 180, 190, 200 and 210 ºC. The resulting data from the experiments can be presented in a plot of the complex viscosity (η*) *vs* frequency.

5.2.3.2 Capillary rheology

Capillary rheometry is based on controlled extrusion of a test material; it enables to reproduce the conditions that polymer melt experiences during injection moulding. The material is forced through a capillary die at a defined piston speed and the melt pressure is recorded. The piston speed can be converted into a value for the shear rate, and the pressure into a value for the shear stress.

Capillary rheology was performed in a HAAKE Rheoflixer high-pressure capillary rheometer (UC3M) using a rod capillary die with 1 mm diameter and 30 mm in length and a transducer pressure sensor with maximum pressure of 1400 bar. With the intention of understanding the rheological behaviour of materials during injection moulding, the relationships between the

apparent viscosity and the shear rate, in a range from 10 to 10^4 s^{-1} at 170, 180 and 190 ºC, were obtained for the polymer and the composite with 1 wt.% solid loading.

The behaviour of the material is described by a modified Cross mathematical model (Equation 5.1).

$$\eta = \frac{\tau_y}{\dot{\gamma}} + \frac{\eta_0}{1 + \left(k\dot{\gamma}\right)^m} \qquad \text{Equation 5.1}$$

The model describes the apparent viscosity of the melt (η) as a function of the shear rate ($\dot{\gamma}$). It supposes the occurrence of a threshold shear stress (τ_y) and a zero viscosity (η_0) considered as the viscosity during the Newtonian plateau at low shear rates. Constants m and k are parameters related to the shift in the melt flow from Newtonian to pseudoplastic behaviour.

5.2.3.3 Activation energy

The viscosity dependence on the temperature is of great importance in injection moulding. The material suffers an abrupt change of temperature when it is injected from the nozzle (200 ºC) to the mould (25 ºC). Viscosity tends to increase as temperature decreases. Considerable variations in viscosity could lead to defects in injected parts.

The dependence of viscosity of polymer melts on temperature can be expressed in the Arrhenius form,

$$\eta_0 = A\exp\left(\frac{E_a}{RT}\right) \qquad \text{(Equation 5.2)}$$

$$\ln(\eta_0) = \ln(A) + \frac{E_a}{RT} \qquad \text{(Equation 5.3)}$$

where η_0 is the zero shear viscosity, R is the gas constant, A is a constant and Ea is the flow activation energy. The activation energy results from the slope of the plot ln(η) *vs* 1/RT, and indicates the inversely proportional relationship of viscosity with temperature.

5.2.4 Physico-chemical characterization

5.2.4.1 Viscosity average molecular weight

The average molecular weight of virgin and injected polymer matrices was estimated by means of viscometry. Measurements were carried out by solving the samples in chloroform at 25 ºC, using a Ubbelohde type or suspended level viscometer. The intrinsic viscosity was obtained

according to ASTM D446 [8]. The value was used to determine the viscosity average molecular weight with the following Mark-Houwink equations [9-11]:

PLLA $[\eta] = 4.41 \times 10^{-4} M_v^{0.72}$ Equation 5.4

PLDA $[\eta] = 2.21 \times 10^{-4} M_v^{0.77}$ Equation 5.5

5.2.4.2 Morphology

Morphology of the composites is studied by macroscopic images taken with a NIKON SMZ 1500 stereoscopic microscope. The dispersion of Mg particles in the polymer matrix is analyzed using an optical polarising microscope (Carl Zeiss Amplival microscope). Scanning electron microscopy (cold-FEG Hitachi S4800) was used to evaluate fracture surfaces.

5.2.4.3 ATR-FTIR

Fourier Transform Infrared Spectroscopy was applied to identify the chemical functional groups of both polylactic acids and their changes during processing. The FTIR spectra were obtained with a Bruker Equinox 55 spectrometer in the 4000 to 650 cm^{-1} region, using an Attenuated Total Reflectance (ATR) modulus.

Table 5.3 FTIR spectra regions of PLA groups and bonds

Region	Group or bond
3600 – 3200 cm^{-1}	-OH stretching vibration (carboxyl acids and alcohols)
3100 - 2800 cm^{-1}	Stretching vibrations of the C-H bonds of the polymeric chain
1754 cm^{-1}	Carbonyl group C=O
1460 - 1300 cm^{-1}	Vibration of the C-C bonds of the polymeric chain
1360 cm^{-1}	Related to the CH bending (wagging)
1300 – 800 cm^{-1}	Related to C-O vibrations appear overlapped with contributions from the C-H bonds.
1182 cm^{-1}	Asymmetric stretching vibration of the C-CO-O
1087 cm^{-1}	Related to the asymmetric stretching vibration of O-C-CO

The most representative bands of polylactic acid and the region where they are found are listed in Table 4.1. The study has been focused on the evolution of selected IR bands (carbonyl and esters groups) related to some representative groups (CH bending) to monitor the changes that the polymer underwent during processing.

5.2.4.4 Thermal behaviour

The crystallinity degree of the materials and its melting and crystallization behaviour were characterized by means of differential scanning calorimetry on a TA Q100 DSC under nitrogen atmosphere, using 7±0.5 mg of each sample. The experimental design was based on a first heating (F10) from 25 ºC to 220 ºC, followed by a cooling to 25 ºC and a second heating to 220 ºC (CR10F10). All the steps were carried out at 10 ºC/min.

The crystalline fraction was calculated by measuring the enthalpy of melting ΔH_m and cold crystallization ΔH_{cc} from the heating curves using Equation 5.3, where ΔH_m^0 is the enthalpy of 100% crystalline PLLA (93.1 J/g) [3].

$$f_c = \frac{(\Delta H_m - \Delta H_{cc})}{\Delta H_m^0} \qquad \text{Equation 5.6}$$

5.2.4.5 X-Ray Diffraction

X-ray diffraction was used to probe the crystal structure of specimens. Samples were analyzed using a wide angle X-ray diffraction, WAXD, apparatus (Bruker D8 Advanced Diffractometer provided with a PSD Vantec detector) by using CuK_α radiation. The spectra was recorded in an angular range of $5º < 2\theta < 40º$ at room temperature. The crystallinity degree is obtained by subtracting the amorphous halo, by comparison to the diffraction pattern obtained from the quenched samples.

5.2.4.6 Mechanical characterization

Mechanical characterization was performed under tensile and compression tests. For tensile tests an Instron 5969 testing machine was used according to ASTM D638M Standard Test Method for Tensile Properties of Plastic. For each condition, five dumbbell-shaped specimens (gauge length: 14 mm, width and thickness: 3.2 mm) were tested at a strain rate of 10^{-3} s^{-1} and ambient conditions. The compressive mechanical behaviour was studied in a universal machine EM2/100/FR-10kN Micro Tests at ambient conditions, using a strain rate of 10^{-3} s^{-1}. Five samples were tested for each material. From the stress-strain curves the yield strength and Young´s modulus were obtained.

Composite modulus values should fall within a domain defined by Reuss (series arrangement, iso-stress criteria) and Voigt (parallel arrangement, iso-strain criteria) models [12-14]. These models predict the composite modulus (E_c) taking into account the modulus of the particulate filler (E_f), the modulus of the polymeric matrix (E_m), and the filler volume fraction (V_f) according to the following Equations:

Reuss model

$$E_c^{lower} = \frac{E_f E_m}{E_f(1-V_f)+E_m V_f}$$ Equation 5.7

Voigt model

$$E_c^{upper} = E_f V_f + E_m(1-V_f)$$ Equation 5.8

Composites Young´s modulus obtained from compressive stress-strain curves was used to calculate the filler strengthening factor (X_f) for each Mg contents according to the modified rule of mixtures (Equation 5.9).

$$E_c = \chi_f E_f V_f + E_m(1-V_f)$$ Equation 5.9

5.3 Results and discussion

5.3.1 Rheological behaviour of polymeric matrices

The rheological behaviour of PLLA and PLDA was evaluated with the aim of understanding the phenomena occurring in processing and determining their melt processability. Figure 5.3 presents the viscosity curves at different temperatures for PLLA and PLDA obtained with the ARES rheometer between 0.1 and 70 Hz. It is worth to notice that PLLA exhibits a considerably higher complex viscosity than PLDA, which is surprising given that both polymers have very similar melt flow index. The higher complex viscosity of PLLA can be due to the stereoregularity of the polymer chain, which is characterized by the presence of only S(-) chiral centers. This result agrees with work of Ahmad reporting that the rheological response is very sensitive to stereoregularity [15].

Complex viscosities ŋ* of both polymeric matrices display first a Newton liquid behaviour followed by a shear-thinning behaviour at high frequencies. PLLA shear thinning behaviour appears at lower frequencies than in the case of PLDA. PLLA complex viscosity is constant with the frequency increasing up to 3 Hz at 180 ºC, and up to 20 Hz at 210 ºC. In the case of PLDA melt, complex viscosity displays a Newton liquid behaviour up to 20 Hz at 180 ºC, and at the whole frequency range studied (0.1 – 70 Hz) at 210 ºC. Comparing to PLDA, PLLA shows a stronger shear thinning tendency and it becomes stronger with decreasing temperature.

Values of E_a were calculated from data of Figure 5.3 and are shown in Figure 5.4. The flow activation energy is one of the most important parameters in polymer flow as it gives an idea on the dependence of the polymer melt viscosity with the temperature. The flow activation energy

of PLLA and PLDA presents similar order of magnitude and values, which indicates that both polymers have similar flow behaviour.

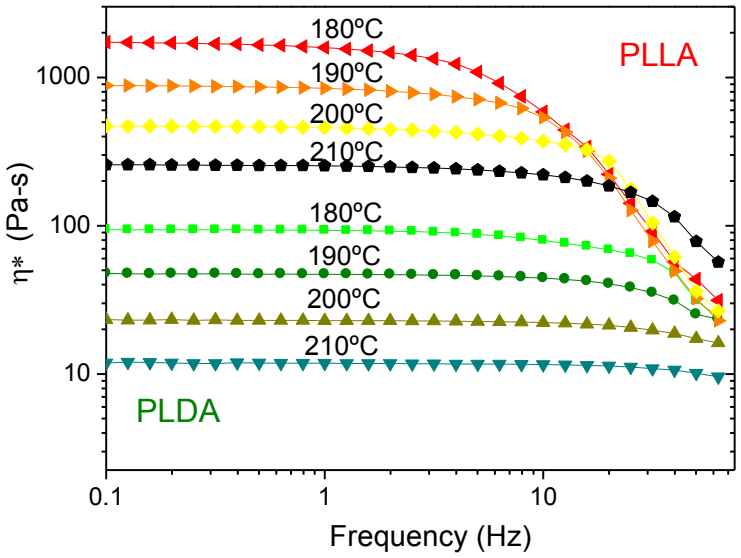

Figure 5.3 Viscosity curves of PLLA and PLDA

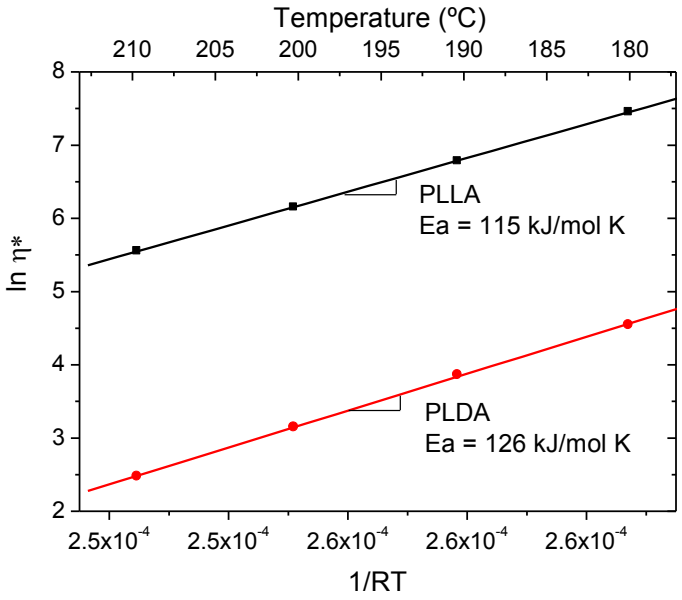

Figure 5.4 Arrhenius plot showing the temperature dependence of PLLA and PLDA zero shear viscosity

5.3.2 Injection moulding of PLLA

Injection moulding of PLLA was successfully achieved at the selected conditions. Some complications, however, appeared during continuous processing of tensile samples. The first five dumbbell-shaped specimens were easily injected and without defects in appearance, but at some point the processability of the material was reduced, injected specimens started to change their colour and incomplete filled parts were injected (Figure 5.5).

The changes in colour and processability could be due to the degradation of the material. First samples are not degraded, but as the time passes, and PLLA that remain in the barrel starts to degrade, degradation products are mixed with new material, then the specimen colour starts changing and the processability of the material becomes compromised. To verify that changes in colour and processability are caused by thermal degradation, FTIR-ATR spectrums of each sample were acquired (Figure 5.6) and the changes on the relative contributions of ester and carbonyl groups were studied (Figure 5.7).

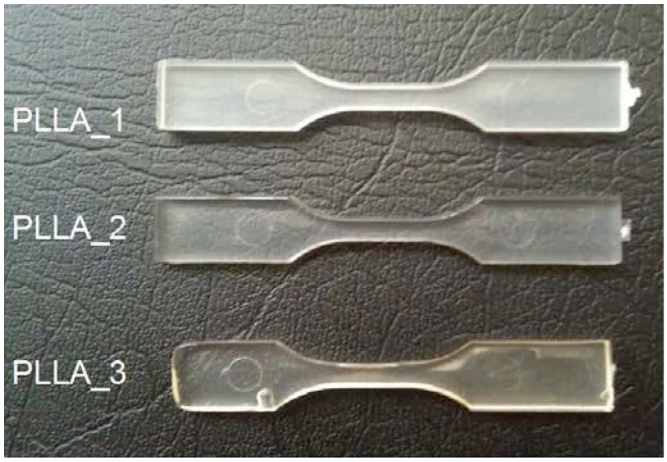

Figure 5.5 Changes in appearance of PLLA injection moulded specimens during continuous processing. (PLLA_1: Specimen without defects, PLLA_2: Specimen started to change in colour, PLLA_3: Incomplete specimen)

ATR-FTIR spectra show significant changes within the area corresponded to OH characteristic band at wavenumbers larger than 3000 cm^{-1} (Figure 5.6 a). The OH band is absent in PLLA pellet and PLLA_1 and _2 spectrums, but it is evident in PLLA_3. This suggests that the concentration of –OH chain ends is higher in PLLA_3 specimen. ATR-FTIR spectra of PLLA_3 from 1650 cm^{-1} to 800 cm^{-1} also show remarkable changes in the intensity peaks of ester linkages at 1182 cm^{-1} (C-CO-O) and 1081 cm^{-1} (O-C-CO) (Figure 5.6 c). The evolution of the

relative contribution of carbonyl and ester peak as a function of change of colour and defects appearance is shown in Figure 5.7. The absorbance of the –CH bending at 1360 cm^{-1} was chosen as a reference given its invariance with PLLA degradation [16].

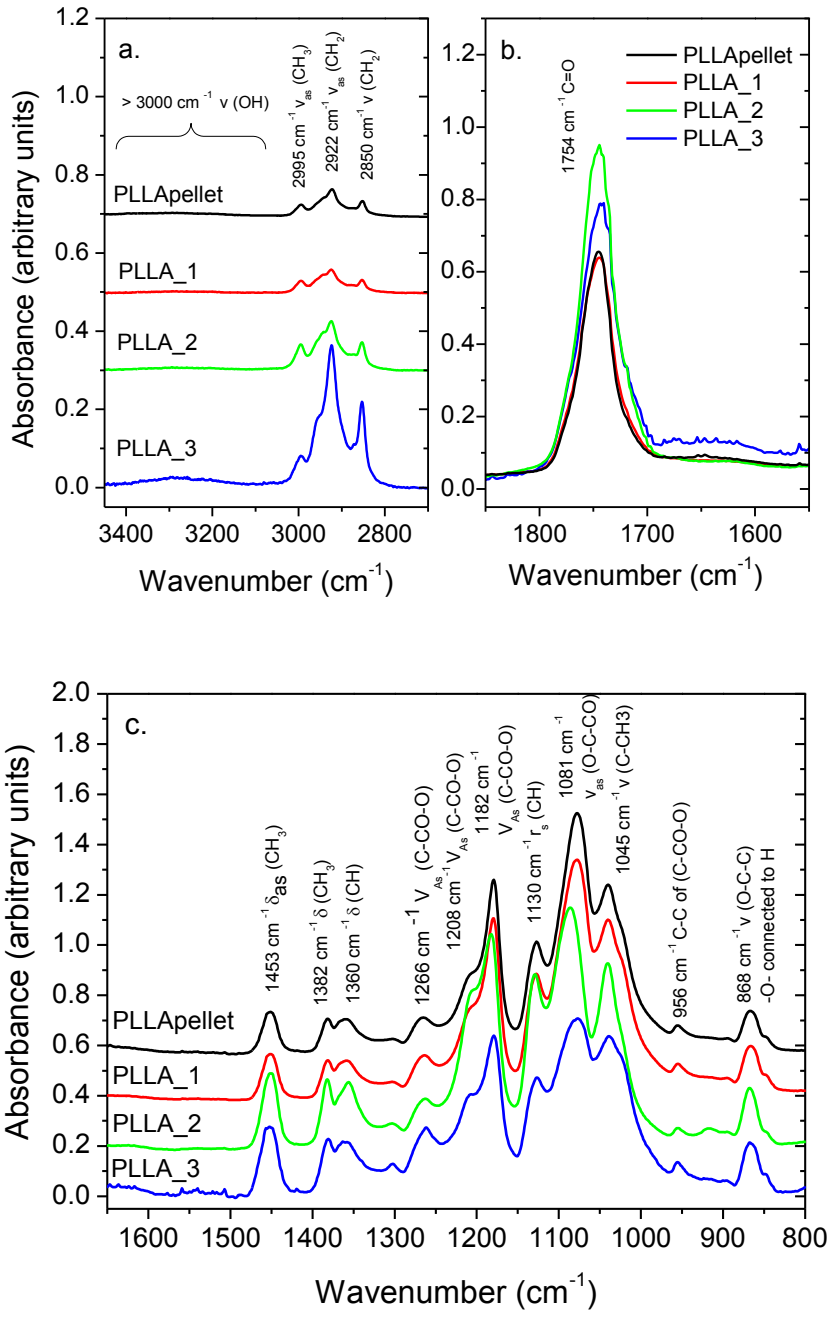

Figure 5.6 ATR – FTIR spectra of PLLA specimens processed by injection moulding. (PLLA_1: Specimen without defects, PLLA_2: Specimen started to change in colour, PLLA_3: Incomplete specimen)

Carbonyl (C=O), carbon-carbonyl-oxygen (C-CO-O) and oxygen-carbon-carbonyl (O-C-CO) relative absorbance decrease with progressing colour changes and increasing defects appearance. The decrement of the relative contribution of ester and carbonyl demonstrates that thermal degradation is occurring during injection moulding of PLLA and it induces the shortening of polylactide molecule either by random main-chain scission or hydrolysis mechanisms [7, 17-19].

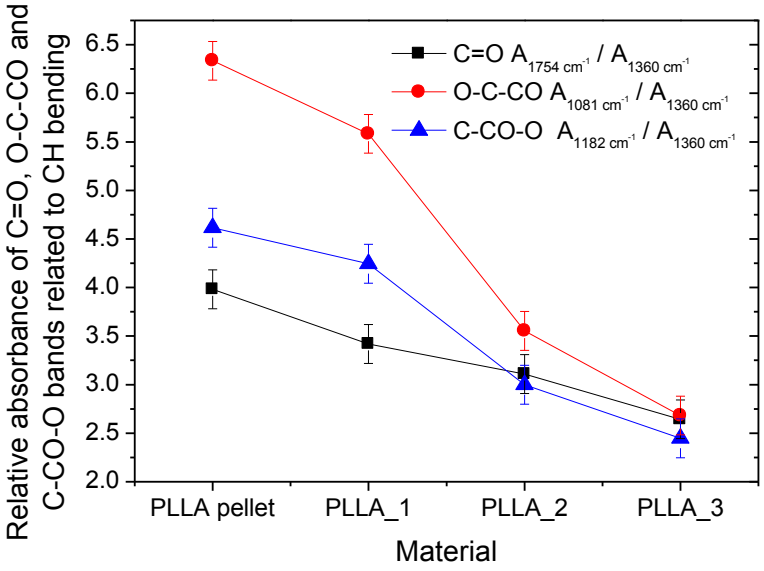

Figure 5.7 Relative absorbance of carbonyl and ester groups related to CH bending for injected PLLA as a function of changes in colour and defects appearance. (PLLA_1: Specimen without defects, PLLA_2: Specimen started to change in colour, PLLA_3: Incomplete specimen)

The effect of injection moulding on PLLA thermal stability was assessed by comparing the molecular weight of PLLA pellet and processed PLLA. Figure 5.8 compares the intrinsic viscosity of PLLA in pellet form to that obtained for injection moulded PLLA. Black squares correspond to the reduced viscosity or Huggins (η_{red} *vs* c) plot and red circles correspond to the inherent viscosity or Kraemer (η_{inh} *vs* c) plot. The lines are the linear extrapolations of Huggins and Kraemer plots to find the inherent viscosity in the intercept, black lines are for PLLA pellet and red lines are for injection moulded PLLA.

The molecular weight of the pellet and injected PLLA_1 were estimated by the Mark-Houwink equation for PLLA using the values obtained from Figure 5.8 for intrinsic viscosity (Table 5.4). Injection moulding of PLLA causes a reduction of almost 20% in the viscosity average molecular weight as shown in Table 5.4. PLLA underwent thermo-mechanical degradation during the injection process, and this leads to the shortening of its molecular weight. The high sensitivity of

PLLA to thermal degradation during injection moulding impeded the fabrication of Polymer/Mg composites using this matrix.

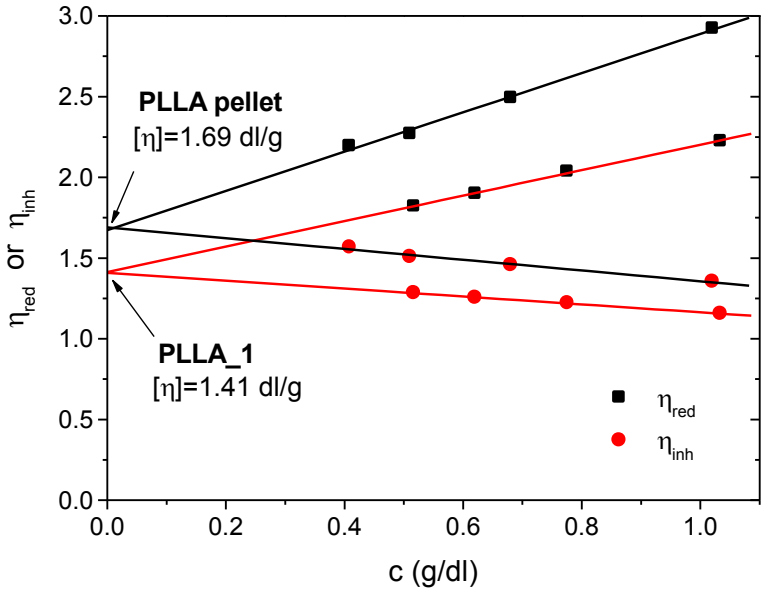

Figure 5.8 Huggins-Kraemer plot to determine the intrinsic viscosity of PLLA pellet and PLLA_1 injected specimens (PLLA_1: Injected specimen without defects)

Table 5.4 Viscosity average molecular weight of PLLA pellet and PLLA_1

PLLA pellet M_v	PLLA_1 M_v	Reduction M_v
95 kDa	74 kDa	22 %

5.3.3 Injection moulding of PLDA/Mg

5.3.3.1. Capillary rheology of PLDA and PLDA/Mg melts

Capillary rheology allows to study the flow behaviour of PLDA and PLDA1Mg measuring the apparent viscosity of the melts at different shear rates and temperatures (Figure 5.9). The behaviour of the material is described by a modified Cross mathematical model (Equation 5.1). The fitting curves are shown in Figure 5.9 as dashed lines and the resulting modified Cross model parameters are shown in Table 5.5.

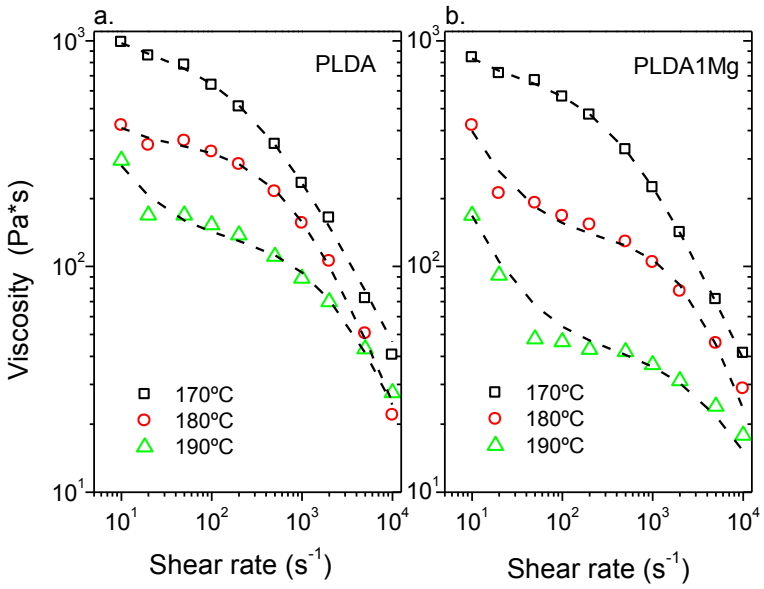

Figure 5.9 PLDA and PLDA1Mg shear viscosity dependence on shear rate at 170, 180 and 190 ºC. (Open symbols: experimental data, Dashed lines: Modified Cross model fitting to rheological data)

Viscosity dependence of PLDA and PLDA1Mg on shear rate presents a shear thinning behaviour, where viscosity decreases with increasing shear rate. Values of m parameter close to 1 corroborate also the pseudoplastic behaviour (Table 5.5). Three regions are clearly differentiated in each curve. The first one, at low shear rates, corresponds to a pseudoplastic behaviour, and the apparent viscosity decreases abruptly with increasing shear rate. This behaviour is more noticeable as temperature increases and is more evident for PLDA1Mg (Figure 5.9 b). The marked decrement of viscosity at lower shear rates implies that a minimum shear stress has to be overcome for the melt to start to flow. The threshold shear stress (τ_y) is higher for PLDA1Mg than for PLDA (Table 5.5). The second region, at medium shear rates, corresponds to a Newtonian plateau, where viscosity is less affected by the increasing shear rate. This intermediate shear rate range is extended with increasing temperature and is shorter for PLDA1Mg than for PLDA. The third region, at higher shear rates, corresponds to a shear-thinning behaviour. In this stage the behaviour of the composite (PLDA1Mg) resembles the behaviour of the polymer without reinforcement (PLDA).

Table 5.5 Parameters of modified Cross model for PLDA and PLDA1Mg obtained from fitting the experimental rheological data

Material	Temperature (ºC)	τ_y (Pa)	η_0 (Pa*s)	m	k
PLDA	170	1196	917	0.81	3.75×10^{-3}
	180	698	345	1.03	1.18×10^{-3}
	190	1470	133	1.01	0.44×10^{-3}
PLDA1Mg	170	1581	700	0.9	2.33×10^{-3}
	180	2668	131	1.27	0.33×10^{-3}
	190	1250	43	0.89	0.20×10^{-3}

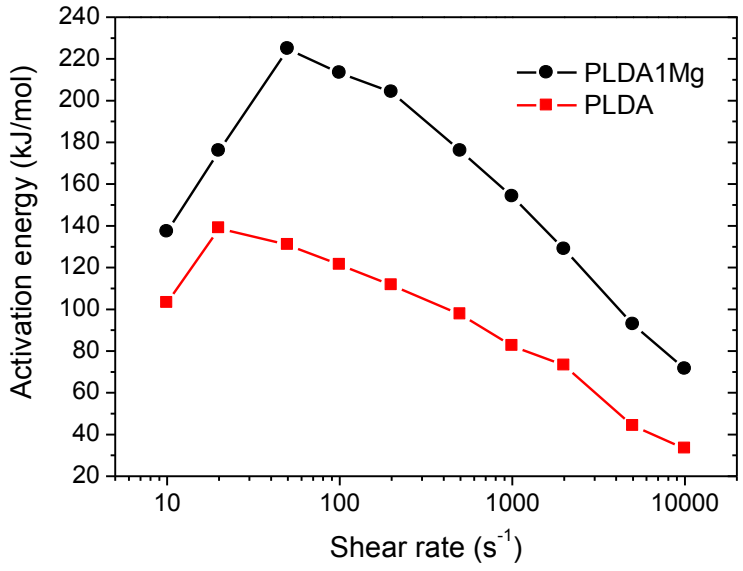

Figure 5.10 PLDA and PLDA1Mg flow activation energy as a function of shear rate

The apparent flow activation energy (E_a) as a function of shear rate (Figure 5.10) was calculated by the Arrhenius temperature dependence of PLDA and PLDA1Mg apparent viscosity as explained in section 5.2.3.3. The flow activation energy gives an idea of the effect of temperature on flow behaviour during processing. From the analysis of this figure it follows that E_a of PLDA1Mg melt is higher than PLDA melt, indicating that the rheology of composite is more affected by temperature than that of the polymer. PLDA1Mg shows maximum E_a (225 kJ/mol) at 50 s^{-1}. PLDA shows maximum flow activation energy (140 kJ/mol) at 20 s^{-1}. The increment of the E_a of PLDA1Mg with respect to PLDA is represented in terms of percentage in Figure 5.11.

As shear rate increases, the percentage of the flow activation energy increment of PLDA1Mg comparing to PLDA increases as well. It is worth to notice that a reinforcement of only 1% of Mg in PLDA can induce an increment on the flow activation energy of the polymer melt as high as 115% at 10^4 s^{-1}.

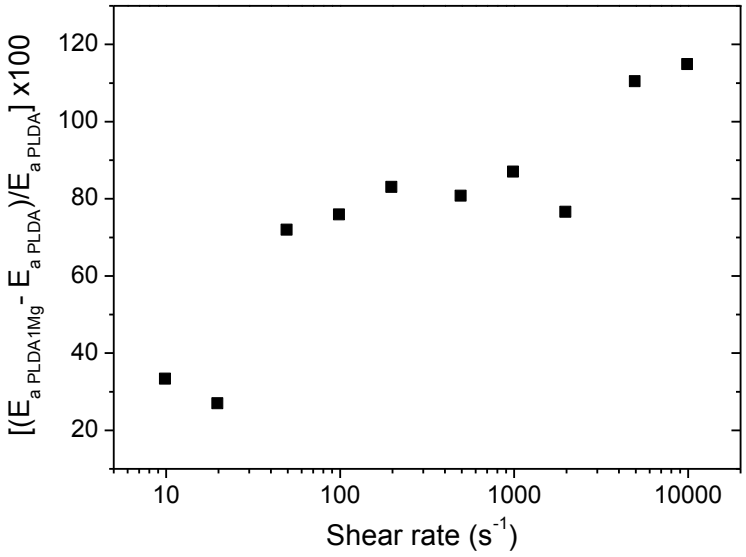

Figure 5.11 Percentage of activation flow energy increment of PLDA1Mg in respect to PLDA

5.3.3.2. Physico-chemical characterization of injected specimens

Macrographs of injected PLDAXMg tensile tests samples are shown in Figure 5.12 and the distribution of Mg particles within the PLDA matrix is pictured in Figure 5.13. It is observed that Mg particles are homogeneously distributed within the polymeric matrix. This implies that the polymer/Mg dried mixture and its further homogenization during injection moulding plasticizing phase is enough to obtain composites with a well distribution of Mg particles.

During processing the molecular structure of the polymeric matrix can change due to the thermo-mechanical degradation inherent to the process, and/or by the addition of Mg particles as explained in Chapter 4 section 4.3.5. Changes of the PLDA chemical structure based on the relative contribution of carbonyl, ester and –OH groups were assessed by ATR-FTIR (Figure 5.14).

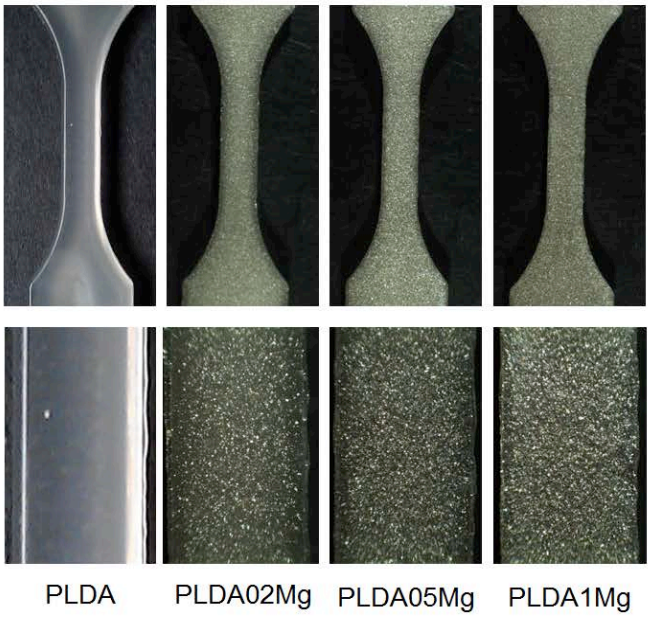

Figure 5.12 Macrographs of injected PLDAXMg dumbbell-shape specimens with X= 0, 0.2, 0.5 and 1 wt.% Mg

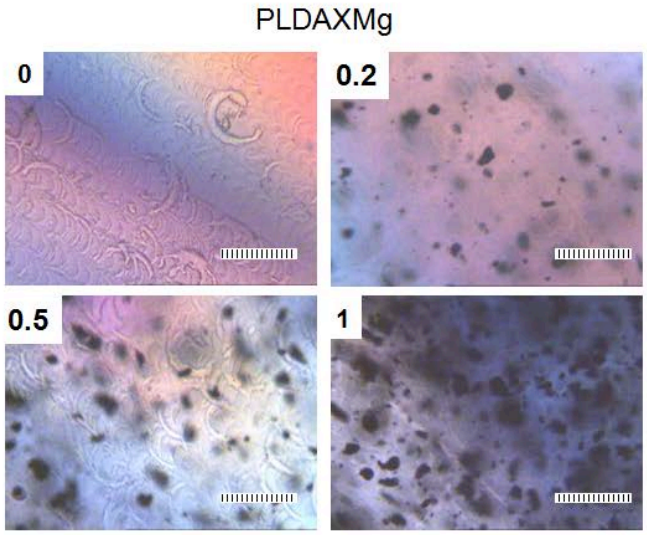

Figure 5.13 Distribution of Mg particles incorporated in a PLDA matrix observed by a polarized light microscope. Injected PLDAXMg specimens with 0, 0.2, 0.5 and 1 wt.% Mg contents. (Scale bar 200 μm)

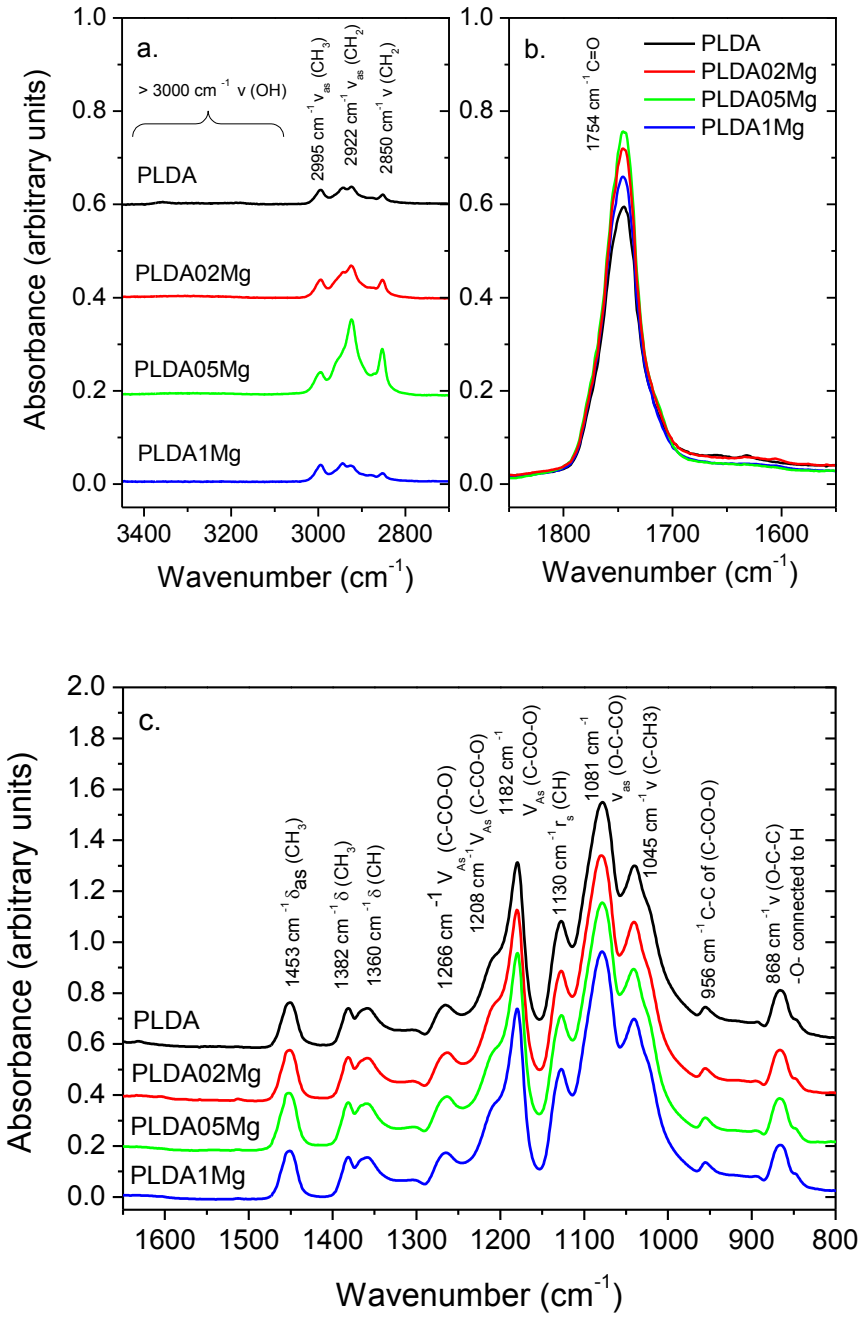

Figure 5.14 ATR – FTIR spectra of injected PLDAXMg specimens with 0, 0.2, 0.5 and 1 wt.% of Mg content

Given that Mg particles could induce the cyclation of the polymer chains, an increase on the relative contribution of the ester and carbonyl groups is expected in the case of thermal degradation occurrence. However, ATR-FTIR spectra of PLDAXMg specimens (Figure 5.14) do

not show remarkable changes of the absorbance intensity of C=O (1754 cm^{-1}), C-CO-O (1182 cm^{-1}) and O-C-CO (1801 cm^{-1}) peaks. The –OH characteristic band (> 3000 cm^{-1}) is absent for all the spectra.

The relative contribution of carbonyl and ester groups is referred to –CH bending at 1360 cm^{-1} and depicted as a function of Mg content in Figure 5.15. Given that no relevant changes or tendencies were evidenced in the evolution of these ratios *vs* the Mg content, it can be deduced that PLDA did not undergo thermal degradation during processing and the effect of Mg particles in the cyclation of the polymer is negligible.

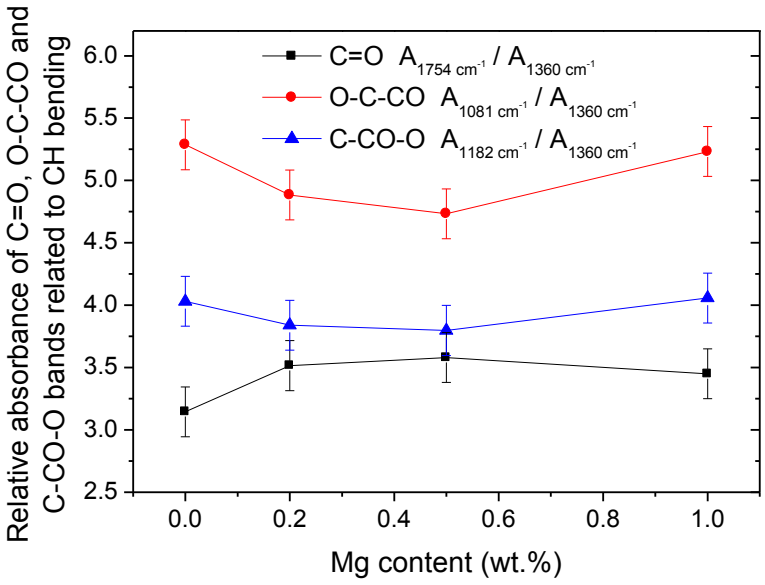

Figure 5.15 Relative contributions of carbonyl and ester groups as a function of Mg content in PLDAXMg composites

Molecular weight estimation using intrinsic viscosity measurements (Figure 5.16) confirms that the effect of processing on the thermal degradation of PLDA is very low. Injection moulding of PLDA causes a reduction of only 8% in the viscosity average molecular weight of the polymer (Table 5.6).

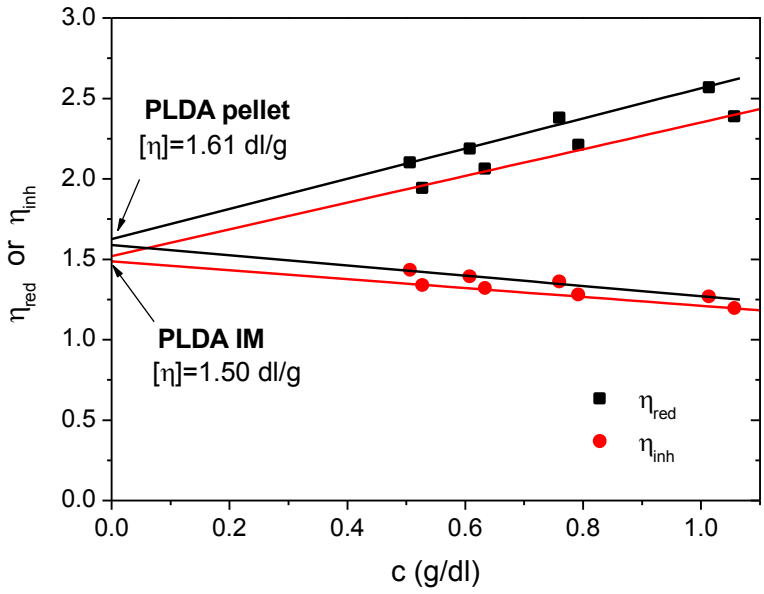

Figure 5.16 Huggins-Kraemer plot to determine the intrinsic viscosity of PLDA and injected PLDA_IM

Table 5.6 Viscosity average molecular weight of PLDA pellet and PLDA_IM

PLDA pellet M_v	PLDA IM M_v	Reduction M_v
103 kDa	94 kDa	8 %

The crystallinity degree of injected specimens was assessed by means of DSC and X-Ray. The first heating (F10) scan (Figure 5.17 F10) and the WAXD patterns of composites (Figure 5.18) are characteristic of materials with a very low crystallinity degree. Thermal properties listed in Table 5.7, indicate that injection moulding produces samples with a crystalline fraction close to 0.1.

DSC analysis shows that T_g does not change with Mg content, except for PLDA reinforced with 1 wt.% of Mg where T_g is shifted to lower temperatures. The cold crystallization temperatures are moved to lower temperatures with increasing Mg content (F10 and CR10F10). This implies that Mg accelerates cold crystallization of PLDA. The change of T_{cc} to higher temperatures in the PLDA1Mg material is related to the formation of percolates in the composite. Therefore, it seems that Mg plays two roles in the polymer matrix: the first one, acting as a nucleating agent to enhance crystallization below the percolation concentration, and the other acting as a barrier to retard crystallization above the percolation concentration. It is seen that the shape and the number of melting peaks depend on the concentration of Mg. PLDA sample evidences a peak

with a small shoulder on the left, and the composites exhibit two melting peaks whose height and distance between them increases with the concentration of Mg. Multiple melting behaviour can be related to the presence of crystals with different crystal forms or different degree of perfection and homogeneity.

During the cooling scan at dynamic conditions (CR10) it is evidenced that PLDA is not able to crystallize at 10 ºC/min, and Mg particles do not seem to have any effect on PLDA cooling behaviour. However, during the second heating (CR10F10) T_{cc} appears at lower temperatures for composites than for PLDA. This indicates that Mg induces the formation of nuclei, either during cooling from the melt or during heating from the glassy state, which favours crystallization and lowers T_{cc}.

The WAXD patterns of PLDAXMg samples fabricated by injection moulding are shown in Figure 5.18. Diffractograms show that injected materials are amorphous. Mg content was estimated from WAXD patterns of injected PLDAXMg specimens. The area under the peak at 36.6º corresponding to (101) reflection gives approximate correlations to the nominal values of Mg content (Figure 5.19). Small divergences between calculated and nominal values were found at 0.2 and 0.5 wt.% Mg contents.

Table 5.7 Thermal properties of PLDAXMg composites reinforced with 0.2, 0.5 and 1 wt.% of Mg particles

F10						
MATERIAL	**T_{m1} (ºC)**	**T_{m2} (ºC)**	**T_g (ºC)**	**T_{cc} (ºC)**	**ΔH (J/g)**	**f_c**
PLDA	154.7	160.3	60	115.2	13.2	0.14
PLDA02Mg	154.3	162.5	60	111.9	6.0	0.06
PLDA05Mg	151.2	161.4	60	107.8	11.8	0.13
PLDA1Mg	150.9	159.6	58	111.1	10.7	0.12
CR10F10						
MATERIAL	**T_{m1} (ºC)**	**T_{m2} (ºC)**	**T_g (ºC)**	**T_{cc} (ºC)**	**ΔH (J/g)**	**f_c**
PLDA	156.5	-	60	130.8	5.8	0.06
PLDA02Mg	154.5	160.7	61	123.9	5.0	0.05
PLDA05Mg	154.2	161.1	60	123.0	4.8	0.05
PLDA1Mg	150.1	157.6	57	123.1	4.8	0.05

Experimental errors: Tm and T_{cc} ± 0.5º C, T_g ± 2º C and f_c ± 0.04

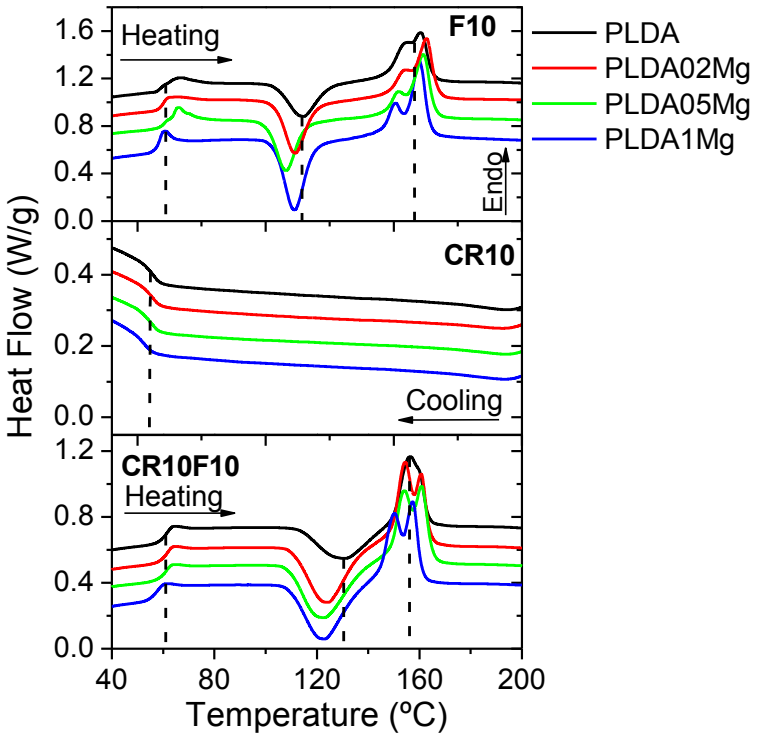

Figure 5.17 DSC of injected PLDAXMg specimens reinforced with 0.2, 0.5 and 1 wt.% of Mg particles

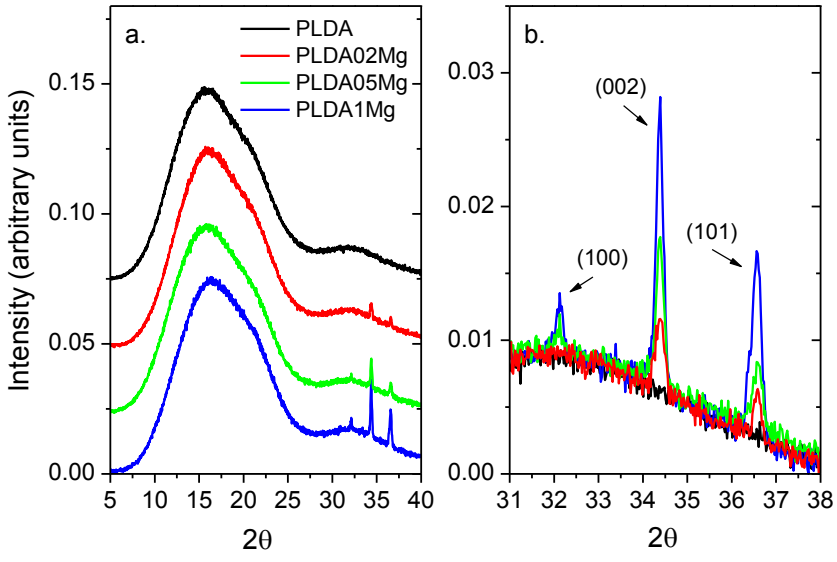

Figure 5.18 WAXD patterns of injected PLDAXMg specimens reinforced with 0.2, 0.5 and 1 wt.% of Mg particles

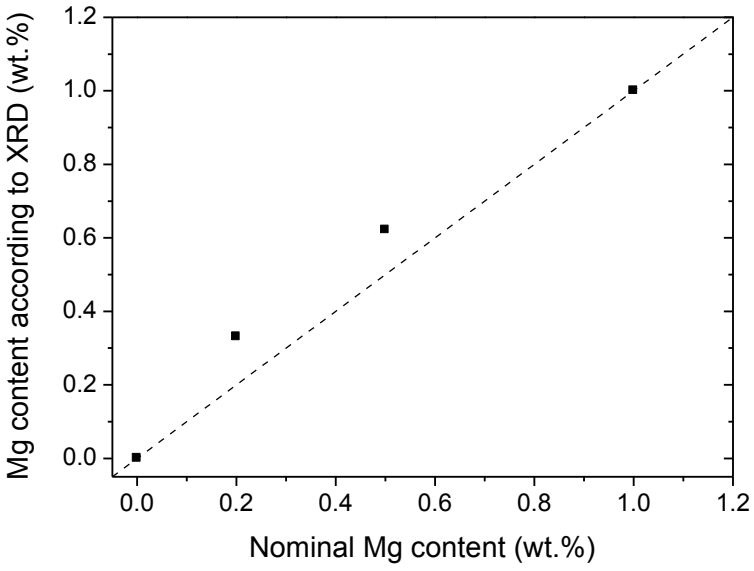

Figure 5.19 Mg content measured by XRD compared to nominal values

5.3.3.3. Mechanical properties

Figure 5.20 shows the stress *vs* strain curves of the uniaxial tensile tests performed to the injected samples. Results of Young´s modulus and tensile strength at yield as a function of Mg content are summarized in Figure 5.21. Reinforcement of PLDA with Mg actually leads to a decrease in Yield strength. The material experiences a change in his tensile behaviour when adding a higher amount of Mg particles. PLDA exhibits a representative curve for ductile materials, whereas PLDA1Mg shows a curve related to brittle materials. Three intrinsic deformation stages can be detected. In the first instance the polymer shows a reversible (visco)-elastic deformation, then, the deformation becomes irreversible and a yield point appears. After the yield point, the stress decrease, being this behaviour referred to as a strain softening. The amount of strain softening decreases with the increment of Mg content. The material becomes more brittle with higher amount of Mg and less tough, as the total area under the curve of the composites is smaller than the area of neat PLDA. With regards to the Young´s modulus, it can be seen that although it is lower than that of PLDA, it slightly increases with increasing the amount of Mg (Figure 5.21).

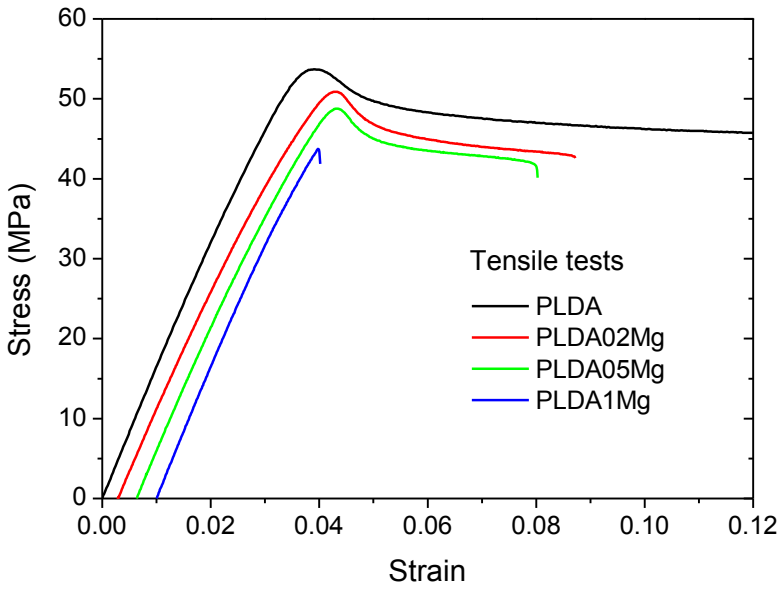

Figure 5.20 Tensile stress *vs* strain curves for PLDA and PLDAXMg composites (curves are shifted for visual clarity)

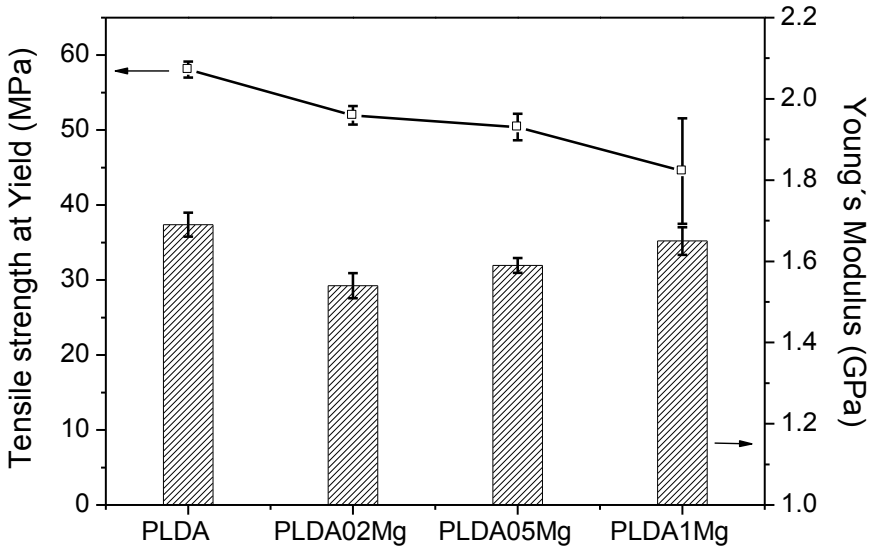

Figure 5.21 Tensile strength and Young´s modulus of PLDAXMg composites as a function of Mg content

Fracture analysis of broken samples at different magnifications (Figure 5.22) clearly shows that PLDA and PLDAXMg composites exhibit a brittle behaviour characterized by the absence of necking, as little or no plastic deformation was involved. Plastic deformation is only evidenced at the fracture surfaces by whitish areas that emerge during tensile deformation over the yield point due to the alignment of the polymer chains. During tensile test, fibrils stretch and cause the alignment of chains; voids are forced to coalesce perpendicular to the applied stress and eventually cause a macroscopic crack that collapses further. The plastically deformed white zone is evident in PLDA but diminishes as the Mg content increases. Imperfections such as pores or microcracks are more common in reinforced materials with 1 wt.% of Mg and their presence induces the decrement of the tensile strength and the increment of the standard deviation of the results.

The compressive mechanical behaviour of PLDAXMg composites is shown in Figure 5.23 and results of yield strength and modulus are summarized in Figure 5.24. Usually, under compression tests higher values of yield strength are obtained when comparing with tensile strength at yield, but the elastic modulus is normally of the same order of magnitude.

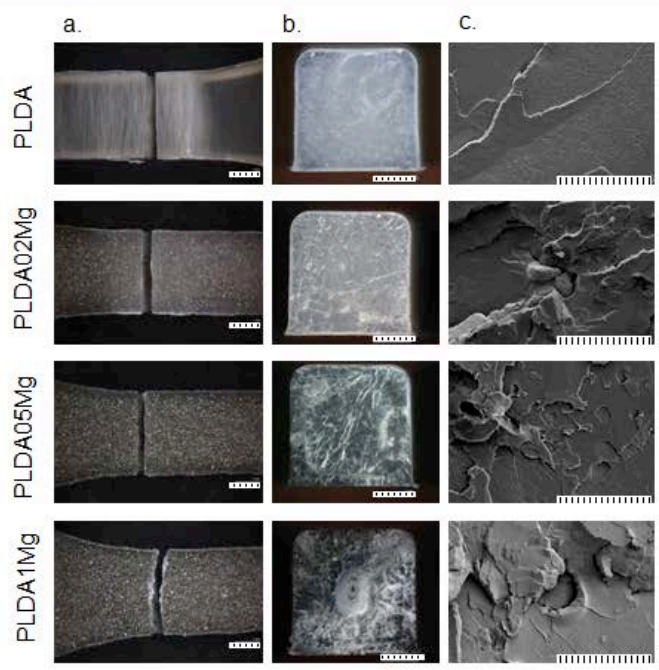

Figure 5.22 PLDAXMg composites fracture (a) and fracture surface by stereoscopic microscope (b) and SEM (scale bar: 1 mm (a,b) and 100 μm (c))

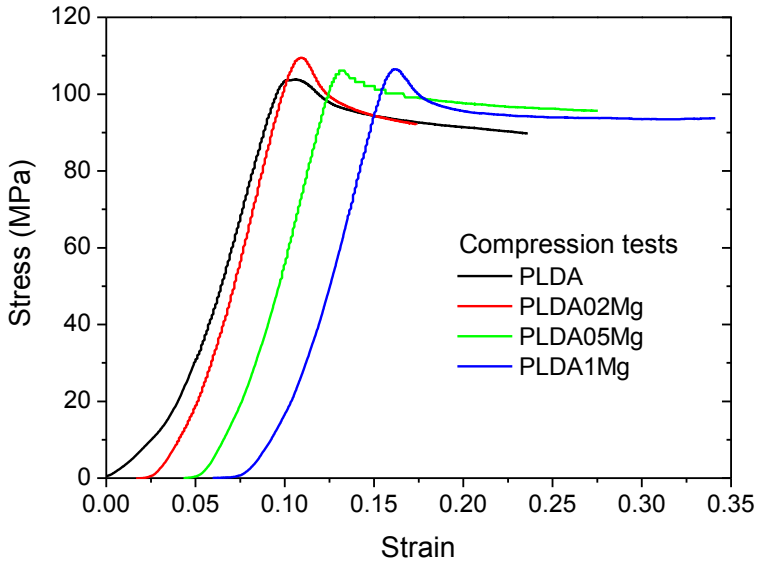

Figure 5.23 Compressive stress *vs* strain curves for PLDAXMg composites with X= 0, 0.2, 0.5 and 1 wt.% of Mg (curves are shifted for visual clarity)

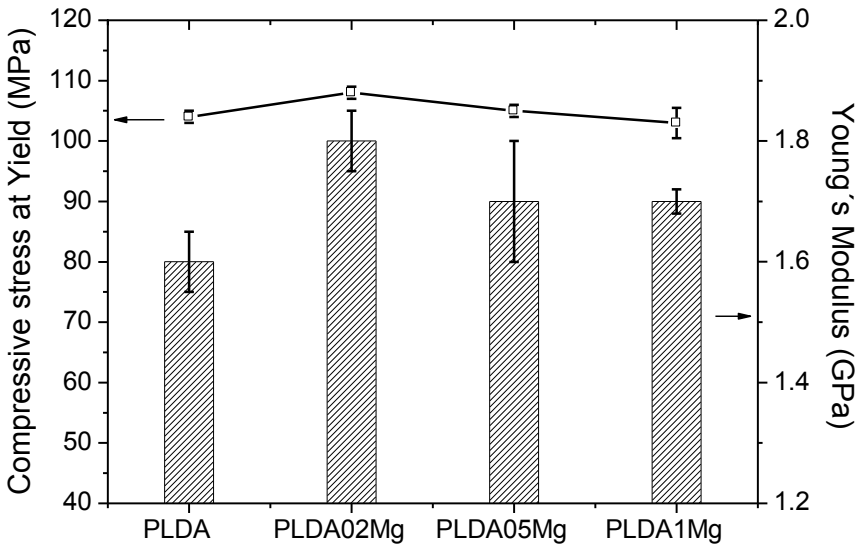

Figure 5.24 Compressive stress at yield and Young´s modulus of PLDAXMg composites as a function of Mg content

Under compression, mechanical properties of composites are better than that of neat PLDA. The best behaviour is detected when the content of Mg is 0.2 wt.%. At higher contents (0.5 and

1 wt.%) composites properties decrease in comparison to PLDA02Mg but still are better than those for neat PLDA. All materials exhibit the following deformation stages: reversible (visco)-elastic deformation, yield stress, strain softening, and constant stress. Curves are representative of ductile materials.

5.3.3.4. Thermal treatment

According to results obtained in Chapter 3, under isothermal crystallization from the glassy state, PLDA IM achieves the highest enthalpy of melting, which is related to the highest crystalline degree, at 125 ºC (Chapter 3 Figure 3.16b). With the aim of studying the effect of crystalline degree on the mechanical performance of PLDA/Mg composites, two opposite conditions were compared, amorphous or as-injected materials (hereafter named as Q samples) and thermally treated materials at 125 ºC ± 1 ºC during one hour (hereafter named as TT samples).

The crystallinity degree that resulted from the thermal treatment was assessed by means of DSC and X-Ray. The first heating scan (Figure 5.25) shows the characteristic thermal behaviour of high crystalline materials, described by the absence of the cold crystallization peak. Thermal properties listed in Table 5.8, indicate that thermal treatment produces samples with a crystalline fraction of around 0.45.

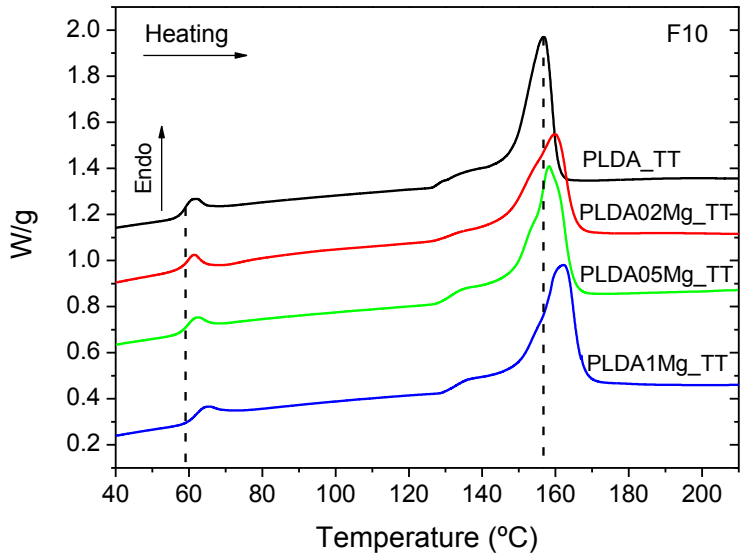

Figure 5.25 DSC of thermal treated PLDAXMg specimens reinforced with X = 0, 0.2, 0.5 and 1 wt.% of Mg particles

Table 5.8 Thermal properties of thermal treated PLDAXMg composites reinforced with 0.2, 0.5 and 1wt.% of Mg particles

	F10				
MATERIAL	**T_m (ºC)**	**T_g (ºC)**	**T_{cc} (ºC)**	**ΔH (J/g)**	**f_c**
PLDA	156.8	59	-	39.51	0.42
PLDA02Mg	160.1	60	-	38.1	0.41
PLDA05Mg	157.9	60	-	42.8	0.46
PLDA1Mg	162.0	62	-	42.1	0.45

Experimental errors: Tm and T_{cc} ± 0.5º C, T_g ± 2º C and f_c ± 0.04

WAXD patterns of PLDAXMg composites show diffractograms of high crystalline materials. Crystalline degree obtained from X-Ray diffraction is very close to the values calculated by means of DSC. X-Ray diffractograms of all samples indicate the presence in all materials of the perfect α-form, characterized by the appearance of two diffractions around 24º and 25º.

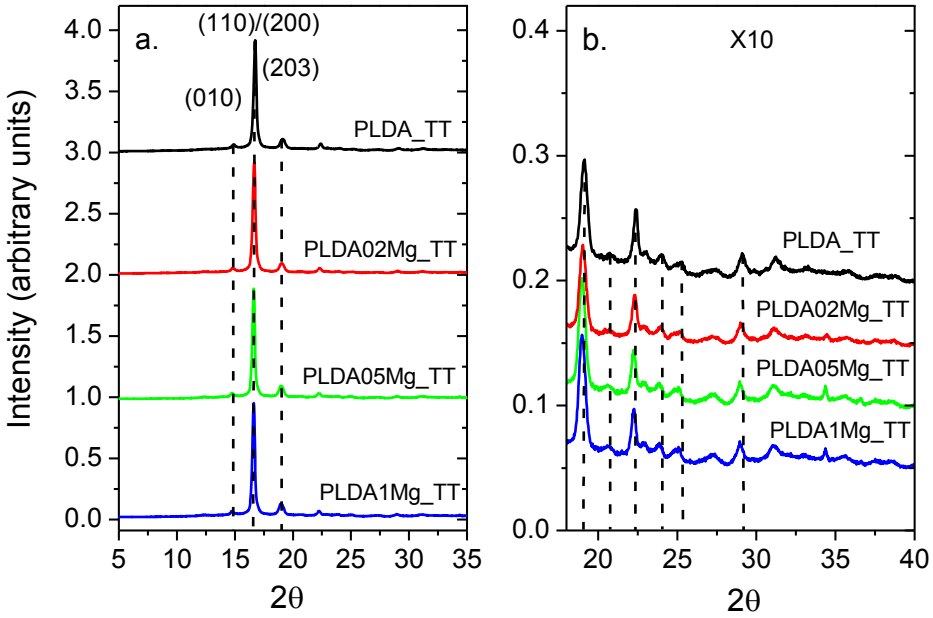

Figure 5.26 WAXD patterns of thermal treated PLDAXMg reinforced with X = 0, 0.2, 0.5 and 1wt.% of Mg particles

The compressive mechanical performance of TT specimens compared to that of quenched specimens without thermal treatment (Q), i.e. amorphous specimens, is shown in Figure 5.27.

Comparison of the results of Young´s modulus and compressive stress at yield as a function of Mg content are summarized in Figure 5.29.

Figure 5.27 depicts basically the behaviour of amorphous composites -materials without thermal treatment and with a crystalline fraction close to 0.1- and high crystalline composites -TT specimens with a crystalline fraction close to 0.45. The stress-strain curves of TT samples differ greatly from the amorphous ones. After the initial elastic response, the curves exhibit yielding and strain softening stage, but TT specimens' compressive behaviour is followed by a linear strain hardening stage with progressing deformation. TT materials show a narrower strain softening stage than that of amorphous materials. The amount of strain softening depends on the thermo-mechanical history of the material. In semi-crystalline polymers strain softening can be reduced or completely removed by a thermal or mechanical treatment [20-23]. Reduction of strain softening can result in a uniform deformation [23] or a more ductile failure [20]. In the case of PLDAXMg composites, the thermal treatment reduces the strain softening, induces a strain hardening with further deformation, and improves the mechanical performance of materials under compression. Due to the crystallization, yield stress increases as well as Young´s modulus. During the compression tests, materials did not fracture, but they plastically deform attaining a barrel shape (Figure 5.28).

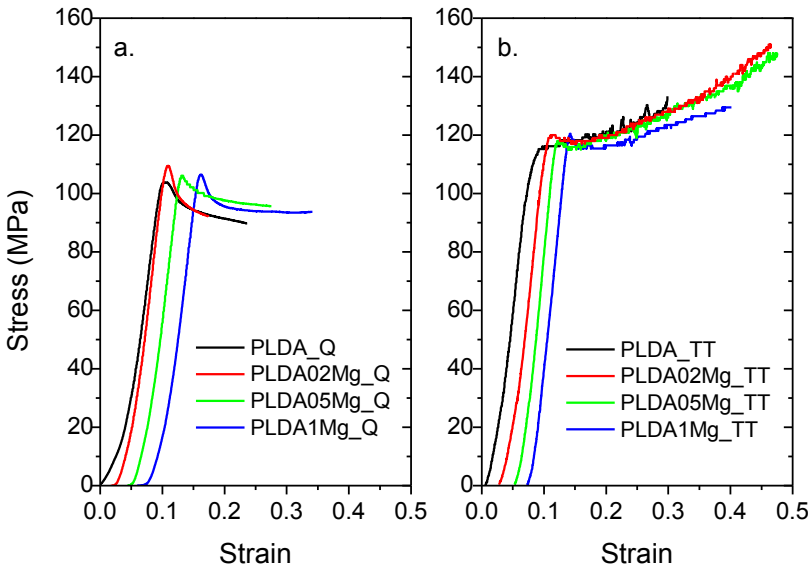

Figure 5.27 Compressive stress *vs* strain curves for PLDAXMg composites without thermal treatment (a) and thermal treated (b) (curves are shifted for visual clarity)

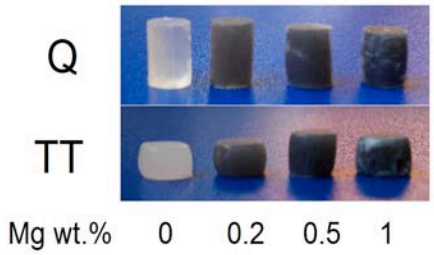

Figure 5.28 Injected PLDAXMg specimens after compression tests with (TT) and without (Q) thermal treatment

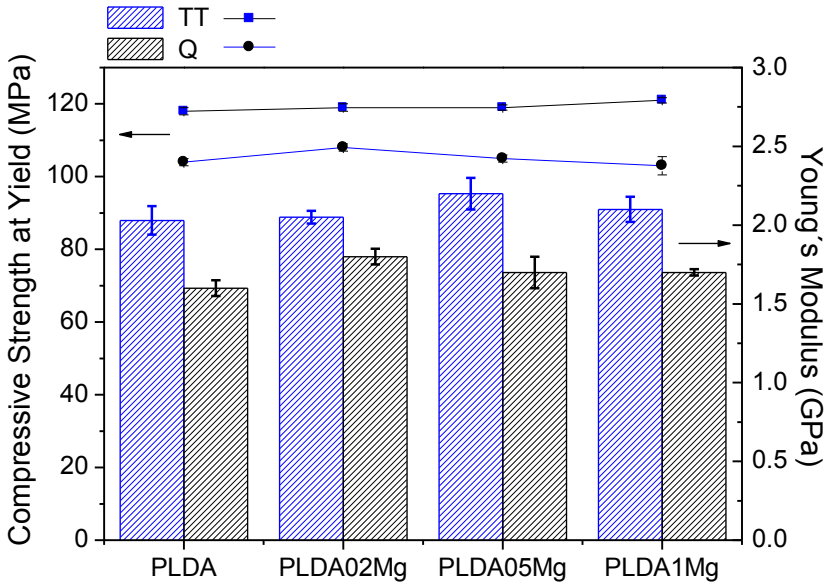

Figure 5.29 Compressive strength at yield and Young´s modulus of PLDAXMg composites with (TT) and without (Q) thermal treatment as a function of Mg content

With the aim of estimating the effect of Mg particles presence on the compressive behaviour of PLDA, classical mechanical models were used with reference to the modulus calculated from stress-strain curves (Figure 5.30). Composite modulus values should fall within a domain defined by Reuss (series arrangement, iso-stress criteria) and Voigt (parallel arrangement, iso-strain criteria) models [12-14].

The particle strengthening factor was found to exhibit a maximum value at 0.2 wt.% Mg content for Q specimens and at 0.5 wt.% Mg content for TT samples. This maximum value lies over the maximum theoretical value predicted by Voigt model, indicating the great reinforcement

enhancement achieved by Mg particles at low mass fractions. Particle strengthening factor at 1 wt.% Mg exhibits the same value for amorphous and thermal treated specimens.

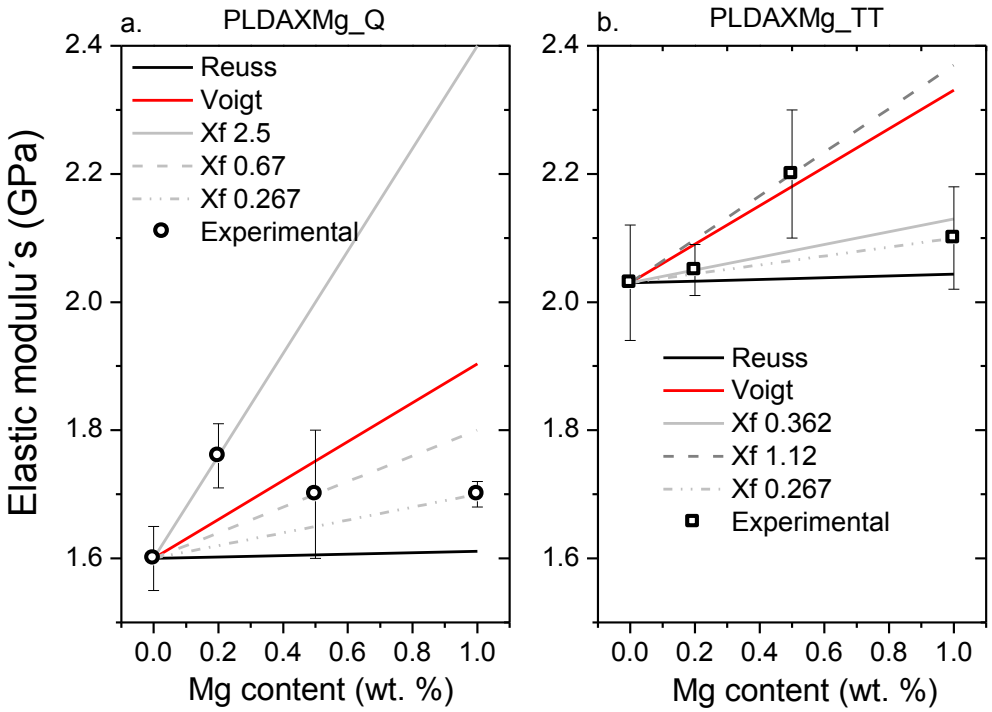

Figure 5.30 Composite experimental elastic modulus evolution with respect to the filler content (points) compared to theoretical approaches (lines)

5.4 Conclusions

PLLA is more sensitive to thermal degradation than PLDA. Processing conditions to which the materials are subjected during injection moulding induce an evident thermal degradation on Poly-L-lactic acid, but hardly induce thermal degradation on Poly-L,D-lactic acid.

Polymer/Mg composites were successfully prepared by injection moulding using PLDA as matrix.

Small weight fractions of Mg particles in PLDA induce important changes in the rheological properties of the polymer. Only 1 wt.% of Mg in PLDA can cause an increment of 115% in the flow activation energy of the polymer.

Given the tremendous changes in polymer rheology induced by Mg particles, only Mg weight fractions of 1% or lower were suitable to be processed by injection moulding using the BOY XS machine.

Composites subjected to tensile tests have a fragile failure and show lower mechanical properties than PLDA. The drop in properties may be due to the presence of pores and microcracks that are more common in Mg-reinforced materials.

PLDAXMg composites show a good mechanical behaviour under compression. It is noted that small additions of Mg particles increases the mechanical properties and has a great strengthening effect. With increasing Mg content the mechanical performance remains better than that of neat PLDA.

The thermal treatment improves the mechanical performance of materials under compression and induces a more ductile and uniform failure.

Additional Comments

The achievements in this research project demonstrating the suitability of processing new polymer/Mg materials by injection moulding caught the attention of the leading European company in biodegradable materials for medical applications Corbion Purac. They have supported our research proposal presented at the National Plan for Scientific Research entitled “Processing and characterization of novel bioresorbable Mg-rich PLA matrix composites for osteosynthesis”.

5.5 References

[1] Oroszlány Á, Kovács JG. Gate type influence on thermal characteristics of injection molded biodegradable interference screws for ACL reconstruction. International Communications in Heat and Mass Transfer 2010;37:766-9.

[2] Drummer D, Cifuentes S, Rietzel D. Suitability of PLA/TCP for fused deposition modeling. Rapid Prototyping Journal 2012;18:500-7.

[3] Lim LT, Auras R, Rubino M. Processing technologies for poly(lactic acid). Progress in Polymer Science 2008;33:820-52.

[4] Auras R, Lim LT, Selke SEM, Tsuji H. Poly-lactic acid. Synthesis, Structures, Properties, and Applications: John Wiley & Sons, Inc. New Jersey; 2010.

[5] Leonard S. Molding of Bioabsorbable Polymers Exposes their Sensitive Side. Medical Product Manufacturing News (MPMN); 2012.

[6] Anderson BJ. Ph D Thesis: Rheology and microstructure of filled polymer melts: University of Illinois at Urbana - Champaign; 2008.

[7] Fan Y, Nishida H, Shirai Y, Tokiwa Y, Endo T. Thermal degradation behaviour of poly(lactic acid) stereocomplex. Polymer Degradation and Stability 2004;86:197-208.

[8] ASTM. D446-12 Standard Specifications and Operating Instructions for Glass Capillary Kinematic Viscometers. West Conshohocken, PA: ASTM International; 2012.

[9] Tsuji H, Ikada Y. Blends of isotactic and atactic poly(lactide)s: 2. Molecular-weight effects of atactic component on crystallization and morphology of equimolar blends from the melt. Polymer 1996;37:595-602.

[10] Perego G, Cella GD, Bastioli C. Effect of molecular weight and crystallinity on poly(lactic acid) mechanical properties. Journal of Applied Polymer Science 1996;59:37-43.

[11] Garlotta D. A Literature Review of Poly(Lactic acid). Journal of Polymers and the Environment 2001;9:63-84.

[12] Callister JW. Materials science and engineering: an introduction. New York: Wiley; 1999.

[13] Fu S-Y, Feng X-Q, Lauke B, Mai Y-W. Effects of particle size, particle/matrix interface adhesion and particle loading on mechanical properties of particulate–polymer composites. Composites Part B: Engineering 2008;39:933-61.

[14] Fu S-Y, Xu G, Mai Y-W. On the elastic modulus of hybrid particle/short-fiber/polymer composites. Composites Part B: Engineering 2002;33:291-9.

[15] Ahmad N. Ph D Thesis: Relationship between rheology and molecular structure of innovative crytalline elastomers. Italy: University of naples; 2013.

[16] Santonja L. Ph D Thesis: Contribution to the study of thermal, biological and photo degradation of polylactide. Valencia, Spain: Universitat Politècnica de València; 2012.

[17] Södergård A, Näsman JH. Stabilization of poly(l-lactide) in the melt. Polymer Degradation and Stability 1994;46:25-30.

[18] Witzke DR. Introduction to Properties, Engineering, and Prospects of Polylactide Polymers: Michigan State University. Department of Chemical Engineering; 1997.
[19] de Jong SJ, Arias ER, Rijkers DTS, van Nostrum CF, Kettenes-van den Bosch JJ, Hennink WE. New insights into the hydrolytic degradation of poly(lactic acid): participation of the alcohol terminus. Polymer 2001;42:2795-802.
[20] Arruda EM, Boyce MC. A three-dimensional constitutive model for the large stretch behavior of rubber elastic materials. Journal of the Mechanics and Physics of Solids 1993;41:389-412.
[21] Boyce MC, Arruda EM. An experimental and anaiytical investigation of the large strain compressive and tensile response of glassy polymers. Polymer Engineering & Science 1990;30:1288-98.
[22] Boyce MC, Parks DM, Argon AS. Large inelastic deformation of glassy polymers. part I: rate dependent constitutive model. Mechanics of Materials 1988;7:15-33.
[23] James HM, Guth E. Theory of the Elastic Properties of Rubber. The Journal of Chemical Physics 1943;11:455-81.

SCALING UP: ACHIEVING A BREAKTHROUGH WITH PROCESSING

CHAPTER 6

"Tell me and I forget. Teach me and I remember. Involve me and I learn"

Benjamin Franklin

Table of contents

6. SCALE UP

6.1. Introduction

Previous chapters (Chapter 4 and 5) have studied the processability of novel PLA/Mg composites by extrusion or injection moulding. While the physico-chemical characterization and the evaluation of mechanical properties led to demonstrate the feasibility of processing these composites at a lab scale, some technical improvements are necessary to bring the production of these novel materials to an industrial scale. In this sense, the main problems encountered during processing at a lab scale must be addressed.

The major drawback when processing composite materials based on biodegradable polymers reinforced with Mg is, undoubtedly, the thermal degradation. Mg particles reduce the thermal stability of the polymeric matrix [1] which could lead to changes in the rheological behaviour and also could impair the final mechanical properties of the composites.

Thermal degradation is primarily responsible for two effects: the deterioration of composites' compression mechanical behaviour with the increasing Mg content in the matrix (Chapter 4) and the drastic changes in the rheology of the material induced by small fractions of Mg (Chapter 5). The consequence of the latter is that only composites with low Mg content ($\leq$ 1 wt.%) could be manufactured by injection moulding. Therefore, it is evidenced the need to reduce thermal degradation during processing in order to obtain composites with higher Mg content without impairing the mechanical behaviour of the material.

This chapter addresses the scaling up of the manufacturing process of PLA/Mg composites by extrusion and compression moulding. The new process reduces the thermal degradation, allows the incorporation of higher Mg content within the polymeric matrix and increases the production efficiency. Materials were manufactured in a mid-size extruder that has similar design attributes to larger extruders used for process development to a pilot-size or small commercial size.

The characterization of PLA/Mg composites was carried out with special emphasis on the study of their mechanical performance at different strain rates. It is essential to study the intrinsic time-dependent performance of materials designed for biodegradable implants in order to predict their behaviour in load bearing situations The principal drawback of polymeric implants in comparison with metallic ones is that, while metals can endure any static load below the yield strength up to relative high temperatures (half the melting temperature), polymers are prone to creep under relative low stresses at ambient temperature. Loosening and failure of an implant is attributed to the molecular mobility that leads to plastic flow due to an external stress [2].

In this chapter, the complex time-dependent behaviour of manufactured composites is analysed thoroughly by means of compression and instrumented indentation tests. The sensitivity of

mechanical properties to strain rate together with the influence of Mg content on the material response have been investigated. Important information regarding the visco-elastic behaviour of PLA/Mg composites is given.

6.2. Materials and methods

6.2.1. Materials

The polylactic acids studied in previous chapters (Chapter 4 and 5) were also used in this one. The poly-L-lactic acid (PLLA) provided by Goodfellow (MFI (210 ºC/2.16 kg) : 35.8 g/ 10 min) and the poly-L,D-lactic acid (PLDA) from Natureworks with a D- isomer content of 4.25% (MFI (210 ºC/2.16 kg) : 35.4 g/ 10 min) were reinforced with irregular shaped Mg particles of 50 µm.

6.2.2. Processing

With the aim of increasing Mg content in the polymeric matrices a new process was designed. The process responds to the need of manufacturing PLLA/Mg and PLDA/Mg composites with higher Mg content continuously and with reproducible results. The processing steps are shown in Figure 6.1 and explained further.

Figure 6.1 Process for manufacturing PLLAXMg and PLDAXMg composites

Polymer pellets are dried under vacuum conditions at 50 ºC during 8 hours to prevent degradation by hydrolysis during extrusion [3]. Pellets are then dry mixed with Mg particles in a beaker. The mixture is carefully fed into a Rondol co-rotating twin-screw continuous extruder (screw diameter 10 mm, L/D ratio 20) where materials are compounded. The cylindrical shape of the screws promotes homogeneous mixing. Extrusion parameters were optimized to prevent thermal degradation and to obtain an adequate viscosity that enabled to roll the material into

filaments, an easy handling and the elimination of defects as sharkskin. Temperatures of the barrel from the nozzle to the feed zone were: 180 ºC / 180 ºC / 160 ºC / 118 ºC. Screw speed was set at 40 rpm. The estimated residence time was 3 minutes. The extruder carefully controls the temperature in each barrel zone. Extruded filaments are then grinded into small pellets in a grinder machine at room temperature. Grinded pellets are moulded into cylinders of 6 mm diameter and 9 mm height using an OPAL 460 automatic hot mounting press. The mould is placed into the press, filled with the pellets, and then the material is heated at 190 ºC during 20 minutes to ensure temperature homogenization. The material is pressed at 130 bars and fast cooled afterwards (quenching treatment Q). Cylinders are taken out from the mould using a special tool designed specifically for that task.

PLLAXMg and PLDAXMg composites with Mg contents of 1, 5, 10 and 15% were manufactured. If higher filler contents are incorporated into the polymers, the torque of the extruder increases substantially and compromises the continuity of the process.

6.2.3. Physico-chemical characterization

6.2.3.1. Viscosity average molecular weight

The effect of processing on the reduction of the molecular weight of both polymers was determined by comparing the average molecular weight of virgin and extruded polymer matrices estimated by means of viscometry. Measurements were carried out by solving the samples in chloroform at 25 ºC, using a Ubbelohde type or suspended level viscometer. The intrinsic viscosity was obtained according to ASTM D446 [4]. The value was used to determine the viscosity average molecular weight with the following Mark-Houwink equations [5] [6]

PLLA $$[\eta] = 4.41 \times 10^{-4} M_v^{0.72}$$ Equation 6.1

PLDA $$[\eta] = 2.21 \times 10^{-4} M_v^{0.77}$$ Equation 6.2

6.2.3.2. Thermal stability

Composites thermal stability and their Mg content were assessed by thermogravimetric measurements using a thermogravimetric analyser (TGA), model TA Q500. Dynamic experiments at 10 ºC/min were carried out under nitrogen atmosphere from 30 ºC to 650 ºC. Three independent experiments were performed for each material using 10 ± 0.5 mg for each sample. The onset temperature (T_o), the temperature of greatest rate of change on the weight loss curve (T_p), the temperature of 50% weight loss (T_{50}) and the final temperature (T_e) were determined. T_o and T_e were calculated by finding the intersection of the baseline and the extrapolated tangent at the inflection point of the weight loss curve. T_p, also known as the

inflection point, was calculated from the first derivative of the weight loss curve. Mg content was determined as the remnant once the experiment has ended, i.e. at 650 ºC.

6.2.3.3. Thermal behaviour

Differential scanning calorimetry was used to determine the crystallinity degree of the materials and their melting behaviour. Experiments were performed in a TA Q100 DSC under nitrogen atmosphere, using 10 ± 0.5 mg of each sample. The experimental design was based on a single heating (F10) from 25 ºC to 220 ºC at 10 ºC /min.

The crystalline fraction was calculated by measuring the enthalpy of melting ΔH_m and cold crystallization ΔH_{cc} from the heating curves using Equation 6.3, where ΔH_m^0 is the enthalpy of 100% crystalline PLLA (93.1 J/g) [3].

$$f_c = \frac{(\Delta H_m - \Delta H_{cc})}{\Delta H_m^0} \qquad \text{Equation 6.3}$$

6.2.4. Mechanical characterization

Composites mechanical behaviour was studied by means of compression and instrumented micro-indentation tests. The dependence of mechanical properties on Mg content and strain rate was thoroughly investigated.

6.2.4.1. Compression tests

Uniaxial compression tests were performed in a universal machine EM2/100/FR-10kN Micro Tests at ambient conditions, using three different strain rates: $0.5x10^{-3}$ s^{-1}, $5x10^{-3}$ s^{-1} and $50x10^{-3}$ s^{-1}. Five cylinders of 6 ± 0.05 mm of diameter and 9 ± 0.05 mm height were tested for each material and strain rate. From the stress-strain curves the Young´s modulus, the yield strength and the strength at the strain-softening plateau were obtained.

6.2.4.2. Instrumented indentation tests

The influence of the strain rate in the hardness and elastic modulus values of PLLA and PLDA samples with different Mg contents, were determined by micro-indentation measurements, using a NanoTest Advantage from Micromaterials at Southampton University in the National Centre for Advanced Tribology (nCATS). Micro-indentations were performed with a Berkovich (three-sided pyramidal) diamond indenter, using a load of 2000 mN for three different loading-unloading rates (25, 50, 200, 400 and 800 mN/s). A maximum hold time of 15 s was applied. In all cases at least 12 indentations have been performed on different regions of the polymer surface.

Hardness, H, and reduced elastic modulus, E_r, have initially been evaluated from the load and depth indentation curves by using the Oliver and Pharr method [7]. Where, H is defined as the mean contact pressure and it is calculated dividing the indenter load, P, by the projected contact area A:

$$H = \frac{P}{A}, \qquad \text{Equation 6.4}$$

Contact area is obtained from contact depth, h_c, calculated from the total penetration depth, h:

$$h_c = h - \varepsilon \frac{P}{S}, \qquad \text{Equation 6.5}$$

where ε is a constant ($\varepsilon \approx 0.75$). The stiffness S, defined as dP/dh, is determined from the unloading curve fitted by a regression function. Known the stiffness and contact area it is possible to determine the reduced modulus E_r:

$$E_r = \frac{\sqrt{\pi}}{2\beta} \frac{S}{\sqrt{A}}, \qquad \text{Equation 6.6}$$

where β is the correction factor for the indenter shape. For a Berkovich indenter, $\beta \approx 1.05$ and A $\approx 24.5 h_c^2$ (The value 24.5 is accurate for a perfect tip; otherwise a calibration function must be used). The reduced modulus, E_r, is related to the elastic modulus, E, and Poisson's ratio, ν, of the specimen and the diamond indenter, E_i and ν_i, as:

$$\frac{1}{E_r} = \frac{\left(1-\nu^2\right)}{E} + \frac{\left(1-\nu_i^2\right)}{E_i} \qquad \text{Equation 6.7}$$

The strain rate, $\dot{\varepsilon}$, is denoted as the imposed rate of deformation during indentation. It is correlated with the displacement rate or the loading rate during indentation body. The strain rate occurs in a direction perpendicular to the surface and may be defined as:

$$\dot{\varepsilon} = k_1 \left[\frac{\dot{h}}{h} \right] \qquad \text{Equation 6.8}$$

where h is the displacement, $\dot{h}$, is the nominal displacement rate and k_1 is a material constant, usually equal to 1 [8, 9]. Therefore, it may be described as the inverse of the time required for the indenter to traverse a contact displacement unit. If the loading rate, $\dot{P}$, is the experimental parameter controlled during the indentation, the strain rate may be expressed as:

$$\dot{\varepsilon} = k_2 \left(\frac{\dot{P}}{P} - \frac{\bar{H}}{H} \dot{h} \right)$$ Equation 6.9

where *P* is the imposed load, *H* is the hardness of the material at a generic depth, $\bar{H}$, is the variation of the hardness with the penetration depth. This equation show that the strain rate varies continuously during the indentation test and decreases from a theoretically infinite value at the first contact to discrete final values which depend on the imposed conditions of maximum load or penetration depth. If $\bar{H} = \partial H / \partial h = 0$, i.e. the hardness of the material, H, does not vary with the penetration depth, it follows that:

$$\dot{\varepsilon} \approx k_2 \left(\frac{\dot{P}}{P} \right)$$ Equation 6.10

where k_2 is equal to 0.5. [8, 9]. According to this the strain rates of the experiments are 6.25×10^{-3} s^{-1}, 12.5×10^{-3} s^{-1}, 50×10^{-3} s^{-1}, 100×10^{-3} s^{-1} and 200×10^{-3} s^{-1}.

Viscoelastic correction

The Oliver and Pharr method is based on the assumption that the contact between the tip and the surface is purely elastic. The elastic modulus of the sample is therefore estimated from the unloading segment of the load-depth curve assuming that the material undergoes purely elastic recovery. However, polymers are viscoelastic solids, and their mechanical characterization using depth-sensing indentation is strongly influenced by viscoelasticity.

A viscoelastic and viscoplastic response is commonly observed in the load-depth curves as an increase in depth during a hold period at maximum load, which is usually termed “creep”. Creep effects during unloading cause the contact stiffness overestimation [10]. In order to avoid this problem, some authors have found that a “hold at peak load” period between loading and unloading in load controlled instrumented indentation measurements facilitates the determination of the instantaneous modulus from the unloading slope [9, 11-13]. Viscosity becomes the dominant factor during unloading either when the hold period before unloading is too short or the unloading rate is too low [10, 14].

Feng and Ngan [14] have presented a scheme by which the creep effects during modulus measurement can be corrected. An accurate estimate for E_r depends on the accurate determination of the elastic contact stiffness S. When creep occurs alongside elastic deformation, this contact stiffness is not the same and must be corrected by the expression

$$\frac{1}{S_c} = \frac{1}{S} + \frac{\dot{h}_h}{\left|\dot{P}\right|} \qquad \text{Equation 6.11}$$

where S_c is the corrected contact stiffness, S is the stiffness calculated from the unloading curve by the Oliver and Pharr method, $\dot{h}_h$ is the indenter displacement rate recorded at the end of the load hold, and $\dot{P}$ the unload rate at the onset of unload. Once the contact stiffness has been corrected, the contact depth can be corrected in order to remove the creep effects in contact-area measurement as well, as suggested by Tang and Ngan [10] .

Creep

Indentation tests offer the possibility to study the dependence of the response of the polymeric material on the load and loading rate. Deformations continue under load, and the indenter continues penetrating the specimen even under constant load. Such viscoelastic or viscoelastic-plastic properties are conventionally analysed as a function of the strain rate applied and in terms of mechanical models which are constructed from a spring and dashpot either in series as Maxwell model, which modelled the steady creep behaviour, or parallel as Kelvin-Voigt model, which modelled the delayed elasticity behaviour, both in a viscoelastic material. The measurement of depth as a function of time (relaxation) during the “hold at peak load” allows the measurement of creep response in visco-elastic materials. Fischer-Cripps [15] work shows how linear spring and dashpot elements can be used to model the viscoelastic response under maximum load of a wide range of materials using the hold period load-displacement data obtained from indentation tests using either spherical or sharp indenters. In the present work, the creep response of PLLA and PLDA with different Mg contents performed with a Berkovich indenter was described by a four-element Maxwell-Voigt model:

$$h^2 = \frac{\pi}{(2\tan^2\theta)}\left(\frac{\pi}{3\sqrt{3}}\right)^{1/2} P_0\left(\frac{1}{E_1^*} + \frac{1}{E_2^*}\left(1-\exp\left(\frac{-t}{\tau_2}\right)\right) + \frac{1}{\eta_1}t\right) \qquad \text{Equation 6.12}$$

where h is the depth, P_o the maximum load and θ is equal to 65.27 º. The symbol E^* is the elastic modulus at plane strain conditions and is defined by Equation 6.13.

$$E^* = \frac{E}{1-\nu^2} \qquad \text{Equation 6.13}$$

Where E is the elastic modulus and *v* is the Poisson´s ratio. The elastic mechanical properties of the material are given in terms of E_1^* and E_2^*. Parameters η_1 and τ_2 are the viscosity and retardation time and quantify the time dependent properties. The Levenberg-Marquardt method

for non-linear least squares curve fitting was used to fit the creep data to Equation 6.12 and find the values for the four unknown parameters. These values were used to estimate $\dot{h}_h$.

6.3. Results and discussion

6.3.1. Effect of processing on viscosity average molecular weight

The comparison of the intrinsic viscosity of PLLA and PLDA pellets to that obtained for processed materials is shown in Figure 6.2. Black squares correspond to the reduced viscosity or Huggins (η_{red} *vs* c) plot and red circles correspond to the inherent viscosity or Kraemer (η_{inh} *vs* c) plot. The lines are the linear extrapolations of Huggins and Kraemer plots to find the inherent viscosity in the intercept, black lines are for virgin materials in their pellet form and red lines are for processed materials.

The viscosity average molecular weight was estimated by the Mark-Houwink equation using the values from Figure 6.2. Results are summarized in Table 6.1. The new extrusion process causes a reduction of M_v of only 6% in PLLA and 8% in PLDA. If the results obtained with this new process are analysed with respect to that obtained with the processes of previous chapters (chapter 4: extrusion at lab scale 7 cc, chapter 5: Injection moulding), it is easily no notice that significant changes in the thermo-mechanical degradation underwent by PLLA were achieved, but the sensitivity of PLDA remains constant. Processing conditions in a lab scale extruder of 7 cc of capacity (chapter 4) lead to a reduction in PLLA viscosity average molecular weight of 20%. PLLA injection moulding (chapter 5) leads to a reduction in M_v of 20%, as well. However, the continuous extrusion in the Rondol extruder generates a shortening in the M_v of only 6%. The thermo-mechanical degradation that PLDA underwent during injection moulding (chapter 5) is the same that the material experiences under continuous extrusion in the Rondol extruder (Mv reduction of 8%).

The process design was determinant for the fabrication of specimens with reduced thermal degradation. The exhaustive control of the temperature by the extruder and the reduction of the residence time of the material at melting temperatures enable the reduction of the thermo-mechanical stress experienced by the material. The cylindrical shape of the screws promotes a homogeneous mixing reducing the mechanical stress on the melt.

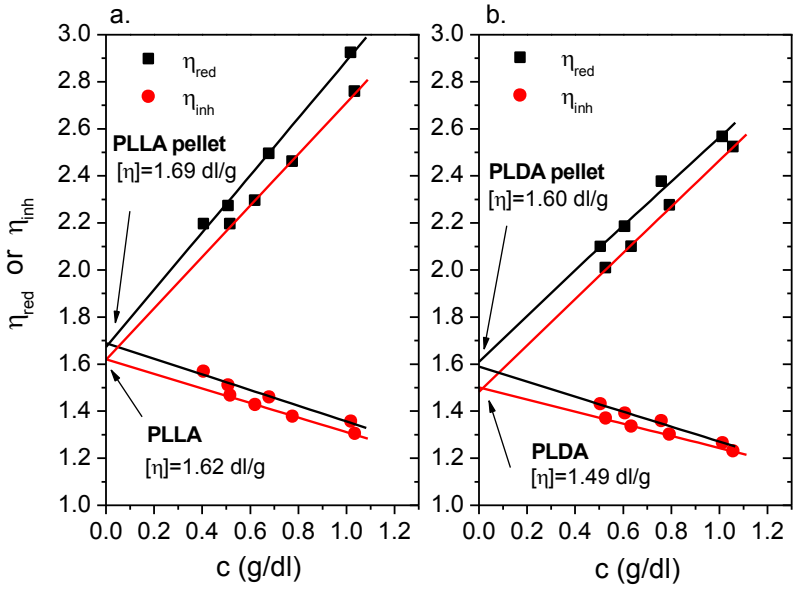

Figure 6.2 Huggins-Kraemer plot to determine the intrinsic viscosity of pellet and processed a. PLLA and b. PLDA

Table 6.1 Viscosity average molecular weight of pellet and processed PLLA and PLDA

	Viscosity (dl/g)	Mv (kDa)	Reduction Mv (%)
PLLA pellet	1.69	95	6.3
PLLA	1.62	89	
PLDA pellet	1.60	103	7.8
PLDA	1.49	95	

6.3.2. Thermal stability

The effect of Mg content on the thermal stability of PLLA and PLDA was evaluated by thermogravimetric analysis. Thermogravimetric curves show that for both polymers (PLLA and PLDA) Mg accelerates their thermal degradation (Figure 6.3). The first derivative of thermogravimetric curves shows the weight loss rate of each material (Figure 6.4).

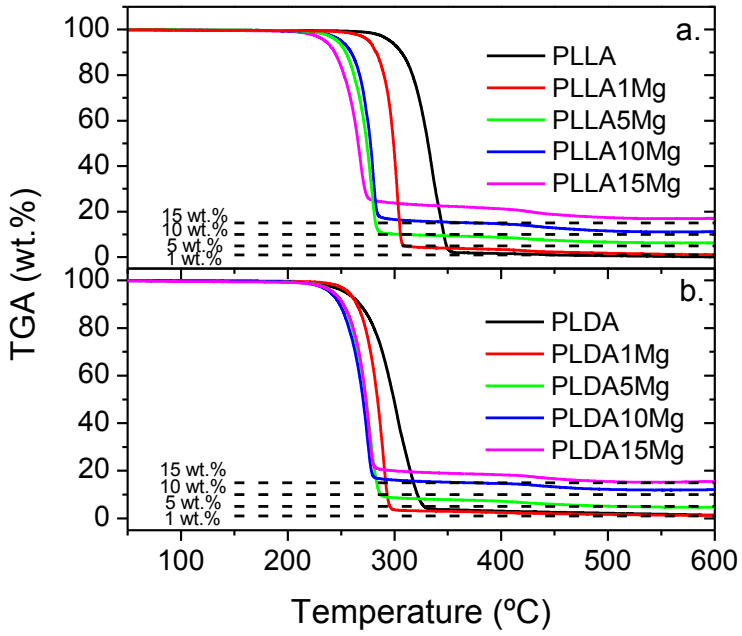

Figure 6.3 Thermogravimetric curves of a. PLLAXMg and b. PLDAXMg composites with X= 0, 1, 5, 10 and 15 wt.% Mg

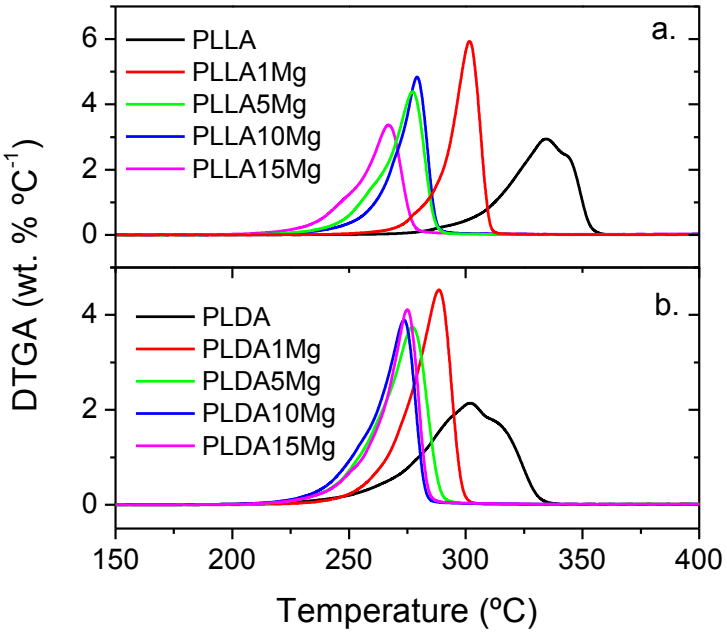

Figure 6.4 First derivative of thermogravimetric curves of a. PLLAXMg and b. PLDAXMg composites with X= 0, 1, 5, 10, 15 wt.% Mg

The peak of the first derivative indicates the point of greatest rate of change on the weight loss curve. DTGA curves clearly show the temperature range over which the loss of mass occurs (Figure 6.4). Composites thermal degradation occurs within a narrower temperature range than polymers thermal degradation. PLLA thermal degradation occurs in the range of 300 – 350 ºC. PLDA starts to degrade earlier and its thermal degradation occurs within 270 – 320 ºC. Thermal degradation of both polymers occurs in a range of 50 ºC, whereas, thermal degradation of composites occurs in a range of 30 ºC.

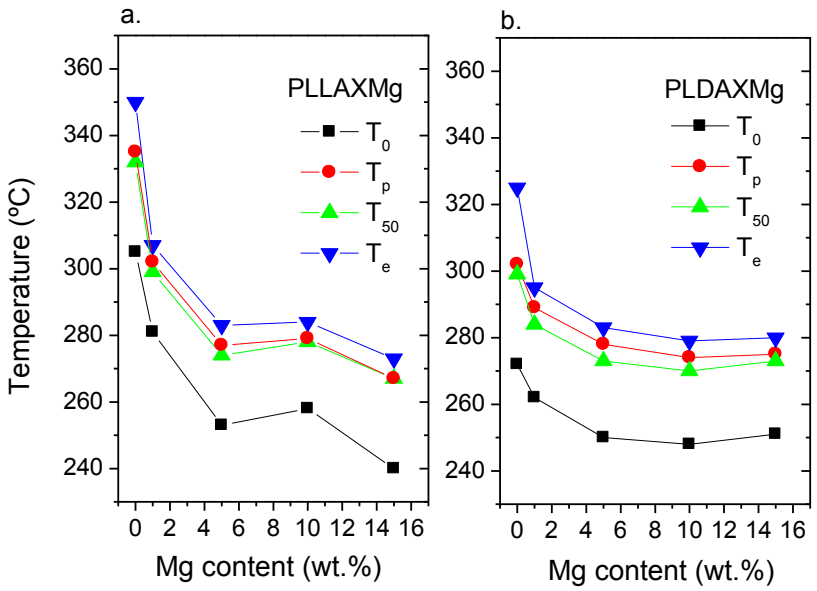

Figure 6.5 Thermal stability parameters of a. PLLAXMg and b. PLDAXMg composites reinforced with X = 0, 1, 5, 10 and 15 wt.% Mg content

Thermal properties - T_0, T_p, T_{50}, T_e - are shifted to lower temperatures with the increment of Mg fraction in the matrix (Figure 6.5). With the addition of Mg, PLDA exhibits a better thermal stability than PLLA. PLLA reduces its onset temperature by 25 ºC with the addition of 1 wt.% of Mg and by 65 ºC with the addition of the highest Mg content (15 wt.%). PLDA reduces its thermal stability by only 20 ºC with the addition of 15 wt.% Mg. PLDA thermal properties reach a plateau with the increment of Mg content. However, PLLA stability temperatures - T_0, T_p, T_{50}, T_e – continue decreasing with the increment of Mg particles fraction.

The greater effect of Mg on PLLA thermal stability in comparison with PLDA can be due to the higher viscosity of PLLA. In chapter 5 the rheological behaviour of both polymeric matrices was studied and it was found that PLLA exhibits a considerably higher complex viscosity than PLDA (section 5.3.1 Figure 5.3). Higher viscosity implies higher shear during the manufacturing

process in the presence of Mg particles, which results in a higher thermal degradation, as evidenced by a lower onset temperature in the characterization by thermogravimetry of composites.

In order to determine the actual Mg content in the composites and to study the homogeneity of Mg dispersion within the polymeric matrices, thermogravimetric experiments were performed in triplicate, and the inorganic content (i.e. ash) quantified for each case. Figure 6.6 compares the Mg content obtained from TGA and the nominal Mg content. The plot presents average values of the three experiments performed for each material, with their respective standard deviation. Mg content according to TGA is in good agreement with the nominal values. Standard deviations are very small, indicating that Mg particles are well distributed within PLLAXMg and PLDAXMg composites. This is also demonstrated by the optical microscopy pictures of composites cross sections (Figure 6.7), where a homogeneous dispersion of particles is evidenced for all the Mg contents.

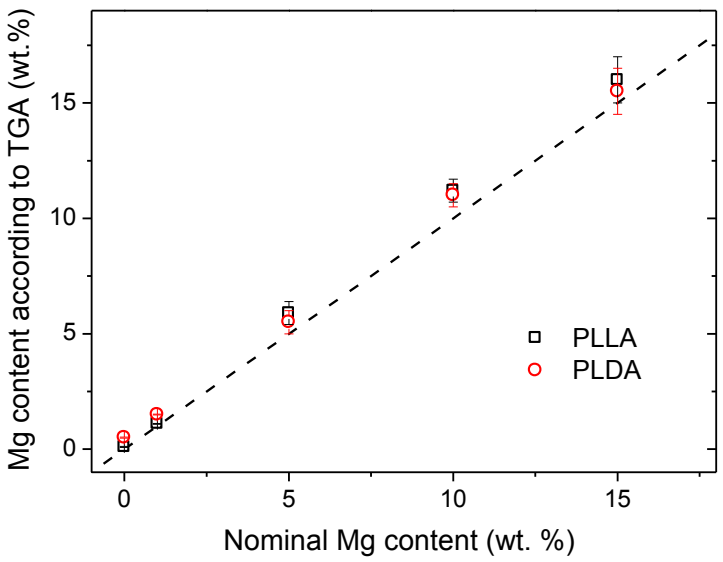

Figure 6.6 Mg content of PLLAXMg and PLDAXMg composites according to thermogravimetric analysis

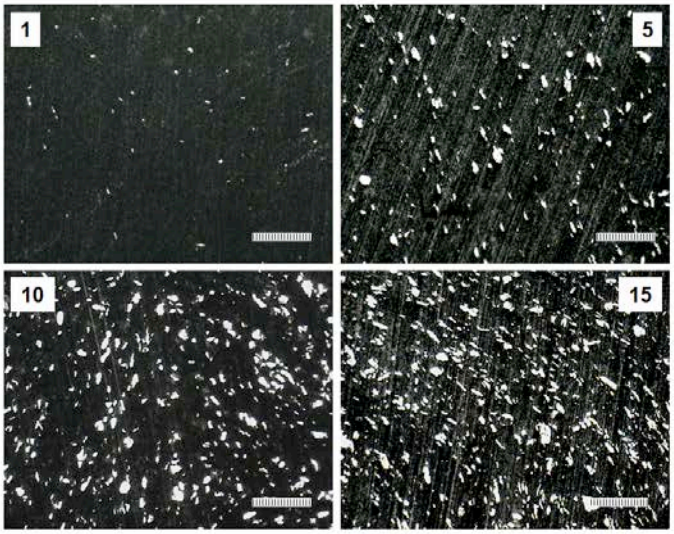

Figure 6.7 Distribution of Mg particles incorporated in a PLDA matrix observed by optical microscopy. PLDAXMg specimens with 1, 5, 10 and 15 wt.% Mg contents. (Scale bar 200 μm)

6.3.3. Thermal behaviour

Differential scanning calorimetric curves of materials moulded under the quenching treatment (Q) are characteristic of amorphous materials (Figure 6.8). Thermal properties are summarized in Table 6.2 for PLLAXMg composites and in Table 6.3 for PLDAXMg composites. According to these tables, crystalline fraction of the specimens is very low; it ranges between 0.09 and 0.18 for PLLAXMg, and between 0.05 and 0.15 for PLDAXMg composites.

Plots exhibit first a glass transition at T_g, then an exothermic phase transition due to cold crystallization at T_{cc} and finally an endothermic transition due to polymer melting at T_m. PLLA and PLDA glass transition occurs at similar T_g (~ 60 ºC ± 2 ºC). For both polymers, T_g is shifted towards higher temperatures with the increment of Mg content. PLLA starts forming crystals during heating at lower temperatures than PLDA. Cold crystallization occurs at ~ 100 ºC in PLLA but at ~ 113 ºC in PLDA. Adding Mg content to PLLA increases always T_{cc}. However, only greater or equal to 10 wt.% Mg content have the same effect in PLDA. Lower contents of Mg (1 and 5 wt.%) in PLDA decrease T_{cc} slightly.

Prior to the dominant melting peak of PLLA appears a small exothermic peak that becomes smaller with the increment of Mg in the polymeric matrix. The exothermic peak could correspond to the transformation of α'-form crystals into their α-form counterparts as explained in chapter 3 (section 3.3.2.2) [16]. T_m decreases slightly with the increment of Mg content.

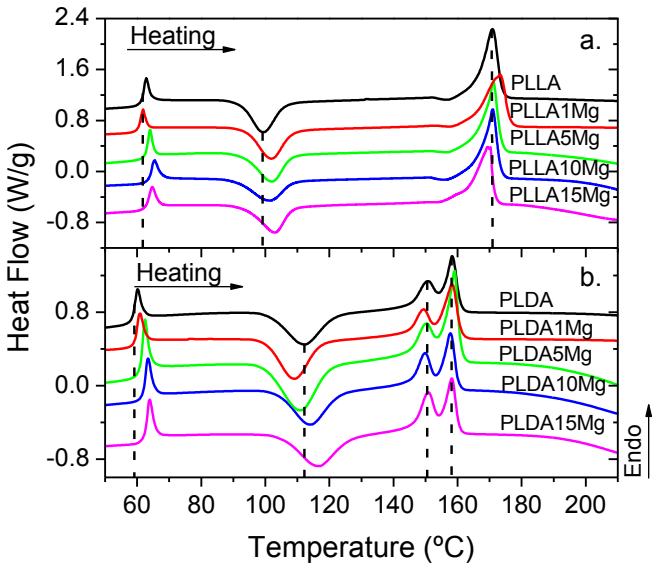

Figure 6.8 Differential scanning calorimetry for the first melting of PLLAXMg and PLDAXMg composites reinforced with X = 0, 1, 5, 10 and 15 wt.% of Mg particles quenched from the melt at 10 ºC/min

Table 6.2 Thermal properties of PLLAXMg composites reinforced with X= 0, 1, 5, 10 and 15 wt.% of Mg particles for the first melting

F10					
MATERIAL	**T_m (ºC)**	**T_g (ºC)**	**T_{cc} (ºC)**	**ΔH (J/g)**	**f_c**
PLLA	171.0	61	99.5	16.8	0.18
PLLA1Mg	173.3	60	101.9	8.6	0.09
PLLA5Mg	171.2	62	101.9	13.4	0.14
PLLA10Mg	170.9	63	101.3	10.0	0.11
PLLA15Mg	170.1	62	103.1	14.6	0.15

Experimental errors: T_m and T_{cc} ± 0.5 ºC, T_g ± 2 ºC and f_c ± 0.04

Table 6.3 Thermal properties of PLDAXMg composites reinforced with X= 0, 1, 5, 10 and 15 wt.% of Mg particles for the first melting

	F10					
MATERIAL	$T_{m\,1}$ (ºC)	$T_{m\,2}$ (ºC)	T_g (ºC)	T_{cc} (ºC)	ΔH (J/g)	f_c
PLDA	151.1	158.2	58	112.2	6.7	0.07
PLDA1Mg	149.2	157.9	58.59	108.9	4.5	0.05
PLDA5Mg	149.9	159.2	60.18	110.8	14.8	0.15
PLDA10Mg	150.0	158.3	60.99	114.0	7.2	0.08
PLDA15Mg	151.0	158.9	61.45	116.8	3.3	0.04

Experimental errors: Tm and T_{cc} ± 0.5 ºC, T_g ± 2 ºC and f_c ± 0.04

A multiple melting behaviour is evidenced in PLDAXMg composites. Double melting endotherms were detected, the first at low temperature (T_{m1}) around 150 ºC and the second at higher temperature (T_{m2}) around 158 ºC (Table 6.3). The multiple melting peaks are indicative of melt-recrystallization behaviour (Chapter 3 section 3.3.2.2). From DSC curves it seems that Mg particles do not have any effect on PLDA melting peaks.

DSC curves also show an evident aging peak for both types of materials (composites based on PLLA and based on PLDA). Polylactic acid aging occurs relatively very fast, this fact was considered for the study of the mechanical properties of the materials. All specimens were allowed to age enough time, in order for the mechanical properties to be no longer dependent on aging time.

6.3.4. Mechanical properties

6.3.4.1. Compression tests

Compressive mechanical behaviour as a function of strain rate is shown in Figure 6.9 for PLLAXMg and Figure 6.10 for PLDAXMg. Results of Young´s modulus, compressive yield strength, and compressive strength at plateau are summarized in Figures 6.11 to 6.13. During compression testing all materials at the whole range of strain rates deformed in a ductile manner. They acquired a barrel shape deformation and did not fracture.

All of the curves present the typical features of amorphous polymers response to uniaxial compression (Figures 6.9 and 6.10): Linear stress growth in the low strain elastic regime, then stress increases more slowly during a non-linear transition to a local stress maximum known as “yield peak” (reached here at a 0.06 strain), followed by a “strain softening” regime characterized by a drop of the stress with strain that leads to a plastic flow regime characterized

by a constant plateau stress and at large enough deformation the material experiences “strain hardening” as stress increases strongly due to chain deformation [17].

In general, for a given material condition Young´s modulus, E_c, and compressive strength at yield, σ_c, are found to increase with the strain rate (Figures 6.11 – 6.12), as expected. The PLLA Young´s modulus initially decreases with 1 wt.% Mg content, which could be attributed to the lower crystalline fraction (Table 6.2), but then, E_c increases with further reinforcement content reaching values close to neat PLLA Young´s modulus or higher. The material with the highest Young´s modulus is PLLA15Mg. PLDAXMg composites exhibit a higher Young´s modulus than PLDA. Increasing Mg content in PLDA matrix, improves PLDA Young´s modulus up to a particle content of 10 wt.%. At 15 wt.% of Mg, Young´s modulus of the composite decreases but maintains higher values than that of neat PLDA (Figure 6.11). The highest Young´s modulus is featured by PLDA10Mg.

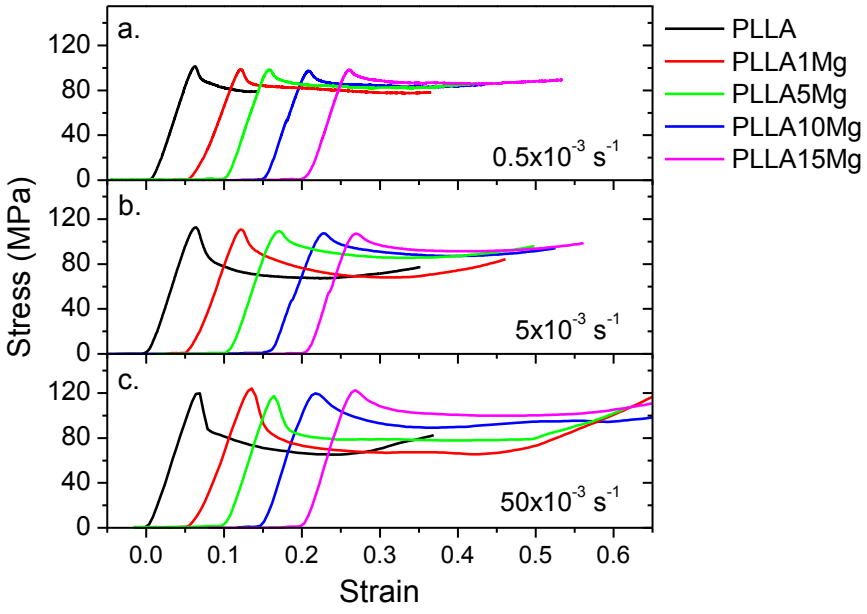

Figure 6.9 Compressive stress *vs* strain curves for PLLAXMg composites at different strain rates

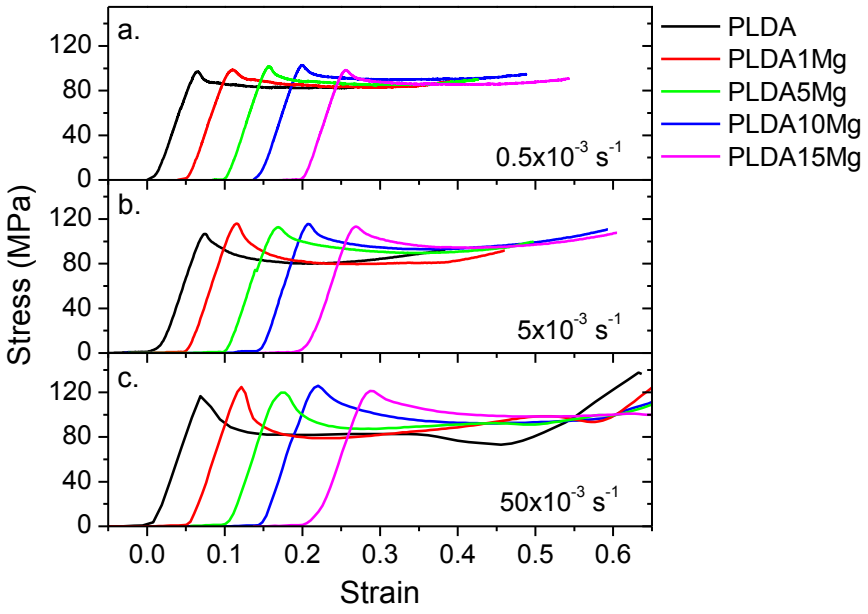

Figure 6.10 Compressive stress *vs* strain curves for PLDAXMg composites at different strain rates

Although PLLA and PLDA have similar molecular weights (89 kDa and 95 kDa respectively), neat PLLA Young´s modulus is higher than that of neat PLDA (Figure 6.3). This behaviour is related to the stereoregularity of PLLA's chains which gives better mechanical properties to the polymer. However, the effect of Mg reinforcement on PLLA is lower than that for PLDA, as E_c of PLDAXMg composites reaches or surpasses the values of the Young´s modulus of PLLAXMg composites.

Values of E_c and σ_c plotted versus the applied strain rate result in a semi-logarithmic relationship with a slope equal to the values that appear for PLLAXMg and PLDAXMg in Table 6.4 for E_c and Table 6.5 for σ_c. Mg reinforcement has a clear effect on Young´s modulus of both polymeric matrices, being this effect more evident with increasing strain rate. The dependence of E with strain rate (slope) is stronger for composites than for neat polymers. PLDA exhibit larger rate dependence than PLLA as well as its composites (Table 6.4).

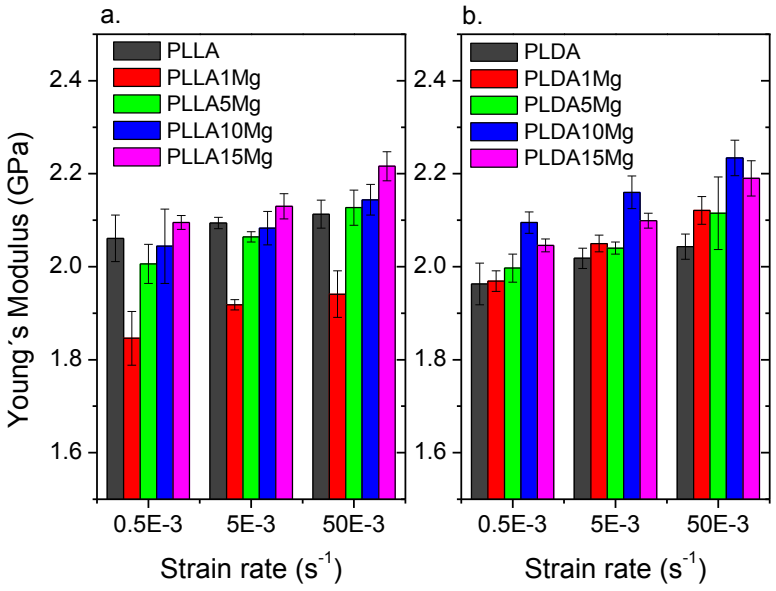

Figure 6.11 Compressive Young´s modulus as a function of Mg content and strain rate for a. PLLAXMg and b. PLDAXMg composites.

Table 6.4 Relationship of Young's modulus with strain rate of PLLAXMg and PLDAXMg composites determined by the slope of the Figure 6.11 in semi-logarithmic scale

Material	E_c/strain rate (GPa/decade)	Material	E_c/strain rate (GPa/decade)
PLLA	0.026 ± 0.004	**PLDA**	0.040 ± 0.009
PLLA1Mg	0.047 ± 0.014	**PLDA1Mg**	0.076 ± 0.003
PLLA5Mg	0.061 ± 0.001	**PLDA5Mg**	0.059 ± 0.009
PLLA10Mg	0.050 ± 0.006	**PLDA10Mg**	0.069 ± 0.003
PLLA15Mg	0.061 ± 0.015	**PLDA15Mg**	0.072 ± 0.011

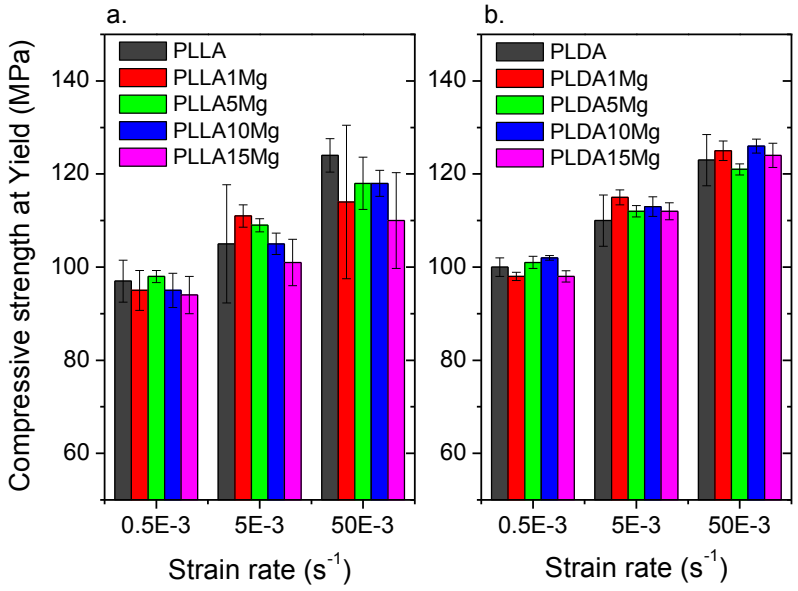

Figure 6.12 Compressive strength at yield as a function of Mg content and strain rate for a. PLLAXMg and b. PLDAXMg composites.

Table 6.5 Relationship of compressive strength at yield with strain rate of PLLAXMg and PLDAXMg composites determined by the slope of the Figure 6.12 in semi-logarithmic scale

Material	σ_c /strain rate (MPa/decade)	Material	σ_c /strain rate (MPa/decade)
PLLA	13.6 ± 3	**PLDA**	11.2 ± 3
PLLA1Mg	14.8 ± 5	**PLDA1Mg**	14.3 ± 1
PLLA5Mg	10.7 ± 2	**PLDA5Mg**	10.0 ± 1
PLLA10Mg	11.7 ± 2	**PLDA10Mg**	11.9 ± 1
PLLA15Mg	8.0 ± 5	**PLDA15Mg**	13.2 ± 1

Regarding the effect of Mg on the compressive strength at yield, it seems that Mg particles do not play any role. The yield stress of composites is the same as the yield stress of the neat polymers at the three strain rates studied. The increment of Mg content does not modify the values of the compressive strength (Figure 6.12) nor its dependence on strain rate (Table 6.5). The value obtained for PLLA yield stress dependence on strain rate (σ_c/strain rate = 13.56 ± 2.88 MPa/decade) is in good agreement with Smit *et al.* findings (14 MPa/decade) [2]. Smit *et al.* studied the time-dependent behaviour of several polylactides by means of compression tests at different strain rates and long-term experiments under static compression or dynamic loading

regime. They found the same rate dependence of polylactides by both types of experiments (14 MPa/decade) and correlate the results obtained by compression with the time-dependent failure of the material. They emphasize that polylactides failures are related to the long-term performance under static loading conditions, a phenomenon that finds its origin in stress-activated molecular mobility leading to plastic flow.

In the plastic flow regime, after the yield point, reinforcing particles of Mg improve the response of the material and modify the mechanical behaviour. It is observed that the greater amount of Mg, the greater compressive strength at the plateau (Figure 6.13). The material has a greater resistance to flow with the increment of Mg content. This plateau stress increases with increasing strain rate for materials with Mg content higher or equal to 5 wt.%. The behaviour of the materials with 1 wt.% of Mg and without reinforcement is different. In these cases the resistance to flow decreases with increasing strain rate.

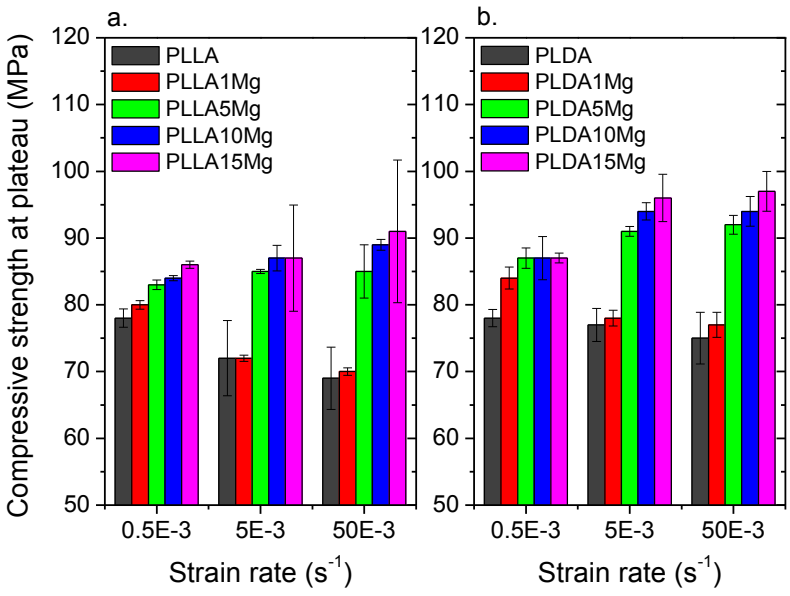

Figure 6.13 Compressive strength at plateau as a function of Mg content and strain rate for a. PLLAXMg and b. PLDAXMg composites.

The strain softening amplitude (SSA) is known as the "stress overshoot" or the difference between the yield stress and the stress at plateau [18]. Figure 6.14 shows the effect of strain rate and Mg content on SSA. It is observed that SSA grows with the strain rate and that Mg particles have a great influence on its magnitude. The amplitude of the strain softening decreases with increasing amount of Mg particles within the polymeric matrix. This occurs both for composite materials based on PLLA and those based on PLDA.

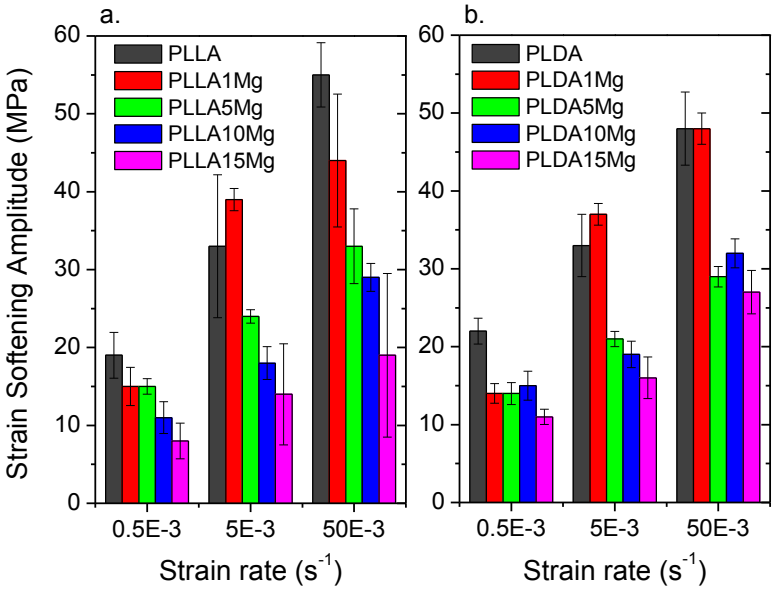

Figure 6.14 Strain softening amplitude as a function of Mg content and strain rate for a. PLLAXMg and b. PLDAXMg composites.

The first part of compressive stress-strain curves (elastic deformation) is controlled by the secondary interactions between chains; the mechanical response in this regime depends on thermal history. Then, material reaches the yield point, or the point where polymer chains mobility is induced by the stress. Beyond that point the stretching of the entangled network instead of thermal history controls the response of the material. The strain softening amplitude is, therefore, an intrinsic property [17, 19].

The balance between strain softening and hardening determines the toughness of a material. Experimental observations have shown that a change in softening can have dramatic effects on the macroscopic behaviour of a polymer [20]. Materials with strong softening and weak hardening behave brittle, and materials with weak softening and strong hardening tough [19]. Decreasing the amount of softening can induce a more uniform and ductile deformation [20, 21]. It has been demonstrated that strain softening can be reduced or completely removed by thermal or mechanical pre-treatments [21-23]. In this research Mg micro-particles were found to reduce PLLA and PLDA strain softening amplitude. Particles impede the flow of polymeric chains during the post-yield regime. This means that the higher the content of Mg in the polymer, the higher the impediment of chains to flow. Therefore the flow resistance increases with increasing Mg fraction in the composite. The increment of compression strength at plateau and the reduction of the strain softening amplitude lead to larger areas under the stress-strain

curve, which implies an increment in material toughness. It can be concluded that the reduction of strain softening induced by Mg particles fraction in PLLA and PLDA have a toughening effect on both polymeric matrices improving their energy storage under deformation.

6.3.4.2. Indentation Tests

Representative load-displacement curves for micro-indentation tests of PLLAXMg and PLDAXMg composites at different strain rates are shown in Figure 6.15. Curves show first the increment of depth with increasing load during the loading step, then a determined load (2 N) is achieved and the deformation of the material continues at that constant load during the holding time (15 s). This plateau shows the creep behaviour of the materials. After the holding time the unloading phase takes place. The contact depth and the maximum depth decrease with increasing strain rate and Mg content, this leads to curves shift to lower displacements.

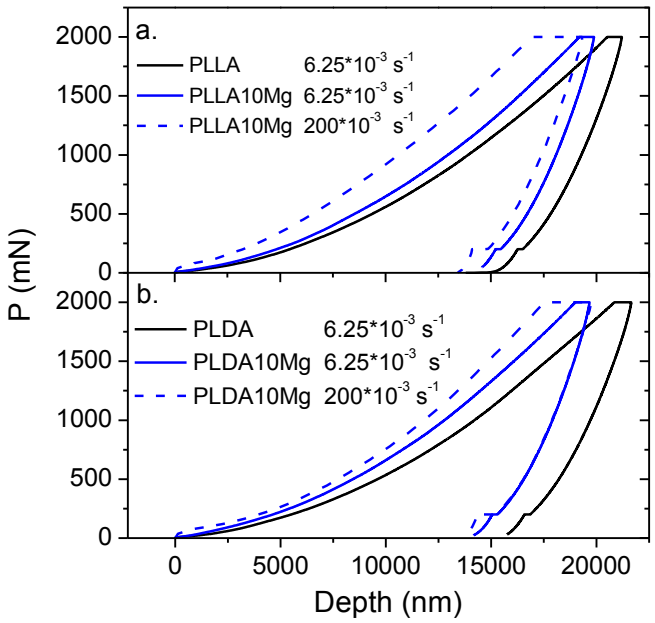

Figure 6.15 Load – displacement indentation curves for a. PLLA and PLLA10Mg and b. PLDA and PLDA10Mg at different strain rates

The creep behaviour dependence of PLLA and PLDA on strain rate and Mg content was also studied by means of micro-indentation. The deformation of the unreinforced materials and composites with a 10 wt.% Mg content at different strain rates for a hold period of 15 s is pictured in Figure 6.16. The curves with open symbols are the experimental data, and the lines represent a non linear least squares fitting to a four element combined Maxwell-Voigt model.

The model provides a good fit for creep results and leads to the values for the elastic constants (E_1 and E_2) and time-dependent properties (η_1 and τ_2) that are resumed in Table 6.6.

Creep curves show two stages: the first consists in a fast increment of deformation with time, and the second consists in a slowdown of the deformation rate until a steady state of constant deformation rate is reached. The secondary steady state is reached by the experiments performed at the fastest strain rate. The experiments performed at $6.25x10^{-3}$ s^{-1} do not reach the secondary state and would need more holding time to reach the steady state.

It seems that Mg particles do not have any influence on the creep behavior of PLLA or PLDA at low strain rates. However at $200x10^{-3}$ s^{-1} the creep curves of the materials reinforced with 10 wt.% of Mg reach lower depth Figure 6.16. This implies that Mg reinforcement restrains chain mobility during creep at constant load.

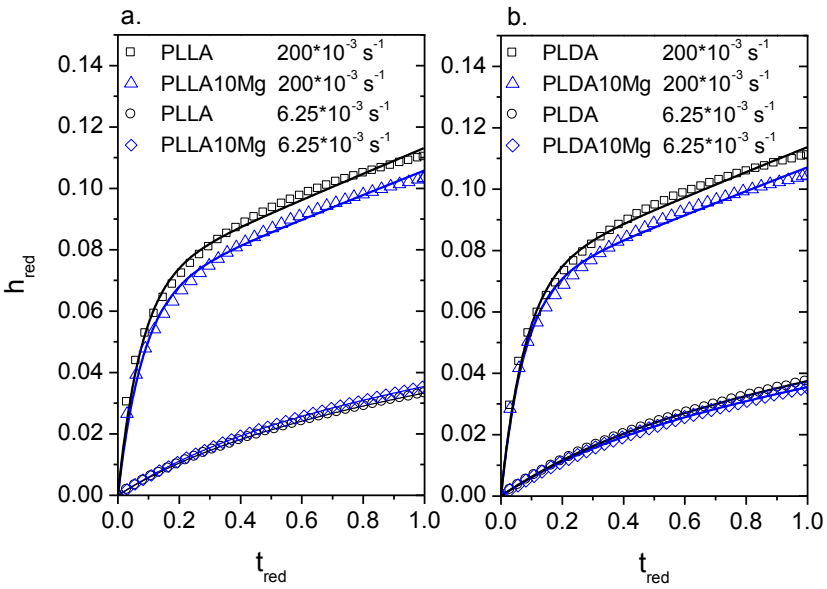

Figure 6.16 Creep response of polymers and composites with 10 wt.% Mg content (t_{red} represents the ratio of the creep time to the load holding time and h_{red} the fractional creep indentation). Open points show experimental results and the solid line the Maxwell-Voigt model fit.

The retardation time τ_2 decreases with increasing strain rate and do not change with the addition of Mg within the polymeric matrices (Table 6.6). The reduction of the time constant implies that the response of the material to stress becomes faster. This means that the mechanical behaviour of the material is approaching an elastic response. This is explained also by the value of the elastic constant E_1, which increases with strain rate and with the addition of Mg particles.

The viscosity, η_1, acquires larger values at $6.25x10^{-3}$ s^{-1} than at $200x10^{-3}$ s^{-1} indicating that the viscous resistance to deformation becomes less important as strain rate increases. The addition of Mg particles increment the value of the viscosity constant, which implies that the reinforcement increments the viscous resistance of the material to flow. This result is in agreement with the results obtained by compression tests.

Table 6.6 Results from least squares fitting to the creep response on conventional load/unload indentation tests on PLLA, PLDA and composites with 10 wt.% Mg content.

Load/unload test to 2N at constant strain rate, hold period 15s	PLLA	PLLA10Mg	PLDA	PLDA10Mg
Strain rate $6.25x10^{-3}$ s^{-1}				
E_1 (GPa)	1.10	1.25	1.06	1.30
E_2 (GPa)	29.00	29.80	24.36	33.85
η_1 (GPa s)	554.33	642.60	492.32	600.71
τ_2 (s)	6.11	6.68	6.55	6.02
Strain rate $200x10^{-3}$ s^{-1}				
E_1 (GPa)	1.32	1.39	1.20	1.43
E_2 (GPa)	9.10	10.32	8.03	10.22
η_1 (GPa s)	243.56	272.68	229.87	287.27
τ_2 (s)	1.16	1.24	1.23	1.16

From the creep curves the indenter displacement rate at the end of the load hold $\dot{h}_h$ is obtained. This value is used to calculate the corrected contact stiffness (Equation 6.11) and estimate the corrected reduced Young's modulus (E_{rc}).

Corrected Young's modulus was calculated using the corrected reduced modulus and Poisson´s ratio value of v=0.36 for PLLA and PLDA (Equation 6.7). Its dependences on strain rate and Mg content are depicted in Figure 6.17.

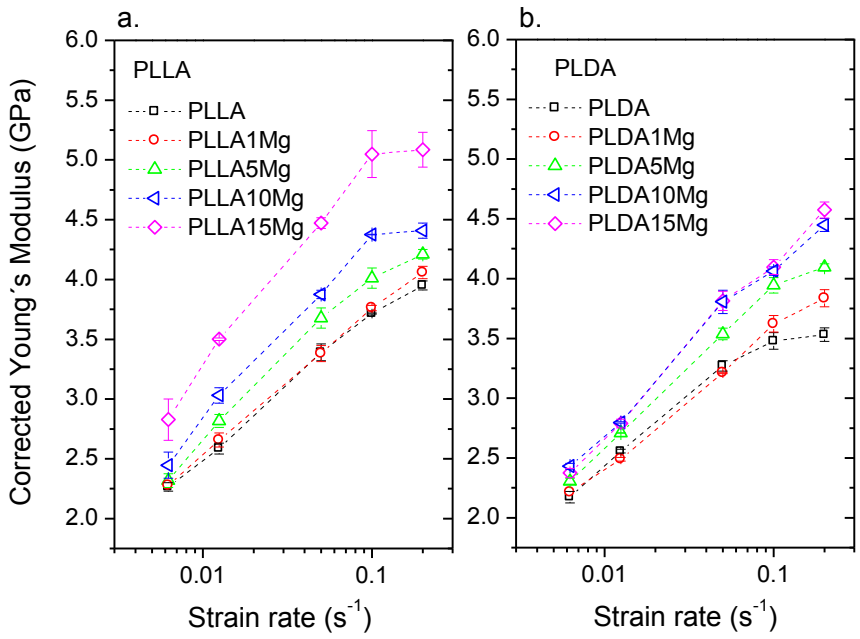

Figure 6.17 Young´s modulus dependence on strain rate and Mg content for PLLAXMg and PLDAXMg composites

Young´s modulus grows with increasing strain rate following a logarithmic growth. Two regimes are evidenced. During the first one, up to 0.1 s^{-1}, the relationship between E_c and the strain rate is linear, and can be described by a steep slope. During the second one, the slope decreases and Young´s modulus reach a saturation point where becomes stable. The semi-logarithmic dependence of E_c with the strain rate for each material is listed on Table 6.7. Slopes become more pronounced - i.e. acquire larger values - with increasing the amount of Mg in the matrix. Young´s modulus of reinforced materials is more sensitive to increase with strain rate than that of neat polymers. The existence of a linear dependence of viscoelastic properties with strain rate has been established for different polymers. Tang *et al.* [24] have found that poly (methyl methacrylate) (PMMA), Epoxy (crosslinked polymer) and polyvinylidene fluoride (PVDF), present a constant change rate of viscoelastic properties with unloading rate. Other authors have published that the mechanical properties under compression of PLLA, a racemic poly-D,L-lactic acid copolymer (PDLLA) and a 70/30 blend of poly-L-lactic acid with poly-D,L-lactic acid copolymer have the same dependence on strain rate [2]. The dependence of PLLA elastic modulus with strain rate has been found to be constant even for different crystallinity degrees [25]. In this research, as demonstrated in Figure 6.17 and table 6.7, the dependence of indentation modulus with strain rate of PLLA and PLDA is very similar. The kinetic behaviour of both polymers (i.e. slope GPa/decade) remains almost the same. It is important to notice, that Mg particles increase the dependence of the modulus with strain rate.

The relationship of composites Young´s modulus with Mg content can also be studied from Figure 6.17. Mg particles increase the modulus of both polymers. The increment of Young's modulus with particle reinforcement is more evident with increasing strain rate. Modulus of composites is improved over PLLA and PLDA, when the fraction of Mg particles is equal or higher than 5 wt.%. Compounds with 1 wt.% of Mg, have a very similar behaviour of unreinforced polymers. PLLAXMg modulus increases with increasing Mg reinforcement at the whole range of particle content. PLDAXMg modulus increases with Mg mass fraction up to a particle content of 10 wt.%. When a particle content of 15 wt.% is achieved, Young's modulus is not improved but approaches similar values to that of the material reinforced with 10 wt.%. Neat PLLA and PLLAXMg composites exhibit higher Young´s modulus than neat PLDA and PLDAXMg composites.

Table 6.7 Relationship between corrected Young's modulus and strain rate of PLLAXMg and PLDAXMg composites

Material	E_c/strain rate (GPa/decade)	Material	E_c/strain rate (GPa/decade)
PLLA	1.22 ± 0.03	**PLDA**	1.13 ± 0.05
PLLA1Mg	1.23 ± 0.01	**PLDA1Mg**	1.18 ± 0.05
PLLA5Mg	1.42 ± 0.07	**PLDA5Mg**	1.36 ± 0.04
PLLA10Mg	1.56 ± 0.05	**PLDA10Mg**	1.38 ± 0.03
PLLA15Mg	1.64 ± 0.07	**PLDA15Mg**	1.47 ± 0.06

Young´s modulus resulted from instrumented micro-indentation tests do not match those obtained by compression tests. This is because comparing modulus data obtained from depth sensing indentation (DSI) experiments with those obtained by conventional macroscopic techniques is a challenging task as the measurements are affected by complete different factors in each technique [26].

Instrumented micro-indentation differs from compression testing in the principle of measurement and the testing geometry. In DSI experiments the volume of deformation is continuously changing, and the distribution of stresses and strains generated beneath the indenter are inhomogeneous. The scale of the volume of deformation in DSI is significantly smaller than in compression testing. The load direction in DSI is evolved radially from the point of first contact, but for compression testing is unidirectional. In indentation testing a combination of compressive, tensile and shear forces are exerted on the material but in compression testing mainly compression stresses are applied [26, 27].

The discrepancy between indentation and conventional bulk measurements generates a big debate within the scientific community. While some studies suggest a very good agreement between indentation modulus and the modulus obtained by dynamic mechanical analysis (DMA), uniaxial compression with harmonic oscillation or tensile tests [25, 26, 28-30], others evidence a significant disparity between the indentation modulus and that obtained by bulk techniques [31-33]. In this chapter, the indentation Young´s modulus of PLLAXMg and PLDAXMg composites were found to be higher than those obtained by uniaxial compression tests. However, the general tendencies of their mechanical properties with strain rate shown under compression are in fair agreement with the behaviour shown under indentation. The increment of modulus with the strain rate, the larger effect of strain rate on composites' modulus than on neat polymers, and the highest modulus exhibited by PLLA15Mg and PLDA10Mg composites is observed in both, the compression and instrumented indentation tests.

The main advantage of instrumented indentation technique over conventional uniaxial compression tests is the ability of extracting mechanical properties from a single indentation print and without destroying the specimen under study. DSI experiments can provide simultaneous information on various mechanical properties. From the load-displacement curve, in addition to the elastic modulus, information concerning the material creep response and its Berkovich hardness can also be obtained.

The behaviour of Berkovich hardness with the strain rate and Mg content appears in Figure 6.18. As seen in the load-displacement curves of Figure 6.15, the increment of the strain rate leads to a shift of the curves to lower depths which implies a decrement on the projected area, A. Berkovich hardness is inversely proportional to the projected area (Equation 6.4), so, as the projected area decreases, the material hardens with increasing strain rate.

Berkovich hardness relationship with strain rate reaches a saturation ramp, where it becomes stable and the material do not hardens with further increment of strain rate. This saturation point appears at a strain rate of 0.05 s^{-1} for both type of materials, composites based on PLLA and based on PLDA, and is independent of Mg content.

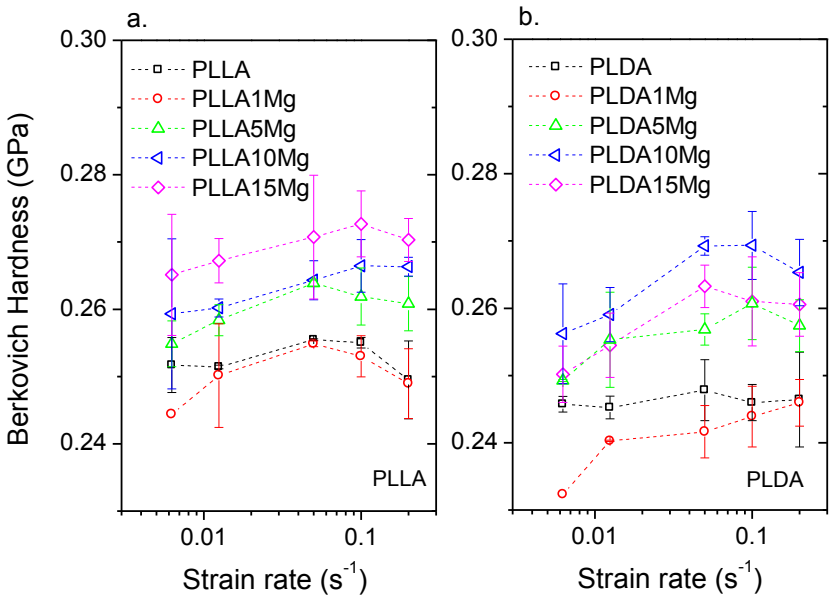

Figure 6.18 Berkovich hardness as a function of strain rate and Mg content for PLLAXMg and PLDAXMg

The addition of Mg particles within the polymeric matrix increases the Berkovich hardness of PLLA and PLDA at Mg contents equal or higher than 5 wt.%. With increasing Mg content H increases for PLLAXMg composites. PLLA15Mg is the material with the highest hardness. In the case of a polymeric matrix based on PLDA, the hardness of the composite with a 15 wt.% of Mg is lower than that of the composite with 10 wt.% but still higher than that of PLDA. PLDA10Mg is the material with the highest hardness. The addition of 1 wt.% of Mg within both polymeric matrices do not improve their hardness.

This research provides important information about the visco-elastic behaviour of PLLAXMg and PLDAXMg composites. Their time-dependent response was illustrated by the behaviour in compression and under indentation at a variety of strain rates. The sensitivity of mechanical properties with strain rate follows the same trends in both techniques. Addition of Mg increases polymeric matrices elastic modulus and induces a higher resistance to flow.

6.4. Conclusions

The scaling up of the extrusion process using a Mid-size extruder enabled the reduction of the thermal degradation of the material and allowed the incorporation of Mg particles up to a 15 wt.% within both polymeric matrices (PLLA and PLDA).

Incorporation of Mg particles within polymeric matrices reduces the thermal stability. The decrement in thermal properties is more evident for PLLAXMg composites than for PLDAXMg.

It was found that Mg particles reinforcement has an effect during the elastic and post yield regimes but do not affect the yield point. Mg particles increase the compressive Young´s modulus and the compressive strength at plateau of polymers but do not increase the compressive strength at yield.

The dependence of composites' mechanical properties on strain rate was found to be high with respect to neat polymers. Mg particles increase the sensitivity of the modulus with strain rate.

Mg particles reduce the strain softening amplitude of both polymers; this effect together with the increment of compression strength at plateau implies an increment in material toughness and an improvement in the energy storage of composites under deformation.

Instrumented indentation results show that addition of Mg particles within the matrix increases the resistance of the polymer to plastic flow, the Young´s modulus and the hardness.

A manufacturing process common in the industry successfully fabricated PLA/Mg composites reinforced with 1 to 15 wt.% of Mg particles. The mechanical properties of the composites can be tailored by the addition of Mg particles and the nature of the matrix. Young´s modulus for PLLAXMg composites range from about 2.2 to 5.0 GPa, while for PLDAXMg ranges from about 2.1 to 4.6 GPa. Compressive strength at yield of PLA/Mg composites exhibits values from 95 to 130 MPa.

Taking into account that Young´s modulus and compressive strength of cortical bone range from 3 to 23 GPa and from 90 to 120 MPa respectively [34], the novel PLA/Mg composites exhibit initial mechanical properties that are suitable for osteosynthesis applications.

6.5 References

[1] Cifuentes SC, Benavente R, González-Carrasco JL. Does magnesium compromise the high temperature processability of novel biodegradable and bioresorbables PLLA/Mg composites? Revista de Metalurgia 2014;50:1-11.

[2] Smit TH, Engels TAP, Söntjens SHM, Govaert LE. Time-dependent failure in load-bearing polymers: a potential hazard in structural applications of polylactides. Journal of Materials Science: Materials in Medicine 2010;21:871-8.

[3] Lim LT, Auras R, Rubino M. Processing technologies for poly(lactic acid). Progress in Polymer Science 2008;33:820-52.

[4] ASTM. D446-12 Standard Specifications and Operating Instructions for Glass Capillary Kinematic Viscometers. West Conshohocken, PA: ASTM International; 2012.

[5] Tsuji H, Ikada Y. Blends of isotactic and atactic poly(lactide)s: 2. Molecular-weight effects of atactic component on crystallization and morphology of equimolar blends from the melt. Polymer 1996;37:595-602.

[6] Perego G, Cella GD, Bastioli C. Effect of molecular weight and crystallinity on poly(lactic acid) mechanical properties. Journal of Applied Polymer Science 1996;59:37-43.

[7] Oliver WC, Pharr GM. An improved technique for determining hardness and elastic modulus using load and displacement sensing indentation experiments. Journal of Materials Research 1992;7:1564-83.

[8] Grau P, Meinhard H, Mosch S. Nanoindentation Experiments on Glass and Polymers at Different Loading Rates and the Power Law Analysis. MRS Online Proceedings Library 1998;522:153.

[9] Briscoe BJ, Fiori L, Pelillo E. Nano-indentation of polymeric surfaces. Journal of Physics D: Applied Physics 1998;31:2395.

[10] Tang B, Ngan AHW. Accurate measurement of tip–sample contact size during nanoindentation of viscoelastic materials. Journal of Materials Research 2003;18:1141-8.

[11] Cheng Y, Ni W, Cheng C. Determining the instantaneous modulus of viscoelastic solids using instrumented indentation measurements. Journal of Materials Research 2005;20:3061-71.

[12] VanLandingham M. Review of instrumented indentation. Journal of Research of the National Institute of Standards and Technology 2003;108:249-65

[13] Ngan A, Tang B. Viscoelastic effects during unloading in depth-sensing indentation. Journal of Materials Research 2002;2002:2604-10.

[14] Feng G, Ngan A. Effects of creep and thermal drift on modulus measurement using depth sensing indentation Journal of Materials Research 2002;17:660-8.

[15] Fischer-Cripps AC. A simple phenomenological approach to nanoindentation creep. Materials Science and Engineering: A 2004;385:74-82.

[16] Pan P, Inoue Y. Polymorphism and isomorphism in biodegradable polyesters. Progress in Polymer Science 2009;34:605-40.

[17] Chen K, Schweizer KS. Theory of Yielding, Strain Softening and Steady Plastic Flow in Polymer Glasses under Constant Strain Rate Deformation. Macomolecules 2011;44:3988-4000.
[18] van Melick HGH, Govaert LE, Meijer HEH. On the origin of strain hardening in glassy polymers. Polymer 2003;44:2493-502.
[19] Meijer HEH, Govaert LE. Multi-Scale Analysis of Mechanical Properties of Amorphous Polymer Systems. Macromolecular Chemistry and Physics 2003;204:274-88.
[20] Klompen ETJ, Engels TAP, Govaert LE, Meijer HEH. Modeling of the postyield response of glassy polymers: Influence of thermomechanical history. Macromolecules 2005;38:6997-7008.
[21] Govaert LE, van Melick HGH, Meijer HEH. Temporary toughening of polystyrene through mechanical pre-conditioning. Polymer 2001;42:1271-4.
[22] van Melick HGH, Govaert LE, Raas B, Nauta WJ, Meijer HEH. Kinetics of ageing and re-embrittlement of mechanically rejuvenated polystyrene. Polymer 2003;44:1171-9.
[23] Hasan OA, Boyce MC. Energy storage during inelastic deformation of glassy polymers. Polymer 1993;34:5085-92.
[24] Tang X-G, Hou M, Truss R, Zou J, Yang W, Dong Z-G, et al. An unexpected plasticization phenomenon and a constant of the change rate of viscoelastic properties for polymers during nanoindentation test. Journal of Applied Polymer Science 2011;122:885-90.
[25] Cifuentes SC, Frutos E, Benavente R, González-Carrasco JL, Lorenzo V. Strain rate effect on semi-crystalline PLLA mechanical properties measured by instrumented indentation tests. European Polymer Journal 2014;59:239-46.
[26] Díez-Pascual AM, Gómez-Fatou MA, Ania F, Flores A. Nanoindentation in polymer nanocomposites. Progress in Materials Science 2015;67:1-94.
[27] Monclus MA, Jennett NM. In search of validated measurements of the properties of viscoelastic materials by indentation with sharp indenters. Philosophical Magazine 2010;91:1308-28.
[28] Herbert EG, Oliver WC, Pharr GM. Nanoindentation and the dynamic characterization of viscoelastic solids. Journal of Physics D: Applied Physics 2008;41:1-9.
[29] Odegard GM, Gates TS, Herring HM. Characterization of viscoelastic properties of polymeric materials through nanoindentation. Experimental Mechanics 2005;45:130-6.
[30] Hayes SA, Goruppa AA, Jones FR. Dynamic nanoindentation as a tool for the examination of polymeric materials. Journal of Materials Research 2004;19:3298-306.
[31] Stojanovic D, Orlovic A, Markovic S, Radmilovic V, Uskokovic P, Aleksic R. Nanosilica/PMMA composites obtained by the modification of silica nanoparticles in a supercritical carbon dioxide–ethanol mixture. Journal of Materials Science 2009;44:6223-32.
[32] Liu, Phang IY, Shen L, Chow SY, Zhang W-D. Morphology and Mechanical Properties of Multiwalled Carbon Nanotubes Reinforced Nylon-6 Composites. Macromolecules 2004;37:7214-22.
[33] Flores A, Naffakh M, Díez-Pascual AM, Ania F, Gómez-Fatou MA. Evaluating the Reinforcement of Inorganic Fullerene-like Nanoparticles in Thermoplastic Matrices by Depth-Sensing Indentation. The Journal of Physical Chemistry C 2013;117:20936-43.

[34] Huiskes R, Mow VC. Biomechanics of bone. In: Mow VC, Huiskes R, editors. Basic orthopaedic biomechanics and mechanobiology. Philadelphia: Lippincott Williams & Wilkins; 2005.

IN VITRO STUDIES OF PLDA/Mg COMPOSITES PROCESSED BY INJECTION MOULDING

CHAPTER 7

"Imagination will often carry us to worlds that never were. But without it we go nowhere"

Carl Sagan

Table of contents

7. *IN VITRO* STUDIES OF PLDA/Mg COMPOSITES PROCESSED BY INJECTION MOULDING

7.1. Introduction

Resorbable materials intended for biodegradable implants must be suitable to gradually lose their mechanical strength while the bone tissue is regenerated, so that the system bone + implant can maintain its mechanical strength. With this in mind, there are three challenges to be addressed: good mechanical properties, control of degradation times and biocompatibility of degradation products [1].

In Chapter 5, the mechanical characterization of PLDA/Mg composites processed by injection moulding demonstrated that the incorporation of Mg particles within the polymeric matrix improved the performance of the composites under compression. But, besides a good mechanical performance, polymer/Mg materials must also have an appropriate degradation rate in accordance with the rate of bone healing, in order to fulfil the requirements for their application in osteosynthesis. The issue that is discussed in this chapter is, in fact, the *in vitro* degradation and biocompatibility of the materials that have been processed by injection moulding. The biodegradation process of PLDA/Mg composites can be better elucidated if the hydrolysis of the polymer and corrosion of Mg in a physiological medium is well understood.

Poly-L,D-lactic acid (PLDA) belongs to the family of aliphatic polyesters, which means that its ester groups are susceptible to be hydrolytically degraded in the physiological environment according to reaction 7.1 [2]. The hydrolysis of ester bonds leads to cleavage of polymer chains, subsequent decrease in molecular weight, and final diffusion of degradation products into the surroundings. PLDA degrades to lactic acid. This acid can be metabolized by the tricarboxylic acid cycle and excreted in the lungs as carbon dioxide and water or in the urine [3, 4].

$$-COO- + H_2O \rightarrow -COOH + HO- \qquad \text{Equation 7.1}$$

As mentioned in Chapter 1, Mg corrodes in aqueous environments forming hydroxides and releasing hydrogen according to the following reaction [5]:

$$Mg + 2H_2O \rightarrow Mg^{2+} + 2(OH)^- + H_2 \qquad \text{Equation 7.2}$$

The existence of chloride (Cl^-), phosphates (PO_4^{3-}) and calcium (Ca^{2+}) ions in body fluids, complicates the corrosion process. Chloride ions transform Mg hydroxide into soluble $MgCl_2$,

resulting in excess OH^- ions that eventually raise pH. Mg^{2+} ions dissolve into the solution, react with PO_4^{3-} and Ca^{2+} and form phosphates containing Mg/Ca that precipitate on the surface [5-7].

The main concerns in the application of Mg and its alloys in the biomedical field are the generation of hydrogen and the local alkalinisation. Fast Mg corrosion forms hydrogen bubbles that are accumulated at the implant surroundings. This phenomenon not only compromises the stability of the implant but can cause the death of a patient if bubbles enter blood vessels leading to embolism [8]. Hydroxides that are produced by Mg corrosion increase the local *in vivo* pH. If the pH exceeds 7.8, the balance of physiological reactions that depend on pH are affected by an alkaline poisoning effect [8, 9].

Understanding the *in vitro* degradation of a composite is a complex task since the matrix can alter the degradation behaviour of the reinforcement and the reinforcement may alter the degradation behaviour of the matrix. Currently there are no studies that explain the *in vitro* degradation of polymer composites reinforced with particles of metallic Mg. However, researches regarding degradation of polymers reinforced with hydroxyapatite, calcium phosphates, bioglasses, Mg salts and Mg oxides [3, 10-12], as well as studies on the effect of polymeric coatings on Mg alloys [13, 14] may help to generate clues about the behaviour of novel polymer/Mg composites.

Poly(alpha-hydroxiacids) degradation behaviour, rate and mechanism can be altered by physical and chemical characteristics of the reinforcing agent such as dispersibility, hydrophobicity or hydrophilicity, acidity or basicity and filler distribution [2, 3]. Some studies regarding the influence of basic filler materials on the degradation behaviour of amorphous D- and L-lactide copolymer [12] and poly-D,L-lactic acid-co-glycolic acid (PLGA) [15] have found that basic fillers retard polymer degradation as they neutralize the acidic endgroups resulting from hydrolysis of the polymer chains. Composites showed less molecular weight decrease than unfilled films but presented an erosion type of degradation. However, other studies suggest that the degradation of basic fillers within the polymeric matrix increase the pH in the surroundings of the reinforcement [3, 16-18]. The high concentration of hydroxide ions accelerates the hydrolytic degradation of poly(alpha-hydroxyacids) and induces porosity that enhances the alkaline surface hydrolytic degradation of the polymer.

Surface treatments or coatings can slow down the initial corrosion rate of Mg and Mg alloys, but in a long term, accelerate Mg corrosion [7]. Nonetheless, different coating processes are reviewed in the literature [13]. Among these processes, polymeric coatings showed a higher improvement in the initial corrosion protection and a better initial cytocompatibility [14]. Degradation rate of polymer coated-Mg can be controlled by films porosity, films thickness and homogeneity, adhesive strength of the polymeric coating on Mg surface and polymer chemical structure and crystallinity [7, 19-23]. Mg corrosion resistance is improved by thicker nonporous

and homogeneous coatings [20, 22]. A high adhesive strength prevents detachment of the coating due to hydrogen release, and also slowdowns Mg corrosion [21, 22]. Regarding the crystallinity, amorphous polymeric coatings protect Mg substrate more uniformly than with semi-crystalline films [22, 23].

The objective of this chapter is to elucidate the degradation behaviour of injection moulded PLDA/Mg composites in order to study their degradation mechanism, morphological changes and biocompatibility under *in vitro* test conditions. The degradation behaviour of PLDA/Mg composites was followed by measuring the hydrogen release, pH evolution, mass variation and water accumulation. The change in mechanical properties is measured under compression tests. Effect of crystallinity degree and Mg content on the degradation behaviour of these novel composites is also studied.

7.2. Materials and methods

7.2.1. Materials

PLDA/Mg composites processed by injection moulding (Chapter 5) were used in these studies. The matrix consists in a poly-L,D-lactic acid (PLDA) from Natureworks with a D-isomer content of 4.25%, and the reinforcement consists in irregular shaped Mg particles of less than 50 μm. The Mg contents within the matrix were 0.2 wt. % and 1 wt.%. Two types of materials were studied: As injected samples (Q), which are amorphous materials with a very low crystallinity degree ($f_c \approx 0.10$), and thermally treated samples (TT), which are materials subjected under a thermal treatment at 125 ± 1 ºC for 1 hour that yields a crystallinity degree close to 0.45. Table 7.1 summarises the nomenclature used for the materials studied in this chapter and their main characteristics (See chapter 5 for more information regarding the processing, thermal and mechanical properties of these composites).

Table 7.1 Nomenclature of the materials used and their main characteristics

Material	Mg content (wt.%)	Crystallinity degree (f_c)
PLDA_Q	0	0.14 ± 0.04
PLDA02Mg_Q	0.2	0.06 ± 0.04
PLDA1Mg_Q	1	0.12 ± 0.04
PLDA_TT	0	0.42 ± 0.04
PLDA02Mg_TT	0.2	0.41 ± 0.04
PLDA1Mg_TT	1	0.45 ± 0.04

The modified Dulbecco's Phosphate Buffered Saline (PBS) from Thermo Scientific was used as the immersion media. Table 7.2 shows the composition of the solution. PBS ion concentrations resemble those of the physiological environment.

Table 7.2 Salts concentration of Phosphate Buffered Saline solution

Salt	Concentration (mol/L)
Na_2HPO_4	0.008
KH_2PO_4	0.002
KCl	0.01
NaCl	0.14

7.2.2. Hydrogen release

For hydrogen release studies, samples with a rectangular prism shape (length: 9.7 ± 0.2 mm, width: 3.3 ± 0.1 mm, height: 8.8 ± 0.5 mm) were used. This type of specimens was cut from the grip section of tensile test specimens processed by injection moulding (not tested under tensile tests). The samples were immersed in PBS in a beaker. The ratio of the volume of dissolution media (ml) to the sample surface area (cm^2) was 20:1. Hydrogen bubbles were collected by a system placed directly above the sample and based on an inverted funnel and a burette (Figure 7.1.a). The burette (10 ml) was also filled with PBS. Hydrogen release is measured by the displacement of PBS level in the burette as H_2 gas evolves (Figure 7.1.b). Experiments were run at a constant temperature of 37 ± 1 ºC by introducing the beakers in a thermostatic bath (Figure 7.1.c). The results correspond to average values of three specimens. Hydrogen evolution was measured twice a day during 21 days. The media was fully renovated every seven days.

7.2.3. pH monitoring

For pH monitoring, samples with a cylindrical shape (height: 7.3 ± 0.3 mm, diameter: 4.7 ± 0.1 mm) were used. Cylindrical specimens were cut from the runners of injection moulded parts. Samples were immersed in PBS and distilled water. The ratio of the volume of immersion media to the sample surface was 20 ml/cm^2. The media were fully renovated every seven days. Experiments were run at a constant temperature of 37 ± 1ºC, by introducing the test tubes in a thermostatic bath. The results correspond to average values of three specimens. pH was recorded with a Lazar equipment. The electrode was calibrated every day with calibration standard solutions of pH 4, 9 and 7. Measurements were performed once a day until completion of the experiment.

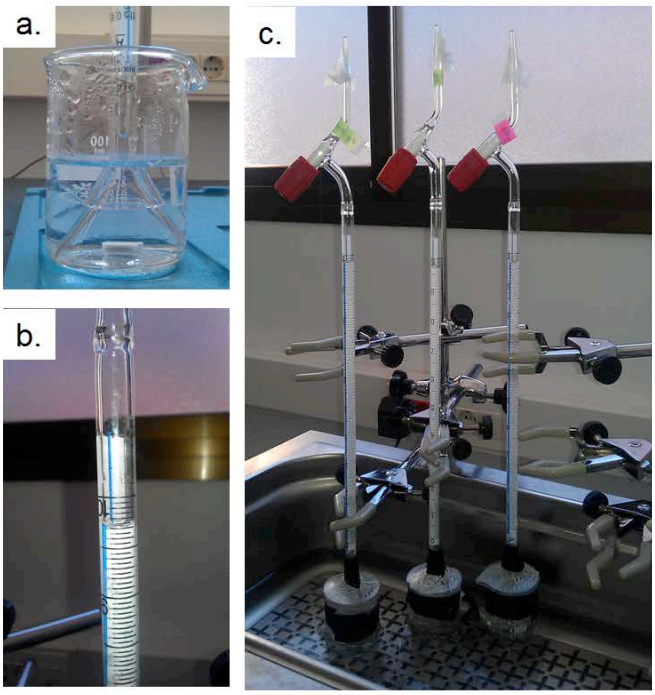

Figure 7.1 Experimental set up for hydrogen release measurements

7.2.4. Water accumulation and mass variation

The change in mass was measured for the samples immersed in PBS. Wet samples were weighted immediately after removing them from the solution and drying their surface with a paper towel; dry samples were measured after keeping them for 8 h under vacuum and 2 weeks in a desiccator. A precision balance was employed to weight all samples within an error of 0.00005 g (0.05mg).

Water accumulation was calculated from the wet mass, Wet (t), and the dried mass, Dry (t), as follows:

$$\text{Water uptake} = \frac{\text{Wet(t)} - \text{Dry(t)}}{\text{Dry(t)}} * 100\% \qquad \text{Equation 7.3}$$

Mass variation was calculated from the dried sample, Dry(t), compared with its initial mass, Mass(0), as follows:

$$\text{Mass variation} = \frac{\text{Dry(t)} - \text{Mass(0)}}{\text{Mass(0)}} * 100\% \qquad \text{Equation 7.4}$$

7.2.5. Morphology

Morphology of the composites is studied by macroscopic images taken with a NIKON SMZ 1500 stereoscopic microscope and by optical microscopy. The surfaces and longitudinal sections are studied.

7.2.6. Mechanical properties

The effect of *in vitro* degradation on the mechanical properties of composites was assessed by compression tests. The compressive mechanical behaviour was studied in a universal machine EM2/100/FR-10kN Micro Tests at ambient conditions, using a strain rate of 10^{-3} s^{-1}. Cylindrical samples tested for pH measurements in PBS were used for compression tests after 21 days of immersion.

7.2.7. Cell Viability

The *in vitro* biocompatibility was analyzed using human mesenchymal stem cells (MSCs). Cell viability was assessed by non-invasive AlamarBlue assay and cell morphology was visualized by confocal laser scanning microscopy (CLSM). These experiments were carried out at Hospital La Paz Madrid by Dra. Laura Saldaña.

7.3. Results and discussion

7.3.1. Hydrogen release

The main concern in the application of Mg and its alloys in the biomedical field is the generation of hydrogen. One mol of Mg (24.31 g) reacts with water and produces one mol of hydrogen gas (22.4 l) (Equation 7.2). This implies that only one gram of Mg can produce a whole litre of H_2.

The problem of hydrogen release in the human body cannot be explained in terms of how much hydrogen is produced but it has to be explained in terms of time. The important fact to know is the rate at which the hydrogen is released. H_2 generation rate must be sufficiently slow to be tolerated by the human body. If significant volumes of gas are build-up at the implant surroundings, its stability can be compromised and, more critically, hydrogen bubbles that enter blood vessels can cause embolism and eventually the death of a patient [8]. Given that H_2 release can be a critical problem *in vivo*, its measurement is crucial to determine the suitability of a Mg-containing material for biomedical applications.

The hydrogen release (ml H_2/cm^2) as a function of immersion time is shown in Figure 7.2 for amorphous and thermally treated PLDA/Mg composites reinforced with 0.2 and 1 wt.% Mg particles. The amount of Mg that reacts and release the measured volume of hydrogen was stoichiometrically calculated according to equation 7.2. These data was used to find the mass loss of Mg with time. Figure 7.3 shows the Mg loss explained in terms of composite mass loss (Figure 7.3.a) and loss of Mg content in the composite (Figure 7.3.b) as a function of immersion days.

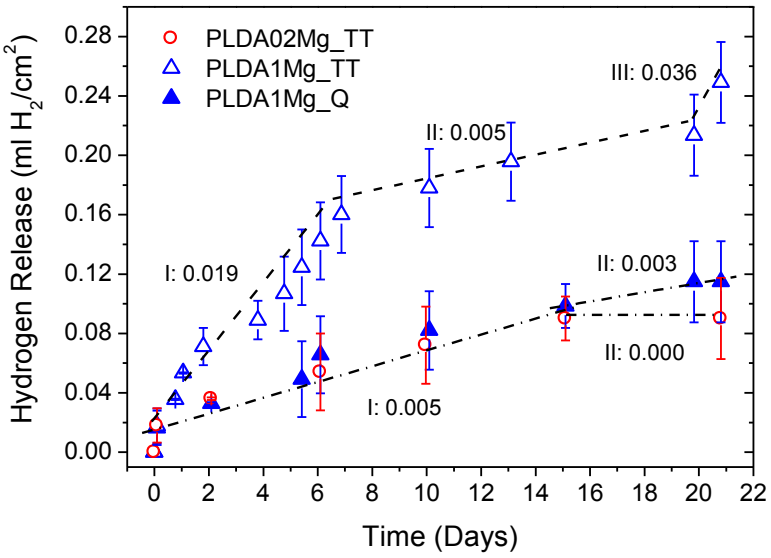

Figure 7.2 Accumulated amount of hydrogen released as a function of immersion time in PBS.

From the analysis of Figure 7.2 it follows that the hydrogen evolution rate depends on Mg content and crystallinity degree of the composite. With higher Mg content and higher crystallinity degree the hydrogen release rate increases. Degradation kinetics of PLDA1Mg_TT can be divided into three ranges, as marked by the lines depicted in the figure; a first one (I) takes place during the first week and is characterized by a slope of 0.019 ml H_2/cm^2 per day, a second one (II) takes place from day 7 until day 20 and is described by a smaller slope and a third one (III) that takes place during the last day where the slope increases suddenly and drastically. Interestingly, degradation kinetics of the thermally treated composite reinforced with 0.2 wt.% of Mg follows the same trend as the amorphous composite reinforced with 1 wt.% of metallic particles. Hydrogen release rate of PLDA02Mg_TT and PLDA1Mg_Q present the same slope during the first two weeks (I: 0.005 ml H_2/cm^2 per day). Beyond that point, H_2 release starts to stabilize for PLDA1Mg_Q, as the rate acquires a smaller slope, but completely stabilizes for PLDA02Mg_TT as it seems that there is no H_2 release during the last week. The explanation of

this behaviour is further addressed taking into account the results of pH, mass variation and morphological changes.

The hydrogen that was released by each sample corresponds to a specific amount of Mg that reacts with the immersion media. Figure 7.3 shows that in 21 days almost half of the Mg content of PLDA02Mg_TT sample has reacted (-45 wt.% of Mg). This corresponds to a mass loss in the composite of 0.09 wt.%. Mg loss in terms of composite mass loss for PLDA1Mg_Q is very similar to that obtained for PLDA02Mg_TT (0.10 wt.%) and corresponds to the corrosion of 10% of the Mg available in the composite. In the case of PLDA1Mg_TT, more than the 20% of the total amount of Mg has been oxidized by water. This amount is equivalent to a mass loss in the composite of 0.22 wt.%.

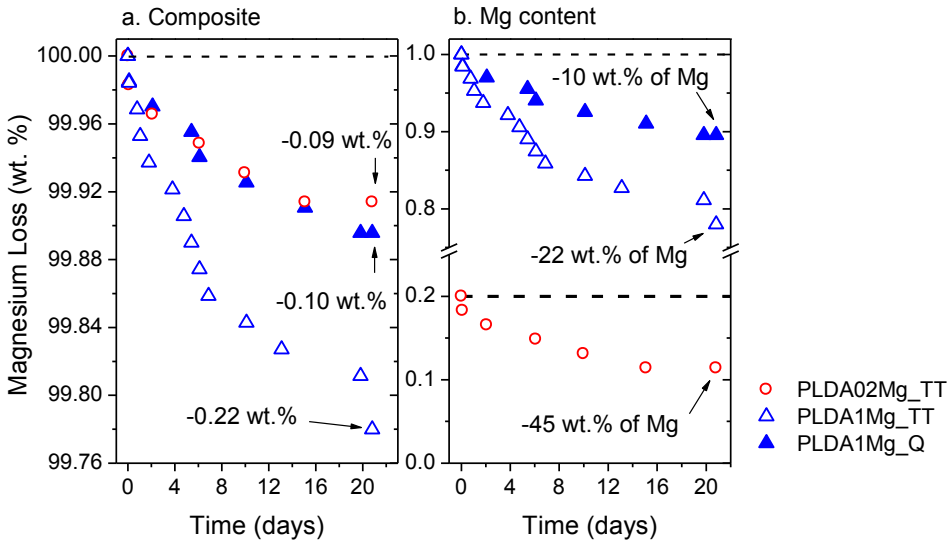

Figure 7.3 Mg loss as a function of immersion time in PBS

In order to determine if PLDA/Mg composites are suitable candidates to be tested in humans, it is important to consider the hydrogen volume that can be tolerated in the human body. F. Witte *et al.* [24] have performed *in vivo* corrosion experiments with Mg alloys containing aluminium and zinc (AZ31, AZ91) as well as rare earth elements (WE43, LAE442) on guinea pigs. They have found that all the Mg alloys formed subcutaneous bubbles that disappeared after 2 – 3 weeks. This implies that guinea pigs can gradually metabolize the hydrogen released by the alloys through a certain mechanism at a lower rate than the hydrogen evolution rate of the four alloys. In other study, G. Song [8] measured the hydrogen evolution rate of AZ91 (0.068 $ml/cm^2/day$) and recommended that a hydrogen evolution rate lower than that of AZ91 may not lead to a subcutaneous bubble in a guinea pig.

G. Song [8] studies were performed in the Hank's solution and using a media volume to surface area ratio of 50:1 (250 ml of solution:5 cm^2), whereas our studies have been carried out in PBS and using a media volume to surface area ratio of only 20:1. Therefore, a straightforward comparison between both studies cannot be performed as there are many factors that influence the data collection. However, a detailed analysis of the factor influence, H_2 gas evolution rate, can help to elucidate some important conclusions. According with Kirkland *et al.* [25], a decrement in the media volume lead to faster H_2 release rates. This implies that the materials studied in this chapter will have slower degradation rates if they were tested at G. Song´s experimental conditions.

The volume of hydrogen released by PLDA/Mg composites is much lower than that of AZ91 alloy studied by G Song [8]. This suggests that an implant made of these novel composites will not create a gas threat as the hydrogen is released with a controllable rate that can be tolerated by the human body.

7.3.2. pH evolution

Another concern regarding Mg reaction with the physiological environment is the alkalization of the surface due to the production of 2 moles of $(OH)^-$ for every mol of Mg that is oxidized (Equation 7.2). Mg dissolution can lead to high pH (10 – 12) in both, non-buffered [26, 27] and buffered solutions [28, 29]. G. Song and S.Z. Song [30] have demonstrated that a small Mg coupon of (1 x 1 x 1 cm^3) can raise the pH value of 250 ml of neutral Hank's solution up to 10 in 15 hours. This is in accordance with our experimental findings with Mg cylinders immersed in PBS with a volume/surface ratio of 20:1, where pH increases above 10 in only one day, in spite of the fact that PBS is a buffered solution. This implies that the buffer capacity of the physiological environment can be surpassed by the corroding Mg leading to a local alkalization. If the local *in vivo* pH value exceeds 7.8 an alkaline poisoning effect can affect the balance of physiological reactions that depend on pH [8].

Variation of pH in the medium containing thermally treated and amorphous PLDA and PLDA/Mg composites samples was monitored during 21 days in distilled water and PBS. PH measurements in distilled water allow the analysis of the nature of the degradation products. Measurements in PBS are made to understand the buffering capacity of the solution and to monitor that a controlled pH range is maintained in the solution.

Figure 7.4 shows the measured pH values in both, distilled water and PBS for amorphous (Figure 7.4.a) and thermally treated samples (Figure 7.4.b). pH of the buffered solution stays stable around 7.25 ± 0.15 for both type of materials, Q and TT. This is indicative that PBS maintained its buffer capacity during the whole experiment. Distilled water presents a slightly acidic pH that ranges from 5.7 and 5.9. The pH of distilled water containing PLDA/Mg composites increases with time, while pH of distilled water containing polymeric samples

decreases. The results are in accordance with the nature of the degradation products of PLDA and Mg.

Poly-L,D-lactic acid degradation proceeds via hydrolysis of the ester bonds that leads to cleavage of polymer chains, subsequent decrease in molecular weight and final diffusion of degradation products into the immersion media. For instance PLDA degradation would decrease the pH of the solution as the main degradation product is lactic acid. Composites contain Mg particles that react with water releasing hydrogen and producing hydroxides that raise the pH.

The increment in pH due to Mg particles corrosion is not enough to reach basic pH values (Figure 7.4). Crystalline materials (TT) exhibit greater pH rise than amorphous (Q). This result is consistent with the behaviour observed in hydrogen evolution where thermally treated materials released H_2 at faster rates than amorphous. Comparing the results based on Mg content of composites it follows that during the first week composites containing 0.2 wt.% and 1 wt.% raise the pH of distilled water to the same extent, but as time passes, the material with higher Mg content generates larger increments in pH.

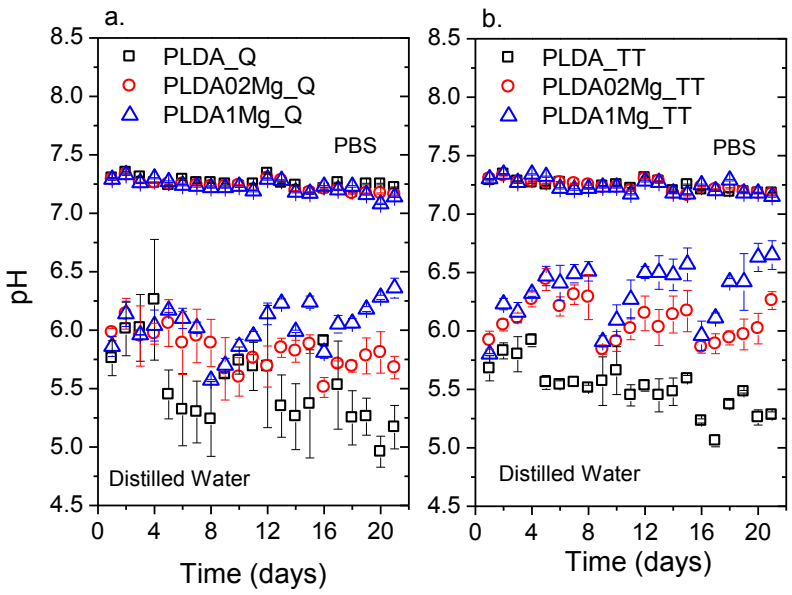

Figure 7.4 Evolution of pH of the composites in distilled water and PBS solution

7.3.3. Water retention and mass variation

Hydrolysis of polylactic acid is controlled by the diffusion of water in the free volume of amorphous phase [2]. The amount of water retained by a polymer depends on several material factors, as the molecular structure, crystallinity degree or the incorporation of additives and fillers. Figure 7.5 shows the percentage of mass gain due to water retention of amorphous and thermally treated PLDA/Mg composites after 21 days immersed in PBS. No considerable changes in water content are observed when comparing amorphous PLDA_Q and PLDA02Mg_Q with their thermally treated (TT) homologous. It also seems that incorporation of 0.2 wt.% Mg particles within a PLDA matrix, does not induce changes on the amount of water absorbed by the matrix. The equilibrium water content of these materials ranges from 0.75 % to 1.25 %, whereas, considerable changes in water retention are observed when PLDA is reinforced with 1 wt. % of Mg particles.

A filler content of 1 wt.% substantially increases the water diffusion into the polymeric matrix. In the case of PLDA1Mg_TT the water content implies a weight gain of near 2%. Amorphous PLDA1Mg duplicates the water gain of PLDA1Mg_TT (Figure 7.5). This is probably due to the higher crystallinity degree of the thermally treated samples. Some authors have reported that the water absorption rate of polylactic acid decreases with higher degrees of crystallinity [31, 32]. This implies that crystallinity affects the water transport through the polymer, as the access of water molecules to the chains inside the rigid crystalline regions is prohibited [33].

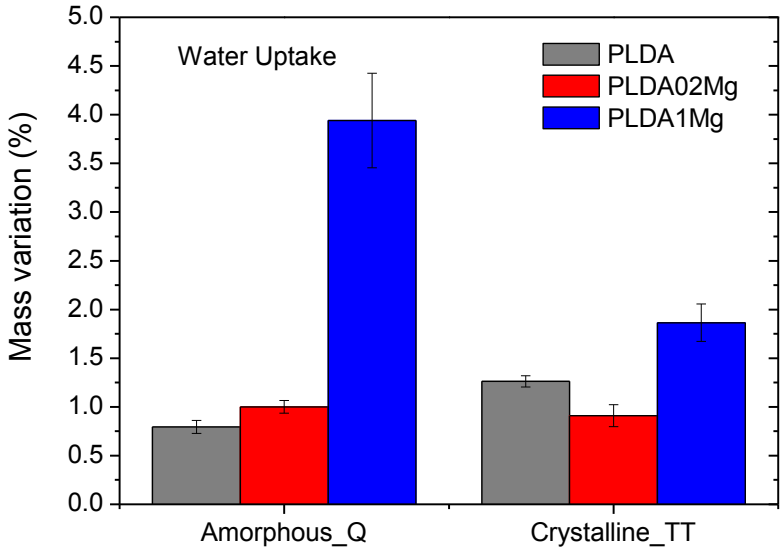

Figure 7.5 Percentage of mass gain due to water uptake after 21 days of immersion in PBS

The incorporation of Mg particles within the matrix can also increase the diffusion of water within the amorphous domains of PLDA. It has been demonstrated that the introduction of hydrophilic additives or comonomers within the polymeric matrix alters the hydrolytic degradation of PLA [2]. The higher hydrophilicity of these systems accelerates the diffusion of water into the material and increases its water content, which leads to enhance the degradation rate of the polymer [34-36].

The increment of water content can also be an indicative of pores formation [3]. Pores can be produced by the reaction of Mg particles. As water diffuses within the matrix, it reaches the surface of Mg particles leading to the corrosion of the metal. When Mg reacts with the aqueous environment, it releases hydrogen and produces hydroxides that can lead to a local alkalinisation in the polymer/particle interface. Given that a high concentration of hydroxide ions can accelerate the hydrolytic degradation of poly (α-hydroxyacids) [17, 37, 38], the ester bonds of those polymer chains that are subjected to a high pH environment are more vulnerable to be attacked. Therefore, degradation of the polymer at the interface will occur faster. Erosion of the particles surroundings can generate pores that increase the water retention of the composite. This phenomenon has been observed in glass fiber-reinforced PLDLLA composites [3, 39]. Interconnected pores (capillaries) were formed in the surface of the reinforcing bio-glass fibers and accelerated the diffusion of water through the polymer [39].

The analysis of the total mass loss can help to clarify whether water retention is due to polymer degradation that induces formation of pores, Mg loss or to the presence of amorphous domains. Figure 7.6 shows the percentage of mass loss of amorphous and thermally treated PLDA/Mg composites after being immersed during 21 days in PBS. It is observed that all the amorphous materials have lost the same mass percentage, indistinctively of Mg content. However, in the case of crystalline materials, the composite with the highest reinforcement content has experienced the largest mass loss. Mass loss of PLDA_TT and PLDA02Mg_TT is very similar to that of amorphous materials. This is in agreement with the results obtained in hydrogen release section, where the Mg loss in terms of composite mass loss for thermally treated PLDA02Mg and amorphous PLDA1Mg exhibits very similar values, 0.09 wt.% and 0.10 wt.% respectively.

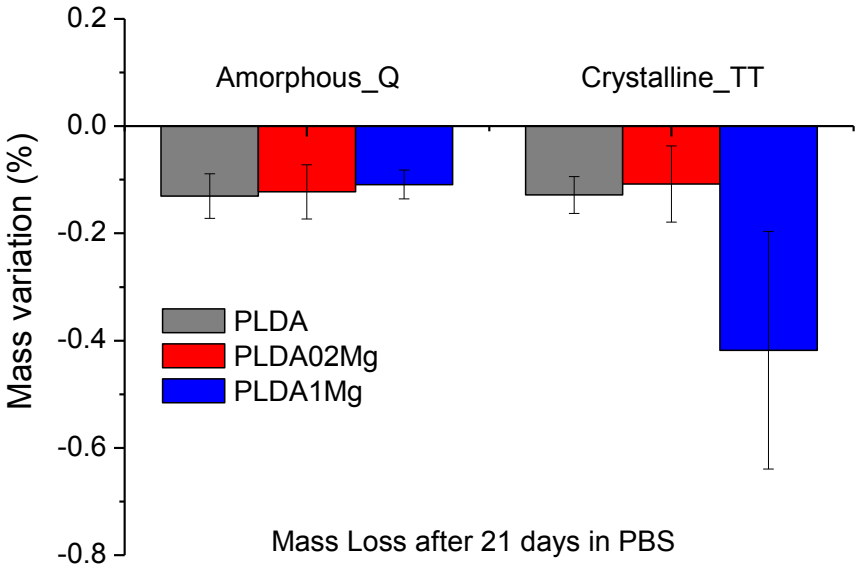

Figure 7.6 Percentage of mass loss after 21 days of immersion in PBS

Although amorphous PLDA1Mg retains more water than its crystalline homologous (Figure 7.5), it is the later composite the one that releases the highest volume of hydrogen (Figure 7.2) and the one that experiences the largest loss of mass (Figure 7.6). This suggests that there must be other factors that affect the degradation of the composite besides the ability of the polymeric matrix to favor water diffusion within it.

It is important to take into account that the crystallinity degree of the polymeric matrix can also alter the corrosion rate of Mg particles inside the polymer. Xu and Yamamoto [23] have found for bulk Mg coated with PLLA and PCL (poly-caprolactone) that the molecular weight and crystallinity degree of the biodegradable polymeric films are important parameters that tailor the corrosion behaviour of Mg substrate. According to their research, PLLA-coated Mg presented a uniform corrosion, whereas PCL-coated Mg presented pitting corrosion and the highest corrosion rate. These results were attributed to the polymer coating microstructure. As PLLA film is amorphous and PCL is semi-crystalline, a uniform Mg corrosion is due to the uniform penetration of water into the amorphous polymeric film. Whereas, in the case of the semi-crystalline film, water penetrates preferentially into the amorphous regions and this fact induces corrosion pits that lead to fast degradation of the substrate [40, 41]. Xu and Yamamoto's findings can help to explain the behaviour of amorphous and thermally treated PLDA/Mg composites.

Although amorphous PLDA1Mg_Q retains more water than crystalline PLDA1Mg_TT, the diffusion of water into the amorphous composite is uniform, whereas water penetrates preferentially into the amorphous domains of crystalline PLDA. The non-uniform distribution of water within a semi-crystalline matrix can induce a localized corrosion on the vulnerable sites of Mg particles surface which enhances the degradation rate of the metallic particles. This could be a possible reason for the higher hydrogen release and mass loss of the crystalline composites in comparison with the amorphous ones.

7.3.4. Morphology

The evolution of PLDA/Mg composites morphology with immersion time as a function of Mg content (0.2 and 1 wt.%) and polymeric matrix structure (amorphous_Q and crystalline_TT) is shown in Figures 7.7 and 7.8. Changes on the surface of the samples can be seen in Figure 7.7. The effects of degradation in volume can be observed in the longitudinal cross-sections of samples shown in Figure 7.8.

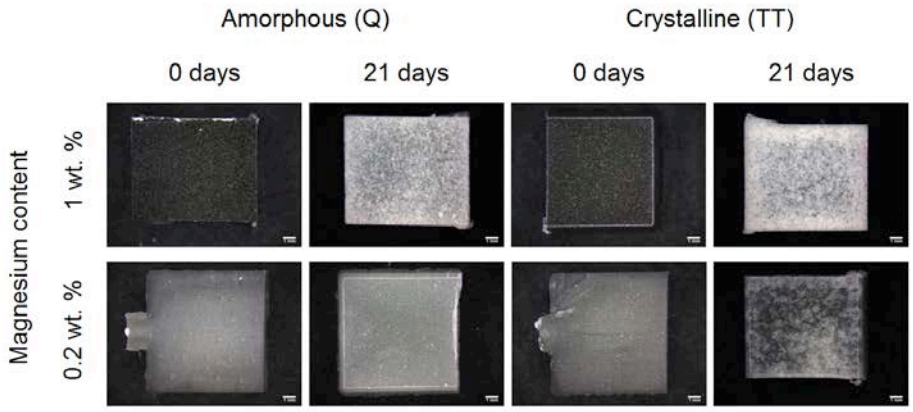

Figure 7.7 Optical macrographs of the surface of PLDAXMg samples

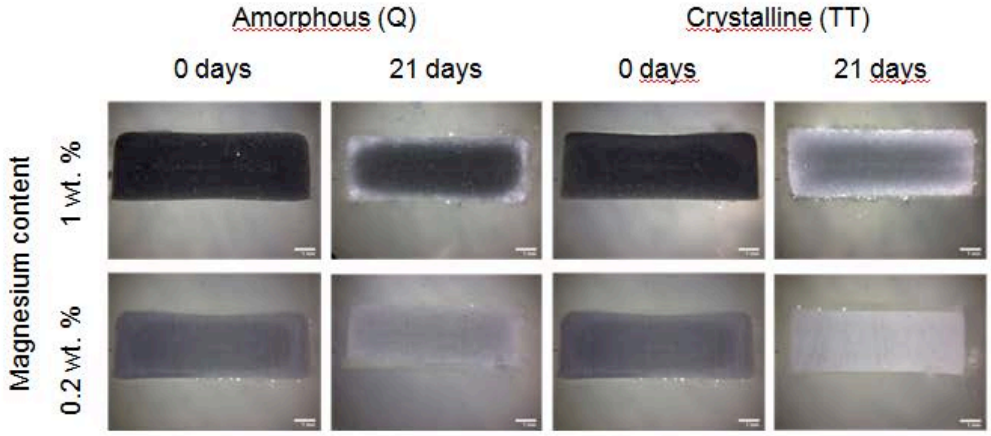

Figure 7.8 Optical macrographs of the cross-sections of PLDAXMg samples

Composites materials present a gray colour. The gray tone is darker with the increment in the percentage of the reinforcement. No colour changes due to the heat treatment were observed. After 21 days immersed in PBS, PLDA/Mg composites lose their characteristic gray colour and their surface become whitish (Figure 7.7). This colour change is due to the reaction with the immersion media of Mg particles present at the surface. The material that underwent fewer changes on its surface morphology is the amorphous material reinforced with 0.2% of Mg. Crystalline materials present more noticeable morphology changes due to degradation at surface.

Cross section pictures show the volumetric evolution of composites degradation (Figure 7.8) and their analysis help to understand how the loss of mass of composites proceeds, giving a hint of their erosion mechanism. It is clearly seen that composite degrades more at the surface than at the core of the sample. Mg particles react at the surface in a greater extent than at the center. A white halo surrounds the central zone of the specimen.

Figure 7.9 shows optical microscopy pictures of the cross-sections border of original PLDA1Mg composites and after 21 days in PBS. A closer view of the cross-sections evidences that the white halo formed at samples surface is due by corroded Mg particles. No cracks or deterioration of the polymeric matrix are evident by optical microscopy.

The corrosion products that can be formed on particles surface are Mg hydroxides or Mg phosphates. Mg corrodes in aqueous environments forming $Mg(OH)_2$ that can precipitate on Mg surface at high local pH values (Equation 7.5) [6]. Chloride ions present in immersion media can transform Mg hydroxide into soluble $MgCl_2$ (Equation 7.6) [7]. Mg^{2+} ions dissolve into the solution and react with phosphates ions of PBS, forming Mg phosphates that can precipitate on

particles surface (Equation 7.7) [5]. The precipitation of white hydroxides and/or phosphates on Mg particles surface changes the gray colour of the composites.

$$Mg_{(solid)} + 2H_2O_{(aqueous)} \rightarrow Mg(OH)_{2(solid)} + H_{2(gas)} \quad (\text{at pH} > 11.5) \qquad \text{Equation 7.5}$$

$$Mg(OH)_{2\ (solid)} + 2Cl^- \rightarrow MgCl_{2\ (soluble)} + 2(OH)^- \qquad \text{Equation 7.6}$$

$$H_nPO_4^{(3-n)-} + Mg^{2+} + OH^- \rightarrow Mg_x(PO_4)_{y\ (solid)} \qquad \text{Equation 7.7}$$

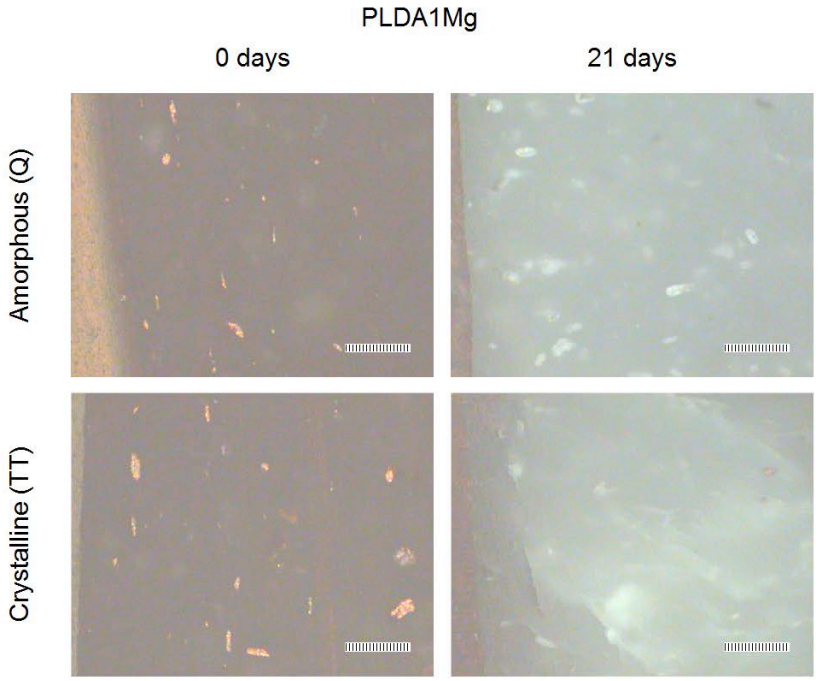

Figure 7.9 Micrographs of the cross-sections border of PLDA1Mg composites samples (Scale bar = 100 µm)

The central part of the degraded samples remains gray but, in comparison with the original samples, it shows a lighter shade (Figure 7.8). It is observed that the crystalline specimens present a lighter gray colour than amorphous materials. Also the white halo due to the reaction of Mg particles is thicker for TT samples than for Q. The loss of gray colour can be directly linked with the corrosion of Mg. Thus the morphologic observations are consistent with the results obtained in the hydrogen release experiments, where Mg present in thermally treated matrices reacted much faster than the one incorporated in amorphous PLDA.

7.3.5. Mechanical properties

The mechanical performance of amorphous and thermally treated materials was studied as a function of degradation time. Figures 7.10 and 7.11 respectively show the stress *vs* strain curves of amorphous (Q) and thermally treated (TT) PLDA (a), PLDA02Mg (b) and PLDA1Mg (c) composites after 0 and 21 days immersed in PBS at 37 ºC. Figure 7.12 depicts the results of Young´s Modulus (a) and compressive strength (b) of amorphous materials and Figure 7.13 shows the results of thermally treated materials.

Although the *in vitro* studies evaluated short term degradation (3 weeks) of the composites, the initial results are very promising. It was found that the strength retention properties of the composites are highly dependent on the crystallinity degree of the polymeric matrix. Amorphous composites show 100% strength retention after 21 days (Figure 7.12), whereas thermally treated composites lost their mechanical resistance after 3 weeks (Figure 7.13). PLDA02Mg_TT and PLDA1Mg_TT suffer a reduction in stiffness of 20 % and in compressive strength of 15 % after three weeks immersed in PBS at 37 ºC (Figure 7.13). Strength retention properties were less dependent on Mg content, as no significant difference was evidenced between the mechanical behaviour of the composite reinforced with 0.2 wt.% of Mg with that reinforced with 1 wt.%. Neat PLDA maintains its mechanical performance after 21 days indistinctively its crystallinity degree.

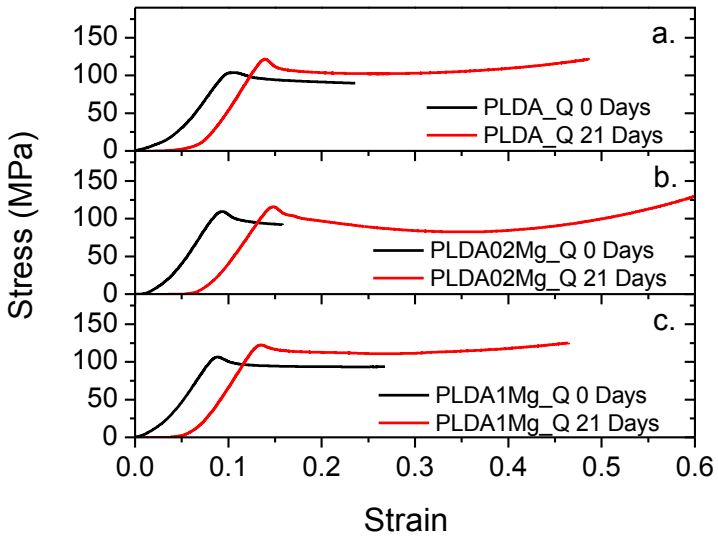

Figure 7.10 Compressive stress *vs* strain curves for amorphous PLDA (a), PLDA02Mg (b) and PLDA1Mg (c) after 0 and 21 days immersed in PBS at 37 ºC

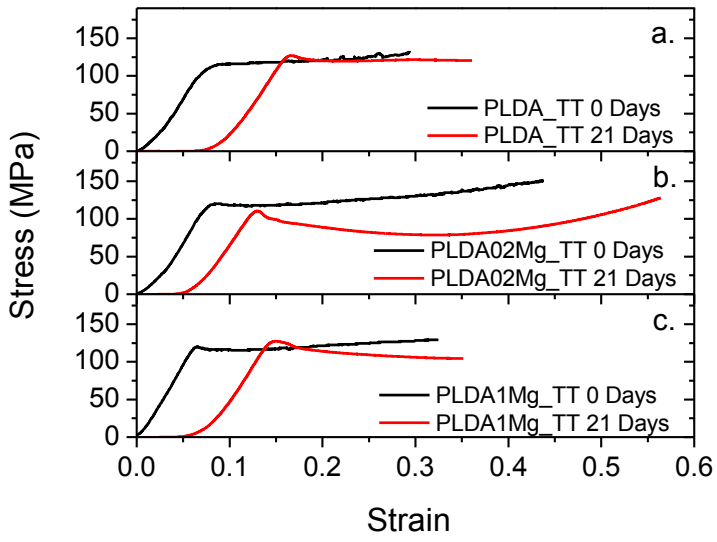

Figure 7.11 Compressive stress *vs* strain curves for thermally treated PLDA (a), PLDA02Mg (b) and PLDA1Mg (c) after 0 and 21 days immersed in PBS at 37 ºC

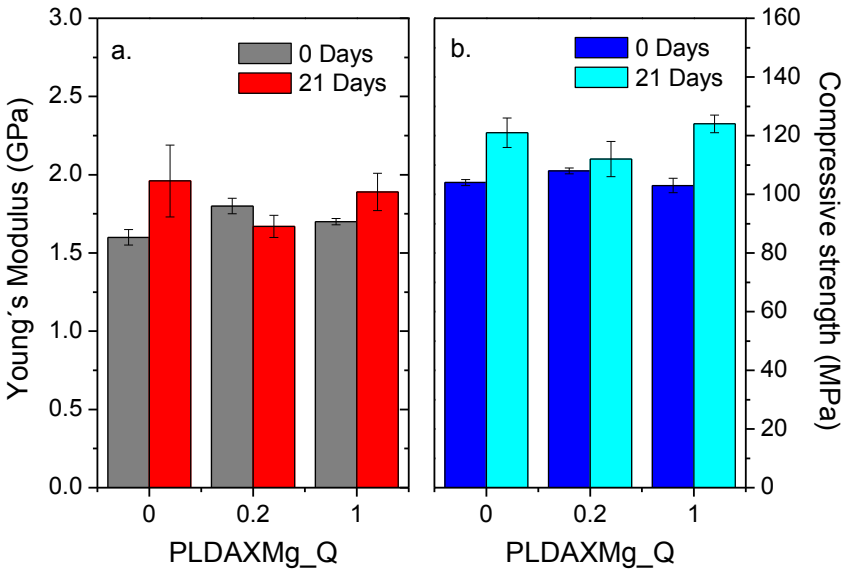

Figure 7.12 Young´s modulus (a) and compressive strength (b) of amorphous PLDA and PLDAXMg composites with X=0.2 and 1wt.% of Mg after 0 and 21 days immersed in PBS at 37 ºC

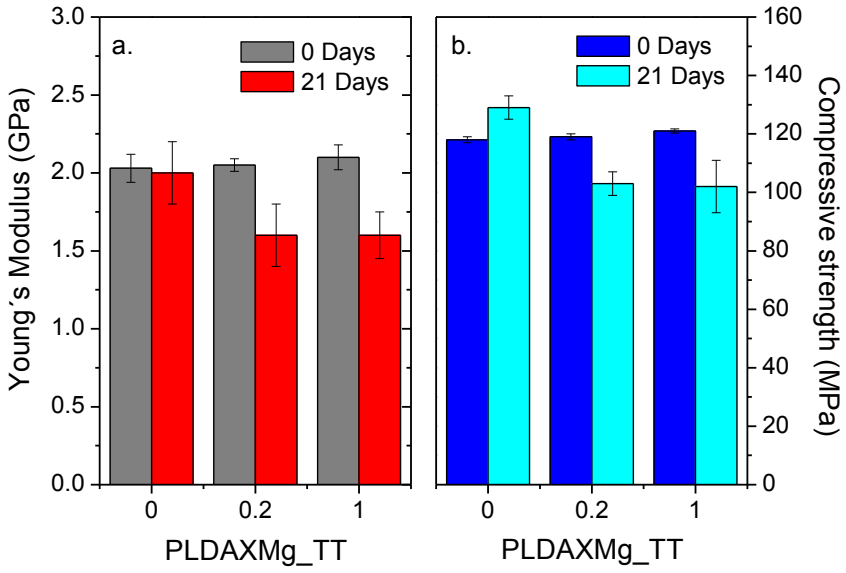

Figure 7.13 Young´s modulus (a) and compressive strength (b) of thermally treated PLDA and PLDAXMg composites with X=0.2 and 1wt.% of Mg after 0 and 21 days immersed in PBS at 37 ºC

Dürselen *et al.* [42] have evaluated the in vitro degradation of PLA in a buffer at 37 ºC and demonstrated that the stiffness of the material remained the same after 1 year but this did not result in an effective load transfer. An adequate strength-tissue ingrowth relationship was not achieved.

Biodegradable implants must, therefore, exhibit a good combination of tissue ingrowth and strength retention in order to accomplish a good *in vivo* mechanical performance. Mg contents of 0.2 and 1 wt.% reduce PLDA strength retention, but their presence in the composite could be advantageous as they would make room for newly regenerating tissue by degrading faster than the polymer and inducing bone healing. The fast eroding particles could be an effective tool to tailor the tissue ingrowth in a biodegradable implant.

7.3.6. Cell viability

Cell viability was tested on thermally treated samples during three weeks. *In vitro* studies demonstrate that Mg reinforcement improves viability of MSCs cultured on the materials (Figure 7.12). Confocal imaging of MSCs shows actin filaments in red and Mg particles in green. Cells are spread on all surfaces and exhibit a typically elongated shape. Cellular viability increases with time and with Mg content. Interestingly MSCs are viable even after 21 days in culture. A Mg content of 1 wt.% has a great effect on cell viability as it induces an increment of 160 % with respect to neat PLDA cell viability.

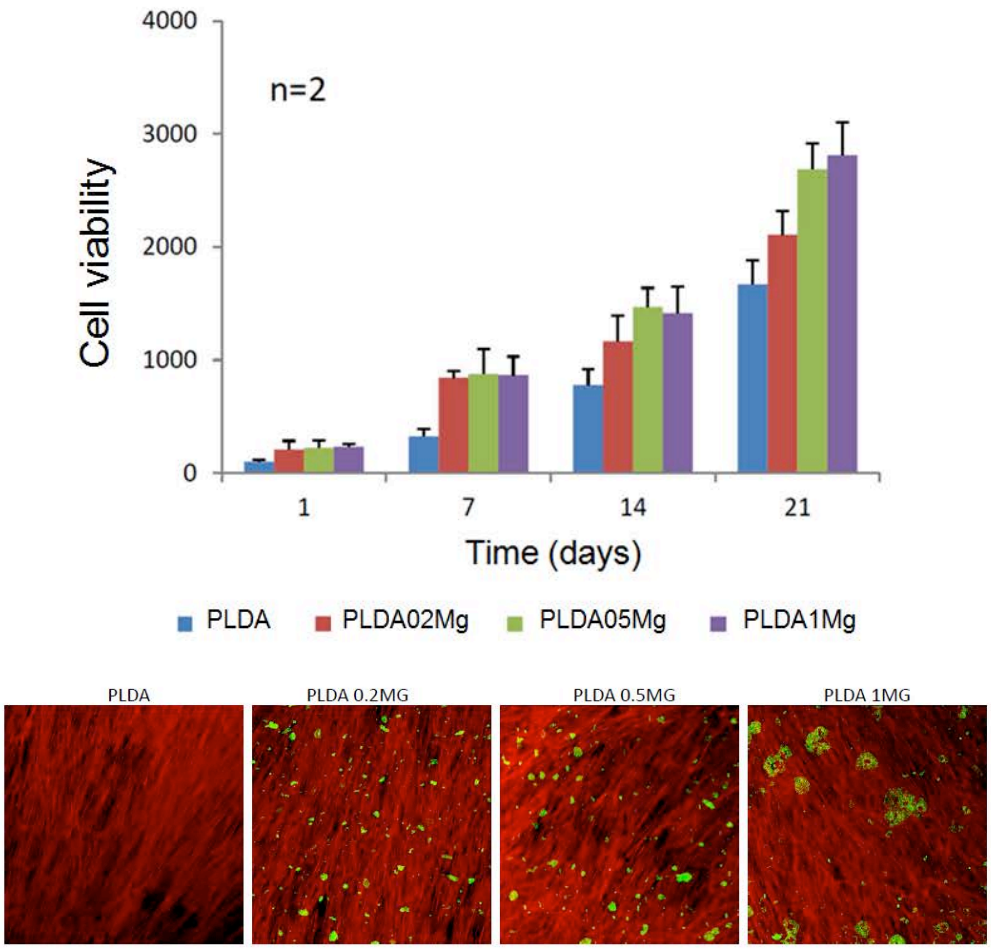

Figure 7.12 Viability and morphology of mesenchymal stem cells (MSCs) cultured on crystalline PLDA/Mg composites

7.4. Conclusions

Results of *in vitro* studies on injection moulded PLDA/Mg composites demonstrate that the degradation rate of these materials depend in great extent on both, crystalline degree and Mg content. All the composites release hydrogen at rates that could be tolerated by human body.

Hydrogen evolution rate is larger for materials with a higher crystalline degree and with higher amount of Mg. A plausible reason for the higher hydrogen release and mass loss of crystalline composites in comparison with amorphous ones could be the non-uniform distribution of water within the semi-crystalline matrix. The preferential diffusion of water through the amorphous domains can induce a localized corrosion on Mg particles that enhances their degradation rate.

The pH of the immersion media that simulates the physiological environment remains neutral throughout the test. The acidic nature of the degradation products of the polymer, and the basicity of hydroxides generated by the reaction of Mg particles was clearly observed by pH measurements in distilled water.

Mg degradation takes place prior degradation of the polymeric matrix. Mg particles at the surface react with immersion media faster than particles localized at composite's core.

The strength retention properties of the composites are highly dependent on the crystallinity degree of the polymeric matrix. After 3 weeks, amorphous composites show 100% strength retention, whereas thermally treated composites lost 20% of stiffness and 15% of compressive strength.

Incorporation of Mg in PLDA matrix improves cell viability of the polymer. The addition of 1 wt.% of Mg particles increases cell viability by nearly 160% with respect to neat PLDA cell viability.

PLDA/Mg composites present an enhanced biocompatibility and controllable degradation rates that can be customized through polymeric matrix crystallinity or Mg particles content. Considering the *in vitro* results, these novel materials have great potential to be used as future materials for biodegradable implants.

7.5. References

[1] Hofmann GO. Biodegradable implants in orthopaedic surgery—A review on the state-of-the-art. Clinical Materials 1992;10:75-80.

[2] Auras R, Lim LT, Selke SEM, Tsuji H. Poly-lactic acid. Synthesis, Structures, Properties, and Applications: John Wiley & Sons, Inc. New Jersey; 2010.

[3] Lehtonen TJ, Tuominen JU, Hiekkanen E. Resorbable composites with bioresorbable glass fibers for load-bearing applications. In vitro degradation and degradation mechanism. Acta Biomaterialia 2013;9:4868-77.

[4] Eglin D, Alini M. Degradable polymeric materials for osteosynthesis: tutorial. European Cells & Materials 2008;16:80-91.

[5] Zhang S, Zhang X, Zhao C, Li J, Song Y, Xie C, et al. Research on an Mg–Zn alloy as a degradable biomaterial. Acta Biomaterialia 2010;6:626-40.

[6] Gunde P. Ph D Thesis: Biodegradable magnesium alloys for osteosynthesis-Alloy development and surface modifications. Zurich: ETH 2010.

[7] Li J, Cao P, Zhang X, Zhang S, He Y. In vitro degradation and cell attachment of a PLGA coated biodegradable Mg6Zn based alloy. Journal of Materials Science 2010;45:6038-45.

[8] Song G. Control of biodegradation of biocompatible magnesium alloys. Corrosion Science 2007;49:1696-701.

[9] Song G. Recent Progress in Corrosion and Protection of Magnesium Alloys. Advanced Engineering Materials 2005;7:563-86.

[10] Navarro M, Ginebra MP, Planell JA, Barrias CC, Barbosa MA. In vitro degradation behavior of a novel bioresorbable composite material based on PLA and a soluble CaP glass. Acta Biomaterialia 2005;1:411-9.

[11] Russias J, Saiz E, Nalla RK, Gryn K, Ritchie RO, Tomsia AP. Fabrication and mechanical properties of PLA/HA composites: A study of in vitro degradation. Materials Science and Engineering C 2006;26:1289-95.

[12] Meer SATvd, Wijn JRd, Wolke JGC. The influence of basic filler materials on the degradation of amorphous D- and L-lactide copolymer. Journal of Materials Science: Materials in Medicine 1996;7:359-61

[13] Hornberger H, Virtanen S, Boccaccini AR. Biomedical coatings on magnesium alloys – A review. Acta Biomaterialia 2012;8:2442-55.

[14] Wu G, Ibrahim JM, Chu PK. Surface design of biodegradable magnesium alloys — A review. Surface and Coatings Technology 2013;233:2-12.

[15] Ara M, Watanabe M, Imai Y. Effect of blending calcium compounds on hydrolytic degradation of poly(dl-lactic acid-co-glycolic acid). Biomaterials 2002;23:2479-83.

[16] Shikinami Y, Okuno M. Bioresorbable devices made of forged composites of hydroxyapatite (HA) particles and poly-L-lactide (PLLA): Part I. Basic characteristics. Biomaterials 1999;20:859-77.

[17] Tsuji H, Ikada Y. Properties and morphology of poly(L-lactide). II. Hydrolysis in alkaline solution. Journal of Polymer Science Part A: Polymer Chemistry 1998;36:59-66.
[18] Burkersroda Fv, Schedl L, Göpferich A. Why degradable polymers undergo surface erosion or bulk erosion. Biomaterials 2002;23:4221-31.
[19] Wong HM, Yeung KWK, Lam KO, Tam V, Chu PK, Luk KDK, et al. A biodegradable polymer-based coating to control the performance of magnesium alloy orthopaedic implants. Biomaterials 2010;31:2084-96.
[20] Degner J, Singer F, Cordero L, Boccaccini AR, Virtanen S. Electrochemical investigations of magnesium in DMEM with biodegradable polycaprolactone coating as corrosion barrier. Applied Surface Science 2013;282:264-70.
[21] da Conceicao TF, Scharnagl N, Dietzel W, Kainer KU. Corrosion protection of magnesium AZ31 alloy using poly(ether imide) [PEI] coatings prepared by the dip coating method: Influence of solvent and substrate pre-treatment. Corrosion Science 2011;53:338-46.
[22] Xu L, Yamamoto A. Characteristics and cytocompatibility of biodegradable polymer film on magnesium by spin coating. Colloids and Surfaces B: Biointerfaces 2012;93:67-74.
[23] Xu L, Yamamoto A. In vitro degradation of biodegradable polymer-coated magnesium under cell culture condition. Applied Surface Science 2012;258:6353-8.
[24] Witte F, Kaese V, Haferkamp H, Switzer E, Meyer-Lindenberg A, Wirth CJ, et al. In vivo corrosion of four magnesium alloys and the associated bone response. Biomaterials 2005;26:3557-63.
[25] Kirkland NT, Birbilis N, Staiger MP. Assessing the corrosion of biodegradable magnesium implants: A critical review of current methodologies and their limitations. Acta Biomaterialia 2012;8:925-36.
[26] Ghali E, Dietzel W, Kainer KU. General and Localized Corrosion of Magnesium Alloys: A critical Review. Journal of Materials Engineering and Performance 2004;13:7-23.
[27] Ghali E, Dietzel W, Kainer KU. Testing of General and Localized Corrosion of Magnesium Alloys: A Critical Review. Journal of Materials Engineering and Performance 2004;13:517-29.
[28] Lorenz C, Brunner JG, Kollmannsberger P, Jaafar L, Fabry B, Virtanen S. Effect of surface pre-treatments on biocompatibility of magnesium. Acta Biomaterialia 2009;5:2783-9.
[29] Schinhammer M, Hofstetter J, Wegmann C, Moszner F, Löffler JF, Uggowitzer PJ. On the Immersion Testing of Degradable Implant Materials in Simulated Body Fluid: Active pH Regulation Using CO2. Advanced Engineering Materials 2013:1-8.
[30] Song G, Song S-Z. Corrosion Behaviour of Pure Magnesium in a Simulated Body Fluid. Acta Physico-Chimica Sinica 2006;22:1222-6.
[31] Li S, Garreau H, Vert M. Structure-property relationships in the case of the degradation of massive poly(α-hydroxy acids) in aqueous media. Journal of Materials Science: Materials in Medicine 1990;1:198-206.
[32] Shogren R. Water vapor permeability of biodegradable polymers. Journal of Environmental Polymer Degradation 1997;5:91-5.

[33] Tsuji H, Ikarashi K. In Vitro Hydrolysis of Poly(l-lactide) Crystalline Residues as Extended-Chain Crystallites:$II. Effects of Hydrolysis Temperature. Biomacromolecules 2004;5:1021-8.
[34] Penco M, Marcioni S, Ferruti P, D'Antone S, Deghenghi R. Degradation behaviour of block copolymers containing poly(lactic-glycolic acid) and poly(ethylene glycol) segments. Biomaterials 1996;17:1583-90.
[35] Cho H, An J. The effect of ε-caproyl/d,l-lactyl unit composition on the hydrolytic degradation of poly(d,l-lactide-ran-ε-caprolactone)-poly(ethylene glycol)-poly(d,l-lactide-ran-ε-caprolactone). Biomaterials 2006;27:544-52.
[36] Kimura Y, Matsuzaki Y, Yamane H, Kitao T. Preparation of block copoly(ester-ether) comprising poly(l-lactide) and poly(oxypropylene) and degradation of its fibre in vitro and in vivo. Polymer 1989;30:1342-9.
[37] Cam D, Hyon S-h, Ikada Y. Degradation of high molecular weight poly(l-lactide) in alkaline medium. Biomaterials 1995;16:833-43.
[38] Yuan X, Mak AFT, Yao K. Surface degradation of poly(l-lactic acid) fibres in a concentrated alkaline solution. Polymer Degradation and Stability 2003;79:45-52.
[39] Ehrenstein G, Schmiemann A. Corrosion phenomena in glass-fiber reinforced thermosetting resins. Handbook of ceramics and composites Synthesis and properties. New York: Marcel Dekker Inc; 1990. p. 231-68.
[40] Xin Y, Hu T, Chu PK. In vitro studies of biomedical magnesium alloys in a simulated physiological environment: A review. Acta Biomaterialia 2011;7:1452-9.
[41] Huan ZG, Leeflang MA, Zhou J, Fratila-Apachitei LE, Duszczyk J. In vitro degradation behavior and cytocompatibility of Mg–Zn–Zr alloys. Journal of Materials Science: Materials in Medicine 2010;21:2623-35.
[42] Dürselen L, Dauner M, Hierlemann H, Planck H, Claes LE, Ignatius A. Resorbable polymer fibers for ligament augmentation. Journal of Biomedical Materials Research 2001;58:666-72.

IN VITRO DEGRADATION OF PLA/Mg COMPOSITES: RELEVANCE OF MATRIX AND FILLER NATURE

CHAPTER 8

"Every kid starts out as a natural-born scientist, and then we beat it out of them. A few trickle through the system with their wonder and enthusiasm for science intact"

Carl Sagan

Table of contents

8. IN VITRO DEGRADATION OF PLA/Mg COMPOSITES: RELEVANCE OF POLYMERIC MATRIX AND Mg PARTICLES NATURE

8.1. Introduction

The novel PLA/Mg composites are materials with great potential for use as biodegradable implants. They have better mechanical properties than the unreinforced polymer [1] (Chapter 6), and moreover, it has been demonstrated that small Mg contents (0.2 – 1 wt.%) increase significantly the viability of human mesenchymal stem cells cultured on the material (Chapter 7). However, exhibiting good initial properties is not enough to achieve an adequate performance *in vivo*. Stability of the material over time is very important; how long the material keeps its functional properties is what matters at all.

For a resorbable implant, the optimal strength retention and total mass loss with time depends on the patient- if it is a pediatric patient or an adult -and the specific orthopaedic application- if it is for craniomaxillofacial surgery, arthroscopy or spinal area [2-4]. Therefore, resorbable medical devices must be developed in order to have an appropriate degradation rate in agreement with the healing rate of bone in the implantation site. This can be achieved by the control of their degradation kinetics.

Kinetics can be controlled if the chemical reactions that are involved in the degradation of the composite are understood. Hydrolysis of the polymeric matrix and corrosion of Mg are the two main reactions that lead to the breaking down of the novel PLA/Mg composites. Understanding degradation kinetics of PLA/Mg composites will allow the prediction of the stability of the implant. *In vivo* degradation kinetics of polymers based on polylactic acid, can be predicted in some extent from their *in vitro* degradation behaviour [5, 6]. In order to control *in vitro* degradation kinetics of PLA/Mg composites, it is necessary to control either the hydrolysis of the matrix and/or the corrosion of Mg.

The hydrolytic degradation rate of poly(α-hydroxyacids) depends on the molecular weight and structure of the polymer, crystallinity degree, and the incorporation of additives, other polymers or fillers [7]. It has been found that a molecule with a low molecular weight ($4x10^4$ Da) has a increased density of terminal groups (carboxyl and hydroxyl) and hence a higher hydrolyzability than a high molecular weight molecule [8]. However, small incorporations of D-lactyde units (0.2 – 1.2 %) have greater effect enhancing PLLA degradation rate than the reduction in molecular weight [9]. Other studies explain that the resistance to hydrolysis of PLA can be improved by forming blends of poly(L-lactide) PLLA and poly(D-lactide) PDLA or forming poly(L-lactide-co-D-lactide) copolymers due to the formation of stable stereocomplexes [10].

The initial crystallinity can also affect the hydrolysis of the polymer. Tsuji *et al*. [11] reported that the hydrolyzability of poly(L-lactide-co-D.-lactide) (P(LLA-DLA); 95/5) decreases with increasing crystallinity. For PLLA [12,13] and PLLA/PDLA blends [14], however, the hydrolytic degradation rate becomes higher with an increase in the crystalline degree. Regarding the addition of polymers or fillers, it has been demonstrated that their hydrophilicity enhances the degradation rate of PLLA [7, 8]. Basic additives like MgO, calcium compounds or tricalcium phosphates were found to reduce the hydrolytic degradation rate of PLA by the neutralization of carboxylic groups formed by the hydrolytic degradation of the polymer [15, 16].

Strategies to decrease Mg corrosion rate have been addressed by tailoring the composition and microstructure of the alloy. Commercial alloys with aluminium (Al) and rare earth elements (REs) (AZ31, AZ91, WE43, WE54, ZM21, ZEK100) have been investigated for their application fixing bone fractures [17]. Although these alloys provide a good initial mechanical performance, concerns appear regarding the cytotoxicity and biosafety of Al and REs. For instance, Al has proved to have neurotoxic effects [18]. Studies with rats have demonstrated that long term intake of REs can change the expression of some genes [19]. Consequently, above certain levels, these alloying elements could be unsuitable for biomedical Mg materials.

More suitable for the intended medical application is the approach of alloying Mg with biologically important elements like Ca and Zn. Binary alloys Mg-Ca, Mg-Zn, ternary alloys Mg-Zn-Ca and bulk metallic glasses improve Mg corrosion resistance and mechanical properties [20, 21].

This chapter aims to clarify the effects of the polymeric matrix properties -nature, and crystallinity- and Mg particles composition and shape, on the control of the degradation rate of the novel PLA/Mg composites. The study of the *in vitro* degradation behaviour and kinetics is addressed by hydrogen release assays, pH monitoring, water uptake, mass loss and changes in morphology. Compressive mechanical properties as a function of degradation time are also studied to analyse the *in vitro* strength retention of the composite.

8.2. Materials and methods

8.2.1. Materials

PLA/Mg cylinders of 9 mm high and 6 mm diameter were processed by extrusion and moulded by compression following the method described in Chapter 6. Two polymers were used for the matrix: poly-L-lactic (PLLA) from Goodfellow and poly-L,D-lactic acid (PLDA) from Natureworks. The viscosity average molecular weight and melt flow index (MFI 210 ºC/2.16 kg) of both polymers was very similar: 89 kDa and 35.8 g/10 min for PLLA and 95 kDa and 35.4 g/10 min for PLDA. As reinforcement, irregular flake-like Mg particles and spherical Mg and Mg5Zn particles of less than 50 μm in size were used.

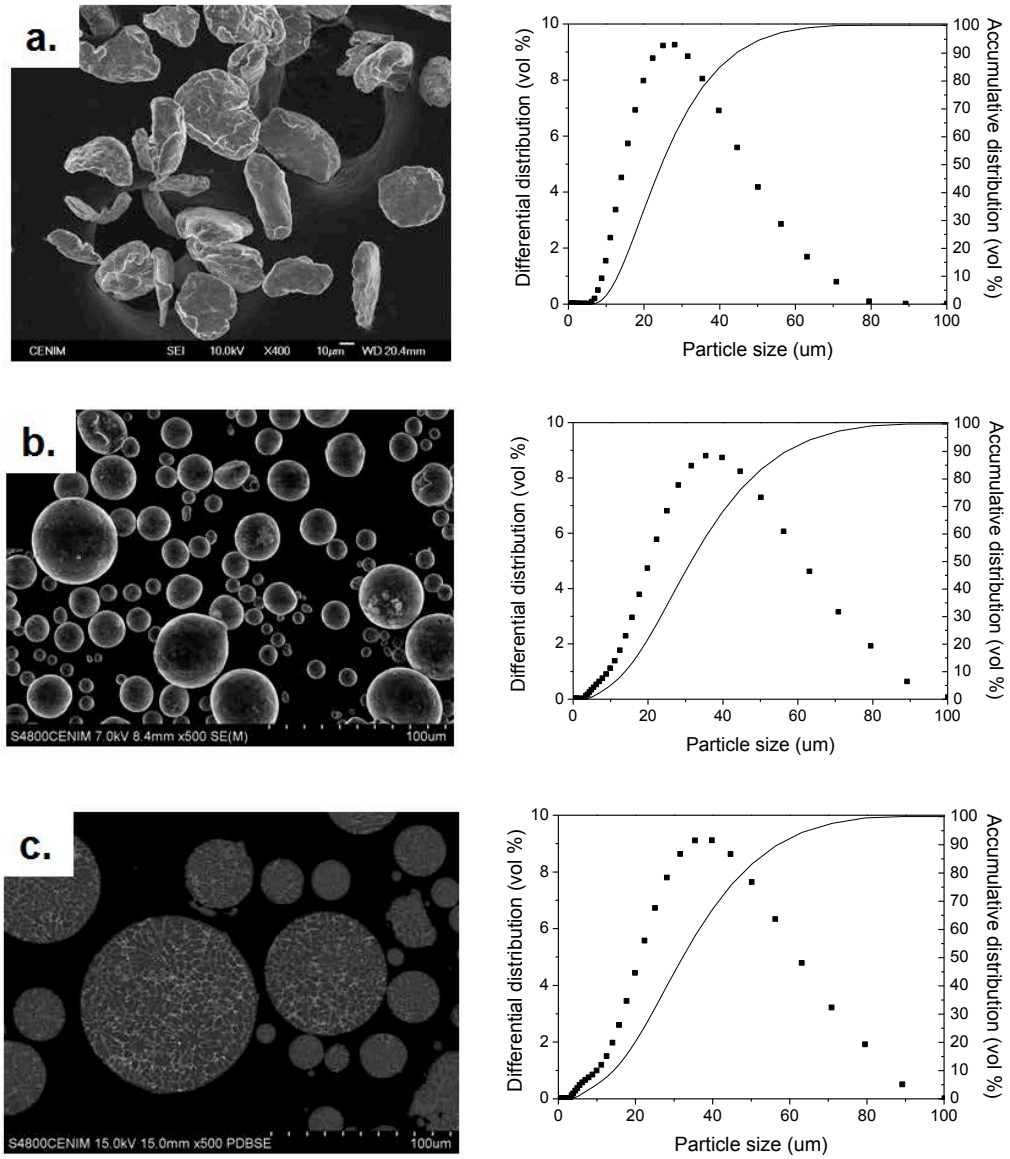

Figure 8.1 SEM images (left) and particle size distribution (right) of a) irregular flake like Mg particles, b) spherical Mg particles and c) spherical Mg5Zn particles

The irregular Mg particles were delivered by Goodfellow, with a purity of 99.9% and a length to width ratio of 1.6:1, with a median particle size of 24.6 μm. The spherical particles were obtained by centrifugal atomization (TLS Technik, Germany) of cast ingots of pure Mg (99.9% Mg; 0.05% Cu, Fe, Si and Al; 0.001% Ni) and electrolytic Zn with a purity of 99.995%. The atomized powder was sieved to retain particles of less than 50 μm, resulting in median particle

diameter of 31.4 μm (Mg) and 32.5 (Mg5Zn). Particle size distribution and aspect ratio were measured by a Malvern 2000 laser-scattering particle size analyser. Figure 8.1 presents images of the three powders and their particle size distribution.

The study of the relevance of matrix nature on the degradation of PLA/Mg composites was performed by comparing the *in vitro* behaviour of three composites reinforced with 10 wt.% of irregular-flake shape Mg particles, but with different polymeric matrices: PLLA, PLDA and crystalline PLDA (hereafter PLDA_TT). The crystalline composite was obtained by a thermal treatment at 125 ºC during 30 minutes.

The study of the relevance of Mg particle shape on the degradation of PLA/Mg composites was carried out by comparing the *in vitro* degradation of two composites with the same polymeric matrix (PLDA) but reinforced with 10 wt.% of Mg particles with different shape: irregular-flake (IRR) and spherical (SPH). The relevance of the nature of the reinforcement was studied by comparing two composites reinforced with spherical particles, but one reinforced with Mg and the other one with Mg5Zn.

For comparison purposes, unreinforced polymers (PLLA, PLDA and crystalline PLDA) and as-cast pure Mg and Mg5Zn cylinders were also processed with the same geometry of composites and submitted to the same *in vitro* testing routine. Table 8.1 summarises the nomenclature used for the materials studied in this chapter and their main characteristics.

Table 8.1 Nomenclature of the materials used and their main characteristics

Material	Matrix	Mg wt.%	Mg shape	f_c
PLLA	Poly-L-lactic acid	0	-	0.18
PLDA	poly-L,D-lactic acid	0	-	0.07
PLDA_TT	Poly-L,D-lactic acid	0	-	0.46
PLLA10Mg	Poly-L-lactic acid	10	Irregular-flake	0.11
PLDA10Mg	Poly-L,D-lactic acid	10	Irregular-flake	0.08
PLDA10Mg_TT	Poly-L,D-lactic acid	10	Irregular-flake	0.47
PLDA10Mg_IRR	Poly-L,D-lactic acid	10	Irregular-flake	0.08
PLDA10Mg_SPH	Poly-L,D-lactic acid	10	spherical	0.07
PLDA10Mg5Zn-SPH	Poly-L,D-lactic acid	10	spherical	0.09
Mg	-	99.9%	-	-
Mg5Zn	-	94%	-	-

The *in vitro* degradation kinetics was assessed by immersion of the specimens in distilled water and in Phosphate Buffered Saline solution (PBS), which is a buffered solution (~ pH 7.4) that simulates human fluids.

8.2.2. Hydrogen release

Measurement of hydrogen release was performed in the PBS solution using a ratio of 20 ml/cm^2 of sample surface. Three cylindrical shape specimens (9 mm high and 6 mm diameter) were used for each condition. Each specimen was placed under an inverted glass funnel with a burette over the top of each funnel to capture the hydrogen. The solution level in each burette was measured twice a day and related to the sample area. Experiments were performed twice: during 7 days and during 28 days.

8.2.3. pH evolution

For the study of pH evolution, specimens were individually introduced into a test tube containing the media in a ratio of volume of media (ml) to specimen surface (cm^2) of 20:1, and then closed to avoid evaporation. Experiments were performed in parallel in a buffered media (PBS) and in distilled water, to study the nature of degradation products by measuring pH changes also in a non buffered media. The media were fully renovated every seven days. Experiments were run at a constant temperature of 37 ± 1 ºC, by introducing the test tubes in a thermostatic bath. The results correspond to average values of three specimens. pH was recorded with a Lazar equipment. The electrode was calibrated every day. Measurements were done after each hour for the first 10 h and then once a day until completion of the experiment. Two set of experiments were performed: one lasting 7 days and a second during 28 days.

8.2.4. Mass variation and water retention

The weight of the cylinders was measured before beginning the experiments and after 7 and 28 days in PBS. Wet samples (Wet (t)) were weighted immediately after removing from the solution and drying their surface with a paper towel; dry samples (Dry (t)) were measured after keeping them for 8 h under vacuum and 2 weeks in a desiccator. Water accumulation was obtained from the wet mass of samples and the dry samples mass. The loss of mass was calculated from the dry samples mass and the initial mass (Mass (0)). A precision balance was employed to weight all samples within an error of 0.05 mg. The results are given in % of mass with respect to the reference sample according to Equations 8.1 and 8.2.

$$\text{Water uptake} = \frac{\text{Wet(t)} - \text{Dry(t)}}{\text{Dry(t)}} * 100\% \qquad \text{Equation 8.1}$$

$$\text{Mass variation} = \frac{\text{Dry(t)} - \text{Mass(0)}}{\text{Mass(0)}} * 100\% \qquad \text{Equation 8.2}$$

8.2.5. Morphology

The cylinders surfaces and longitudinal sections were characterised by optical microscopy (OM) and scanning electron microscopy (SEM) equipped with energy dispersive X-ray spectroscopy (EDS). Longitudinal diametric sections were cut and mechanically polished with 9 μm diamond paste; a thin graphite layer was deposited on the samples for SEM examination.

8.2.6. Mechanical properties

The effect of *in vitro* degradation on the mechanical properties of composites was assessed by compression tests. The compressive mechanical behaviour was studied in a universal machine EM2/100/FR-10kN Micro Tests at ambient conditions, using a strain rate of $5x10^{-3}$ s^{-1}. Cylindrical samples tested for pH measurements in PBS were used for compression tests after 7 and 28 days of immersion.

8.3. Results and discussion

8.3.1. Relevance of matrix nature

The role that plays the nature and crystallinity degree of the polymeric matrix on the degradation of PLA/Mg composites can be understood by comparing the *in vitro* degradation kinetics of PLLA10Mg, PLDA10Mg and PLDA10Mg_TT composites. The joint analysis of the amount of H_2 released, the changes in pH in buffered and non-buffered media, variations in mass and morphology of each material can lead to elucidate the relevance of the polymeric matrix in tailoring the degradation rate of PLA/Mg composites.

8.3.1.1. Hydrogen release

Figure 8.2 shows the hydrogen release in H_2 ml / cm^2 as a function of immersion time in PBS for three composites with different polymeric matrices: amorphous PLLA, amorphous PLDA and crystalline PLDA. The hydrogen release of as cast Mg is shown as a reference. In order to compare the materials with greater clarity and to facilitate an explanation of the results, Figure 8.2 is divided into 4 zones. The first one (I) goes from day 1 to 6, the second zone (II) from day 6 to 12, the third one (III) takes the range from 12 – 20, and the last one (IV) from 20 to 28. Table 8.2 summarizes the slopes of the curves for each material and in each zone.

In the first zone the material that has the highest hydrogen release rate is the PLLA10Mg, and the one with the lowest rate is the PLDA10Mg. During the first 6 days the crystalline material (PLDA10Mg_TT) releases more than 1.7 times the hydrogen that releases the amorphous PLDA10Mg composite. Meanwhile, the composite with the poly-L-lactic acid matrix releases 1.4 times more hydrogen than the material with the PLDA matrix.

In the second zone, PLLA10Mg and PLDA10Mg_TT release H_2 at the same rate of the first week and PLDA10Mg hydrogen release rate increases. In this region, at day 11 all the materials release the same amount of hydrogen, approximately 5.3 ml/cm^2.

In zone III all materials decrease their hydrogen release rate and tend to achieve stabilization at day 20. In the third zone the material having the highest rate of hydrogen release is PLLA10Mg, followed by the PLDA10Mg_TT and the one with the lowest slope is the PLDA10Mg. In zone IV the hydrogen release reaches equilibrium and slopes of all materials tend to zero. At day 28 PLLA10Mg has released 10% more hydrogen than amorphous and crystalline composites having PLDA as a matrix. PLDA10Mg_TT releases more hydrogen than its amorphous homologous during the whole experiment, until it reaches stabilization in zone IV, where it evolves the same amount of hydrogen as PLDA10Mg.

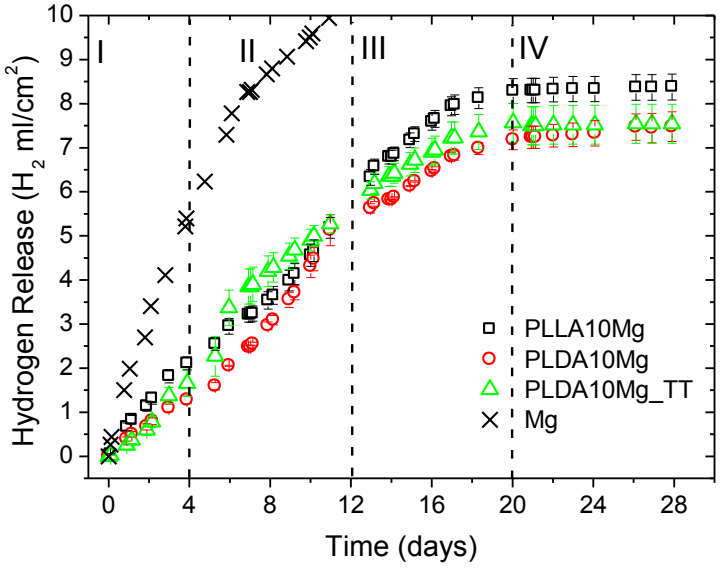

Figure 8.2 Accumulated amount of hydrogen released as a function of immersion time in PBS

All the composites release hydrogen at a lower rate than the metallic Mg. A monolithic Mg cylinder produces in only 7 days the total amount of hydrogen that the PLLA10Mg releases in nearly a month (8 ml H_2/cm^2).

The amount of Mg that reacted was calculated stoichiometrically from the data of volume of hydrogen evolved. Figure 8.3 shows the mass loss of Mg in terms of mass loss percentage with reference to the composite material and depending on the immersion time. It is observed that all the composites lost nearly the 6% of their mass, which means that nearly 60% of all the Mg present in the materials has reacted after 28 days.

Table 8.2 Hydrogen release in ml/cm^2 per day in each zone of Figure 8.2

Material	H_2 ml/cm^2 per day			
	I	II	III	IV
PLLA10Mg	0.48	0.49	0.35	0.012
PLDA10Mg	0.31	0.56	0.28	0.038
PLDA10Mg_TT	0.44	0.45	0.30	0.012
Mg	1.8	0.45	0.24	0.24

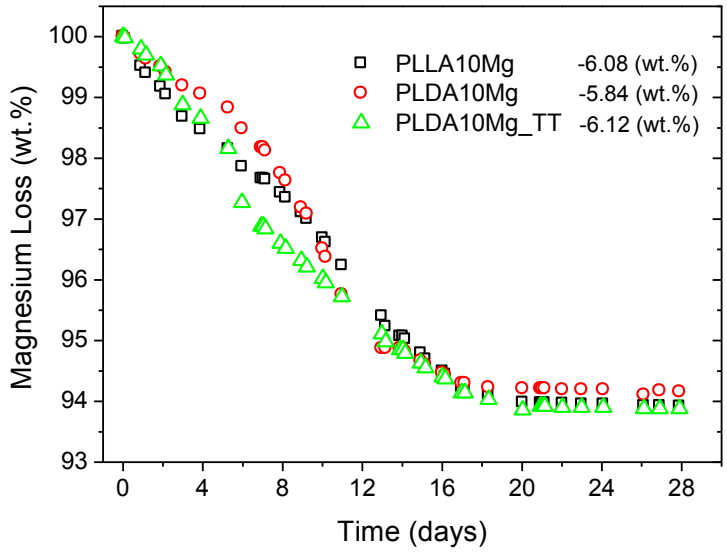

Figure 8.3 Mg loss in terms of mass loss with respect to the composite as a function of immersion time in PBS

Comparing the amorphous matrices it follows that hydrogen release rate of PLLA10Mg is higher than that of PLDA10Mg. As both polymers have similar molecular weight, and crystallinity degree, the explanation of this behaviour relies on the nature of the polymer. The percentage of D-lactyl units in the polymer affects its hydrolysis [7]. Stereocopolymers poly(L-lactide co-D-lactide) have greater hydrolysis resistance than PLLA [10]. Tsuji *et al*. have found that the addition of poly(D-lactide) to PLLA generates a strong interaction between PLLA chains and PLDA chains that results in stereocomplex formation [22]. This interaction disturbs the diffusion of water into the material and lowers the hydrolytic degradation rate [14, 23-25]. Diffusion of water within PLLA may proceed easier than in PLDA, given the stronger chain interactions

between PLDA chains. This could explain the higher hydrogen release of PLLA10Mg composite in comparison to PLDA10Mg.

The composite with the crystalline matrix releases a higher amount of hydrogen during the first three weeks than its amorphous homologous. This behaviour could be explained by the analysis of the diffusion of water through both different matrices. Water penetrates uniformly within an amorphous matrix, whereas it diffuses preferentially into the amorphous regions of a semi-crystalline matrix [7]. This has been the explanation of some studies that have demonstrated that a semi-crystalline polymeric coating induces pitting corrosion and enhances the corrosion rate of Mg substrate [26]. If water penetrates preferentially into amorphous domain of crystalline PLDA, then the surface of Mg particles in PLDA10Mg_TT is surrounded by hydrated amorphous domains and non-hydrated ordered structures. The non-uniform distribution of water around each particle can induce a localized corrosion of the metal, which eventually can enhance its degradation rate.

8.3.1.2. pH evolution

The evolution of pH in both immersion media, PBS and distilled water, containing the composites and polymeric reference samples, was monitored during 28 days. Figure 8.4.a shows the measured pH values for the unreinforced polymers, Figure 8.4.b depicts the pH evolution of composites in distilled water, and Figure 8.4.c shows the pH behaviour of the buffered media containing the composites.

Measurements in PBS demonstrate that a controlled neutral pH, ranging from 7.2 to 7.5, is maintained during the whole test for the polymeric samples used as references (Figure 8.4.a) and also for composites (Figure 8.4.c). On the contrary, Mg cylinders corrosion in PBS surpassed PBS buffer capacity, as the pH increased above 10 in only one day (not shown in Figures). This behaviour of Mg in a buffered solution is widely documented [27-29] and elucidates one important concern regarding the applicability of Mg alloys in the biomedical field, the possible alkalization of the physiological environment.

PH of distilled water containing the unreinforced polymers ranges between 6.8 and 5.0 (Figure 8.4.a). All the polymers exhibit the same pH behaviour. In the case of composites, pH rises sharply up to about 10 during the first day. Behaviour of pH during the first week is the same for all the composites. From then on pH starts to diminish. During the last week, the material that more increases the pH of distilled water is PLLA10Mg, the behaviour of both composites with PLDA matrix is very similar and their pH increment is lower than that of PLLA10Mg. This behaviour is in agreement with hydrogen release results, where the PLLA10Mg releases the highest amount of hydrogen, which consequently induces the highest alkalinisation of the media. PLDA10Mg and PLDA10Mg_TT release a lower volume of H_2 than that of PLLA10Mg. If less hydrogen is produced, this means that less $(OH)^-$ are released to the media. The

explanation of this behaviour is elucidated together with the analysis of mass variation, water retention and morphology in the following sections of this chapter.

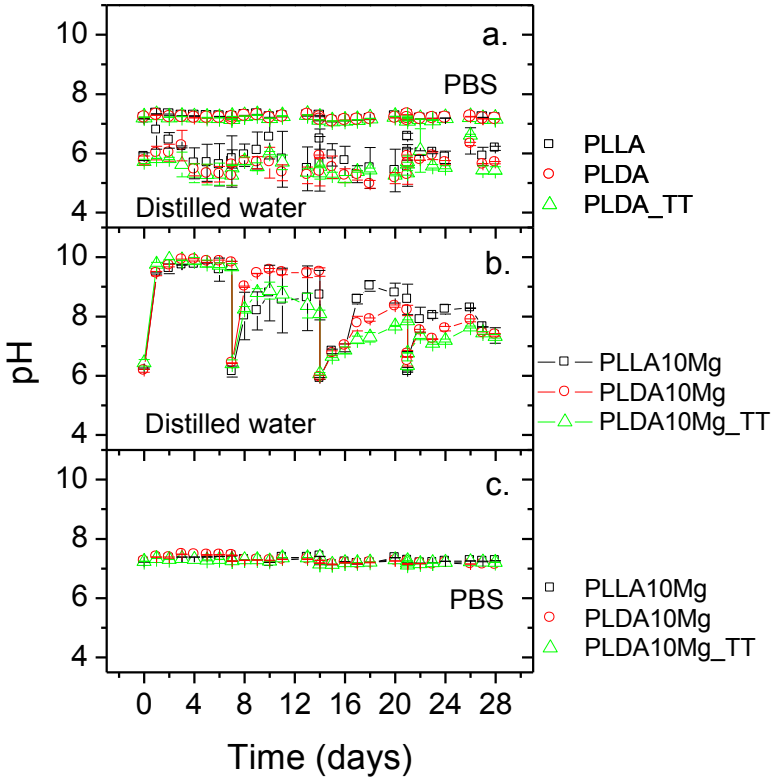

Figure 8.4 Evolution of pH of unreinforced polymers in distilled water and in PBS (a), composites in distilled water (b) and composites in PBS (c)

8.3.1.3. Mass variation and water retention

The amount of water that the unreinforced polymers and the composites retained after 7 and 28 days of immersion in PBS is depicted in Figure 8.5.a. The accumulation of water (or PBS solution) within the matrix can be due to the presence of amorphous domains within the polymeric matrix where water diffuses preferentially, or to the presence of pores, cracks and capillars that are formed as a consequence of the degradation of the polymeric matrix and Mg particles. The amount of retained water can be correlated with the extent of composite degradation [30-32].

Regarding unreinforced polymers behaviour, their water retention does not exceed the 1%. There are no remarkable differences between the water retention of PLLA and PLDA. However

crystalline PLDA_TT retains less water than amorphous PLDA after the first week. This is due to the decrement of water absorption rate with increasing crystallinity degree in polylactic acids [33-36]. After 28 days, all the polymers exhibit the same water equilibrium content around 0.8 %. This value falls within the range of the equilibrium water content of poly(alpha-hydroxyacids), which goes from 0.3% to 2.6% depending on the monomer unit [7, 30].

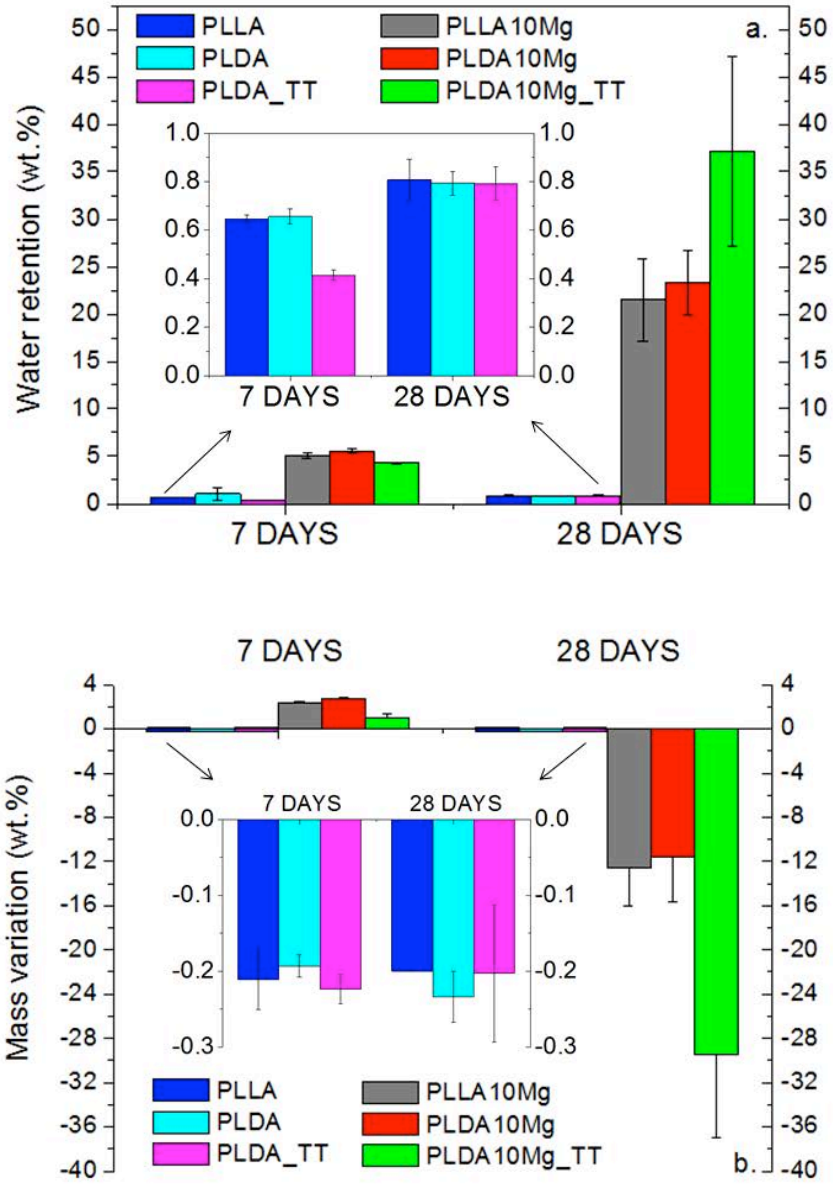

Figure 8.5 Unreinforced polymers and composites percentage of mass gain due to water uptake (a) and mass variation (b) after 7 and 28 days of immersion in PBS

Water diffusion through polymeric matrices increases with the incorporation of Mg particles and with time. A Mg content of 10 wt.% increases the accumulation of water in the matrix by nearly ten times after 1 week in PBS. If the unreinforced PLLA and PLDA retained at 7 days 0.65 % of water, the composites (PLLA10Mg and PLDA10Mg) accumulate around 5.0 % of solution. Unreinforced crystalline PLDA_TT presented a water uptake of 0.4% but the composite accumulates 4.2 % of water within the matrix. Comparison of polymers water retention with that of composites turns out to be more impressive at 28 days. After four weeks, PLLA10Mg and PLDA10Mg composites retain 30 times the amount of water accumulated by the polymer references. The water uptake of the crystalline composite (PLDA10Mg_TT) is 50 times the amount of water that the unreinforced crystalline polymer retains. Therefore, it is demonstrated that the incorporation of Mg particles within the matrix increases the diffusion of water within the amorphous domains of the polymer.

If the results are analyzed with respect to time, it is observed that the water retained by unreinforced polymers after being immersed in PBS for 28 days, increases very slightly in comparison to the amount that they accumulated at 7 days. However, composites with amorphous matrices (PLLA10Mg and PLDA10Mg) retained at 28 days 4 times more water than that retained in a week. The crystalline composite water uptake after 4 weeks is almost ten times the amount of moisture accumulated during the first week. The increment of water retention with degradation time implies the increment of paths, like pores or cracks, which accelerate and facilitate the diffusion of water within the polymeric matrix. The greater increment in water uptake of the crystalline composite in respect to the amorphous ones implies that it underwent more changes due to degradation (i.e. Mg corrosion or polymer hydrolysis) than the other composites.

The evolution of *in vitro* degradation can also be analyzed by the results of mass variation (Figure 8.5.b). It is observed that unreinforced polymers underwent a very slight mass loss and no differences between them are evidenced. On the other hand, composites evidence first a mass gain at 7 days and all the composites lose mass after 4 weeks. The increment in mass percentage can occur due to precipitating reaction products (Mg hydroxides or phosphates) formed during Mg corrosion that can remain in the samples. Then, as material degradation progresses, Mg particles continue reacting and the polymer starts also to degrade, creating pores and cracks that may generate mass loss. This hypothesis is verified considering that the percentage in mass loss calculated by differences in weight (Figure 8.5.b) is larger than the Mg loss calculated from hydrogen release (Figure 8.3). This implies that the loss of mass is not only due to Mg reaction, but also it is due to hydrolysis of polymeric matrices.

Composites with amorphous matrix exhibit a similar mass loss (around -12 wt.%). Interestingly, the material that loses the highest amount of mass is the crystalline composite (PLDA10Mg_TT). These finding is somewhat puzzling, since the crystalline composite is not the

material that releases the highest amount of hydrogen after 28 days. This behaviour, however, can be explained analyzing the morphology of degraded samples, and comparing them with the original specimens.

8.3.1.4. Morphology

Changes in composites morphology with time are shown through Figure 8.6 – 8.8. Figure 8.6 shows the degraded cylinders, after 7 and 28 days immersed in PBS and as processed original cylinders. Cross sections of the samples are shown in Figure 8.7 by stereoscopic and optical microscopy. Figure 8.8 compares the morphology of amorphous PLDA10Mg and crystalline PLDA10Mg_TT by backscattered images of their longitudinal sections after 28 days of immersion in PBS.

Amorphous cylinders (PLLA10Mg and PLDA10Mg) swell with increasing degradation time and consequently their dimensions change and their volume increases (Figure 8.6). On the contrary, crystalline composite does not present swelling. PLLA10Mg exhibits erosion at composite surface after 28 days. Cracks are formed on PLDA10Mg composite, after only 7 days. The cracks become larger and deeper with increasing time. Cracks may be responsible for the increment on hydrogen release rate in zone II of Figure 8.2. A crack exposes more surfaces to the media; therefore, it is easier for the solution to diffuse inside the material. As a consequence, available reaction sites increase and as a result hydrogen release rate becomes greater. Regarding the crystalline material, it presents erosion after 7 days. Material is detached from its surface leaving holes.

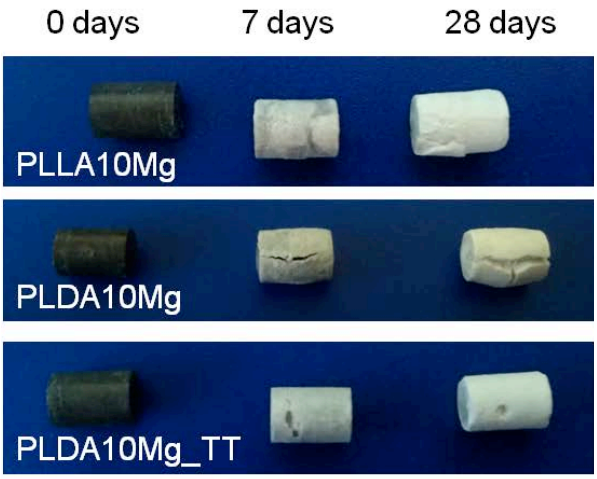

Figure 8.6 Photographs of the composites from left to right: original, after 7 days, and after 28 days immersed in PBS.

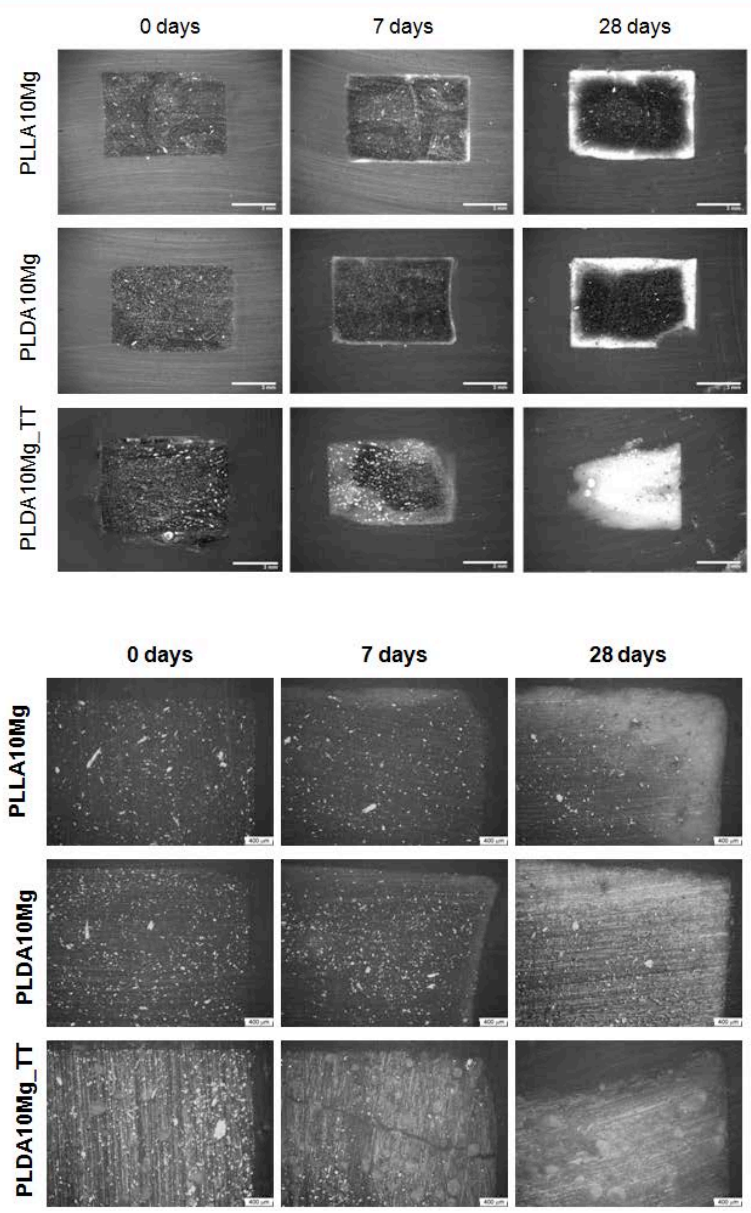

Figure 8.7 Cross section pictures taken by stereoscopic microscopy (a) and by optical microscopy (b)

Stereoscopic and optical microscopy images show that degradation of PLLA10Mg and PLDA10Mg composites proceeds with a very similar behaviour (Figure 8.7). Mg particles at the surface react first, and as time lapses particles corrosion proceeds from the surface to the core. This is evidenced by the formation of a white halo at samples surface, which becomes wider with increasing immersion time. Regarding the crystalline composites PLDA10Mg_TT, the white halo is thicker than that of amorphous composites at day 7 and it seems that degradation proceeded through all the sample bulk at day 28, as even Mg particles at the core are corroded. Cross section of PLDA10Mg_TT shows a wide grey halo distributed non-uniformly through the

sample at day 7. At day 28 it is evident the erosion of the sample and also the absence of gray zones across de section, almost the whole sample has become white. The specimen dimensions decrease, as the borders and edges have detached from the composite. This would explain the highest water uptake by the system at 28 days (Figure 8.5.a) and the highest mass loss.

In order to compare the behaviour of an amorphous composite with that of crystalline, cross sections of PLDA10Mg and PLDA10Mg_TT cylinders were observed by scanning electron microscopy and the evolution of Mg particles and the integrity of the cylinders was analyzed. Figure 8.7 shows the images of amorphous (PLDA10Mg) and crystalline (PLDA10Mg_TT) composites, after 28 days immersed in PBS, at the centre and at the border of cylindrical samples.

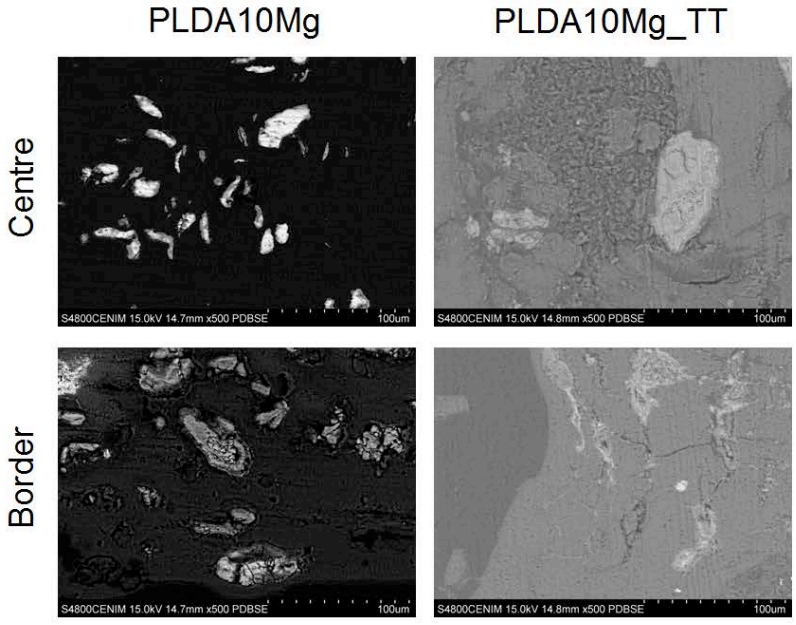

Figure 8.8 Backscattered electron images of longitudinal sections of PLDA10Mg and PLDA10Mg_TT composites after 28 days of immersion in PBS

It is clearly observed that the crystalline matrix is more deteriorated than the amorphous one. PLDA10Mg_TT presents corroded Mg particles, cracks and detachments at the border. At the centre of the cylinder, Mg particles are corroded and polymeric matrix shows evident damage. On the contrary, metallic Mg is still present at the centre of PLDA10Mg composite, only few Mg particles with reaction phases at their surface can be seen. Polymeric matrix does not exhibit deterioration at the centre of the amorphous sample. However, at the border it is evident that the polymer that surrounds the particles is degraded and Mg is fully corroded.

Some studies indicate that increasing the crystallinity of poly-L-lactic acid decreases its degradation rate [37, 38]. However, Tsuji *et al.* have shown that the hydrolyzability is higher for the crystallized polymers than for the amorphous, in the case of mixtures of poly-L-lactide with poly-D-lactide [14]. The enhanced hydrolysis of polylactic films with a higher initial crystallinity degree can be explained by the increased density of terminal groups (carboxyl -COOH and hydroxyl -OH) in the amorphous region between the crystalline regions in comparison with that in a completely amorphous polymer [12]. The high density of hydrophilic terminal groups enhances the diffusion of water molecules within the matrix and increases the water content. Additionally, the high number of terminal groups per unit mass cause loose chain packing in the amorphous region between the lamellae, which increases the diffusion rate of water as well. The elevated water diffusion rate accelerates the hydrolysis of the amorphous regions in the semi-crystalline matrix in comparison to the degradation in a completely amorphous one, and that leads a faster mass loss in a crystallized polymer [7, 12].

8.3.2. Relevance of particle shape and nature

The analysis of Mg particle shape and composition relevance in the *in vitro* degradation behaviour of the novel polymer/Mg materials was performed by comparing the degradation rates of three composites reinforced with different type of particles: Mg irregular shaped particles, Mg spherical particles, and spherical particles of Mg5Zn.

8.3.2.1. Hydrogen release

Figure 8.9 shows the accumulative hydrogen release of the three composites and the references Mg and Mg5Zn cylinders. The Figure is divided in four zones where the hydrogen release rate was calculated for each material and the values of the slopes are summarized in Table 8.3.

It is observed that particles shape plays a very important role by tailoring the degradation behaviour of PLA/Mg composites. After 28 days, the composite reinforced with irregular particles releases more volume of hydrogen than both composites reinforced with spherical particles. In zones I and II, the hydrogen release rate of PLDA10Mg-IRR is higher than that of PLDA10Mg-SPH and PLDA10Mg5Zn-SPH. In zone III the rate of H_2 released increases for -SPH and decreases for –IRR, but the composite with irregular particles keeps evolving more hydrogen than the material with spherical Mg and Mg5Zn. In zone IV the hydrogen release rate reaches a slope that tends to zero for all the three materials.

In order to understand the relevance of the particle nature, both materials reinforced with –SPH particles are compared. It is observed that after 28 days, composite reinforced with Mg5Zn releases a higher hydrogen volume (6.5 ml H_2/cm^2) than PLDA10Mg-SPH (5.1 ml H_2/cm^2). This is coherent with the behaviour of as-cast metallic references (Mg and Mg5Zn) where Mg5Zn

evolves much more hydrogen than Mg. Mg alloy produces in only 4 days the volume of H_2 per cm^2 that PLDA10Mg-SPH releases during the whole experiment (5.1 ml H_2/cm^2). Meanwhile, Mg5Zn releases more than four times that volume in only 6 days (21 ml H_2/cm^2) (out of scale in Figure 8.9).

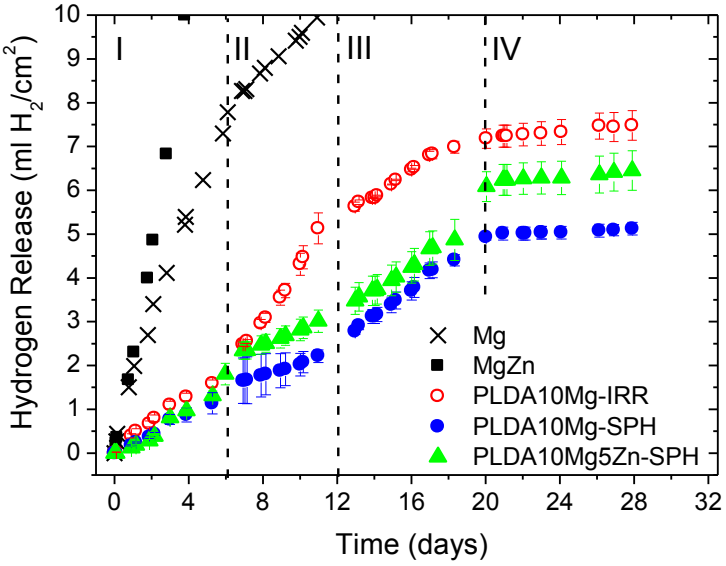

Figure 8.9 Accumulated amount of hydrogen released as a function of immersion time in PBS

Table 8.3 Hydrogen release in ml/cm^2 per day in each zone of Figure 8.9

Material	H_2 ml/cm^2 per day			
	I	II	III	IV
Mg	1,23	0,40	0,25	0,25
Mg5Zn	3,44	4,62	5,60	5,17
PLDA10Mg-IRR	0,31	0,57	0,25	0,04
PLDA10Mg-SPH	0,21	0,21	0,31	0,02
PLDA10Mg5Zn-SPH	0,29	0,20	0,28	0,03

The amount of Mg that has reacted to evolve the measured hydrogen was stoichiometrically calculated and depicted as mass loss with respect to the composite in Figure 8.10. It is important to note that –IRR composite has lost almost a 6% of its total mass, which corresponds

to the 60% of the Mg particles. Whereas, the 36% and the 46% of the total amount of Mg and Mn6Zn particles present in –SPH composites, respectively, have reacted.

Alloying Mg with Zn is reported to reduce Mg corrosion rate when it is found as a solid solution in the alloy [39]. According to the Mg-Zn phase diagram [40] the limit of Zn content in order to stay in solid solution during rapid solidification of Mg-Zn alloys is a 6.2% in mass. However, the hydrogen release results show that neither the Mg5Zn cast alloy, nor the reinforced composites with atomized Mg5Zn particles exhibit better corrosion behaviour than Mg or PLDA10Mg-SPH respectively. This can be explained, if it is considered that Zn is not present as a solid solution in the Mg matrix, but it has precipitated as a second phase. Figure 8.1.c shows a picture of Mg5Zn particles. The presence of a second phase becomes evident as bright intergranular zones which, according to the Mg-Zn diagram, correspond to MgZn precipitates. The potential differences between Mg matrix and the second phase might lead to micro-galvanic corrosion mechanisms that increases Mg corrosion rate [39, 41].

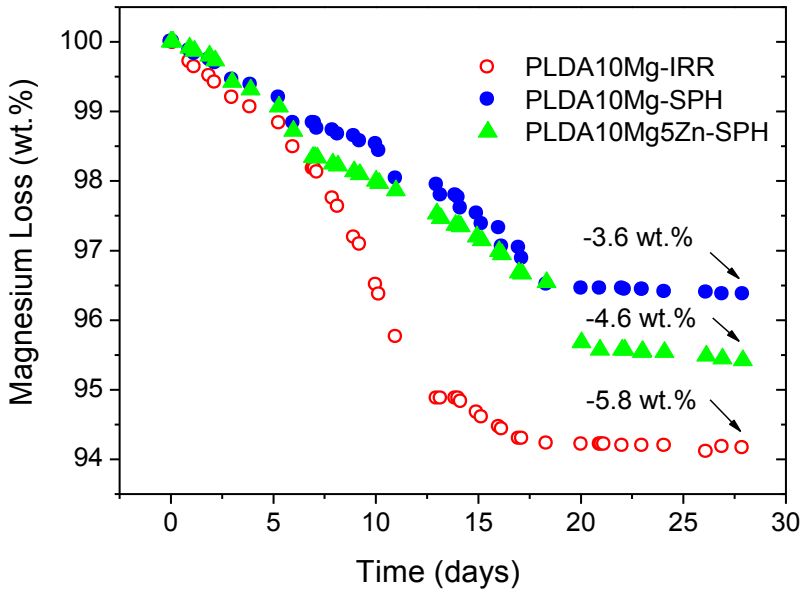

Figure 8.10 Mg loss in terms of mass loss with respect to the composite as a function of immersion time in PBS

Although Mg5Zn alloy releases an immense amount of hydrogen (day 28: 130 ml H_2/cm^2) at a rate that increases with time (Table 8.3), the composite reinforced with Mg5Zn spherical particles releases hydrogen at a controlled rate and in smaller quantities than the material reinforced with Mg with irregular particles. This fact implies that the reinforcement shape is even more relevant than the composition of the particle in the control of the degradation kinetics of novel PLA/Mg composites.

The more straightforward explanation of the lower corrosion rate of –SPH composites with respect to the –IRR relies on the surface area of particles. Keeping in mind that a sphere has the smallest surface area of all surfaces that enclose a given volume, it results for the same mass of particles, that the total surface area of Mg irregular particles is much larger than that of the spherical ones. Therefore, there are more places available for the reaction between Mg and PBS in the PLDA10Mg-IRR composite, which would explain its faster hydrogen release.

8.3.2.2. pH evolution

Variation of pH in the immersion media containing the composites was monitored for 28 days in both, distilled water and PBS (with a renewal of solution each week). Figure 8.11 shows the measured pH values. It is observed that a neutral pH was kept during the whole experiment in PBS containing the composites. On the contrary, Mg and Mg5Zn cylinders have degraded so rapidly that surpassed the buffer capacity of PBS in less than 24 hours reaching pH values close to 10 (not shown in Figure 8.11).

Unreinforced PLDA varies pH values of distilled water between 6.3 and 5.0, whereas PLDA/Mg composites raise sharply the pH of distilled water up to 10 during the first 1.5 day and then it diminishes steadily. Worthwhile to point out is that the composite reinforced with irregular flake-like Mg particles causes the smaller increments in pH. The difference between PLDA10Mg-IRR and PLDA10Mg-SPH increases with time, so that after 28 days of immersion, the solution of the composite reinforced with irregular particles has a pH of 7.4 *versus* 8.9 of the solution of the composite reinforced with spherical particles. This is a contradictory result, taking into account that PLDA10Mg-IRR is the material that releases the highest amount of hydrogen, which implies that it must induce the largest increment in pH as well. This behaviour may be understood considering that the polymeric matrix can degrade and release lactic acid to the medium, which induce a pH decrement that can compensate the increment in pH caused by the reaction of Mg with distilled water.

It is also hypothesized that the polymer reinforced with the irregular particles has degraded more during melt processing. The greater surface of irregular flake-like shape particles can increase the friction and thermal stresses that polymer underwent during extrusion leading to reduction of the molecular weight. Shorter polymer chains are more susceptible to hydrolysis and release degradation products to the media earlier than a less degraded polymer. As PLDA reinforced with spherical particles can have undergone less thermo-mechanical stress during processing, it takes longer for the matrix to release lactic acid to distilled water, so that pH maintains basic values due to Mg corrosion.

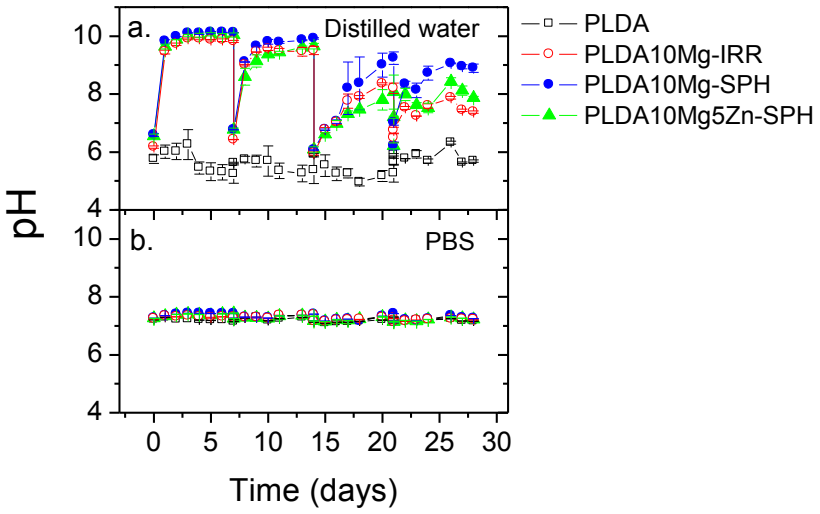

Figure 8.11 Evolution of pH of unreinforced PLDA and composites in distilled water and PBS

8.3.2.3. Mass variation

The water uptake measurements give an idea of the amount of solution that the cylinders have absorbed at determined time (7 days and 28 days). In Chapter 7 and section 8.3.1.3 of the current chapter, it has been discussed that each sample can retain PBS solution due to amorphous domains and to pores, cracks and capillars that are formed as a consequence of the particles and polymer degradation [30] so that, the water retention can be correlated with good criteria with composite degradation. Figure 8.12.a shows the results for the three composites and the reference (unreinforced PLDA). The most remarkable outcome is that PLDA10Mg-IRR retains more than twice the liquid retained by –SPH composites (5.2 *vs* 2.1 %), which increases to more than three times after 28 days (23.3 *vs* 6.9%). Composites reinforced with spherical particles exhibit very similar water uptake values. Water uptake of unreinforced PLDA is maintained at equilibrium values regardless of the immersion time (0.8 - 1%).

Figure 8.12.b shows the mass variation of the three composites and the reference after 7 days and 28 days immersed in PBS. Composite materials exhibit a mass gain during the first week, whereas unreinforced PLDA loss 0.2% of mass. The mass gain indicated that Mg degradation products (phosphates and/or hydroxides) have remained in the samples. After four weeks immersed in PBS, all samples lose mass, being the composite reinforced with irregular particles the one that loses the highest amount (≈ -12 %). This confirms that the composite reinforced with the irregular particles degrades much faster than the ones reinforced with spherical particles. Mass loss of unreinforced PLDA resulted negligible. Both samples with spherical reinforcements have a similar behaviour, they loss much less weight than the –IRR composite.

Water uptake and mass variation analysis show that the influence of the particle morphology on the degradation behaviour of PLDA/Mg composites is much greater than that of particles composition. This observation is in agreement with hydrogen release results.

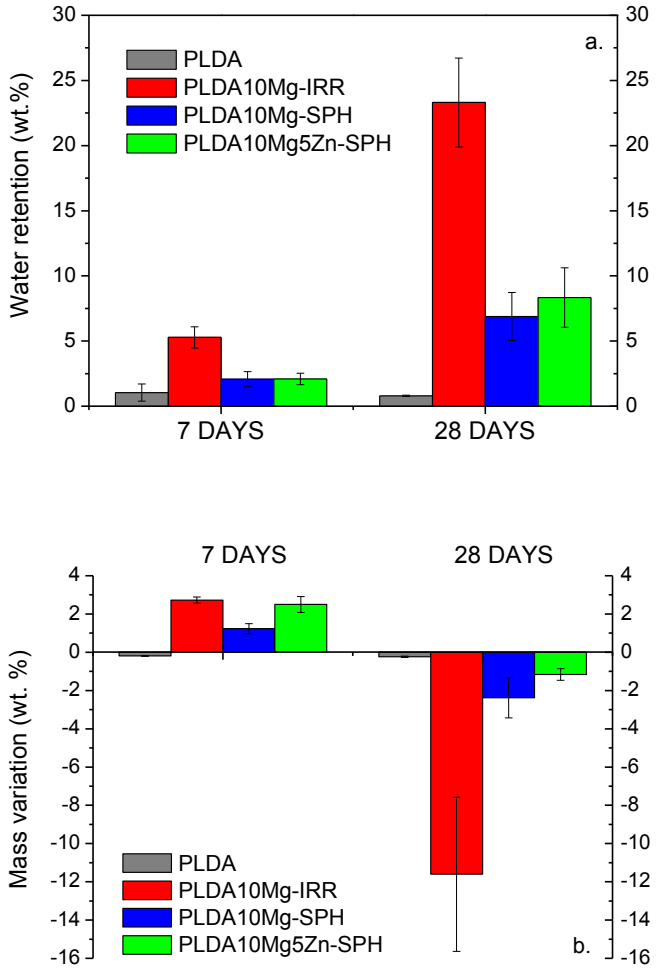

Figure 8.12 Unreinforced PLDA and composites percentage of mass gain due to water uptake (a) and mass variation (b) after 7 and 28 days of immersion in PBS

8.3.2.4. Morphology

Figure 8.13 shows the cylinders of PLDA10Mg-IRR, PLDA10Mg-SPH and PLDA10Mg5Zn-SPH composites, as processed and after 7 and 28 days immersed in PBS. It is clearly observed that degradation of composite reinforced with irregular flake-like particles lead to swelling of the specimen and subsequent formation of deep and long cracks. On the contrary, the –SPH

composites neither present cracks nor modification of the cylinder shape after 28 days of immersion.

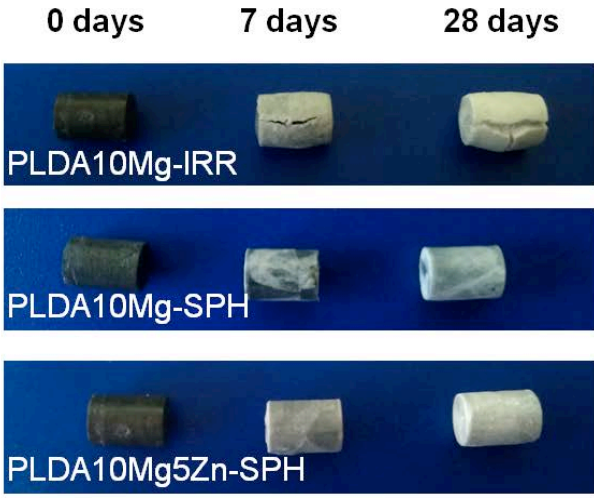

Figure 8.13 Photographs of the composites from left to right: original, after 7 days, and after 28 days immersed in PBS.

The formation of cracks may be the responsible of the increment in PLDA10Mg-IRR hydrogen release rate after 6 days of immersion in PBS (Figure 8.9 and table 8.3) and also can help to understand pH decrements in distilled water (Figure 8.11). Cracks expose new polymer surface to the media, which implies an increment in water diffusion inside the composite, that accelerates hydrolysis of PLDA and Mg corrosion, which eventually leads to both: an increment in H_2 evolved and a decrement on pH due to the release of lactic acid to immersion media.

Figure 8.14 shows the cross sections of the three composites observed by stereoscopic microscopy (Figure 8.14.a) and by optical microscopy (Figure 8.14.b). The three materials show similar degradation mechanisms. Mg particles corrosion proceeds from the surface to the core, forming a white halo. It is observed the surface erosion of the composite reinforced with irregular shape particles.

Figure 8.15 presents backscattered electron images of the three composites after 28 days of immersion in PBS solution at the centre and at the border of the specimens. It is clearly seen that reaction phases (dark contrast) with a higher amount of oxygen are detected at the border of the samples, but at the centre only some particles appear partially transformed. This partial transformation seems to be more abundant in the case of –IRR composite. At the border there is a clear difference between composites. Irregular particles in PLDA10Mg-IRR appear almost

fully transformed, with the reaction phase broken down into small chips. In the case of –SPH composites particles appear either with a Mg or a Mg5Zn core, still untransformed. Mg5Zn particles show a smaller metallic untransformed core, which indicates the faster degradation rate of this material in comparison with pure Mg.

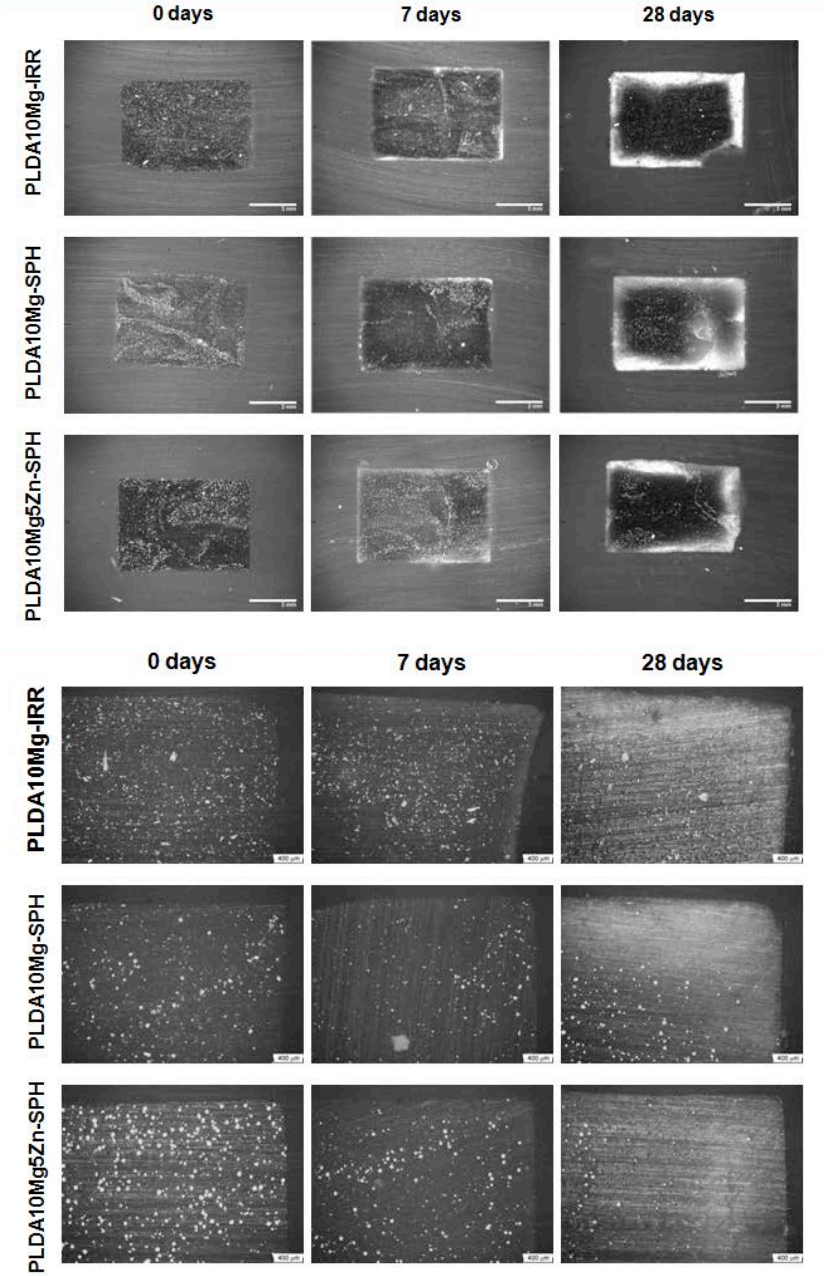

Figure 8.14 Cross section pictures taken by stereoscopic microscopy (a) and by optical microscopy (b)

The microstructure of the degraded composites shows that particles that are close to the surface react before those that are further away. This indicates that degradation of the composite is controlled by the diffusion of water/PBS within the polymeric matrix. Although the conditions are given for the composites to underwent bulk erosion [42], water needs time to diffuse among the polymer chains, when the solution reaches the particles inside the specimen, corrosion proceeds at the surface of the specimen and surface erosion takes place.

Another important feature that was observed in the photographs of the cylinders in Figure 8.13 is the formation of deep cracks in the degraded PLDA10Mg-IRR composite, already after 7 days of immersion. Cracks are also evident by SEM, as shown in Figure 8.16, corresponding to the composites after 28 days immersed in PBS. –SPH composites also present cracks but in a lower extent. An easier formation of cracks on PLDA10Mg-IRR can be explained due to the larger surface area of flake like particles in comparison with spherical ones. Hydrogen released at the surface of Mg particles could lead to specimen expansion, swelling and further cracking. Moreover, formation of $Mg(OH)_2$ at the particle/matrix interface produces an increase of the particle volume that can lead to internal stresses due to the accommodation of the volume, and help to promote the formation of cracks. Once the cracks are formed, they act as fast paths for the diffusion of the water into the material and accelerate the degradation rate.

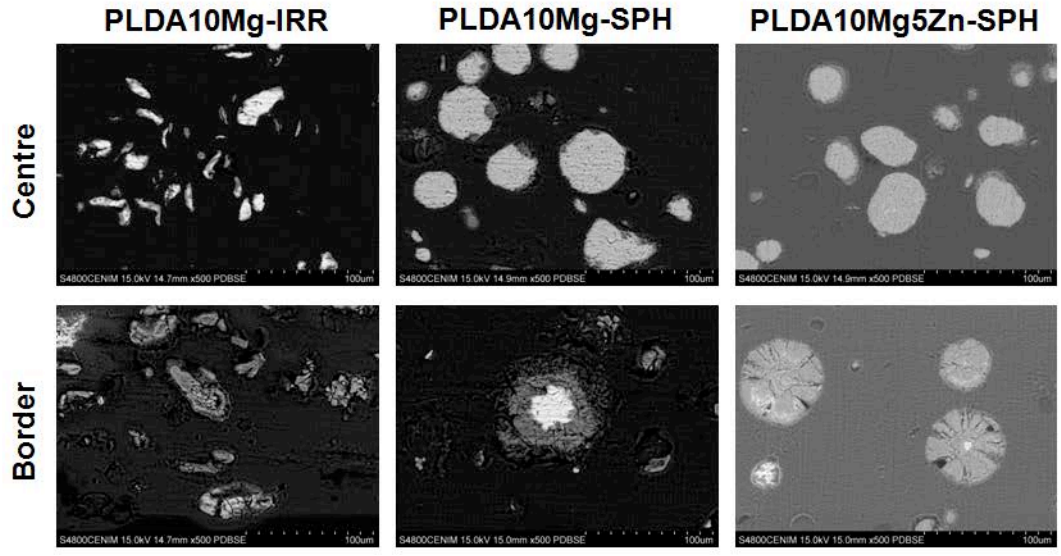

Figure 8.15 SEM images of composites after 28 days of immersion at the centre of the cross section (up) and at the border (down). (x500)

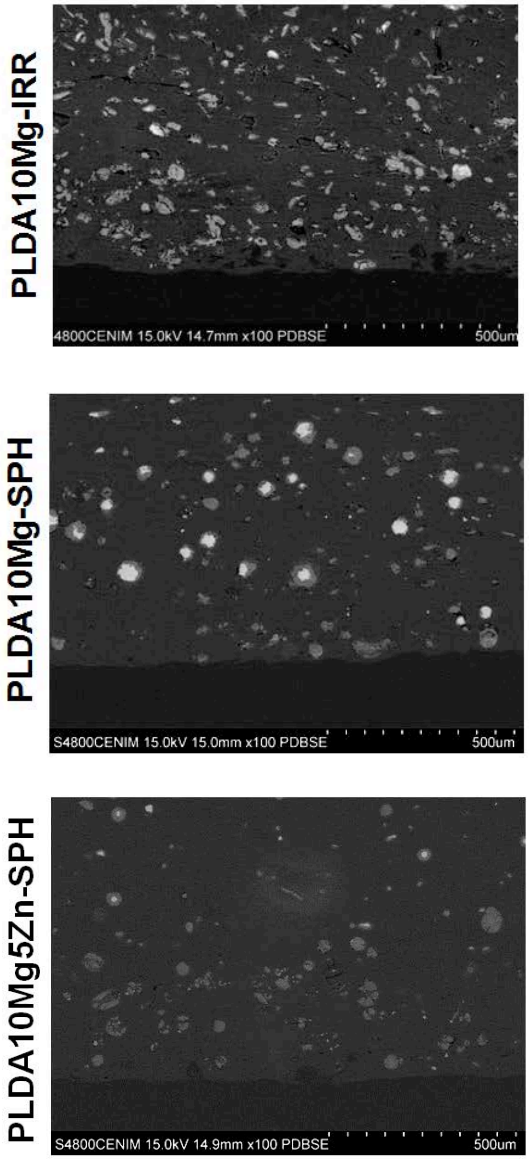

Figure 8.16 SEM images at the border of composites after 28 days of immersion (x100)

8.3.2.5. Mechanical properties

Given that PLDA10Mg-SPH was the composite material that exhibited the best *in vitro* degradation behaviour; its mechanical performance was studied as a function of degradation time. Figure 8.17 shows the stress *vs* strain curves of the as processed cylinders and after 7 and 28 days immersed in PBS at 37 ºC. Figure 8.18 shows the results of Young's Modulus and compressive strength at yield as a function of immersion time.

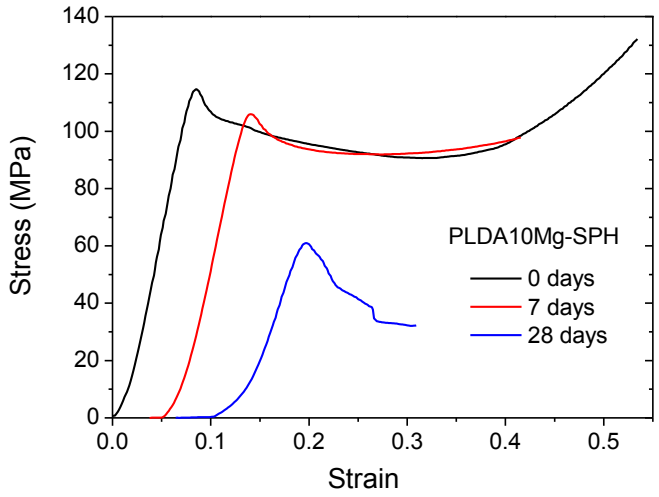

Figure 8.17 PLDA10Mg-SPH Stress *vs* strain curves as a function of immersion time in PBS

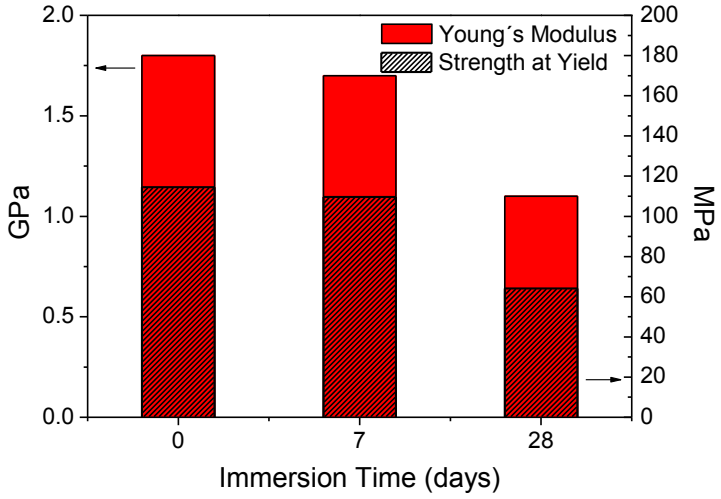

Figure 8.18 PLDA10Mg-SPH compressive mechanical properties as a function of immersion time in PBS

PLDA10Mg-SPH gradually loses its compressive resistance as time passes. The mechanical loss is desired for a resorbable implant in order to facilitate the transfer of stresses to the healing bone [43]. The decrease in mechanical properties is thus expected, and can be referred to the corrosion of Mg particles that enhances the hydrolysis at polymer/matrix interface, leading to the deterioration of the union between particles and the polymeric matrix. It is observed that a

week in PBS leads to a reduction of Young´s modulus and compressive strength of only 0.1 GPa and 5 MPa respectively. This implies a lost of 7% in stiffness and 4% in resistance. After near a month the loss of mechanical properties becomes greater. The modulus and the compressive strength at yield are reduced by 40% compared with the original material.

Results in the open literature are scarce and limited to flexural and compressive properties of polylactic acid reinforced with bio-glass fibres for which a compressive strength loss by 60% and 90% of random and unidirectional composites was reported after only 14 days [44]. Lehtonen *et al.* [30] developed composites with longer strength retention. The flexural modulus of these composites decreases by 35 – 65 % after 4 weeks depending on the chemical composition of the glass fibres. From the comparative analysis of these and our results it follows that *in vitro* degradation rate of the novel PLA/Mg composites makes it a good candidate as resorbable material for load bearing applications. A deeper analysis is meaningless since it is assumed that the optimal rate of mechanical properties and mass loss depends on the given orthopaedic application, implantation site, healing rate and load bearing [2-4, 45]. These results, however, provide a proper understanding before the implementation of finer aspects of composite processing at semi-industrial or industrial scale, leading to successful trial-and–error approaches.

8.4. Conclusions

In vitro degradation behaviour of PLA/Mg composites can be tailored by changing the characteristic of the matrix and/or the metallic reinforcement. These novel composites when immersed in PBS do not surpassed the buffer capacity of the solution.

Composites exhibit surface degradation. The crystalline composite PLDA10Mg_TT presented the fastest degradation and the largest mass loss and water uptake, and also higher hydrogen release than its amorphous homologous. Within the amorphous matrices (PLLA and PLDA), PLLA allowed the highest hydrogen release rate.

Regarding the characteristics of the reinforcement, it was found that particle shape plays a very important role controlling the degradation behaviour of PLA/Mg composites. The lower surface of spherical particles reduced the reaction sites which decrease Mg particles corrosion rate, in comparison with irregular particles, and additionally retard the appearance of macroscopic cracks in the composite.

Alloying with 5% of Zn led to the precipitation of intergranular precipitates that impaired corrosion resistance of Mg. However, the composite reinforced with spherical Mg5Zn particles, exhibited better corrosion behaviour than the material reinforced with irregular Mg particles. This

implies that particle shape played a more important role on controlling PLA/Mg degradation rate than particle nature.

The best *in vitro* degradation behaviour was obtained with the material composed by an amorphous PLDA matrix reinforced with spherical particles of Mg. PLDA10Mg-SPH underwent a loss of compressive resistance of only 4% after 7 days, and 40% after 28 days. This retention of strength falls within a suitable range expected for bioresorbable composites.

8.5. References

[1] Cifuentes SC, Frutos E, González-Carrasco JL, Muñoz M, Multigner M, Chao J, et al. Novel PLLA/magnesium composite for orthopedic applications: A proof of concept. Materials Letters 2012;74:239-42.

[2] Wall A, Board T. Tendon Healing in a Bone Tunnel: A Biomechanical and Histological Study in the Dog. In: Banaszkiewicz PA, Kader DF, editors. Classic Papers in Orthopaedics: Springer London; 2014. p. 453-6.

[3] Nieminen T, Rantala I, Hiidenheimo I, Keränen J, Kainulainen H, Wuolijoki E, et al. Degradative and mechanical properties of a novel resorbable plating system during a 3-year follow-up in vivo and in vitro. Journal of Materials Science: Materials in Medicine 2008;19:1155-63.

[4] Lippman C, Hajjar M, Abshire B, Martin G, Engelman R, Cahill D. Cervical spine fusion with bioabsorbable cages. Neurosurgical Focus 2004;16:E4.

[5] Swift G. Requirements for biodegradable water-soluble polymers. Polymer Degradation and Stability 1998;59:19-24.

[6] Tsuji H. Polylactides. In: Doi Y, Steinbüchel A, editors. Biopolymers Weinheim, Germany: Wiley-VCH; 2002. p. 129-77.

[7] Auras R, Lim LT, Selke SEM, Tsuji H. Poly-lactic acid. Synthesis, Structures, Properties, and Applications: John Wiley & Sons, INC.; 2010.

[8] Hyon SH, Jamshidi K, Ikada Y. Effects of residual monomer on the degradation of DL-lactide polymer. Polymer International 1998;46:196-202.

[9] Saha SK, Tsuji H. Effects of molecular weight and small amounts of d-lactide units on hydrolytic degradation of poly(l-lactic acid)s. Polymer Degradation and Stability 2006;91:1665-73.

[10] Karst D, Yang Y. Effect of Arrangement of L-Lactide and D-Lactide in Poly[(L-lactide)-co-(D-lactide)] on its Resistance to Hydrolysis Studied by Molecular Modeling. Macromolecular Chemistry and Physics 2008;209:168-74.

[11] Tsuji H, Tezuka Y, Yamada K. Alkaline and enzymatic degradation of L-lactide copolymers. II. Crystallized films of poly(L-lactide-co-D-lactide) and poly(L-lactide) with similar crystallinities. Journal of Polymer Science Part B: Polymer Physics 2005;43:1064-75.

[12] Tsuji H, Mizuno A, Ikada Y. Properties and morphology of poly(L-lactide). III. Effects of initial crystallinity on long-term in vitro hydrolysis of high molecular weight poly(L-lactide) film in phosphate-buffered solution. Journal of Applied Polymer Science 2000;77:1452-64.

[13] Tsuji H, Ikada Y. Properties and morphology of poly(l-lactide) 4. Effects of structural parameters on long-term hydrolysis of poly(l-lactide) in phosphate-buffered solution. Polymer Degradation and Stability 2000;67:179-89.

[14] Tsuji H, Del Carpio CA. In Vitro Hydrolysis of Blends from Enantiomeric Poly(lactide)s. 3. Homocrystallized and Amorphous Blend Films. Biomacromolecules 2002;4:7-11.

[15] Meer SATvd, Wijn JRd, Wolke JGC. The influence of basic filler materials on the degradation of amorphous D- and L-lactide copolymer. Journal of Materials Science: Materials in Medicine 1996;7:359-61

[16] Ara M, Watanabe M, Imai Y. Effect of blending calcium compounds on hydrolytic degradation of poly(dl-lactic acid-co-glycolic acid). Biomaterials 2002;23:2479-83.

[17] Wu G, Ibrahim JM, Chu PK. Surface design of biodegradable magnesium alloys — A review. Surface and Coatings Technology 2013;233:2-12.

[18] El-Rahman SSA. Neuropathology of aluminum toxicity in rats (glutamate and GABA impairment). Pharmacological Research 2003;47:189-94.

[19] Yang W, Zhang P, Liu J, Xue Y. Effect of Long-Term Intake of Y3+ in Drinking Water on Gene Expression in Brains of Rats. Journal of Rare Earths 2006;24:369-73.

[20] Seyedraoufi ZS, Mirdamadi S. Synthesis, microstructure and mechanical properties of porous Mg瑂Zn scaffolds. Journal of the Mechanical Behavior of Biomedical Materials 2013;21:1-8.

[21] González S, Pellicer E, Fornell J, Blanquer A, Barrios L, Ibáñez E, et al. Improved mechanical performance and delayed corrosion phenomena in biodegradable Mg–Zn–Ca alloys through Pd-alloying. Journal of the Mechanical Behavior of Biomedical Materials 2012;6:53-62.

[22] Tsuji H. Poly(lactide) Stereocomplexes: Formation, Structure, Properties, Degradation, and Applications. Macromolecular Bioscience 2005;5:569-97.

[23] Tsuji H. In vitro hydrolysis of blends from enantiomeric poly(lactide)s Part 1. Well-stereo-complexed blend and non-blended films. Polymer 2000;41:3621-30.

[24] Tsuji H. Autocatalytic hydrolysis of amorphous-made polylactides: effects of l-lactide content, tacticity, and enantiomeric polymer blending. Polymer 2002;43:1789-96.

[25] Tsuji H. In vitro hydrolysis of blends from enantiomeric poly(lactide)s. Part 4: well-homo-crystallized blend and nonblended films. Biomaterials 2003;24:537-47.

[26] Xu L, Yamamoto A. Characteristics and cytocompatibility of biodegradable polymer film on magnesium by spin coating. Colloids and Surfaces B: Biointerfaces 2012;93:67-74.

[27] Lorenz C, Brunner JG, Kollmannsberger P, Jaafar L, Fabry B, Virtanen S. Effect of surface pre-treatments on biocompatibility of magnesium. Acta Biomaterialia 2009;5:2783-9.

[28] Schinhammer M, Hofstetter J, Wegmann C, Moszner F, Löffler JF, Uggowitzer PJ. On the Immersion Testing of Degradable Implant Materials in Simulated Body Fluid: Active pH Regulation Using CO2. Advanced Engineering Materials 2013:1-8.

[29] Song G, Song S-Z. Corrosion Behaviour of Pure Magnesium in a Simulated Body Fluid. Acta Physico-Chimica Sinica 2006;22:1222-6.

[30] Lehtonen TJ, Tuominen JU, Hiekkanen E. Resorbable composites with bioresorbable glass fibers for load-bearing applications. In vitro degradation and degradation mechanism. Acta Biomaterialia 2013;9:4868-77.

[31] de Jong SJ, Arias ER, Rijkers DTS, van Nostrum CF, Kettenes-van den Bosch JJ, Hennink WE. New insights into the hydrolytic degradation of poly(lactic acid): participation of the alcohol terminus. Polymer 2001;42:2795-802.

[32] Ehrenstein G, Schmiemann A. Corrosion phenomena in glass-fiber reinforced thermosetting resins. Handbook of ceramics and composites Synthesis and properties. New York: Marcel Dekker Inc; 1990. p. 231-68.

[33] Plackett DV, Holm VK, Johansen P, Ndoni S, Nielsen PV, Sipilainen-Malm T, et al. Characterization of l-polylactide and l-polylactide–polycaprolactone co-polymer films for use in cheese-packaging applications. Packaging Technology and Science 2006;19:1-24.

[34] Li S, Garreau H, Vert M. Structure-property relationships in the case of the degradation of massive poly(α-hydroxy acids) in aqueous media. Journal of Materials Science: Materials in Medicine 1990;1:198-206.

[35] Shogren R. Water vapor permeability of biodegradable polymers. Journal of Environmental Polymer Degradation 1997;5:91-5.

[36] Tsuji H, Ikarashi K. In Vitro Hydrolysis of Poly(l-lactide) Crystalline Residues as Extended-Chain Crystallites:$II. Effects of Hydrolysis Temperature. Biomacromolecules 2004;5:1021-8.

[37] Cam D, Hyon S-h, Ikada Y. Degradation of high molecular weight poly(l-lactide) in alkaline medium. Biomaterials 1995;16:833-43.

[38] Tsuji H, Ikada Y. Properties and morphology of poly(L-lactide). II. Hydrolysis in alkaline solution. Journal of Polymer Science Part A: Polymer Chemistry 1998;36:59-66.

[39] Gu X, Zheng Y, Cheng Y, Zhong S, Xi T. In vitro corrosion and biocompatibility of binary magnesium alloys. Biomaterials 2009;30:484-98.

[40] Massalski TB. Binary Alloy Phase Diagrams. In: Okamoto H, Subramanian PR, Kacprzak L, editors. United States of America: ASM International; 2001. p. 2571.

[41] Song GL, Atrens A. Corrosion Mechanisms of Magnesium Alloys. Advanced Engineering Materials 1999;1:11-33.

[42] Burkersroda Fv, Schedl L, Göpferich A. Why degradable polymers undergo surface erosion or bulk erosion. Biomaterials 2002;23:4221-31.

[43] Törmälä P, Pohjonen T, Rokkanen P. Bioabsorbable polymers: materials technology and surgical applications. Proceedings of the Institution of Mechanical Engineers, Part H 1998;212:101-11.

[44] Felfel RM, Ahmed I, Parsons AJ, Walker GS, Rudd CD. In vitro degradation, flexural, compressive and shear properties of fully bioresorbable composite rods. Journal of the Mechanical Behavior of Biomedical Materials 2011;4:1462-72.

[45] Jiang G, Evans ME, Jones IA, Rudd CD, Scotchford CA, Walker GS. Preparation of poly(ε-caprolactone)/continuous bioglass fibre composite using monomer transfer moulding for bone implant. Biomaterials 2005;26:2281-8.

CHAPTER 9

CONCLUDING REMARKS

"It is good to have an end to journey toward; but it is the journey that matters, in the end"

Ernest Hemingway

Table of contents

9. CONCLUDING REMARKS

9.1 Summary and conclusions

In this doctoral thesis novel biodegradable and bioresorbable composite materials for osteosynthesis devices based on polylactic acid and Mg were designed and developed. For the matrix, poly-L-lactic acid and poly-L,D-lactic acid with a 4.25% of D-lactyl were used. As reinforcement, irregular shape Mg particles and spherical Mg and Mg5Zn particles were used. PLA/Mg composites were fabricated by means of solvent-free common processes used in industry: extrusion/compression and injection moulding at a lab scale and extrusion/compression at a mid-scale. To assess the material processability, physico-chemical, thermal degradation and mechanical characterization were performed.

The aim was to improve and broaden the applications of current bioresorbable materials used in osteosynthesis. Benefits of PLA are: (1) it is a bioplastic able to be processed by thermoplastic processes (2) it is biodegradable and biocompatible and (3) it has been used since the 80´s in orthopaedic surgery, currently being commercially available, which implies that surgeons already have experience using it. Benefits of Mg are: (1) it has mechanical properties close to that of cortical bone (2) it is biodegradable and biocompatible and (3) it enhances the activity of osteoblasts and has antibacterial properties.

However, these materials present also some drawbacks. On one hand, the polylactic acid is associated with foreign body reactions, osteolysis and weaker mechanical properties in comparison with permanent metallic devices, which limits its applications to low-load bearing fractures. On the other, Mg and its alloys present a high degradation rate which leads to the formation of dangerous subcutaneous gas bubbles and a pH increment that causes bone damage and osteolysis. This fact has limited the incorporation of Mg alloys into orthopaedic implants industry. The long-term goal of this thesis focuses on providing solutions that would lead to cheaper and less intrusive orthopaedic surgery.

In the material developed in this thesis, polylactic acid and Mg particles operate in a kind of simbiosis, each covering for the other´s limitations: while Mg improves polylactic acid mechanical properties, and biocompatibility, the polymeric matrix slows down the degradation rate of Mg, preventing high pH and controlling the hydrogen release.

Experimental results provide evidence that novel PLA/Mg composites have a great potential as resorbable and biocompatible biomaterials for applications in osteosynthesis, due to their controllable degradation rate and adequate mechanical properties.

Specific conclusions of this thesis are listed below:

- Incorporation of Mg particles within polymeric matrices reduces their thermal stability, Mg acts as depolymerisation catalyst, likely reducing polylactic acid molecular weight and inducing the formation of cyclic oligomers. The decrement in thermal properties is more evident for PLLA/Mg composites than for PLDA/Mg, due to PLLA's higher viscosity.

- Mg particles increase polylactic acid compressive Young´s modulus until a specific Mg content were mechanical properties drop dramatically, due to the effect of Mg on PLA thermal degradation. Mg particles improve the mechanical properties of neat PLA when the strengthening effect of fillers is greater than the thermal degradation effect.

- Given the severe particle matrix interactions, incorporation of Mg particles in the polylactic acid matrix also induces significant changes in the rheological properties of the polymer. Only 1 wt.% of Mg in PLDA can cause an increment of 115% in the flow activation energy of the polymer. This implies that only composites with low Mg content ($\leq$ 1wt. %) could be manufactured by injection moulding at the lab scale.

- PLA/Mg composites reinforced with 1 to 15 wt.% of Mg particles were successfully fabricated by extrusion/compression moulding at a mid-scale. The mechanical properties of the composites can be tailored by the addition of Mg particles and the nature of the matrix. These novel PLA/Mg composites exhibit initial mechanical properties that are suitable for osteosynthesis applications (Young´s modulus: 2.0 – 5.0 GPa, which is higher than that of polymeric matrices, and compressive strength: 95 – 130 MPa, which is similar to that of PLLA and PLDA).

- Mg particles reduce the strain softening amplitude of both polymers; this effect together with the increment of compression strength at plateau implies an increment in material toughness and an improvement in the energy storage of composites under deformation. They also increase the resistance of the material to plastic flow and the hardness.

- The results of *in vitro* studies on PLA/Mg composites demonstrate that the degradation rate of these materials depend in great extent on crystalline degree, Mg content and Mg particle shape. All the composites release hydrogen at rates that could be tolerated by human body and, when immersed in PBS, they did not surpass the buffer capacity of the solution.

- Hydrogen evolution rate is larger for materials with a higher crystalline degree and with higher amount of Mg. A plausible reason for the higher hydrogen release and mass loss of crystalline composites in comparison with amorphous ones could be the non-uniform distribution of water within the semi-crystalline matrix. The preferential diffusion of water

through the amorphous domains can induce a localized corrosion on Mg particles that enhances their degradation rate.

- The strength retention properties of the composites are highly dependent on the crystallinity degree of the polymeric matrix. After 3 weeks, amorphous composites show 100% strength retention, whereas thermally treated composites, reinforced with 0.2 or 1 wt.% of Mg, lost 20% of stiffness and 15% of compressive strength.

- Regarding the characteristics of the reinforcement, it was found that particle shape plays a very important role controlling the degradation behaviour of PLA/Mg composites. The lower surface of spherical particles reduced the reaction sites which decrease Mg particles corrosion rate, in comparison with irregular particles, and additionally retard the appearance of macroscopic cracks in the composite.

- Alloying with 5 wt.% of Zn led to the precipitation of intergranular precipitates that impaired corrosion resistance of Mg. However, the composite reinforced with spherical Mg5Zn particles, exhibited better corrosion behaviour than the material reinforced with irregular Mg particles. This implies that particle shape played a more important role on controlling PLA/Mg degradation rate than particle nature.

- The best *in vitro* degradation behaviour, within the composites reinforced with 10 wt.% of Mg, was obtained with the material composed by an amorphous PLDA matrix reinforced with spherical particles of Mg. PLDA10Mg-SPH underwent a loss of compressive resistance of only 4% after 7 days, and 40% after 28 days. This retention of strength falls within a suitable range expected for bioresorbable composites.

9.2 Future perspectives

This doctoral thesis opens a new path in the long journey of research in biomaterials for medical applications. Great advances have been reached through extensive research in the design and processing of polylactic acid-based composites reinforced with Mg. However, in order for these materials to improve the quality of people´s life and reach an actual impact on society, there is still a long way to go.

Further research on this topic must consider the up-scale of implants fabrication and all the process engineering. Rheological properties of PLA/Mg composites must be evaluated with more extent and solutions to reduce thermal degradation, like the incorporation of a stabilizer to prevent depolimerization, should be evaluated.

In vivo tests in animals are determinant to test the suitability of PLA/Mg composites for a given application (spinal, craneo-maxillofacial, ankle, knee surgery…). Long term mechanical and biological properties must be evaluated. The proper design of *in vivo* tests must be supported by an adequate identification of clinical applications.

If the material is focused to a specific application, the optimization of the implant design, and implant components (polymeric matrix and Mg-based reinforcement particles) is another study that should be addressed.

APPENDIX A

Table of contents

A. APPENDIX

A.1. Biological characterization

Cell viability, surface characterization and response to microbial adhesion of PLA/Mg composites were studied in collaboration with the Hospital La Paz in Madrid and the University of Extremadura, under the national project BIOMAGCOM (MAT2012-37736-C05-03).

Dra Laura Saldaña performed the cell viability assays in the Hospital La Paz. Dr Ciro Perez, Dra Maria Luisa Gonzalez, Dra Amparo Gallardo, Dr Miguel Angel Pacha and Dra María Coronada Fernández conducted the trials of bacterial adhesion and surface characterization at the University of Extremadura.

Due to the high relevance of the results, some of the most important outcomes are mentioned in this section of this thesis.

A.1.1 Cell viability and morphology on PLDA/Mg composites

Mesenchymal Stem Cells (MSCs) purchased from Lonza (Basel, Switzerland) were seeded on the materials and incubated in growth medium for 1, 7 and 14 days. The culture medium was replaced with an equal amount of fresh medium at day 7 in cultures maintained for 14 days. Cell viability was assessed using the alamarBlue assay (Biosource, Nivelles, Belgium), which incorporates a non-fluorescent redox indicator that turns into a bright red fluorescent dye in response to metabolic activity. This dye is generally used to measure the viability of a given cell population, and the assay can be used to measure quantitatively an increase in cell number as a function of metabolic activity. Briefly, cells were incubated for 3 h in Dulbecco's modified Eagle medium containing 10% alamarBlue dye and, after excitation at 530 nm, the fluorescence emitted at 590 nm was quantified using a spectrofluorimeter (Synergie4, Evry, France). To visualize nuclear morphology, cells were fixed with 4% (w/v) formaldehyde in PBS and stained with PBS containing 3×10^{-6} M 4,6-diamidino-2-phenylindole (DAPI, Sigma, Madrid, Spain). To examine the arrangement of actin filaments, fixed cells were permeabilized with 0.1% Triton X-100 in PBS and stained with PBS containing 4 × 10-7 M phalloidine-TRITC (Sigma). Images of fluorescently stained cells were obtained using a Leica TCS SPE confocal microscope (Wetzlar, Germany).

In vitro studies show that Mg reinforcement improves viability of MSCs cultured on the materials for 14 days (Fig A.1, upper pannel). Confocal imaging of MSCs stained for actin filaments (red) and nuclei (blue) reveals normal nuclear morphologies on all samples (Fig A.1, lower pannel). MSCs grown on the materials formed a cell monolayer and exhibited a clearly expanded

typically elongated shape. Actin polymerized in a dense meshwork of well-defined stress fibers distributed through the cell body of cells on the three polymer-based materials.

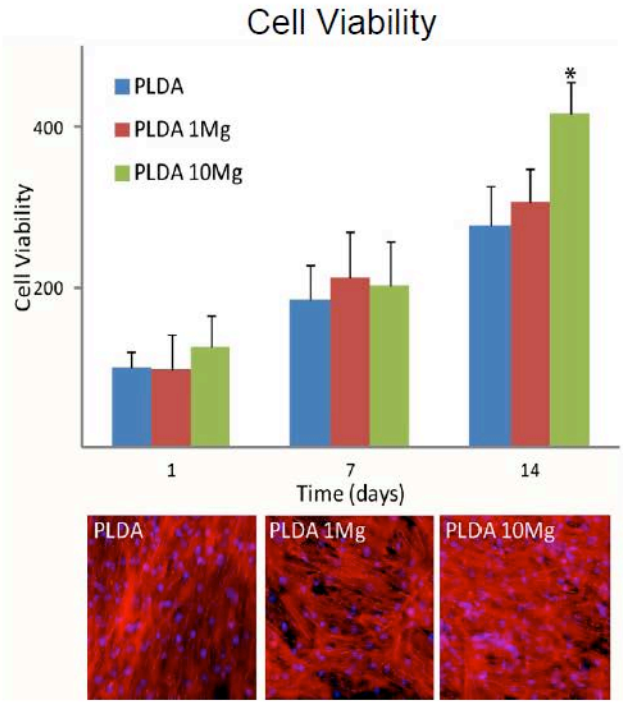

Figure A.1 Cell viability and morphology on PLDA/Mg composite

A.1.2 Surface characterization and response to microbial adhesion

The hydrophobicity of PLDA and PLDA/Mg surfaces was quantified by means of contact angle measurements. For bacterial adhesion studies, the biofilm-forming strain *Staphylococcus epidermis* ATCC35983 was used. The bacterial inocula were grown in Trypticase Soy Broth (TSB). For bacterial adhesion studies, the bacteria were re-suspended in phosphate buffered saline (PBS). Then, the bacterial suspension was added to the samples and was subjected to slight orbital shaking of 20 rpm, for 60 min at 37 ºC. Quantification of the surface density of bacteria on samples were carried out with an epifluorescence microscope (Leitz DIAPLAN, Leitz Wetzlar, Germany) by staining the adhered microorganisms with the kit Live/Dead Baclight L-7012 (Invitrogen SA, Spain). Bacteria were counted with the software NIS-Elements BR 4.10 (Nikon Instruments INC., Melville, USA). For biofilm formation studies, the incubation with the samples was performed under orbital motion, for 24 h at 37 ° C, and bacterial biofilm viability

was quantified through its ATP content by bioluminescence. Statistical analysis was performed using analysis of variance (ANOVA). All data are presented as mean ± SD of at least three independent experiments in duplicate.

Figure A.2 shows the images of a water drop on PLDA and PLDA/Mg composites surfaces. Showing contact angles of 96 ± 7 for PLDA, 73 ± 3 for PLDA1Mg and 77 ± 4 for PLDA10Mg. It is observed that Incorporation of Mg particles in PLDA reduces the hydrophobicity of the polymer.

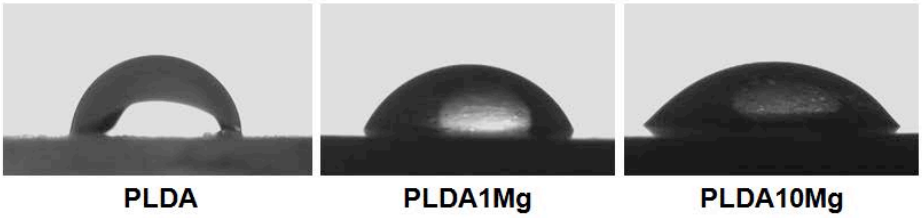

Figure A.2 Contact angle of PLDA and PLDA/Mg composites reinforced with 1 and 10 wt.% of Mg particles

Focusing on the initial viability of adhered bacteria (Figure A.3), all bacteria deposited on the PLDA surface are 100% viable (green), while bacteria attached to the PLDA1Mg and PLDA10Mg surface show a loss in viability (yellow-orange).

After 24h, bacterial biofilm viability of the composites PLDA/Mg was reduced in respect with that of PLDA (Figure A.4). Mg decreases biofilm viability by 65% compared to PLDA control. It can be concluded that PLDA/Mg composites have high antibacterial action, decreasing viability of bacteria included in the biofilm, providing added value to be used as an osteosynthesis material.

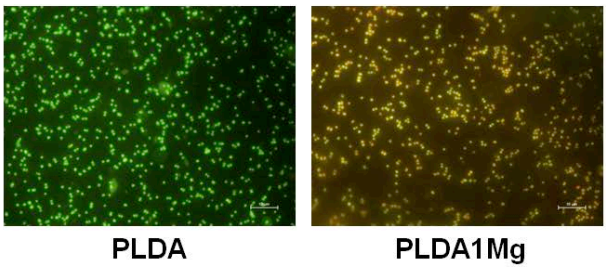

Figure A.3 Initial viability of adhered bacteria deposited on PLDA and PLDA/Mg composites

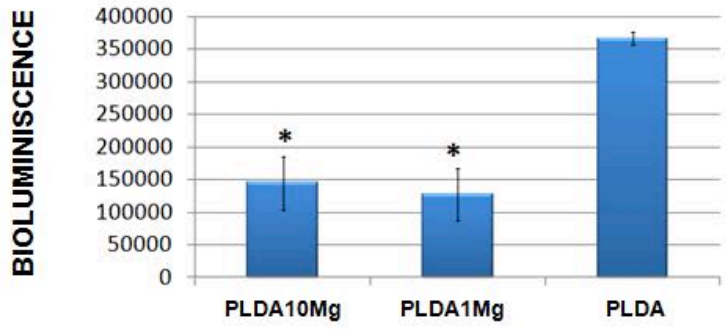

Figure A.4 Surface density of *S. epidermidis* bacteria adhered on the samples: PLDA, PLDA1Mg and PLDA10Mg after 24 hours

A.2. Publications

Authors	N. Argarate, B. Olalde, G. Atorrasagasti, J. Valero, **S.C. Cifuentes**, R. Benavente, M. Lieblich J.L. González Carrasco
Title	Biodegradable Bi-layered coating on polymeric orthopaedic implants for controlled release of drugs
Journal	**Materials Letters** 132 (2014) 193 - 195

Abstract: A novel bone substitute incorporating biodegradable coatings on poly(D,L-lactide-co-lactide) (PLDL) implant has been developed. The polymer coatings were investigated as carrier of eugenol (EG) and dexamethasone (DM) which are suitable drugs to give antibacterial and anti-inflammatory function to the implant. The dip coating method was employed to coat the PLDL implant with poly(L-lactic acid) (PLLA) polymer. It has been observed that the thickness of the coating increased with the polymer concentration and the repetition of the dipping process showed an additive coating thickness compared to the single dipping.Moreover, it has been proved that a sequential drug release of EG and DM has been reached by incorporating the drugs onto each layer coating.

Authors **S.C. Cifuentes**, E. Frutos, R. Benavente, J.L. González Carrasco, V. Lorenzo

Title Strain rate effect on semi-crystalline PLLA mechanical properties measured by instrumented indentation tests

Journal **European Polymer Journal** 59 (2014) 239 – 246

Abstract: Poly-L-lactic acid, PLLA, is a widely studied biomaterial, currently approved for use in a range of medical devices. Its mechanical properties can be tailored giving the material different crystallinity degrees. PLLA presents a complex non-linear behaviour that depends not only on structural parameters such as crystallinity degree but also on external parameters such as strain rate and temperature. Failure of polymeric implants is attributed to their intrinsic time-dependent performance under static loading conditions. This work explores the potential of instrumented indentation tests as a suitable technique to measure the complex non-linear time-dependent mechanical properties of PLLA. The applicability of the Oliver–Pharr method, typically used in ceramic and metallic materials, is discussed through the sensitivity of elastic modulus, hardness and material creep response to different strain rates. Likewise, the strain rate influence depending on the crystallinity degree is considered, providing important information about viscoelastic behaviour of PLLA. Whereas possible, results are compared with those obtained from tensile and Dynamic Mechanical Analysis tests extracted from the literature.

Authors **S.C. Cifuentes**, R. Benavente, J.L. González Carrasco

Title Does magnesium compromise the high temperature processability of novel biodegradable and bioresorbables PLLA/Mg composites?

Journal **Revista de Metalurgia**

01/2014 50(2):e011. doi: http://dx.doi.org/10.3989/revmetalm.011

Abstract : This paper addresses the influence of magnesium on melting behaviour and thermal stability of novel bioresorbables PLLA/Mg composites as a way to investigate their processability by conventional techniques, which likely will require a melt process at high temperature to mould the material by using a compression, extrusion or injection stage. For this purpose, and to avoid any high temperature step before analysis, films of PLLA loaded with magnesium particles of different sizes and volume fraction were prepared by solvent casting. DSC, modulated DSC and thermogravimetry analysis demonstrate that although thermal stability of PLLA is reduced, the temperature window for processing the PLLA/Mg composites by conventional thermoplastic routes is wide enough. Moreover, magnesium particles do not alter the crystallization behaviour of the polymer from the melt, which allows further annealing treatments to optimize the crystallinity in terms of the required combination of mechanical properties and degradation rate.

Appendix

Authors **S.C. Cifuentes,** E. Frutos, J.L. González-Carrasco , M. Muñoz, M. Multigner, J. Chao, R. Benavente, M. Lieblich

Title Novel PLLA/magnesium composite for orthopedic applications: A proof of concept

Journal **Materials Letters** 74(1) (2012) 239 - 242

Abstract: This work aims to develop polymer/magnesium composites as new biodegradable and bioresorbable materials for osteosynthesis implants. The polymeric matrix will benefit from the higher strength and modulus of the Mg particles, whereas Mg will benefit from the surrounded protective polymeric matrix that will control its degradation rate. To provide a proof of concept a set of specimens were processed by combining solvent casting of PLLA (poly-L-lactic acid) loaded with 30 wt% of Mg particles and further molding by compression. Mechanical characterization reveals that reinforcing the polymer matrix with Mg particles improves its mechanical properties (hardness up to 340 MPa and yield strength up to 100 MPa). Interestingly, Young's modulus determined by ultramicroindentation increases up to 8 GPa. From the DSC analysis it follows that the unloaded and loaded polymer has similar crystallinity, which indicates that the improvement in mechanical properties is purely the effect of particle reinforcement.

Authors D. Drummer, **S.C. Cifuentes,** D. Rietzel

Title Suitability of PLA/TCP for fused deposition modeling

Journal Rapid Prototyping Journal 18(6) (2012) 500 - 507

Abstract:

Purpose – Fused deposition modeling (FDM) is a layer by layer technology with the potential to create complex and individual parts from thermoplastic materials such as ABS. The use of Polylactic acid (PLA) and tricalcium phosphate (TCP) as resorbable composite is state of the art in tissue engineering and maxillofacial surgery. The purpose of this paper is to evaluate the processing conditions and the performance of parts (e.g. mechanical properties) manufactured with a FDM machine. **Design/methodology/approach –** In this paper, the general suitability of PLA for the processing with FDM is evaluated and material specific effects (e.g. crystallization and shrinkage) are shown. Therefore, the characterization of the semi-crystalline biodegradable material by thermal, mechanical and microscopic analysis is carried out. **Findings –** Facts, which affect the functional properties of the samples, are analyzed. Among them, the processing temperature and sample size significantly affect the morphology of the final components. Components from PLA/TCP with sufficient mechanical properties for their potential use as scaffolds are obtained. **Originality/value –** Thus, the paper shows that by thermal analysis it is possible to identify major influences on processing and part properties.

A.3. Congress and seminars

Authors **S.C. Cifuentes – MIT Technology Review Innovator under 35**

Title A new material that improve bone implant

Congress **Emerging Technologies Conference – EmTech Spain**. Valencia, Spain. November 12th – 13th , 2014

Type Oral presentation

Abstract: Polylactic acid and magnesium operate in a kind of symbiosis, each covering for the other's "defects": on one hand, the magnesium gives more robustness to the matrix, so that this can be used as a bone implant, unlike other biodegradable materials which are not sufficiently solid; on the other, the matrix slows down the release of magnesium into the organism, therefore preventing high-concentration and reducing its degradation.

Results are promising, however before being adopted in day-to-day orthopaedic surgery, the new material needs extensive in-vivo tests on animals, which is what Cifuentes looks forward to, pending the approval of the necessary funding. Her research project involves PLA producers such as Corbion Purac in the Netherlands, which are greatly interested in the medical application of this and other biomaterials.

Will the synergy between a bioactive metal and a bioplastic finally turn the tables on steel and titanium and allow for cheaper, less intrusive orthopaedic surgery?.

Authors **S.C. Cifuentes,** L. Saldaña, V. Lorenzo, M. Lieblich, R. Benavente, J.L. González-Carrasco

Title Suitability of novel PLA/Mg composites for biodegradable implants

Congress **6th Symposium on Biodegradable Metals. BIOMETALS** Maratea, Italy. August 24th – 29th, 2014

Type Oral presentation

Abstract: Implants that can be metabolized by the human body have appeared as one of the most attractive and promising solutions to overcome limitations and improve the features of current implantable devices. Biodegradable polymers and magnesium (Mg) alloys have played an important role writing the history of resorbable implants [1,2]. This paper presents the processing by extrusion/compression moulding, mechanical characterization, thermal characterization and *in vitro* biocompatibility of a novel generation of resorbable materials based on a polymeric matrix reinforced with metallic Mg particles.

Authors	**S.C. Cifuentes,** R. Gavilán, A. San Román, M. Lieblich, R. Benavente, J.L. González-Carrasco
Title	Effect of magnesium particle shape on *in-vitro* degradation kinetics of novel PLA/Magnesium composites
Congress	**6th Symposium on Biodegradable Metals. BIOMETALS** Maratea, Italy August 24th – 29th , 2014
Type	Poster

Abstract: In some cases, metallic prosthetic devices must be removed by a second surgical procedure. Biodegradable devices appear as an alternative to avoid this risky and costly practice. One of the main drawbacks of bioresorbable polymers is their low mechanical strength that leads to the need to oversize the implants. With magnesium base materials, on the other hand, hydrogen may form so quickly that became accumulated around the implant at a rate difficult to deal with by the tissue [1, 2]. In the present work, an alternative material, which consists in the incorporation of Mg particles into a polymer matrix [3], has been processed and the degradation kinetics studied as a function of the shape of the Mg reinforcing particles.

Authors	**S.C. Cifuentes,** E. Frutos, R. Benavente, J.L. González-Carrasco, V. Lorenzo
Title	Strain rate effect on semi-crystalline PLLA mechanical properties measured by instrumented indentation tests
Congress	**MACRO - IUPAC.** Chiang Mai, Thailand. July 6th – 11th, 2014
Type	Poster

Abstract: Poly (L-lactide) is a widely studied biomaterial, currently approved for use in a range of medical devices. Its mechanical properties can be tailored giving the material different crystallinity degrees, and with this different applications. This material, as a polymer, is prone to creep under relative low stresses at ambient temperature. In fact, this is the principal cause of loosening of biodegradable polymeric fixations. Therefore, the need of a reliable mechanical test that considers time dependencies of the material arises in order to predict the viscoelastic behaviour of PLLA components properly. This work explores the potential of instrumented indentation as a suitable technique to measure the complex non-linear time-dependent mechanical properties of PLLA. The sensitivity of elastic modulus, hardness and material creep response to strain rate is investigated. The applicability of the Oliver-Pharr method is also discussed. Likewise, the strain rate influence depending on the crystallinity degree is considered. The results of this study provide important information about PLLA viscoelastic behaviour.

Authors **S.C. Cifuentes,** R. Benavente, T. Osswald, F.A. López, J.L. González-Carrasco

Title Processing and characterization of novel melt injected PLDA/Mg composites

Congress **EUROMAT** Seville, Spain. September 8th - 13th, 2013

Type Oral presentation

Abstract: The biodegradable polymer-based composites (ie: polylactic acid - PLA) loaded with particles of Mg, respond to a new strategy to solve the high in vitro degradation rates of Mg alloys and the limitations posed by polymers currently bioreaborbibles [1]. These materials have a degradation profile modulated by the volume fraction and particle size of Mg, thus, it is expected that as reabsorption occurs, it allows the regeneration of bone tissue, maintaining stable the mechanical performance of the system implant-bone. To fabricate the PLA bone fixation implants the polymer is usually processed by injection moulding. This paper studies the influence of Mg particles on the mechanical properties of PLDA / Mg composite processed by injection. Composites with different mass fractions of Mg (0.2%, 0.5% and 1%) have been manufactured from a homogeneous mixture of PLDA and cpMg particles of about 50 m in diameter. The mechanical characterization has been addressed by tensile and compression tests. The crystallinity and thermal stability of the material have been determined by means of DSC and TGA techniques.

Authors **S.C. Cifuentes,** E. Frutos, R. Benavente, J.L. González-Carrasco

Title Study of the effect of the PLLA crystallinity on its creep behaviour at ambient temperature by using instrumented microindentation techniques

Congress **Micromaterials European User Meeting**. Valletta, Malta. October 24th – 25th, 2012

Type Poster

Abstract: Most of the resorbable osteosynthesis materials are composed by poly-L-lactic acid, PLLA. This kind of materials must be suitable to gradually lose their mechanical strength while degradation products are metabolized by the human body during the bone regeneration. So that the system Bone+Implant can maintain its mechanical strength. There are three challenges to be addressed: good mechanical properties, control of degradation times and the degradation products must be biocompatible. The mechanical properties and degradation times depend on the crystallinity of the material. This property can be tailored with the cooling rate during processing, with isothermal treatments from the melt or with annealing processes. The aim of this project is to deep into the potential of the ultramicroindentation techniques to analyse the relevant mechanical properties at ambient temperature of PLLA with different crystallinity degrees.

Appendix

Authors **S.C. Cifuentes,** J. Chao, T. Osswald, R. Benavente, J.L. González-Carrasco

Title Comportamiento mecánico de materiales compuestos PLDA/Mg, de interés en aplicaciones médicas, procesados mediante moldeo por inyección

Congress **XXXV Congreso de la Sociedad Ibérica de Biomecánica y Biomateriales.** Madrid, Spain. October 19th – 20th , 2012

Type Oral presentation

Abstract: A partir de una mezcla homogénea de PLDA (4,25% D-lactyl) y partículas de Mg puro de tamaño inferior a 50 micras, se fabricaron, mediante inyección, probetas de tracción y compresión con diferentes fracciones de magnesio (0.2%, 0.5% y 1% en masa). Las condiciones de procesado llevaron a obtener materiales con un 13±4% de cristalinidad. Dicha cristalinidad aumenta a un 40±4% tras un tratamiento de templado, cuyas condiciones (125 ±1 ºC, 1 h) se optimizaron a partir del estudio mediante DSC de una serie de tratamientos térmicos. La caracterización mecánica en las probetas con y sin tratamiento térmico, se abordó con ensayos de tracción, y compresión. La Figura muestra, a modo de ejemplo, los resultados de ensayos de compresión en muestras sin tratamiento térmico. La cristalinidad de los materiales y el efecto del Mg en la cristalización del polímero fueron determinadas por medio de DSC y Rayos-X. A través de imágenes de microscopía óptica y de barrido se analizó la superficie de fractura y la buena eficiencia del procesado en la dispersión homogénea de las partículas metálicas en la matriz polimérica.

Authors **S.C. Cifuentes,** R. Benavente, F. López, M. Muñoz, J.L. González-Carrasco

Title Análisis térmico de nuevos materiales compuestos PLLA/Mg de interés en aplicaciones médicas

Congress **XXXIV Congreso de la Sociedad Ibérica de Biomecánica y Biomateriales.** Córdoba, Spain. November 4th – 5th , 2011

Type Oral presentation

Abstract: El desarrollo de materiales compuestos PLLA/Mg como biomateriales biorreabsorbibles responde a una nueva estrategia para, por una parte, mejorar la bioactividad y las propiedades mecánicas del polímero y, por otra, modular la velocidad de degradación del Mg, sin la necesidad de incorporar elementos de aleación no biocompatibles. El procesado de este tipo de materiales puede abordarse mediante diversas rutas que, en la mayoría de los casos a nivel industrial, incluyen una etapa a temperatura elevada. Resulta entonces de gran interés, el estudio de la estabilidad térmica del material para predecir su comportamiento térmico durante su procesado. El análisis se realiza mediante termogravimetría, TGA, y calorimetría diferencial de barrido, DSC, en materiales con diferentes contenidos de Magnesio haciendo posible vislumbrar el efecto del metal en la degradación térmica y la cristalización del polímero.
